

**A COMPUTATIONAL STUDY OF FLOW
AROUND A ROTATING DISC IN FLIGHT**

DISSERTATION

by

AXEL ROHDE

Submitted to

FLORIDA INSTITUTE OF TECHNOLOGY

In Partial Fulfillment of the
Requirements for the Degree of

DOCTOR OF PHILOSOPHY

in

AEROSPACE ENGINEERING

Melbourne, Florida
December, 2000

Copyright © 2000 Axel Rohde.

All Rights Reserved.

NOTICE:

A digital copy of this dissertation can be downloaded free of charge from the author's website at www.microcfd.com. The file is in portable document format (PDF) and is platform independent. The PDF file is intended for on-screen viewing and reading only. Making physical copies of this dissertation from its printed original, microfilm, or PDF file is expressly prohibited! Hardcopies can be ordered online. The distribution of the PDF file itself, via email, server, or any type of computer media is also prohibited.

To my parents,
For their continued support,
Which has made it all possible.

And to all my teachers, present and past,
For instilling the proper knowledge in me,
Which has enabled me to pursue this path.

BLANK PAGE

We the undersigned committee hereby approve
the attached dissertation by Axel Rohde,

“A Computational Study of Flow around a Rotating Disc in Flight”.



Paavo Sepri, Ph.D.

Associate Professor, Mechanical and Aerospace Engineering Department



Pierre Larochelle, Ph.D., P.E.

Associate Professor, Mechanical and Aerospace Engineering Department



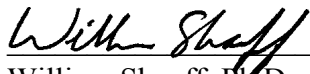
Pei-feng Hsu, Ph.D.

Associate Professor, Mechanical and Aerospace Engineering Department



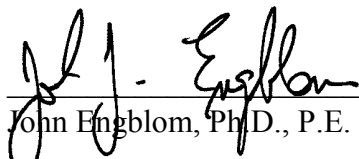
Lakshminarayanan Krishnamurthy, Ph.D.

Professor, Mechanical and Aerospace Engineering Department



William Shoaff, Ph.D.

Professor/Department Head, Computer Science Department



John Engblom, Ph.D., P.E.

Professor/Department Head, Mechanical and Aerospace Engineering Department

ABSTRACT

A COMPUTATIONAL STUDY OF FLOW AROUND A ROTATING DISC IN FLIGHT

Dissertation in Aerospace Engineering by Axel Rohde

Major Advisor: Paavo Sepri, Ph.D.

This dissertation presents a computational fluid dynamics (CFD) study of the flow around a rotating disc in forward flight. The computer model of the disc was an oblate ellipsoid of 6:1 radius ratio, which is similar in shape to common sport discs. The flow was computed on a boundary fitted hexahedral mesh of 60x40x80 cells at a Mach number of 0.5 and a diameter based Reynolds number of 30,000. The angle of attack was held constant at 5 degrees, while the spin ratio, defined as the ratio of rim speed to forward speed, was varied between 0, 0.5, 1, and 1.5.

The numerical algorithm was based on a finite volume description of the unsteady, compressible Navier Stokes equations and incorporated an eigensystem analysis of their inviscid subset. The stability of the fully explicit time marching scheme relied on the total variation diminishing (TVD) principle. No turbulence modeling was implemented, since the flow is predominantly laminar at the prescribed Reynolds number.

The results indicate that flow separation on the aft portion of the disc can be entirely eliminated through rotation, which imparts a centrifugal force on the boundary layer and at the same time increases surface traction around the aft rim. At a spin ratio of 1, a single line of boundary layer separation is curled around the receding rim, where surface traction is minimal. The influence of rotation on aerodynamic forces appears to be weak. Lift peaks slightly at a spin ratio near 0.5, whereas drag grows slowly with increasing rotation rate. The pitching moment is virtually unaffected by rotation. For counter-clockwise spin, a small left steering force is observed.

The software for the computational analysis was developed on a *Windows* PC, equipped with a 1GHz Pentium processor and 384MB of RAM. Restricted by the small integration time step, a single run took nearly two weeks to converge. An installation file for the software as well as data files for all computations can be downloaded from the author's website at www.micro CFD.com. Also available for free download is a complete digital copy of this dissertation in portable document format (PDF).

TABLE OF CONTENTS

LIST OF ILLUSTRATIONS	ix
LIST OF SYMBOLS	x
1. INTRODUCTION	1
1.1 A Brief History	1
1.2 Aerodynamic Overview	1
1.3 Literature Review	3
1.4 Motivation and Objective	4
2. SOLUTION OVERVIEW	7
2.1 Physical System	7
2.2 Mathematical Model	8
2.3 Computational Method	11
2.3.1 The TVD Concept	11
3. PRELIMINARY ANALYSIS	13
3.1 Equations for Inviscid Flow	13
3.2 Eigensystem Analysis	14
3.2.1 Eigenvalues and Right Eigenvectors	14
3.2.2 Left Eigenvectors	16
3.2.3 Eigensystem for 2-D Flow	17
3.2.4 Interpretation of Results	17
3.3 The Shock Tube Problem	19
3.3.1 Analytical Solution	20
3.3.2 Numerical Solution	25
3.3.2.1 ROE Scheme	28
3.3.2.2 TVD Scheme	36
3.3.2.3 ULT Scheme	44

4. SOLUTION DETAIL	53
4.1 Equations for Viscous Flow (FNS)	53
4.2 Curvilinear Coordinate System	55
4.3 Coordinate Transformation	56
4.4 Finite Volume Approximation	58
4.5 Discretization Scheme	60
4.5.1 Boundary Conditions	61
4.5.1.1 Surface Boundary	61
4.5.1.2 Outer Boundary	65
4.5.2 Initial Condition	66
4.5.3 Boundary Layer Resolution	67
4.5.4 Integration Time Step	67
4.6 Aerodynamic Coefficients	68
5. RESULTS	71
5.1 Flow Field	72
5.2 Boundary Layer	73
5.3 Surface Forces	75
5.4 Aerodynamic Data	79
5.5 Conclusion	80
REFERENCES	81
APPENDIX A	83
APPENDIX B	113
APPENDIX C	153

LIST OF ILLUSTRATIONS

Figure 1-1: Aerodynamic Forces Acting on a Frisbee	3
Figure 1-2: Laminar versus Turbulent Flow	5
Figure 2-1: 3-D View of Ellipsoidal Disc	7
Figure 2-2: Cross-Section of 3-D Finite Volume Mesh	8
Figure 3-1: Eigenvector Subspace	18
Figure 3-2: Shock Tube	19
Figure 3-3: Shock Tube Flow at Time $t = 0.25$ (Analytical Solution)	22
Figure 3-4: Finite Volume Model	27
Figure 3-5: Shock Tube Flow at Time $t = 0.25$ (ROE Solution)	30
Figure 3-6: Shock Tube Flow – Wave Diagram (ROE Solution)	33
Figure 3-7: Flux Limiter Function	37
Figure 3-8: Shock Tube Flow at Time $t = 0.25$ (TVD Solution)	38
Figure 3-9: Shock Tube Flow – Wave Diagram (TVD Solution)	41
Figure 3-10: Shock Tube Flow at Time $t = 0.25$ (ULT Solution)	45
Figure 3-11: Shock Tube Flow – Wave Diagram (ULT Solution)	48
Figure 4-1: Local and Global Coordinate System	55
Figure 4-2: Volume of Hexahedron	59
Figure 4-3: Surface Boundary	62
Figure 4-4: Surface Velocity	63
Figure 4-5: Net Force and Moments	68
Figure 5-1: Longitudinal Pressure Comparison	76
Figure 5-2: Longitudinal Traction Comparison	77
Figure 5-3: Traction in Lateral and Oblique Plane	78
Table 5-1: Aerodynamic Data	79

LIST OF SYMBOLS

a	speed of sound	\vec{L}	left eigenvector
\vec{a}	eigenflux component system	$\vec{\vec{L}}$	matrix of left eigenvectors
AR	aspect ratio	L/D	lift-to-drag ratio
\vec{b}	eigenflux component system	\vec{m}	numerical viscosity modifier system
c_p	specific heat at constant pressure	M	Mach number
c_p	coefficient of local surface pressure	\vec{M}	net moment vector
\vec{c}_t	vector coefficient of local traction	\hat{n}	unit normal vector
c_v	specific heat at constant volume	\vec{n}	numerical viscosity modifier system
\vec{c}	artificial compression system	p	pressure
C_{Aft}	aft force coefficient	Pr	Prandtl number
C_{Drag}	drag force coefficient	\vec{q}	heat flux vector
C_{Left}	left force coefficient	q_∞	free-stream dynamic pressure
C_{Lift}	lift force coefficient	\vec{Q}	flow system
C_{Pitch}	pitching moment coefficient	\vec{r}	radius vector
C_{Roll}	rolling moment coefficient	R	gas constant
C_{Up}	up force coefficient	\vec{R}	right eigenvector
C_{Yaw}	yawing moment coefficient	$\vec{\vec{R}}$	matrix of right eigenvectors
dA	differential area	Re	Reynolds number
$d\vec{A}$	differential area vector	s	entropy per unit mass
dV	differential volume	SR	spin ratio
D	diameter	t	time
e	internal energy per unit mass	\vec{t}	traction vector
e_k	kinetic energy per unit mass	T	temperature
\vec{f}	force per unit area vector	TV	total variation
\vec{f}	eigenflux system	u, v, w	Cartesian velocity components
\vec{F}	flux system	\vec{u}	flux correction system
\vec{F}	net force vector	\vec{v}	velocity vector
\vec{g}	flux correction system	\vec{v}_∞	wind vector
h	enthalpy per unit mass	V_∞	wind speed
I, J, K	curvilinear coordinates	x, y, z	Cartesian coordinates
$\vec{\vec{I}}$	identity tensor		
\vec{l}	non-dimensional eigenvalue system		

α	angle of attack
γ	glide angle; ratio of specific heats
δ	boundary layer thickness
ΔA	cell face area
Δn	cell spacing
Δs	entropy change per unit mass
Δt	time step
ΔV	cell volume
ε	numerical viscosity parameter
$\bar{\varepsilon}$	numerical viscosity system
κ	thermal conductivity
λ	eigenvalue
$\bar{\lambda}$	eigenvalue system
μ	viscosity
ρ	density
$\bar{\bar{\sigma}}$	stress tensor
τ	ratio of time step and cell spacing
$\bar{\bar{\tau}}$	viscous stress tensor
Ω	rotation rate
$\bar{\Omega}$	rotation vector

Subscripts

$A.C.$	aerodynamic center
C	contact
CS	control surface
CV	control volume
D	diaphragm
H	head of expansion fan
i, j, k	curvilinear indices
n	normal component
o	stagnation value
S	shock
T	tail of expansion fan
sur	surface value
x, y, z	Cartesian components; metrics
∞	ambient or free-stream value

Superscripts

0	initial value
p	time level

BLANK PAGE

1. INTRODUCTION

This chapter starts with a brief history of flying discs, including an overview of the aerodynamics involved. Thereafter, a short literature review is presented on past research in disc aerodynamics, highlighting some of the major works. The chapter concludes with the original statements of motivation and objectives that were initially proposed.

1.1 A Brief History

The rotary flying disc has been known as early as the ancient Greek Olympics, and it has remained an Olympic discipline ever since that era. The flying disc as a sport became very popular during the latter half of this century with the advent of Frisbees®. Their original shape was derived from pie tins tracing back to the Frisbie Pie Company, which was founded around the turn of the century near Yale University [18]. Throwing empty pie tins, turned upside down, became a popular leisure activity of Yale students during the 1920's. After the Second World War, Frederick Morrison, a resident of Los Angeles, realized the commercial potential of throwing pie tins. As plastic technologies had evolved, he built the prototype of the modern flying disc using butyl stearate. The Wham-O Corporation, a California based toy manufacturer, bought Morrison's idea and coined the trademark "Frisbee" after its predecessor, the "Frisbie" pie tin. Although the shape of the Frisbee was patented by Wham-O, its name became synonymous with many other brands of injection molded plastic sport discs throughout the world. The quest for the perfect aerodynamic shape of a flying disc still continues today. A "perfect" design combines total stability—no steering to either side—with maximum range. Alan Adler, a lecturer at the Stanford University, may have achieved this task by perfecting his version over the past ten years, which is known as the Aerobie Superdisc®.

1.2 Aerodynamic Overview

Aerodynamically, flying discs are intriguing because of their simplicity in shape, which is in direct contrast to their exceptional flying capabilities. A flying disc is both an airfoil and a gyroscope, the former producing lift, and the latter providing stability. From an aerodynamicist's viewpoint, a flying disc is essentially a wing of low aspect ratio. The aspect ratio AR of a wing is defined to be the square of its span divided by the wing's planform area [5],

$$AR = \frac{(\text{Wing Span})^2}{\text{Planform Area}} \quad (1.1)$$

The planform area of a disc is its circular projection, and the span is equal to its diameter D . Thus, the aspect ratio of a disc is simply,

$$AR = \frac{D^2}{\pi (D/2)^2} = \frac{4}{\pi} \approx 1.273 \quad (1.2)$$

Generally, a wing with a high aspect ratio has a high lift-to-drag ratio L/D , and conversely, a low aspect ratio wing is characterized by a low value of L/D . For example, high performance gliders have long wings with aspect ratios as high as forty, and a corresponding lift-to-drag ratio of about forty, whereas for fighter planes, both aspect ratio and maximum lift-to-drag ratio are usually no greater than five [5].

The direct correlation between aspect ratio and maximum lift-to-drag ratio can be explained as follows: whenever a wing produces lift, the difference in pressure levels between the upper and lower surface generates a cross-flow around the wing tips, resulting in wing tip vortices which annihilate a small portion of lift. The greater the aspect ratio, the lesser is the adverse effect of wing tip vortices as compared to the proportion of lift generated by the remaining wing. This explains why sailplanes have such excellent glide performance, and why fighter planes nearly drop out of the sky after engine failure. For unpowered flight, the lift-to-drag ratio is simply equal to the cotangent of the glide angle γ [6],

$$\cot \gamma = \frac{L}{D} \quad (1.3)$$

One would expect the lift-to-drag ratio of a flying disc to be close to unity, because its aspect ratio is not much greater than one, either. For a lift-to-drag ratio between one and two, the corresponding glide angle would lie somewhere between 30 and 45 degrees. Such a steep descent, however, is usually not the case when we look at the flight of a Frisbee from a tall building, for instance. Most discs have a glide angle somewhere between 10 and 20 degrees, which implies a lift-to-drag ratio between three and five. A wind tunnel experiment carried out by students at Brown University, using three different Frisbees, suggests that a lift-to-drag ratio as high as seven or eight can easily be achieved under optimum conditions for angle of attack, wind speed, and rotation rate.

It is needless to point out, that a rotating flying disc possesses considerable aerodynamic efficiency for its low aspect ratio. What makes it even more attractive though, is its gyroscopic nature which enables a stable flight. Without rotation, a Frisbee would act like a wing, and no matter how carefully thrown, it could not maintain steady flight. Due to its angular momentum, however, a rotating disc is able to resist small disturbances in pitch and roll. In contrast, a wing by itself is aerodynamically unstable, which means that even the smallest disturbance from the steady flight equilibrium will result in continuous pitch up or pitch down until the entire wing is stalled. Birds and conventional airplanes have tails to overcome the inherent instability of their wings. The augmented stability of the tail though is at the expense of the negative lift it produces. During steady, level flight, tails push down, which is an inefficiency as far as overall lift is concerned. Flying discs, on the other hand, have their stability “built in” and are thus free from added inefficiencies.

The only type of flight instability experienced by a rotating disc is its tendency to steer to the left or right during forward flight, which stems from the fact that the center of lift does not necessarily coincide with the center of gravity. Depending on the location of the center of lift, which can be either forward or aft with respect to the center of gravity, the disc will experience an aerodynamic pitching moment. Due to gyroscopic precession, however, a pitching moment will result in banking to either side, depending on the sign of the pitching moment and the orientation of the spin. Without using any rigorous mathematical formulation, gyroscopic precession can simply be defined as the 90 degree advancement of a net effect of any force acting normal to the plane of rotation. In other words, the effect which the applied force would have produced on a non-spinning disc will be carried by the spin through a quarter turn.

The disc shown in Figure 1-1 would therefore bank to the right, because its center of lift is slightly aft of the center of gravity, or center of mass. Due to symmetry, the center of mass is located along the axis of rotation. The thrower can compensate this effect by releasing the disc with a small opposite bank angle, which disc enthusiasts often refer to as the *hyzer* angle [18]. A disc thrown with just the right *hyzer* angle will preserve its initial tilt and will also fly along a straight path, similar to an airplane making a low wing approach for a cross wind landing.

Next to the apparent rolling moment, a spinning disc also experiences a minor side force, known as the *Magnus force* [14]. Heinrich Gustav Magnus, a German physicist, discovered in 1852 that the flow of air over a rotating cylinder creates lift, because the difference in flow speed over its top and bottom surface results in a difference in pressure. One can think of a spinning disc as a short section of a rotating cylinder. The Magnus effect is more pronounced for sliced golf balls and tennis balls, which have larger lateral surface areas. For a rotating disc, the side drift due to the Magnus force is hardly noticeable.

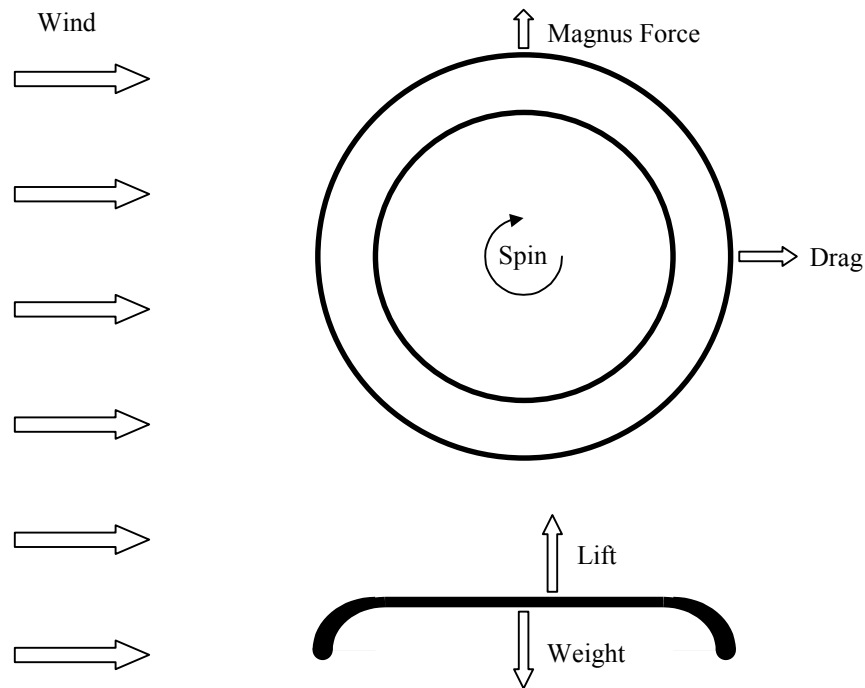


Figure 1-1: Aerodynamic Forces Acting on a Frisbee

1.3 Literature Review

A general description of flying disc aerodynamics, as given above, can be found in many textbooks on disc sport, for example by Shelton [19] and Simon [20]. A comprehensive article on Frisbee aerodynamics was written in 1990 by a former Swiss disc-throwing champion, Macé Schuurmans [18]. The article, published in the popular British journal *New Scientist*, thoroughly explains the aerodynamic forces on Frisbees, their origin, as well as their effect on overall flight dynamics.

Although most interest in flying discs is of purely recreational nature, a few researchers have devoted their time to the subject. In 1960, Mugler and Olstad performed a series of wind tunnel tests at the NASA Langley Research Center, investigating the aerodynamic characteristics of a lenticular shape at transonic speed [12]. At the time, NASA conducted an extensive study of general lifting bodies suitable for reentry vehicles. The non-rotating lenticular shape turned out aerodynamically unstable and was later abandoned.

Along this line of research, Paul Katz published a paper in 1968 in the *Israeli Journal of Technology* [10]. His work, done under the Israeli Ministry of Defense, was focused mainly on stability criteria and flight trajectories rather than disc aerodynamics per se. His research was motivated by the idea that a rotating disc in supersonic flight could be a possible candidate for replacement of ballistic artillery shells.

Another, more modern, military application of a (very slowly) rotating disc in flight is the ellipsoidal radar dome on top of the Boeing 767 Airborne Warning and Control System (AWACS). Unfortunately, no aerodynamic data for the AWACS could be found in the published literature, and a direct request for information made to Boeing turned out unsuccessful.

In 1980, a group of students at Brown University designed and calibrated a wind tunnel force balance for testing of Frisbees. Evaluating three different molds, many measurements of lift and drag were taken for varying wind speed, rotation rate, and angle of attack. As mentioned earlier, the experimental data suggest that excellent lift-to-drag ratios can be achieved—as high as eight—under optimum conditions (see Appendix C). Although this student report is probably the only source of experimental data available on Frisbees, the results have never been published.

The most insight into Frisbee aerodynamics was gained through an experiment performed by two Japanese researchers at Kyushu University in 1989. Nakamura and Fukamachi conducted a wind tunnel flow visualization over a Frisbee mounted on a rotating shaft, utilizing a smoke wire method which they had developed earlier. Their findings were published in 1991 under the title “*Visualization of Flow past a Frisbee*” in the journal *Fluid Dynamics Research* [13]. A video tape of the entire experiment was also made, which can be requested from the address listed with the article.

In summary, Nakamura’s and Fukamachi’s research findings were as follows: The camber of a Frisbee creates a pair of longitudinal vortices near the rim as air flows over it at a vanishing angle of attack. Even when the Frisbee is not rotating, this vortex pair induces considerable downwash, thereby producing lift. The onset of rotation further strengthens this vortex pair, which results in enhanced downwash and increased lift. In addition, the rotation creates a differential in the strength of the two vortices, resulting in a slightly asymmetric flow field.

1.4 Motivation and Objective

It is the author’s opinion that the aerodynamics of rotary flying discs have not been thoroughly studied. Until now, very little analytical or experimental work could be found in the literature [8]. Computational studies on flow past rotating discs are either non-existing, or they have never been published. One reason for the apparent lack of interest for the subject matter in aerodynamic research could be that the application of flying discs has been purely recreational so far.

From the perspective of a fluid dynamicist, however, the rotating disc in flight should be intriguing because of its simple shape, which is in direct contrast to the complex flow pattern surrounding it. What seems even more surprising is the fact that the center of lift nearly coincides with the center of mass for most sport discs, resulting in long-range stability, despite the flow asymmetry induced by the rotation. Moreover, the excellent glide angle of most Frisbees is in direct contrast to their low aspect ratio.

The mystery of disc aerodynamics could possibly be unveiled through a *computational fluid dynamics* (CFD) analysis. The advantages of CFD over traditional wind tunnel testing are manifold: (1) the only necessary hardware needed for testing is a computer; (2) once the governing flow equations are solved around a particular aerodynamic shape, the entire flow field is known in terms of local velocity, pressure, density, and temperature; (3) aerodynamic forces such as lift and drag, as well as any pitching or rolling moments can be easily computed from the solution by integration of the surface forces.

The initial objective of the proposed research was to carry out a CFD analysis for various disc shapes under a multitude of flight conditions, for example, by varying forward speed, rotation rate, and angle of attack. As the development of the computer program progressed, however, it became evident that a single flow simulation at reasonable resolution would take more than two weeks to compute, even on a PC equipped with an Intel 1GHz Pentium processor and 384MB of system RAM. Under these circumstances, the numerical analysis had to be limited to only a few flight configurations of a single, “generic” disc shape. Instead of computing the flow over an actual Frisbee, which is turbulent to a large extent, it was decided to select a more streamlined shape of comparable thickness, an ellipsoid of 6:1 radius ratio. The difference between laminar and turbulent flow for the two shapes is illustrated in Figure 1-2 below. Turbulence modeling—as initially proposed—has therefore been excluded, which resulted in a significant time saving.

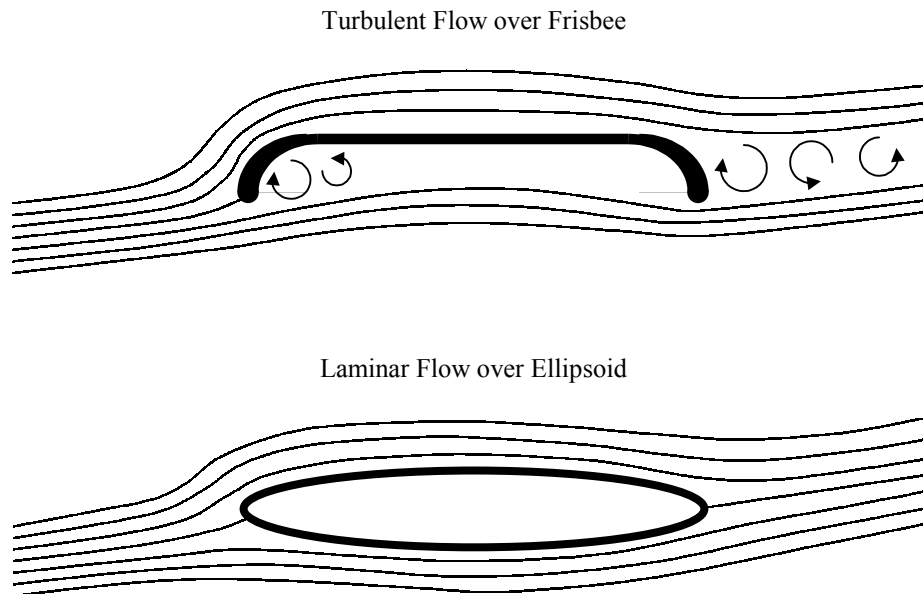


Figure 1-2: Laminar versus Turbulent Flow

A few more compromises had to be made in order to reduce the computation time to two weeks for a single run. The flow Reynolds number, a dimensionless ratio measuring inertial to viscous effects, was reduced by nearly a factor of six from the typical value associated with common sport discs. As a result, the average boundary layer thickness approximately doubled, which eased the resolution requirement near the disc’s surface. Also, despite the fact that the flow over Frisbees is in the incompressible range ($M < 0.1$), it was decided to develop a compressible flow solver—which is more physical—and run the simulation at a Mach number of 0.5 instead. In subsonic flow, the effect of compressibility on boundary layer growth is minimal. Although the higher Mach number increases the pressure range, the relative pressure distribution at $M = 0.5$ is comparable to that of an incompressible flow field, and thus aerodynamic coefficients are similar in both regimes. For a compressible flow solver, the total computation time decreases with increasing Mach number, which is why the higher Mach number was chosen.

Upon conclusion of the study, a few fundamental questions are addressed, including the following: How does the rotation rate affect lift and drag? Does the aerodynamic center move through the onset of rotation, and if so, what is the effect on flight stability? How does rotation influence boundary layer growth and flow separation? Can the experimental research findings—particularly the flow visualization of Nakamura and Fukamachi—be verified, and to what degree?

BLANK PAGE

2. SOLUTION OVERVIEW

This chapter contains a brief overview of the basic physical system and mathematical model for the computation of flow over a rotating disc in forward flight. Also included is a general outline of the computational method for solving the governing equations, explaining the main underlying concept. The details of the mathematical description and algorithm development are presented in the following chapters.

2.1 Physical System

The shape of our “generic” disc, represented by an ellipsoid of 6:1 radius ratio, is depicted in Figure 2-1. Typically, an ellipsoid is generated through the rotation of an ellipse around its major or minor axis. Rotation around the major axis produces a *prolate* ellipsoid, comparable to the shape of a submarine, whereas rotation around the minor axis results in an *oblate* ellipsoid, or disc. The disc shown below is the actual computer model used in all computations. Its dimension and flight parameters were chosen to roughly match the flow Reynolds number and spin ratio—and thus the boundary layer effects—of common sport discs. According to Macé Schuurmans [18], the typical forward speed of a Frisbee generally ranges between 5 and 15 m/s at a rotation rate of about 5 to 15 revolutions per second, depending on the thrower. Thus an average spin ratio SR , defined as the ratio of rim speed to forward speed, for a sport disc would be,

$$SR = \frac{\pi D f}{V_\infty} = \frac{\pi (0.25\text{m})(10\text{rps})}{(10\text{m/s})} \approx 0.8 \quad (2.1)$$

For the same disc diameter D and forward speed V_∞ , and based on a viscosity μ , density ρ_∞ , and speed of sound a_∞ of air at sea-level conditions, the corresponding flow Reynolds and Mach number would be,

$$Re = \frac{\rho_\infty V_\infty D}{\mu} = \frac{(1.225\text{kg/m}^3)(10\text{m/s})(0.25\text{m})}{(1.7894 \times 10^{-5}\text{kg m}^{-1}\text{s}^{-1})} \approx 170,000 \quad (2.2)$$

$$M = \frac{V_\infty}{a_\infty} = \frac{10\text{m/s}}{340\text{m/s}} \approx 0.03 \quad (2.3)$$

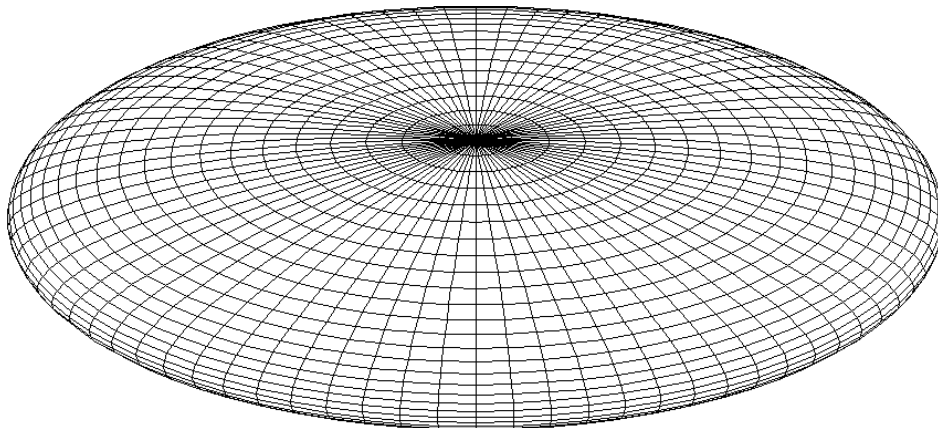


Figure 2-1: 3-D View of Ellipsoidal Disc

For small angles of attack, $\alpha \leq 5^\circ$, the flow over our ellipsoidal disc shall be assumed fully laminar, implying that no turbulence shall be present, neither in boundary layer nor wake. Transition to turbulence generally does not occur at Reynolds numbers below 300,000 for streamlined bodies [17]. In order to accelerate convergence of the computation, the flow Mach number was not matched in our analysis, which only has a minimal effect on boundary layer growth in fully subsonic flow. All computations were carried out at a Mach number of $M = 0.5$ and a reduced flow Reynolds number of $Re = 30,000$. The angle of attack was held fixed at 5 degrees, while the spin ratio was varied between 0, 0.5, 1, and 1.5.

2.2 Mathematical Model

The CFD analysis of our rotating disc in forward flight is based on a finite volume description of the unsteady, compressible Navier Stokes equations, solved on a boundary fitted, curvilinear, structured mesh. A longitudinal cut through the actual finite volume mesh used in all computations is shown in Figure 2-2. The finite “volumes” consist of hexahedral cells—distorted cubes, some of them compressed—which are generated when the 2-D mesh shown below is rotated around its vertical axis of symmetry. Cells near the surface are highly flattened, in order to resolve the strong gradients present within the boundary layer. Flow gradients weaken as one moves further away from the disc, and at the spherical outer boundary, which is several disc diameters away from the center of the disc, the flow is assumed to be undisturbed.

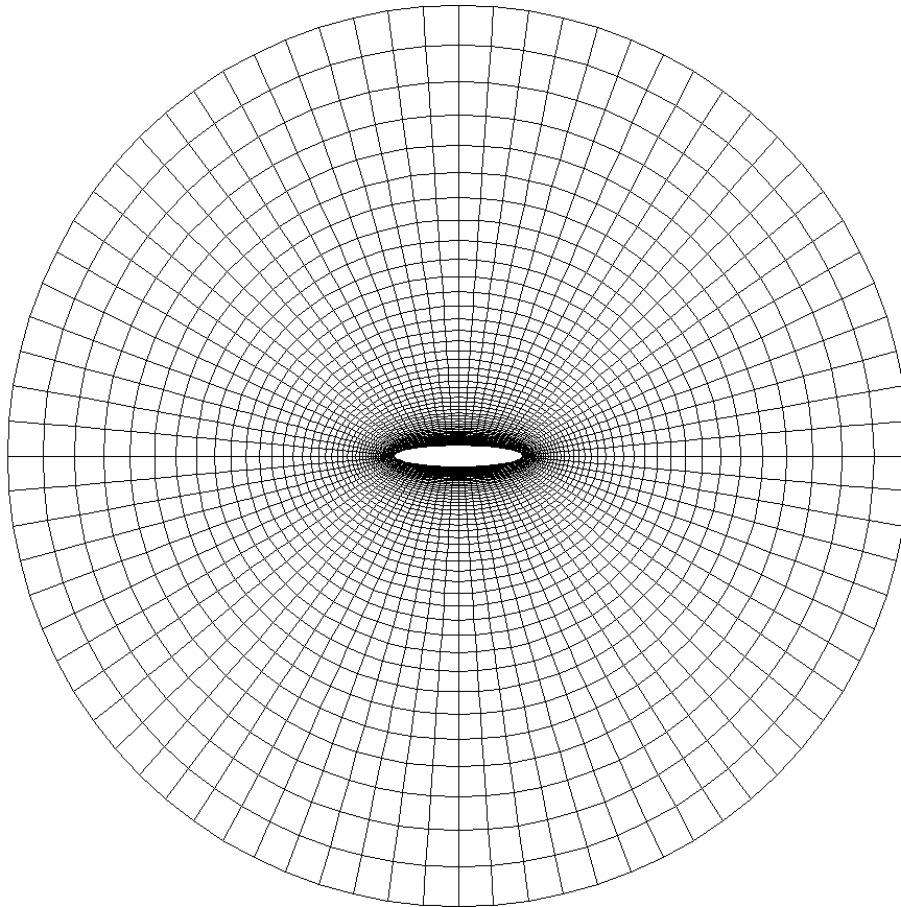


Figure 2-2: Cross-Section of 3-D Finite Volume Mesh

It is important to point out that the mesh remains fixed in space at all times. Whether or not the disc is rotating solely affects the surface boundary condition. Therefore, the governing flow equations for an inertial frame of reference can be used. For a calorically perfect gas—constant specific heats—with negligible body forces, the five conservation equations are stated below in a coordinate independent integral format (note that the momentum equation is a vector equation with three components). Collectively, these equations are referred to in the literature as the “full” Navier Stokes equations (FNS).

Mass:

$$\frac{\partial}{\partial t} \int_{CV} \rho dV + \oint_{CS} \rho \vec{v} \cdot d\vec{A} = 0 \quad (2.4)$$

Momentum:

$$\frac{\partial}{\partial t} \int_{CV} \vec{v} \rho dV + \oint_{CS} \vec{v} \rho \vec{v} \cdot d\vec{A} = \oint_{CS} \vec{\sigma} \cdot d\vec{A} \quad (2.5)$$

Energy:

$$\frac{\partial}{\partial t} \int_{CV} \rho e_o dV + \oint_{CS} \rho e_o \vec{v} \cdot d\vec{A} = \oint_{CS} (\vec{\sigma} \cdot \vec{v} - \vec{q}) \cdot d\vec{A} \quad (2.6)$$

The integral subscripts CV and CS represent cell volume and cell surface, respectively. The vector differential $d\vec{A} = \hat{n} dA$ incorporates the outward unit normal into its differential surface. Based on a local fluid density ρ , the stagnation energy per unit mass e_o is defined as the sum of internal and kinetic energy,

$$e_o = c_v T + \frac{1}{2} \vec{v} \cdot \vec{v} \quad (2.7)$$

The general stress tensor $\vec{\sigma}$ can be split into two parts, one relating to the thermodynamic pressure p using the identity tensor \vec{I} , the other part being the viscous stress tensor $\vec{\tau}$,

$$\vec{\sigma} = \vec{\tau} - p \vec{I} \quad (2.8)$$

Assuming a constant coefficient of viscosity μ , the viscous stress tensor $\vec{\tau}$ is a function of velocity gradients, and based on a locally orthogonal frame of reference can be expressed as follows,

$$\vec{\tau} = \mu \left(\nabla \vec{v} + (\nabla \vec{v})^T \right) - \vec{I} \frac{2}{3} \mu \nabla \cdot \vec{v} \quad (2.9)$$

where $\nabla \vec{v}$ and its transpose shall be recognized as dyadic products between velocity vector and gradient operator. A zero bulk viscosity $\mu' = \lambda + \frac{2}{3} \mu$ is implied in Equation (2.9) according to Stokes' hypothesis.

The heat flux vector \vec{q} can be related to its temperature gradient via Fourier's law of heat conduction, where the thermal conductivity κ shall be assumed constant,

$$\vec{q} = -\kappa \nabla T \quad (2.10)$$

Density, pressure, and temperature are connected by the perfect gas law, where the gas constant R is the difference between the specific heats at constant pressure and constant volume, c_p and c_v , respectively,

$$p = \rho R T \quad (2.11)$$

$$R = c_p - c_v \quad (2.12)$$

Further, the thermal conductivity κ can be related to the dynamic viscosity μ via the Prandtl number Pr ,

$$\kappa = \frac{c_p}{Pr} \mu \quad (2.13)$$

Based on kinetic gas theory, the Prandtl number for air, which is primarily a mixture of diatomic gases, can be determined through Eucken's relation [22],

$$Pr = \frac{4\gamma}{9\gamma - 5} \quad (2.14)$$

where,

$$\gamma = \frac{c_p}{c_v}$$

For air, $\gamma = 7/5 = 1.4$, and thus $Pr = 28/38 = 0.74$. A Prandtl number near unity implies that momentum and thermal diffusion in a gas both occur on the same scale. In practical terms, it means that the thin thermal and velocity boundary layers near a heated aerodynamic surface roughly coincide.

With the above constitutive relations, the system of integral conservation equations is now closed. We have five equations for five unknowns: three velocity components and two thermodynamic state variables, such as pressure and temperature. In order to obtain a solution, we still need an initial condition and two sets of boundary conditions, one for the disc surface, and the other for the far-field outer boundary.

The initial condition of the flow is somewhat arbitrary and should not influence the steady state solution. However, it is common practice to simply initialize the flow properties at all interior volume cells with their free stream values. Physically, this would represent an impulsive start of the disc from rest.

The free stream boundary condition—as the name implies—simply forces the flow properties at the outer boundary to their free-stream values, i.e., uniform velocity according to the general flow direction, as well as uniform pressure and temperature depending on ambient conditions. The gradients of all flow properties are set to zero at the outer boundary, which is consistent with the idea of undisturbed uniform flow.

The surface boundary condition is expressed in two parts, a *no-slip* condition for the velocity components, and a *no-flux* condition for the energy exchange. The no-slip condition implies that fluid particles in contact with the surface have no relative velocity with respect to it—they literally *stick* to the surface. For a rotating disc, there is a non-zero velocity component—with respect to the fixed frame of reference—in the tangential direction. The radial and normal velocity components at the surface, however, are always zero. The no-flux condition requires that no heat is exchanged between the disc and the surrounding fluid, or in other words, the disc is perfectly insulated. As a result, the temperature at the surface will not be uniform, but rather be equal to that of the nearby fluid.

2.3 Computational Method

The conservation equations are solved numerically in their finite volume format, by starting with an initial condition of uniform flow, which is equivalent to an instantaneous acceleration of the disc from rest. By explicitly marching in time, the flow field is then integrated until an asymptotic state is achieved. The term “asymptotic” implies that the converged solution may not be frozen in time, but rather experience small periodic oscillations near the surface and within the wake. This phenomenon is physically consistent with the continuous shedding of vortices that may take place, depending on the flow Reynolds number. Once the flow is fully accelerated and developed, rotation is added in finite increments by altering the surface boundary condition. In between angular accelerations, the solution is again marched in time until a new steady or asymptotic state sets in.

The spatial discretization of the fluxes involved in each integration time step is modeled according to the *total variation diminishing* (TVD) concept, which is explained in more detail in the following subsection. The TVD algorithm employed in this program is essentially comprised of two parts: centrally split fluxes, which are equivalent to a central difference formula within a finite difference context, and small corrective *eigenfluxes*, whose function is to limit the overall flux exchange such that stability of the computation is always guaranteed. The centrally split fluxes by themselves contain no numerical viscosity, and their unrestrained flux would quickly lead to numerical oscillations in the flow field and subsequent divergence. The eigenfluxes, however, prevent these oscillations by recognizing the local wave character through an eigensystem analysis and appropriately limiting the flux exchange. Earlier numerical schemes, such as the popular flux vector splitting (FVS) algorithms, contain a hefty amount of inherent *numerical viscosity*, which dampen unwanted oscillations within the flow field, but also smear boundary layer gradients beyond recognition. The TVD schemes, on the other hand, are designed such that the amount of numerical viscosity can either be determined through a control parameter, or minimized by setting such parameter equal to zero. This feature makes the TVD algorithms highly desirable for compressible viscous flow computations, because of their ability to preserve strong gradients within boundary layers.

2.3.1 The TVD Concept

To better grasp the total variation diminishing (TVD) concept, we shall briefly shift our focus away from the more complex FNS equations to a much simpler model equation. Written in differential form, we shall consider the following one-dimensional conservation equation for general *waves*,

$$\frac{\partial u}{\partial t} + \frac{\partial f(u)}{\partial x} = 0 \quad (2.15)$$

For $f(u) = au$, with $a > 0$ being a constant, Equation (2.15) would be the well known linear wave equation. If the wave speed a is not a constant, but rather a function of u or x , or both, then the wave is nonlinear. Physically, the difference between a linear and nonlinear wave is as follows: a linear wave always preserves its own character, in other words, its initial shape, or waveform remains unchanged as it travels through a quiescent medium. In comparison, a nonlinear wave generally becomes distorted while traveling. For example, a nonlinear wave that started out as a single sinusoid could either become expanded over time—and ultimately vanish through attenuation—or undergo compression and eventually turn into a square wave. For now, visualize the variation of u along x over a period of time for such a traveling wave. Except for square waves, where a one-sided limit applies, both u and its derivative, $\partial u/\partial x$, are known at any given point in space. An interesting property of physical solutions governed by Equation (2.15) is that $|\partial u/\partial x|$ integrated over the entire domain along x does not increase with time for fixed boundary conditions. This integrated quantity is referred to as the total variation, and shall be denoted by TV ,

$$TV = \int \left| \frac{\partial u}{\partial x} \right| dx \quad (2.16)$$

Thus for a physically correct solution to Equation (2.15), TV does not increase with time. In practical terms, this implies that although a waveform can change its character, it cannot grow over time, i.e., maxima cannot increase, and minima cannot decrease. Also, the amount of oscillation within a solution can only decrease over a time period, e.g., a maximum cannot split into two maxima and a minimum. For a numerical solution of Equation (2.15), in which $\partial u/\partial x$ can be discretized by $(u_{i+1} - u_i)/\Delta x$, Equation (2.16) can be rewritten as,

$$TV(u) = \sum_i |u_{i+1} - u_i| \quad (2.17)$$

Equation (2.17) defines the total variation in x of a discrete numerical solution. If $TV(u^p)$ and $TV(u^{p+1})$ represent Equation (2.17) at subsequent time levels, a numerical algorithm is total variation diminishing, if

$$TV(u^{p+1}) \leq TV(u^p) \quad (2.18)$$

Therefore, any numerical scheme that follows the physical behavior of a conservation equation of the general form given by Equation (2.15) must be a TVD scheme. The TVD property implies, both physically and numerically, that the amount of variation present within a solution at any time is limited by its initial and boundary conditions. This concept will become clear in the next chapter, when different TVD schemes are applied to the one-dimensional, inviscid flow within a *shock tube*.

3. PRELIMINARY ANALYSIS

An important subset of the full Navier Stokes (FNS) equations is introduced in this chapter: the Euler equations of inviscid flow. The FNS equations inherit their wave-like character directly from the Euler equations, which will become evident in an eigensystem analysis. In eigenvector format, the conservation equations of inviscid flow fit the general form of a wave equation, for which the TVD concept can be readily utilized. Based on the general three-dimensional results of the analysis, the equation subset for one-dimensional inviscid flow is then applied to the shock tube problem, which will illustrate the wave character of the equations. Different TVD algorithms are presented from a literature review and are individually applied to solve the flow within a shock tube. The numerical results from each computation are compared to an analytical solution of the shock tube problem in order to evaluate each algorithm. The derivation of the eigensystem for the Euler equations was aided by the analysis software *Mathematica* from Wolfram Research, Inc. Similar results found in the literature [23-26] are less compact.

3.1 Equations for Inviscid Flow

The conservation equations for inviscid flow, which are commonly referred to as the Euler equations, are derived from the FNS equations by eliminating the viscous stress tensor and heat flux vector. This can be accomplished by simply setting the dynamic viscosity μ equal to zero—thus the name *inviscid*. For the subsequent eigensystem analysis, it is advantageous to write the Euler equations in a column vector format, where each column represents the full set of conserved properties—mass, momentum, and energy. Note that all column vectors, being five dimensional, are denoted by half arrows and are thus distinguishable from three-dimensional physical vectors. Written in compact column format, the Euler equations are,

$$\frac{\partial}{\partial t} \int_{CV} \bar{Q} dV + \oint_{CS} \bar{F} dA = 0 \quad (3.1)$$

where,

$$\bar{Q} = \begin{bmatrix} \rho \\ \rho u \\ \rho v \\ \rho w \\ \rho e_o \end{bmatrix}, \quad \bar{F} = \begin{bmatrix} \rho v_n \\ \rho u v_n + p n_x \\ \rho v v_n + p n_y \\ \rho w v_n + p n_z \\ \rho h_o v_n \end{bmatrix}$$

The velocity across a cell boundary is simply defined as the dot product of local velocity vector and outward unit normal vector to the boundary,

$$v_n = \bar{v} \cdot \hat{n} = u n_x + v n_y + w n_z, \quad n_x^2 + n_y^2 + n_z^2 = 1 \quad (3.2)$$

The stagnation energy and enthalpy per unit mass are the sum of static and dynamic parts, respectively,

$$e_o = e + e_k, \quad h_o = h + e_k \quad (3.3)$$

$$e_k = \frac{1}{2} (u^2 + v^2 + w^2)$$

with e_k being the kinetic energy per unit mass. Static energy, enthalpy, and pressure can all be expressed in terms of the local speed of sound a , a function of temperature, and the ratio of specific heats γ ,

$$e = \frac{a^2}{\gamma(\gamma-1)}, \quad h = \frac{a^2}{\gamma-1}, \quad p = \frac{\rho a^2}{\gamma} \quad (3.4)$$

where,

$$a^2 = \gamma R T, \quad \gamma = c_p / c_v$$

3.2 Eigensystem Analysis

The first step in determining the eigensystem of the above conservation equations is to derive the corresponding Jacobian or transformation matrix, which can be found by taking partial derivatives of the flux vector components F_i with respect to the flow vector components Q_j after expressing the flux vector solely in terms of the flow vector. Only the resulting transformation matrix shall be presented here,

$$[A] = \frac{\partial F_i}{\partial Q_j} = \begin{bmatrix} 0 & n_x & n_y & n_z & 0 \\ (\gamma-1)e_k n_x - u v_n & v_n - (\gamma-2)u n_x & u n_y - (\gamma-1)v n_x & u n_z - (\gamma-1)w n_x & (\gamma-1)n_x \\ (\gamma-1)e_k n_y - v v_n & v n_x - (\gamma-1)u n_y & v_n - (\gamma-2)v n_y & v n_z - (\gamma-1)w n_y & (\gamma-1)n_y \\ (\gamma-1)e_k n_z - w v_n & w n_x - (\gamma-1)u n_z & w n_y - (\gamma-1)v n_z & v_n - (\gamma-2)w n_z & (\gamma-1)n_z \\ [(\gamma-1)e_k - h_o]v_n & h_o n_x - (\gamma-1)u v_n & h_o n_y - (\gamma-1)v v_n & h_o n_z - (\gamma-1)w v_n & \gamma v_n \end{bmatrix} \quad (3.5)$$

We can now rewrite the Euler equations in the format of a general wave equation,

$$\frac{\partial}{\partial t} \int_{CV} \bar{Q} dV + \oint_{CS} \bar{F}(\bar{Q}) dA = 0 \quad (3.6)$$

where,

$$\bar{F}(\bar{Q}) = [A]\bar{Q}$$

Analogous to the wave speed a of the 1-D model equation presented in Section 2.3.1, the transformation matrix $[A]$ can be interpreted as a wave speed with local and directional dependence for a nonlinear multi-dimensional wave. The multi-dimensional character is really twofold: (1) we are now working in a 3-D flow field, where waves can travel in any direction; (2) there are different types of waves, all traveling at their own characteristic speeds, which are determined by the *eigenvalues* of the transformation matrix $[A]$.

3.2.1 Eigenvalues and Right Eigenvectors

The eigenvalues of the transformation matrix $[A]$ are the roots λ_i of the characteristic equation,

$$\det([A] - \lambda[I]) = 0 \quad (3.7)$$

where $[I]$ is the identity matrix. It turns out that three eigenvalues are distinct and two are repeated,

$$\lambda_i = \{v_n - a, v_n, v_n + a, v_n, v_n\} \quad (3.8)$$

Each right eigenvector \bar{R}_i , corresponding to eigenvalue λ_i , must satisfy the following matrix equation,

$$[A] \bar{R}_i = \lambda_i \bar{R}_i \quad (3.9)$$

Being column vectors, the right eigenvectors can be collectively written in matrix form, such that,

$$(R-1): \quad [R] = [\bar{R}_1 \quad \bar{R}_2 \quad \bar{R}_3 \quad \bar{R}_4 \quad \bar{R}_5] = \begin{bmatrix} 1 & 1 & 1 & 0 & 0 \\ u - a n_x & u & u + a n_x & n_y & -n_z \\ v - a n_y & v & v + a n_y & -n_x & 0 \\ w - a n_z & w & w + a n_z & 0 & n_x \\ h_o - a v_n & e_k & h_o + a v_n & u n_y - v n_x & w n_x - u n_z \end{bmatrix} \quad (3.10)$$

It should be noted at this point that the eigenvectors of repeated eigenvalues are not distinct! They span a subspace and any vector within this subspace is also an eigenvector of the same repeated eigenvalue. In the general space \mathbb{R}^5 above—for which \bar{R}_1 through \bar{R}_5 form a basis—the eigenvectors \bar{R}_4 and \bar{R}_5 , which belong to the repeated eigenvalues $\lambda_4 = \lambda_5 = v_n$, span a two dimensional subspace. Any linear combination of \bar{R}_4 and \bar{R}_5 is itself a member of that subspace and is thus also an eigenvector. For example, a sixth eigenvector, which would satisfy the equation $[A] \bar{R}_6 = \lambda_2 \bar{R}_6$, could be formed as follows,

$$\bar{R}_6 = \left(\frac{-n_z}{n_x} \right) \bar{R}_4 + \left(\frac{-n_y}{n_x} \right) \bar{R}_5 = \begin{bmatrix} 0 \\ 0 \\ n_z \\ -n_y \\ v n_z - w n_y \end{bmatrix} \quad (3.11)$$

The following sets of right eigenvectors, again written in matrix format, are equally valid with (R-1),

$$(R-2): \quad [R] = [\bar{R}_1 \quad \bar{R}_2 \quad \bar{R}_3 \quad \bar{R}_4 \quad \bar{R}_6] = \begin{bmatrix} 1 & 1 & 1 & 0 & 0 \\ u - a n_x & u & u + a n_x & n_y & 0 \\ v - a n_y & v & v + a n_y & -n_x & n_z \\ w - a n_z & w & w + a n_z & 0 & -n_y \\ h_o - a v_n & e_k & h_o + a v_n & u n_y - v n_x & v n_z - w n_y \end{bmatrix} \quad (3.12)$$

$$(R-3): \quad [R] = [\bar{R}_1 \quad \bar{R}_2 \quad \bar{R}_3 \quad \bar{R}_5 \quad \bar{R}_6] = \begin{bmatrix} 1 & 1 & 1 & 0 & 0 \\ u - a n_x & u & u + a n_x & -n_z & 0 \\ v - a n_y & v & v + a n_y & 0 & n_z \\ w - a n_z & w & w + a n_z & n_x & -n_y \\ h_o - a v_n & e_k & h_o + a v_n & w n_x - u n_z & v n_z - w n_y \end{bmatrix} \quad (3.13)$$

3.2.2 Left Eigenvectors

The set of left eigenvectors can be determined from the inverse of the right eigenvector matrix, $[L]=[R]^{-1}$. For the first set of right eigenvectors (R-1), the matching set of left eigenvectors written in matrix format is,

$$(L-1): \quad [L] = \begin{bmatrix} \bar{L}_1 \\ \bar{L}_2 \\ \bar{L}_3 \\ \bar{L}_4 \\ \bar{L}_5 \end{bmatrix} = \begin{bmatrix} \frac{(\gamma-1)e_k + av_n}{2a^2} & \frac{(1-\gamma)u - an_x}{2a^2} & \frac{(1-\gamma)v - an_y}{2a^2} & \frac{(1-\gamma)w - an_z}{2a^2} & \frac{\gamma-1}{2a^2} \\ \frac{a^2 - (\gamma-1)e_k}{a^2} & \frac{(\gamma-1)u}{a^2} & \frac{(\gamma-1)v}{a^2} & \frac{(\gamma-1)w}{a^2} & \frac{1-\gamma}{a^2} \\ \frac{(\gamma-1)e_k - av_n}{2a^2} & \frac{(1-\gamma)u + an_x}{2a^2} & \frac{(1-\gamma)v + an_y}{2a^2} & \frac{(1-\gamma)w + an_z}{2a^2} & \frac{\gamma-1}{2a^2} \\ \frac{v - v_n n_y}{n_x} & n_y & \frac{n_y^2 - 1}{n_x} & \frac{n_y n_z}{n_x} & 0 \\ \frac{v_n n_z - w}{n_x} & -n_z & \frac{-n_y n_z}{n_x} & \frac{1 - n_z^2}{n_x} & 0 \end{bmatrix} \quad (3.14)$$

Being row vectors, the left eigenvectors are denoted by a left pointing half arrow. Each left eigenvector and corresponding eigenvalue satisfy the following matrix equation, and thus bear the name ‘‘left’’ eigenvector,

$$\bar{L}_i [A] = \lambda_i \bar{L}_i \quad (3.15)$$

The above left eigenvector matrix becomes singular for $n_x = 0$, and simply multiplying the last two rows by n_x does not alleviate the problem; the matrix remains singular along certain directions, and a zero row vector emerges. It turns out that the inverse matrix of the second and third set of right eigenvectors, (R-2) and (R-3), yield a similar result, carrying the singularity in the n_y and n_z component, respectively,

$$(L-2): \quad [L] = \begin{bmatrix} \bar{L}_1 \\ \bar{L}_2 \\ \bar{L}_3 \\ \bar{L}_6 \\ \bar{L}_7 \end{bmatrix} = \begin{bmatrix} \frac{(\gamma-1)e_k + av_n}{2a^2} & \frac{(1-\gamma)u - an_x}{2a^2} & \frac{(1-\gamma)v - an_y}{2a^2} & \frac{(1-\gamma)w - an_z}{2a^2} & \frac{\gamma-1}{2a^2} \\ \frac{a^2 - (\gamma-1)e_k}{a^2} & \frac{(\gamma-1)u}{a^2} & \frac{(\gamma-1)v}{a^2} & \frac{(\gamma-1)w}{a^2} & \frac{1-\gamma}{a^2} \\ \frac{(\gamma-1)e_k - av_n}{2a^2} & \frac{(1-\gamma)u + an_x}{2a^2} & \frac{(1-\gamma)v + an_y}{2a^2} & \frac{(1-\gamma)w + an_z}{2a^2} & \frac{\gamma-1}{2a^2} \\ \frac{v_n n_x - u}{n_y} & \frac{1 - n_x^2}{n_y} & -n_x & \frac{-n_x n_z}{n_y} & 0 \\ \frac{w - v_n n_z}{n_y} & \frac{n_x n_z}{n_y} & n_z & \frac{n_z^2 - 1}{n_y} & 0 \end{bmatrix} \quad (3.16)$$

$$(L-3): \quad [L] = \begin{bmatrix} \bar{L}_1 \\ \bar{L}_2 \\ \bar{L}_3 \\ \bar{L}_8 \\ \bar{L}_9 \end{bmatrix} = \begin{bmatrix} \frac{(\gamma-1)e_k + av_n}{2a^2} & \frac{(1-\gamma)u - an_x}{2a^2} & \frac{(1-\gamma)v - an_y}{2a^2} & \frac{(1-\gamma)w - an_z}{2a^2} & \frac{\gamma-1}{2a^2} \\ \frac{a^2 - (\gamma-1)e_k}{a^2} & \frac{(\gamma-1)u}{a^2} & \frac{(\gamma-1)v}{a^2} & \frac{(\gamma-1)w}{a^2} & \frac{1-\gamma}{a^2} \\ \frac{(\gamma-1)e_k - av_n}{2a^2} & \frac{(1-\gamma)u + an_x}{2a^2} & \frac{(1-\gamma)v + an_y}{2a^2} & \frac{(1-\gamma)w + an_z}{2a^2} & \frac{\gamma-1}{2a^2} \\ \frac{u - v_n n_x}{n_z} & \frac{n_x^2 - 1}{n_z} & \frac{n_x n_y}{n_z} & n_x & 0 \\ \frac{v_n n_y - v}{n_z} & \frac{-n_x n_y}{n_z} & \frac{1 - n_y^2}{n_z} & -n_y & 0 \end{bmatrix} \quad (3.17)$$

Depending on the direction of the unit normal vector, a singularity in the left eigenvectors can thus be avoided by choosing the appropriate matrix. To minimize numerical error during the computation, the largest component of the normal vector—measured by its absolute value—should always be located in the denominator.

3.2.3 Eigensystem for 2-D Flow

The transformation matrix and complete eigensystem for 2-dimensional flow can easily be derived from the more general 3-dimensional result by eliminating appropriate rows and columns within the matrices and simplifying the remainder by setting $w = n_z = 0$. For example, the transformation matrix $[A]$ for 2-D flow is obtained after eliminating the fourth row and fourth column, and by redefining some of the quantities involved,

$$v_n = \vec{v} \cdot \hat{n} = u n_x + v n_y, \quad n_x^2 + n_y^2 = 1 \quad (3.18)$$

$$e_k = \frac{1}{2} (u^2 + v^2) \quad (3.19)$$

The set of eigenvalues reduces to the first four, $\lambda_i = \{v_n - a, v_n, v_n + a, v_n\}$, only one being repeated.

Choosing the first set of eigenvectors, both left and right, the matrix of right eigenvectors for 2-D flow is obtained after eliminating the fourth row and fifth column from the general result, whereas the left eigenvector matrix is found by deleting the fifth row and fourth column from its original 5x5 matrix. It is interesting to note that after applying the above 2-D definitions, the singularities in the last row of the new 4x4 left eigenvector matrix disappear! The first and third element of the fourth row can be simplified to,

$$\frac{v - v_n n_y}{n_x} = \frac{v - (u n_x + v n_y) n_y}{n_x} = \frac{v - u n_x n_y - v (1 - n_x^2)}{n_x} = v n_x - u n_y \quad (3.20)$$

$$\frac{n_y^2 - 1}{n_x} = \frac{-n_x^2}{n_x} = -n_x \quad (3.21)$$

3.2.4 Interpretation of Results

It was demonstrated earlier that two of the five right eigenvectors form a 2-dimensional subspace, within the general 5-dimensional space spanned by all right eigenvectors, and that every member of this subspace is itself an eigenvector. This phenomenon was attributed to the fact that their corresponding eigenvalues are repeated, which creates a “symmetry” within the eigenvector space. Although it may seem difficult to visualize any symmetry within a 5-dimensional vector space, part of this symmetry reveals itself when we geometrically interpret the 2-dimensional subspace as a plane. The eigenvectors \vec{R}_4 , \vec{R}_5 , and \vec{R}_6 shall now demonstrate this effect. Upon careful observation, they can be recast as shown in Equation (3.22), where \vec{t}_x , \vec{t}_y , and \vec{t}_z are tangent vectors which all lie in the plane defined by the unit normal vector \hat{n} ; their subscripts denote the vanishing component along the corresponding major axis, which can clearly be seen in Figure 3-1. Although all tangent vectors are depicted with equal length, they are not unit vectors and thus carry the standard vector symbol rather than the caret. Needless to say, the orthogonality relation holds between the tangent vectors and the surface unit normal, which is restated in Figure 3-1.

$$\bar{R}_4 = \begin{bmatrix} 0 \\ n_y \\ -n_x \\ 0 \\ un_y - vn_x \end{bmatrix} = \begin{bmatrix} 0 \\ \bar{t}_z \\ \bar{v} \cdot \bar{t}_z \end{bmatrix}, \quad \bar{R}_5 = \begin{bmatrix} 0 \\ -n_z \\ 0 \\ n_x \\ wn_x - un_z \end{bmatrix} = \begin{bmatrix} 0 \\ \bar{t}_y \\ \bar{v} \cdot \bar{t}_y \end{bmatrix}, \quad \bar{R}_6 = \begin{bmatrix} 0 \\ 0 \\ n_z \\ -n_y \\ vn_z - wn_y \end{bmatrix} = \begin{bmatrix} 0 \\ \bar{t}_x \\ \bar{v} \cdot \bar{t}_x \end{bmatrix} \quad (3.22)$$

It was shown earlier that \bar{R}_6 can be expressed as a linear combination of \bar{R}_4 and \bar{R}_5 . Geometrically, this implies that for each normal vector only two tangent vectors are needed to define the same plane. Any two tangent vectors rotated around the unit normal vector \hat{n} will result in another set of equally valid tangent vectors defining the same planar surface. The unit normal vector, being the axis of rotation, can thus be seen as the axis of symmetry for the vector space defined.

$$\hat{n} \cdot \bar{t}_x = \hat{n} \cdot \bar{t}_y = \hat{n} \cdot \bar{t}_z = 0$$

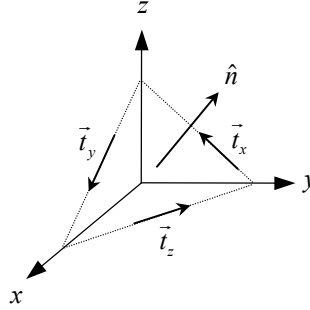


Figure 3-1: Eigenvector Subspace

What has been omitted so far is the physical interpretation of the eigenvectors themselves. In simple terms, which way do the eigenvectors point? It was mentioned earlier that the different speeds at which waves travel through the flow field are determined by their eigenvalues. The direction of wave travel has already been specified by the unit vector \hat{n} normal to the surface under consideration—recall that we are trying to determine the magnitude of the mass, momentum, and energy flux across a given surface element.

The Euler equations contain three types, or families of waves, one for every distinct eigenvalue. Each family of waves carries a different *signal*. The waves traveling at the speed of the flow (v_n) are called entropy waves, their signal being entropy, whereas waves traveling at the speed of sound relative to the flow ($v_n \pm a$) are called acoustic waves. Unfortunately, the signal carried by acoustic waves is not quantifiable in simple thermodynamic terms, but let us just say that they carry acoustic information.

In essence, the eigenvectors point along the direction of the strongest signal. Any signal, whether physical or numerical in nature, is never completely noise free. In our case, numerical noise is introduced into the flow field through discretization error, as well as the accumulative effect of machine round-off error. However, one can minimize the noise and thus obtain the strongest possible signal through proper *tuning*. The eigenvectors are optimally *tuned* with respect to the flow and thus deliver the best *signal-to-noise ratio* when it comes to computing the fluxes across a surface element.

3.3 The Shock Tube Problem

A benchmark test for inviscid flow solvers is the shock tube problem. A shock tube is a long thin tube, closed on both ends, with a membrane or diaphragm located around midsection, which separates two regions of stagnant gas at different pressures. Upon instantaneous removal of the separation membrane, the pressure imbalance creates a flow along the tube, which is characterized by three steadily moving waves: a shock wave, a contact discontinuity, and an expansion fan. Based on the instantaneous location of each wave, one can divide the general flow within a shock tube into five sections, which is illustrated below.

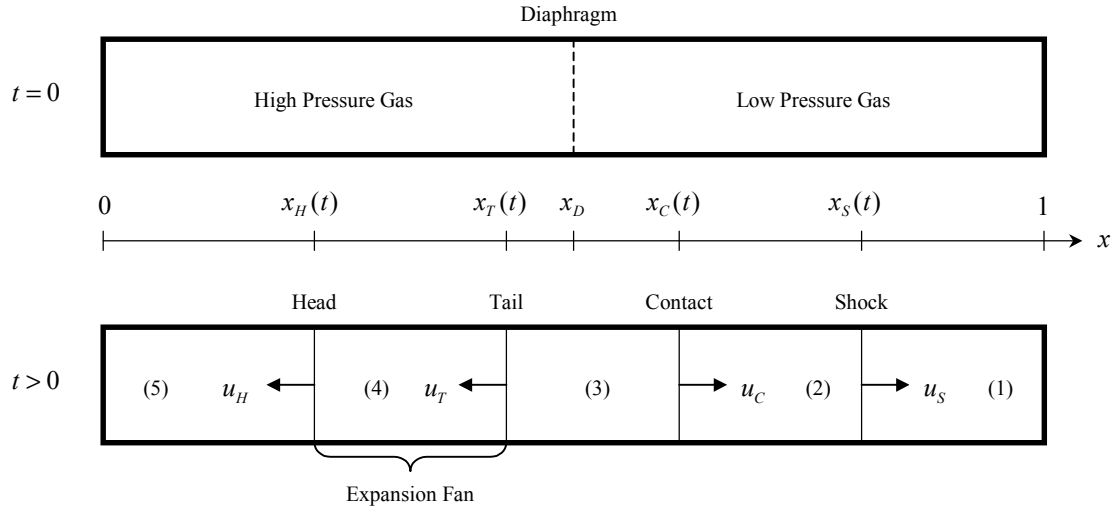


Figure 3-2: Shock Tube

Section (1) contains the undisturbed gas of the low pressure or *driven* section. A shock wave propagates into section (1) at supersonic speed, based on the speed of sound of the undisturbed gas within section (1). Across the shock wave, the flow experiences a sharp rise in pressure and temperature, which remains uniform throughout section (2). Section (2) and (3) are separated by a contact discontinuity, which also travels toward the right, at the same speed as the local flow speed, which is uniform throughout both sections. The pressures within section (2) and (3) are equal and uniform, although there is a temperature drop and density rise across the contact discontinuity. The third wave within the shock tube is an expansion fan, which is marked by a continuous rise in pressure, temperature, and density. The expansion fan covers all of section (4); its width increases over time as the head and tail of the fan travel towards the left at different speeds, the head moving slightly faster than the tail. Section (5) contains the undisturbed gas of the high pressure or *driver* section. Although a diaphragm temperature ratio is generally included in the analysis of shock tube flow, it is assumed to be unity here.

The shock tube problem is a classical problem in inviscid flow theory, because it clearly demonstrates the wave character of the underlying Euler equations. An analytical solution to the problem exists up to the point in time where either the shock wave or the head of the expansion is reflected by the respective end of the tube. The flow field resulting from multiple wave reflections, as well as the interaction of waves as they pass through each other when traveling in opposite directions can only be solved numerically. Although the flow discontinuities created by both contact and shock wave can easily be handled analytically, from a numerical viewpoint they can become rather challenging. Thus the development of suitable numerical algorithms for the shock tube problem has been a formidable task for decades. Three of the most popular algorithms—all based on the TVD principle—will be evaluated subsequently in comparison to the analytical solution, which is presented first.

3.3.1 Analytical Solution

The analytical solution to the shock tube problem is based on inviscid flow theory and its derivation can be found in most textbooks on compressible flow [2]. Therefore, only the result shall be stated here, followed by a numerical example. According to Figure 3-2, the analytical solution for the flow within a shock tube is carried out from right to left, starting with the driven section. The first and major step towards the solution is to compute the pressure rise across the shock wave, which separates section (1) and (2),

$$\frac{p_2}{p_1} = \frac{p_2}{p_1} \left(1 - \frac{\gamma-1}{2\gamma} \frac{a_1}{a_s} \frac{p_2/p_1 - 1}{u_s/a_1} \right)^{\frac{-2\gamma}{\gamma-1}} \quad (3.23)$$

The shock speed u_s is a function of shock pressure ratio and speed of sound of the driven section,

$$u_s = a_1 \sqrt{\frac{\gamma+1}{2\gamma} \left(\frac{p_2}{p_1} - 1 \right) + 1} \quad (3.24)$$

The ratio of sound speeds between the driver and driven section can be expressed in terms of temperatures,

$$\frac{a_1}{a_s} = \left(\frac{T_s}{T_1} \right)^{\frac{1}{2}} \quad (3.25)$$

Although the shock pressure ratio is completely specified by the initial conditions of diaphragm pressure and temperature ratios, its analytic expression is yet implicit. In order to carry out a numerical example, one has to solve the shock pressure ratio through an iterative method. This can be a cumbersome task, if the exponent in Equation (3.23) is not an integer and if the term within the brackets becomes negative during the iteration. For air, which has a ratio of specific heats of 1.4, the above exponent is indeed an integer (-7). Once the shock pressure ratio is computed, the shock speed is known, and thus the shock location can be determined. Based on the local coordinate system depicted in Figure 3-2, and assuming that the diaphragm was instantaneously removed at time $t = 0$, the shock location becomes a simple function of time,

$$x_s(t) = x_D + u_s \cdot t \quad (3.26)$$

The temperature rise and change in sound speeds across the shock can be expressed in terms of pressures,

$$\frac{T_2}{T_1} = \left(\frac{a_2}{a_1} \right)^2 = \frac{p_2}{p_1} \frac{\frac{\gamma+1}{\gamma-1} + \frac{p_2}{p_1}}{1 + \frac{\gamma+1}{\gamma-1} \frac{p_2}{p_1}} \quad (3.27)$$

The induced flow velocity behind the shock can be written in terms of pressure rise and shock speed,

$$u_2 = \frac{a_1^2}{\gamma u_s} \left(\frac{p_2}{p_1} - 1 \right) \quad (3.28)$$

The contact discontinuity travels with the mean flow, the velocity of which is constant throughout section (2) and (3). Thus,

$$u_2 = u_C = u_3 \quad (3.29)$$

The location of the contact discontinuity is again a function of time similar to the shock wave location,

$$x_C(t) = x_D + u_C \cdot t \quad (3.30)$$

Although the pressure across the contact discontinuity remains unchanged, there is a rise in density and a drop in temperature. For a known pressure and speed of sound, the density of section (3) is obtained through the perfect gas equation, which can always be applied,

$$p_3 = p_2 \quad (3.31)$$

$$a_3 = a_5 - \frac{\gamma-1}{2} u_3 \quad (3.32)$$

$$\rho_3 = \frac{\gamma p_3}{a_3^2} \quad (3.33)$$

The expansion fan of section (4) is marked through its head and tail, whose speed and location are,

$$u_T = u_3 - a_3 \quad (3.34)$$

$$x_T(t) = x_D + u_T \cdot t \quad (3.35)$$

$$u_H = -a_5 \quad (3.36)$$

$$x_H(t) = x_D + u_H \cdot t \quad (3.37)$$

Unlike the other sections, the flow speed and thermodynamic state within the expansion fan are not uniform, but are a continuous function of both space and time. For $t > 0$,

$$u_4(x, t) = \frac{2}{\gamma+1} \left(\frac{x-x_D}{t} + a_5 \right) \quad (3.38)$$

$$a_4(x, t) = u_4(x, t) - \frac{x-x_D}{t} \quad (3.39)$$

$$p_4(x, t) = p_5 \left(\frac{a_4(x, t)}{a_5} \right)^{\frac{2\gamma}{\gamma-1}} \quad (3.40)$$

The flow properties of section (5), the undisturbed gas of the driver section, are known in terms of temperature and pressure through the initial conditions. Again, it should be emphasized that prior to the removal of the diaphragm the gases in both driver and driven section are stagnant.

In order to demonstrate the above analytic solution, a numerical example has been calculated for a diaphragm pressure ratio of five and a temperature ratio of one. The results have been plotted for a shock tube of unit length at a non-dimensional time $t = 0.25$, where the speed of sound in the driven section is chosen to be one unit of length per one unit of time. All thermodynamic properties were non-dimensionalized with respect to the initial properties of the driven section. Results are shown in Figure 3-3 for Mach number, velocity, density, pressure, temperature, as well as entropy change.

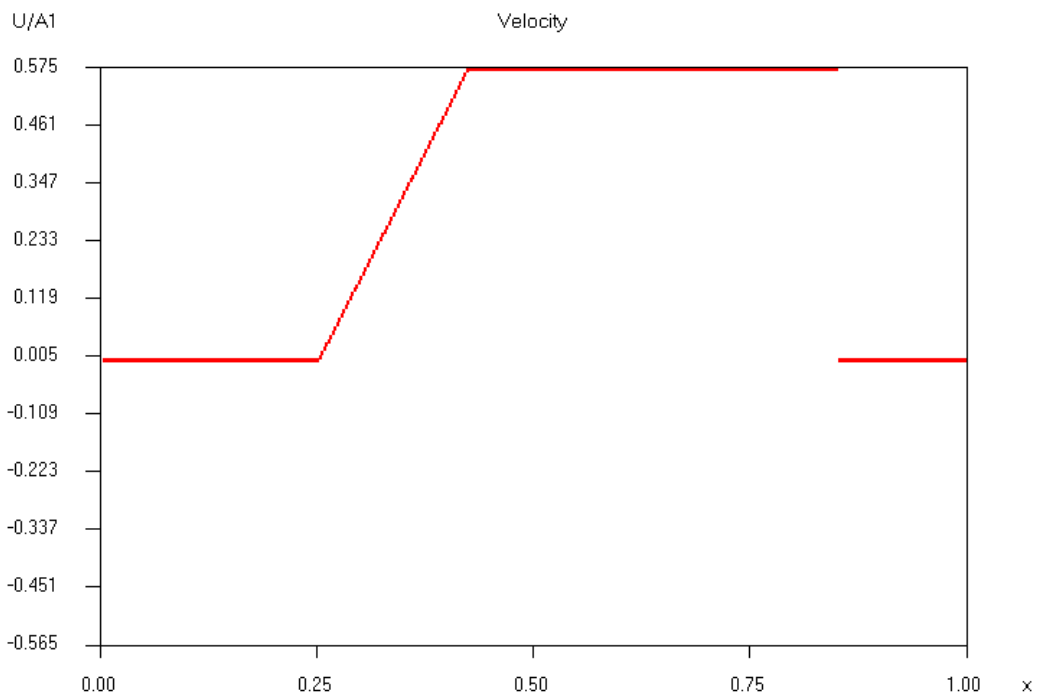
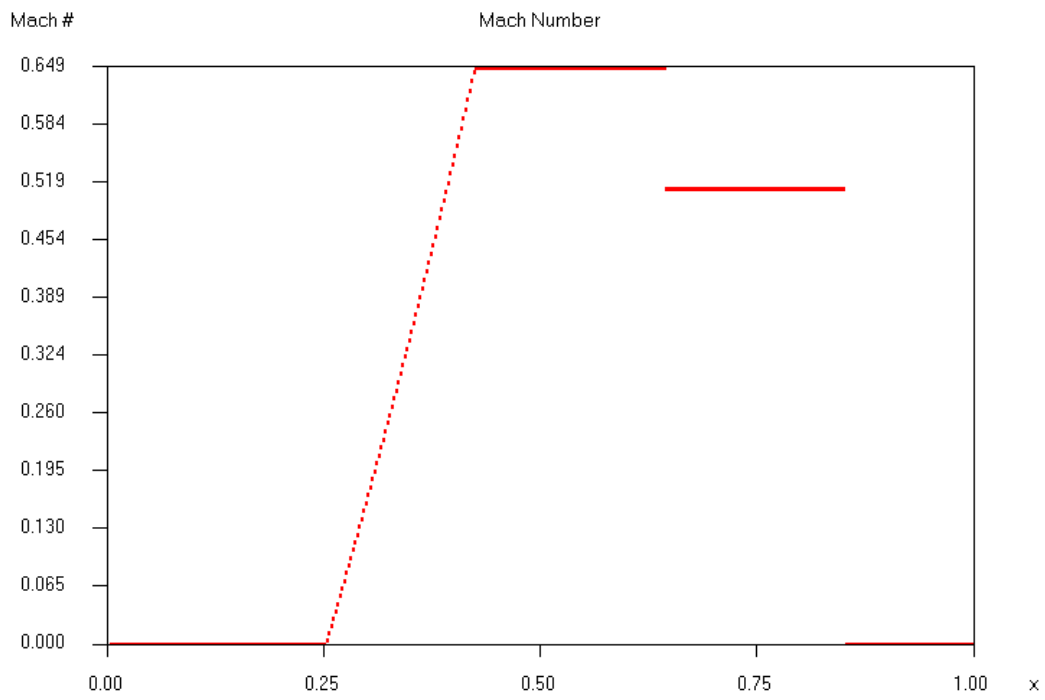


Figure 3-3: Shock Tube Flow at Time $t = 0.25$ (Analytical Solution)

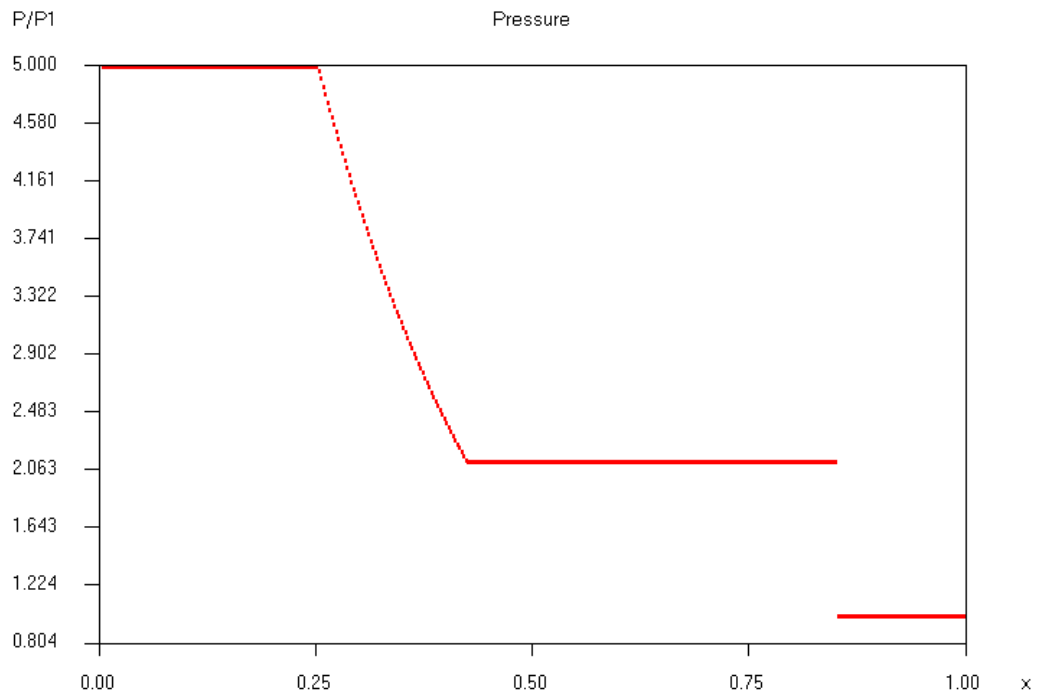
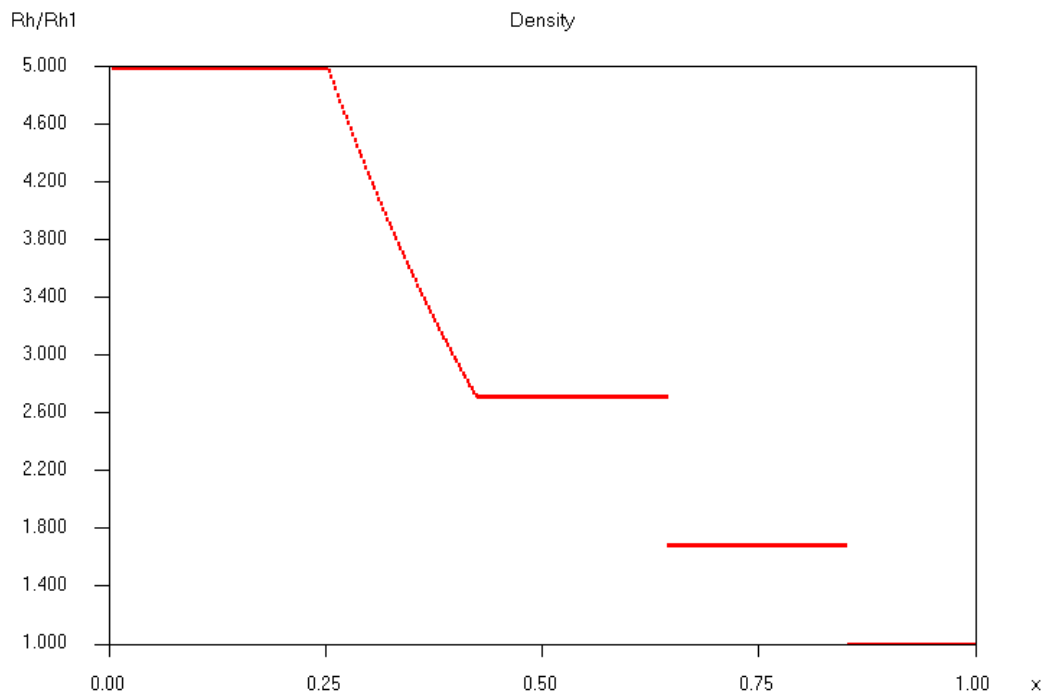


Figure 3-3 Continued—(Analytical Solution)

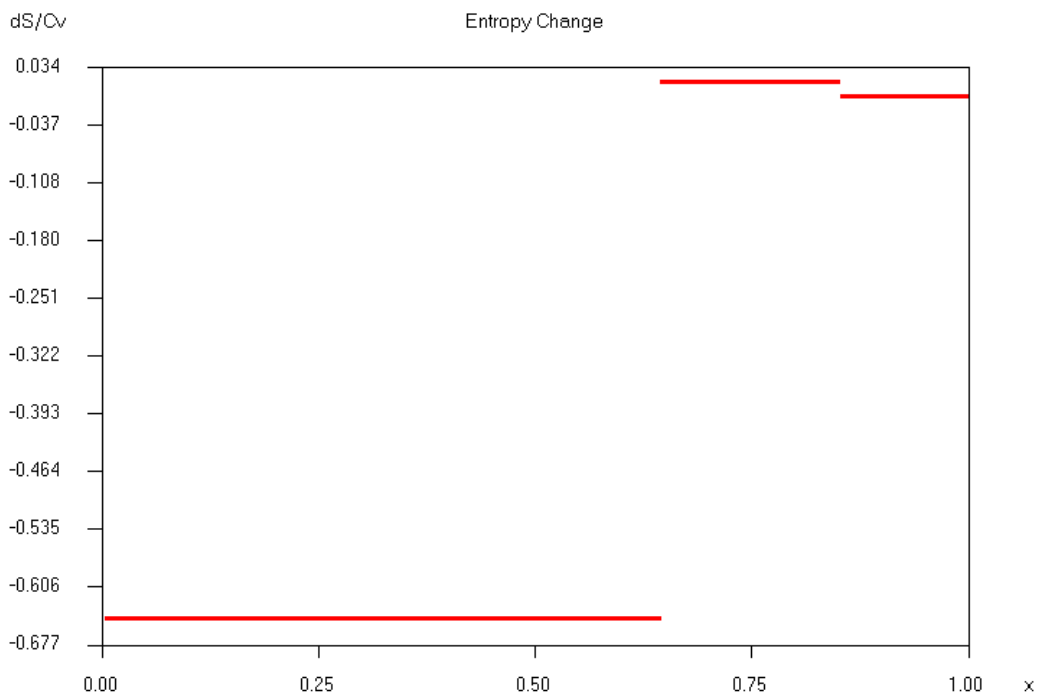
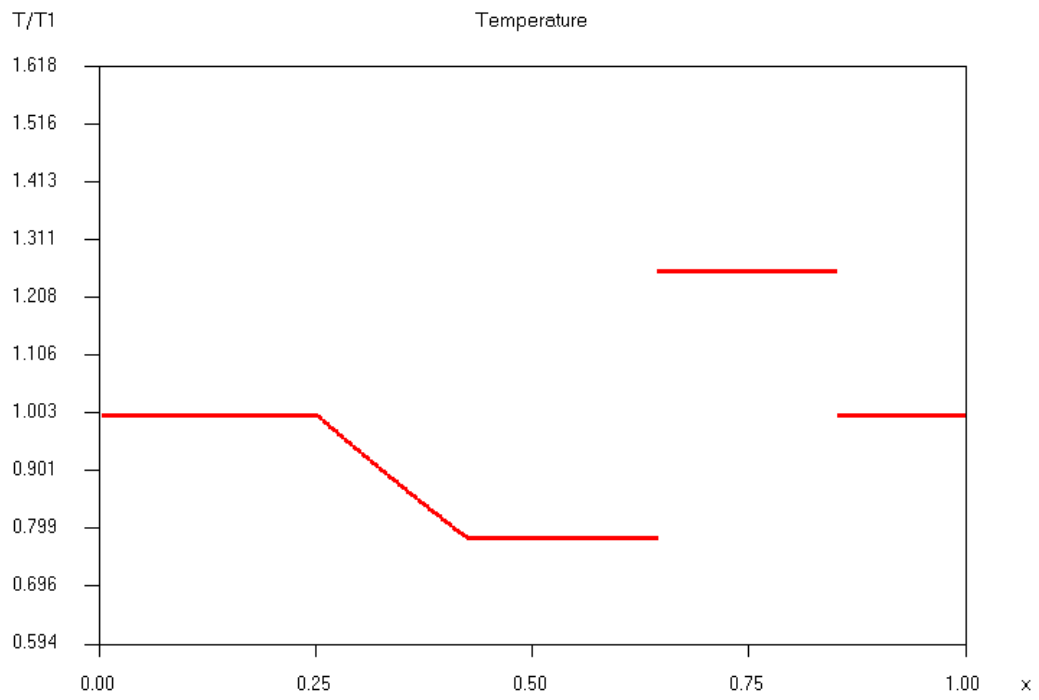


Figure 3-3 Continued—(Analytical Solution)

The change in entropy is calculated relative to the entropy per unit mass initially present within the driven section and is non-dimensionalized by the constant volume specific heat coefficient,

$$\frac{\Delta s}{c_v} = \frac{s - s_1}{c_v} = \gamma \ln\left(\frac{T}{T_1}\right) + (1 - \gamma) \ln\left(\frac{p}{p_1}\right) \quad (3.41)$$

It should come as no surprise that the entropy of the driver section is negative with respect to the driven section due to their initial pressure difference. Nonetheless, the total entropy present within the entire shock tube increases with time—after the diaphragm is removed—due to the irreversible losses that occur, and thus the second law of thermodynamics is always satisfied.

The graphs presented in Figure 3-3 clearly demonstrate the jump discontinuities in flow properties across the shock wave and contact, which will be the main comparison feature for the numerical solutions presented in the next section. The contact discontinuity was referred to earlier as an entropy wave, and not surprisingly, the main entropy change within the shock tube does occur across the contact. The only other entropy change within the flow is seen across the shock wave, which is relatively small in comparison.

An intrinsic feature of the graphs reveals itself in the different wave speeds at which the shock, contact, and expansion fan travel. Recall that the speed of sound within the driver and driven section is the same, and the non-dimensional scale is chosen such that a sonic wave advances 0.25 units of distance in 0.25 units of time. This is exactly the case for the expansion head, whereas the shock wave covers about 0.35 units of distance within the same time frame. Thus it can be seen from the plots that the head of the expansion fan travels at sonic speed towards the left, the shock wave propagates at supersonic speed towards the right, while both the contact wave and tail of the expansion fan travel at subsonic speed behind them. One should not confuse the speed of wave propagation with the local flow speed. As can clearly be seen in the Mach number plot, the local flow speed is subsonic everywhere. It should be noted though that the local Mach number is based on the local speed of sound, which changes with temperature. For higher diaphragm pressure ratios, such as $p_5/p_1 = 15$, the flow speed behind the shock wave may become supersonic.

3.3.2 Numerical Solution

The numerical solutions to the shock tube problem are all derived from the one-dimensional Euler equations and their eigensystem, which comprises a much simpler subset of the equations presented earlier. Written in compact column format, the governing conservation equations are,

$$\frac{\partial}{\partial t} \int_{CV} \bar{Q} dV + \oint_{CS} \bar{F} dA = 0 \quad (3.42)$$

where,

$$\bar{Q} = \begin{bmatrix} \rho \\ \rho u \\ \rho e_o \end{bmatrix}, \quad \bar{F} = \begin{bmatrix} \rho u \\ \rho u^2 + p \\ \rho h_o u \end{bmatrix}$$

The stagnation energy and enthalpy per unit mass are somewhat simplified, inasmuch as their kinetic part is reduced by two components,

$$e_o = e + e_k, \quad h_o = h + e_k, \quad e_k = \frac{1}{2} u^2 \quad (3.43)$$

Once more, static energy, enthalpy, and pressure can all be expressed in terms of the local speed of sound,

$$e = \frac{a^2}{\gamma(\gamma-1)}, \quad h = \frac{a^2}{\gamma-1}, \quad p = \frac{\rho a^2}{\gamma} \quad (3.44)$$

The eigensystem of the above conservation equations is equally simplified compared to the original system. Since we are left with only three conservation equations, we only get three eigenvalues, which are distinct,

$$\lambda_i = \{u-a, u, u+a\} \quad (3.45)$$

The matrices of right and left eigenvectors reduce to 3x3 in size, and since they no longer carry any directional singularity, a single set suffices,

$$[R] = [\bar{R}_1 \quad \bar{R}_2 \quad \bar{R}_3] = \begin{bmatrix} 1 & 1 & 1 \\ u-a & u & u+a \\ h_o - au & e_k & h_o + au \end{bmatrix} \quad (3.46)$$

$$[L] = \begin{bmatrix} \bar{L}_1 \\ \bar{L}_2 \\ \bar{L}_3 \end{bmatrix} = \begin{bmatrix} \frac{(\gamma-1)e_k + au}{2a^2} & \frac{(1-\gamma)u-a}{2a^2} & \frac{\gamma-1}{2a^2} \\ \frac{a^2 - (\gamma-1)e_k}{a^2} & \frac{(\gamma-1)u}{a^2} & \frac{1-\gamma}{a^2} \\ \frac{(\gamma-1)e_k - au}{2a^2} & \frac{(1-\gamma)u+a}{2a^2} & \frac{\gamma-1}{2a^2} \end{bmatrix} \quad (3.47)$$

One might be tempted to multiply the matrix of left eigenvectors by a^2 in order to eliminate the denominator. After all, any eigenvector can be multiplied by a constant without changing its direction, and since we are working in a functional space, the speed of sound, which varies locally, is still considered to be a constant. However, such simplification would be ill advised, since the resulting eigenvector matrices would no longer satisfy the matrix equation that is intrinsically used within the algorithm,

$$[L][R] = [I] \quad (3.48)$$

The system of integral conservation equations of (3.42) are solved numerically by slicing the shock tube into a finite number of control volumes as shown in Figure 3-4. The number of these *finite volume elements* determines the resolution of the computed flow field and should be quite large ($N > 100$). Based on the premise that flow properties within each volume element are constant, the system of integral conservation equations can then be rewritten in algebraic or *discrete* form. For example, a central discretization scheme, where the fluxes between elements are computed as simple arithmetic averages, would look as follows,

$$\bar{Q}_i^{p+1} = \bar{Q}_i^p - \frac{\Delta t}{\Delta V_i} (\bar{F}_{i+1/2} \Delta A_{i+1/2} - \bar{F}_{i-1/2} \Delta A_{i-1/2}) \quad (3.49)$$

where,

$$\bar{F}_{i+1/2} = \frac{1}{2} \bar{F}(\bar{Q}_i^p) + \frac{1}{2} \bar{F}(\bar{Q}_{i+1}^p)$$

$$\bar{F}_{i-1/2} = \frac{1}{2} \bar{F}(\bar{Q}_i^p) + \frac{1}{2} \bar{F}(\bar{Q}_{i-1}^p)$$

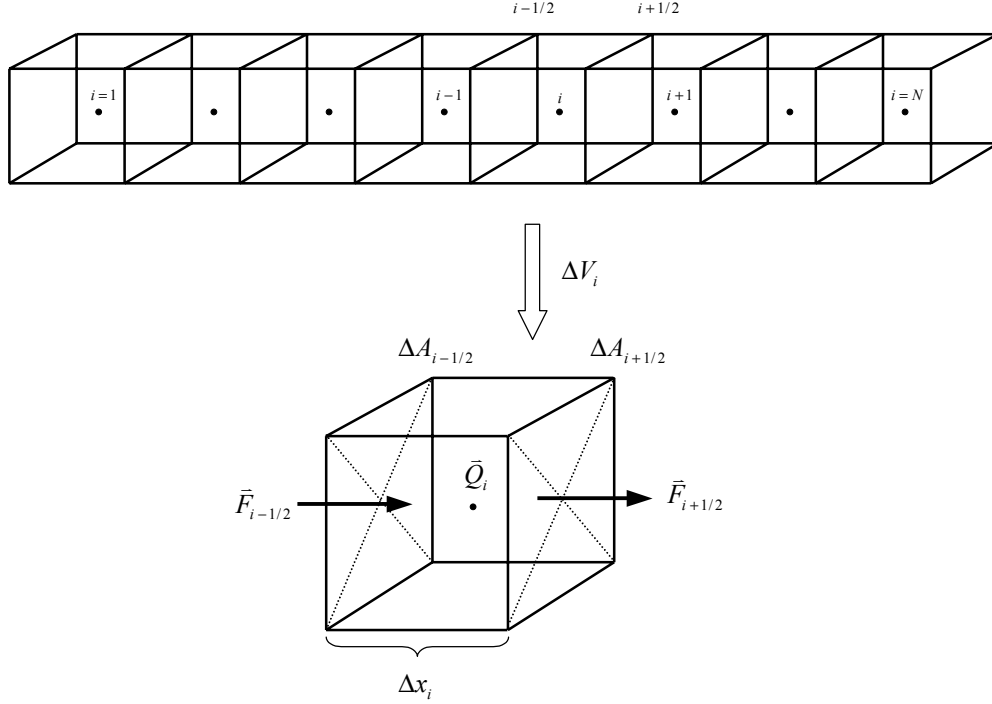


Figure 3-4: Finite Volume Model

The superscripts in Equation (3.49) denote subsequent time levels. Consistent with the original integral formulation, the fluxes are multiplied by the area of the cell faces they travel across. The discretization shown in Figure 3-4 is uniform, consisting of equally spaced elements of constant volume and constant area cell faces. Therefore, Equation (3.49) could be simplified by setting, $\Delta V_i = (\Delta x)^3$, and $\Delta A_i = (\Delta x)^2$, for $\Delta x_i = \text{constant}$, however it was decided for expository purposes to leave the finite volume formulation in its more general form. The flux vectors shown in Figure 3-4 both point to the right, and thus are both positive, since the positive x -direction is towards the right. Depending on the local flow, of course, the sign of the flux vectors can change, and thus fluxes can travel in either direction.

The discretization carried out in Equation (3.49) is simple and straightforward and would work well if applied to a viscous flow model at very low Reynolds number, which contains plenty of dissipation. In the absence of dissipative mechanisms, which is the case for inviscid flow, numerical discretization errors would grow quickly and render the computation unstable. Thus the above discretization scheme would fail if applied to shock tube flow. However, by adding a small amount of corrective flux to Equation (3.49), the scheme can be turned into a stable and well-behaved TVD scheme:

$$\bar{Q}_i^{p+1} = \bar{Q}_i^p - \frac{\Delta t}{\Delta V_i} (\bar{F}_{i+1/2} \Delta A_{i+1/2} - \bar{F}_{i-1/2} \Delta A_{i-1/2}) + \frac{1}{2} (\bar{f}_{i+1/2} - \bar{f}_{i-1/2}) \quad (3.50)$$

The additional flux terms $\bar{f}_{i\pm 1/2}$ shall be referred to as *eigenfluxes*, since they are intimately tied to the eigenvalues and eigenvectors of the Euler equations. Denoting the matrix of right eigenvectors by \bar{R} ,

$$\bar{f}_{i+1/2} = \bar{R}_{i+1/2} \cdot \bar{b}_{i+1/2} \quad (3.51)$$

where

$$\bar{R}_{i+1/2} = \bar{R}(\bar{Q}_{i+1/2}^p), \quad \bar{Q}_{i+1/2} = \frac{1}{2}(\bar{Q}_i^p + \bar{Q}_{i+1}^p) \quad (3.52)$$

The construction of the vector \bar{b} involves the eigenvalues and left eigenvectors of the local flow, a local length scale, as well as the global integration time step. Its exact assembly depends on the specific TVD scheme employed, three of which are presented in the following subsections. The numerical implementation of the initial and boundary conditions is independent of the flow solver. For a shock tube that is equally divided into driver and driven section, the initial condition is expressed as follows,

$$\bar{Q}_i^0 = \begin{bmatrix} \rho_5 \\ 0 \\ \rho_5 c_v T_5 \end{bmatrix} \text{ for } i = 1, \dots, N/2; \quad \bar{Q}_i^0 = \begin{bmatrix} \rho_1 \\ 0 \\ \rho_1 c_v T_1 \end{bmatrix} \text{ for } i = N/2 + 1, \dots, N \quad (3.53)$$

$$\text{where } \frac{\rho_5}{\rho_1} = \frac{P_5/P_1}{T_5/T_1} \quad \text{and} \quad \frac{T_5}{T_1} = 1$$

The reflection boundary condition at the end walls is implemented through *ghost* cells, which lie outside the physical domain and *mirror* the flow properties of the interior,

$$\bar{Q}_0^p = \begin{bmatrix} \rho \\ -\rho u \\ \rho e_o \end{bmatrix}_1^p \quad \text{and} \quad \bar{Q}_{N+1}^p = \begin{bmatrix} \rho \\ -\rho u \\ \rho e_o \end{bmatrix}_N^p \quad (3.54)$$

3.3.2.1 ROE Scheme

The ROE scheme was discovered in 1981 by Philip Roe [15] and is commonly referred to in the literature as Roe's first-order upwind method for the Euler equations. Although it inherits most of the TVD properties, it is not considered a TVD scheme per se for two reasons: (1) its spatial accuracy is only of first order, whereas true TVD schemes are generally second-order accurate; (2) its entropy law is not properly enforced near sonic points, and as a result expansion shocks can form at sonic points within expansion fans. According to Roe, the vector \bar{b} is formed as follows,

$$\bar{b}_{i+1/2} = |\bar{l}_{i+1/2}| \bar{a}_{i+1/2} \quad (3.55)$$

where,

$$\bar{a}_{i+1/2} = \bar{L}_{i+1/2} \cdot \Delta \bar{Q}_{i+1/2}^p \quad (3.56)$$

$$\Delta \bar{Q}_{i+1/2}^p = \bar{Q}_{i+1}^p - \bar{Q}_i^p, \quad \bar{L}_{i+1/2} = \bar{L}(\bar{Q}_{i+1/2}^p)$$

and,

$$\bar{l}_{i+1/2} = \bar{\lambda}_{i+1/2} \tau_{i+1/2} \quad (3.57)$$

$$\tau_{i+1/2} = \frac{\Delta t \Delta A_{i+1/2}}{\frac{1}{2}(\Delta V_i + \Delta V_{i+1})}, \quad \bar{\lambda}_{i+1/2} = \bar{\lambda}(\bar{Q}_{i+1/2}^p) = \begin{bmatrix} u-a \\ u \\ u+a \end{bmatrix}_{i+1/2}$$

In the above, $\bar{\bar{L}}$ denotes the matrix of left eigenvectors, where $\bar{\lambda}$ are the eigenvalues written in vector format. The local length scale incorporated into the scalar τ represents the distance between cell centers. In Roe's original formulation, all flow quantities evaluated at cell faces were mass averaged, which is computationally more expensive. The arithmetic averaging employed here yields equally valid results and is much simpler.

The computational results for the shock tube problem, based on the ROE scheme, are presented over the next several pages using both profile plots and wave diagrams. A wave diagram is essentially a collection of profile plots for subsequent time levels in form of a contour map. The non-dimensionalization is identical to the analytical solution presented earlier, such that all profile plots can directly be compared. The graphs of Figure 3-5 are generally in good agreement with the analytical results shown in Figure 3-3. The changes in flow properties across the shock wave and contact discontinuity are no longer pure jumps, but are spread over several points. The contact is considerably more smeared than the shock, although both waves are clearly recognizable. The edges of all wave fronts, including the expansion fan, are significantly softened due to the action of numerical viscosity, which is characteristic of any first-order accurate scheme. The wave diagrams of Figure 3-6 further reveal the strong presence of numerical viscosity, particularly at later times when the reflected waves interact with each other.

Numerical, or artificial, viscosity is introduced in the discretization process and cannot be avoided. Although it causes diffusion, which is seen in the smearing effect it has on discontinuities, numerical viscosity is needed to some degree in order to enforce the entropy law. Recall that the Euler equations have been stripped of physical viscosity, the mechanism which guarantees that the overall entropy of a flow can only increase in time. It can be demonstrated [11] that the numerical viscosity present in the ROE scheme is simply $\bar{\varepsilon} = |\bar{l}|$. At sonic points, the first eigenvalue goes to zero, $\lambda_1 = u - a = 0$, and thus the numerical viscosity in the first equation of eigenvectors vanishes. With no other entropy enforcing mechanism present, a physically incorrect expansion shock may develop in a numerical solution. This phenomenon can be observed when solving shock tube flow for diaphragm pressure ratios of around twenty, using the original ROE scheme. To overcome the inadequacy of Roe's algorithm near sonic points, Ami Harten [7] proposed a simple entropy fix by introducing the following numerical viscosity function,

$$\text{Viscos}(x) = \begin{cases} \frac{1}{2}(x^2/\varepsilon + \varepsilon) & \text{if } |x| \leq \varepsilon \\ |x| & \text{if } |x| > \varepsilon \end{cases} \quad (3.58)$$

$$0 < \varepsilon \leq 0.5$$

Applied to Roe's scheme,

$$\bar{b}_{i+1/2} = \text{Viscos}(\bar{l}_{i+1/2}) \bar{a}_{i+1/2} \quad (3.59)$$

the numerical viscosity is now always positive,

$$\bar{\varepsilon} = \text{Viscos}(\bar{l}) \geq \varepsilon \quad (3.60)$$

When solving shock tube flow using the modified ROE scheme, the expansion shock disappears by setting $\varepsilon = 0.1$, which is commonly referred to as the numerical viscosity parameter, a non-dimensional quantity. In our computations, the diaphragm pressure ratio was low enough such that the flow within the expansion fan is subsonic everywhere. Therefore, a numerical viscosity parameter was not needed, and by setting $\varepsilon = 0$ it is implied that the absolute value function is used.

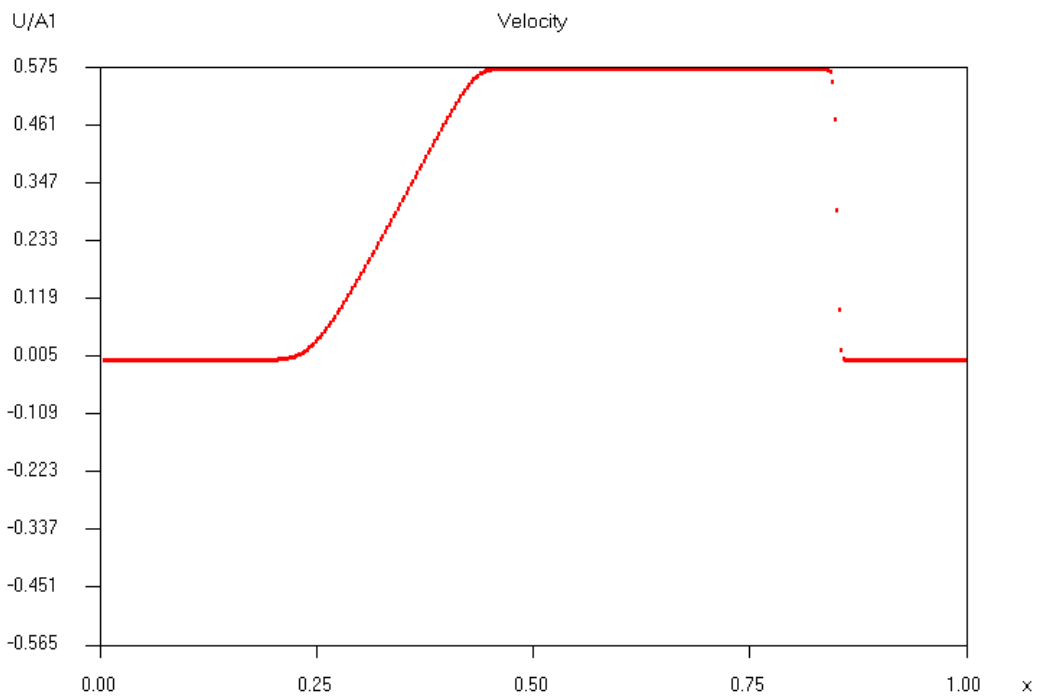
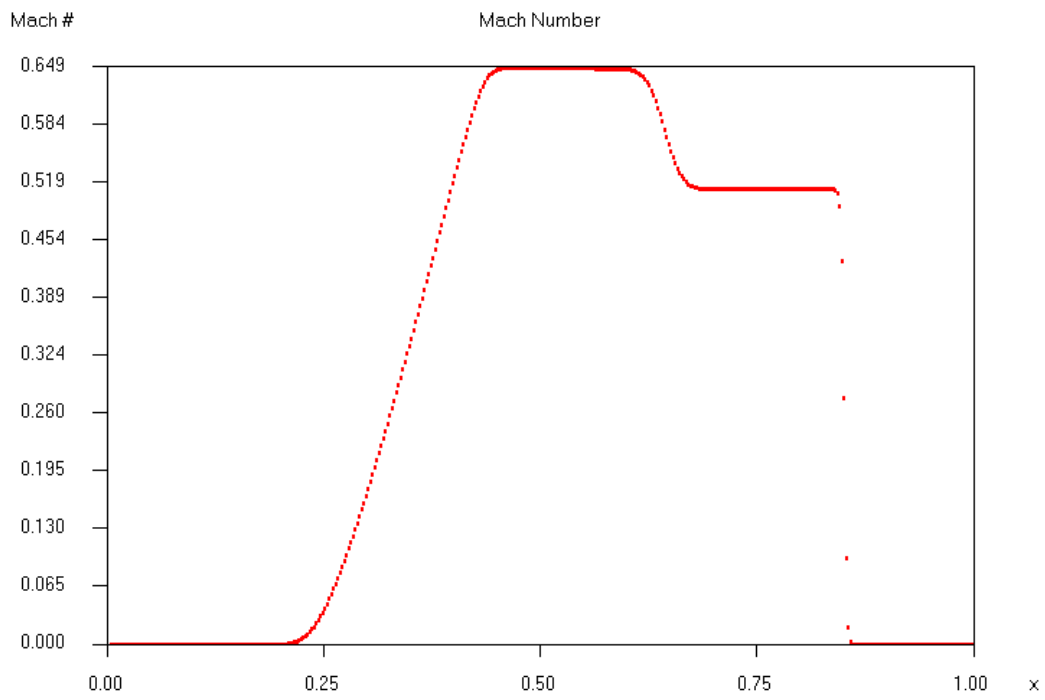


Figure 3-5: Shock Tube Flow at Time $t = 0.25$ (ROE Solution)

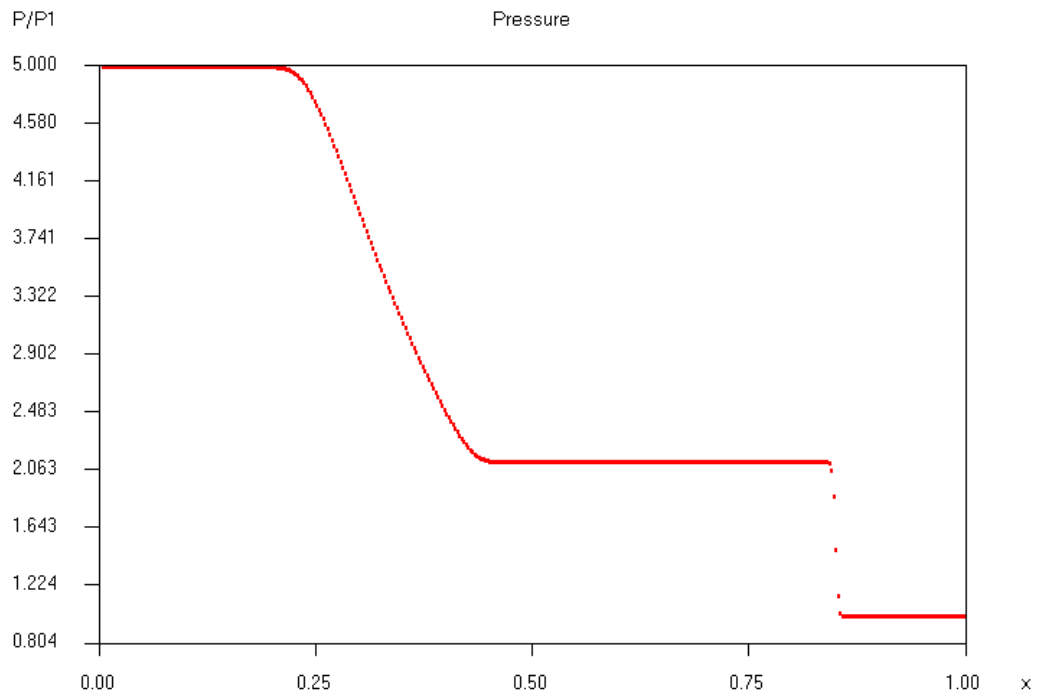
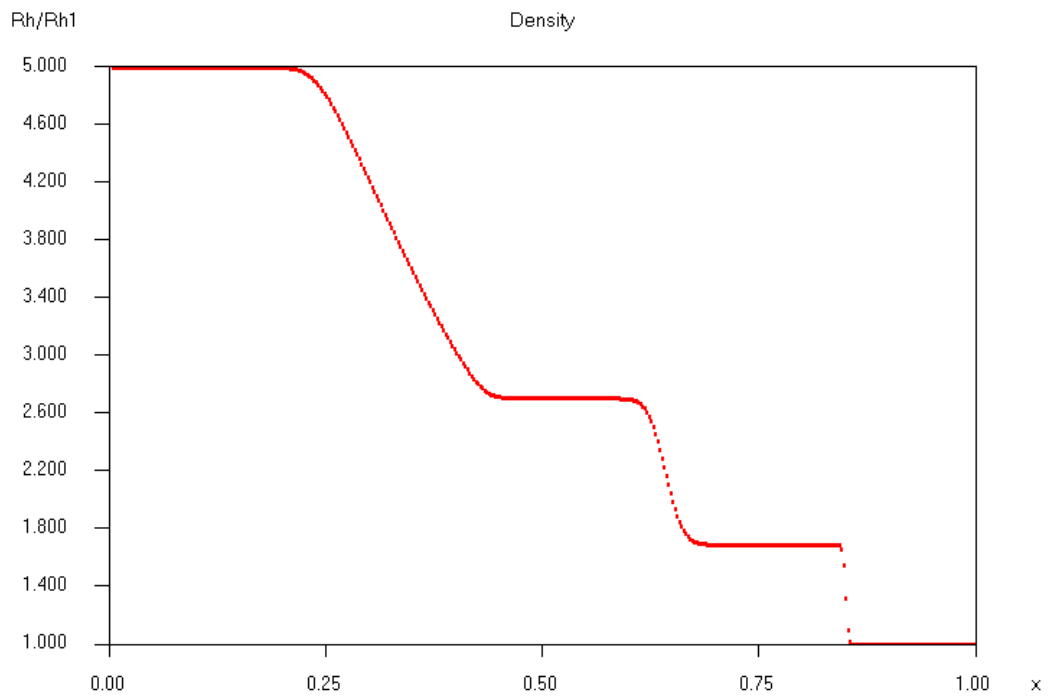


Figure 3-5 Continued—(ROE Solution)

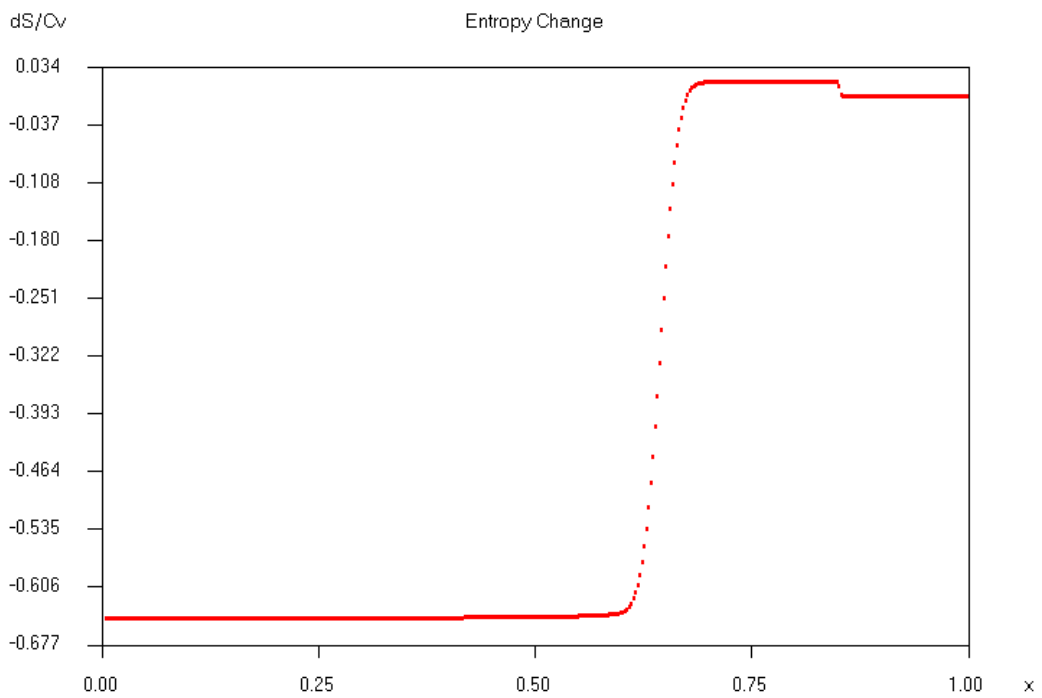
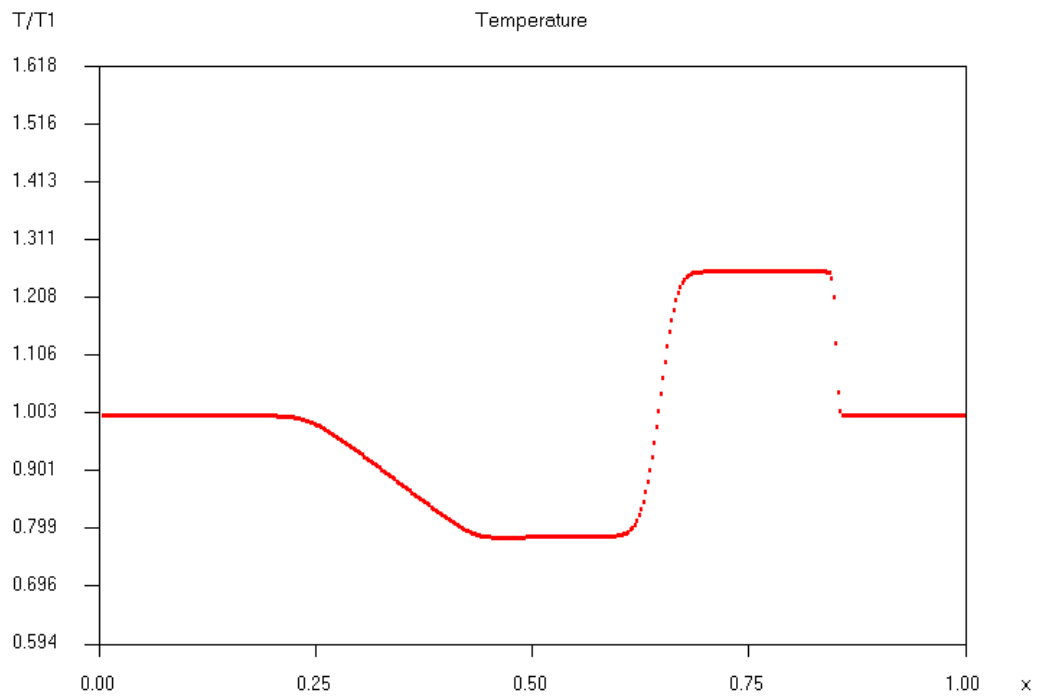


Figure 3-5 Continued—(ROE Solution)

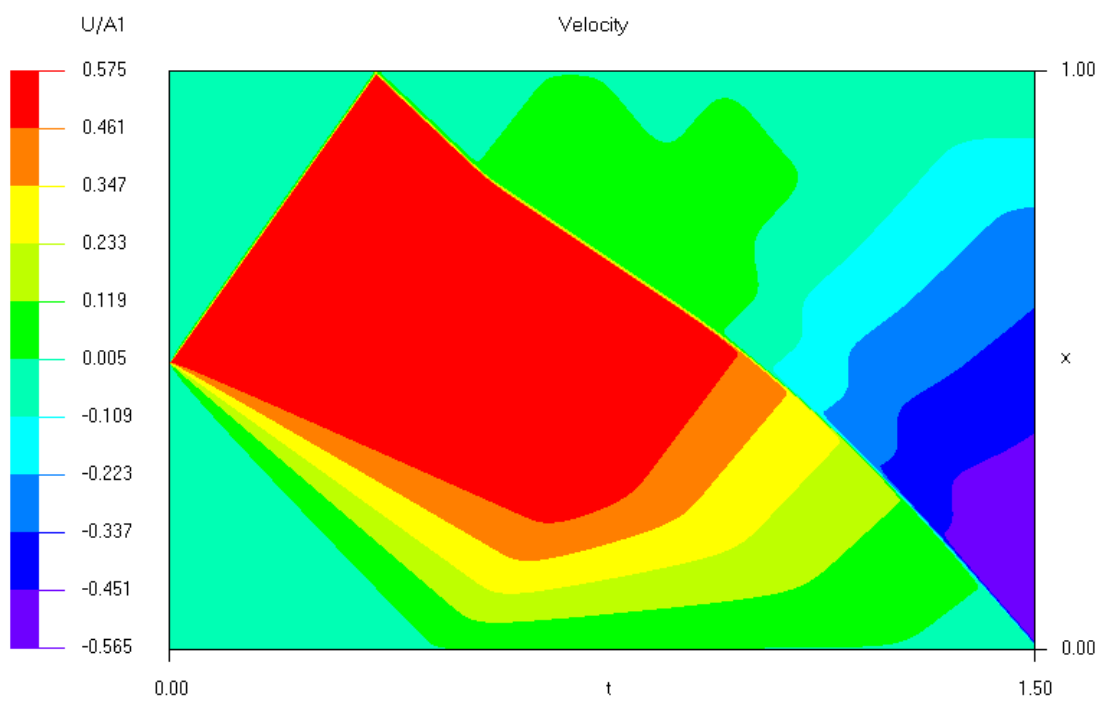
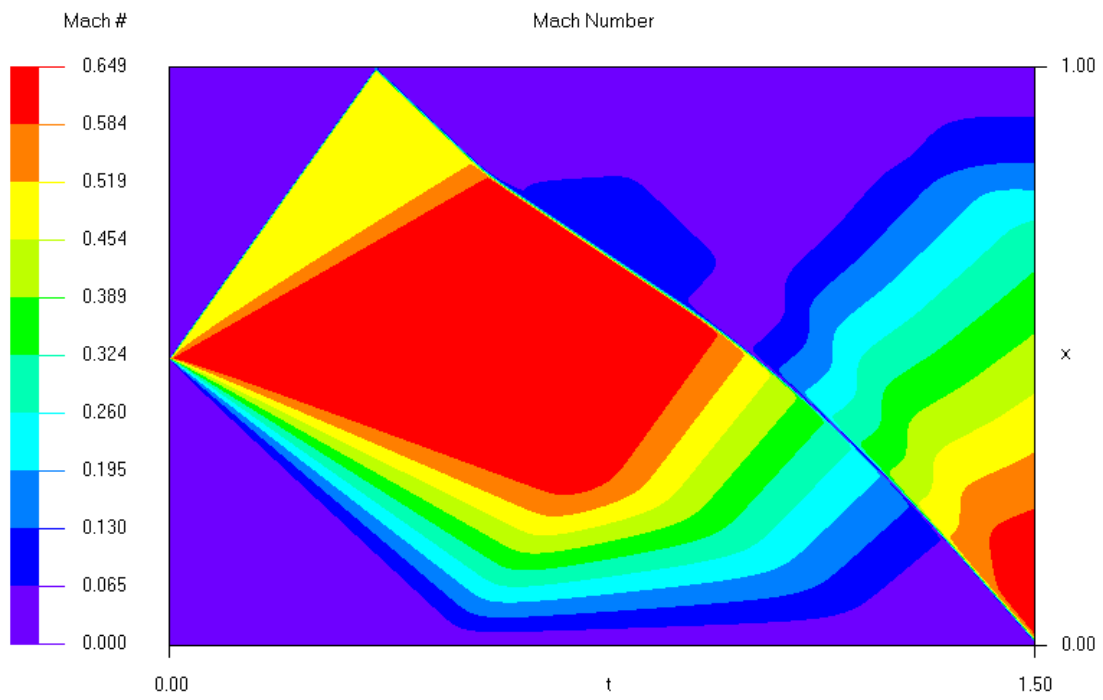


Figure 3-6: Shock Tube Flow – Wave Diagram (ROE Solution)

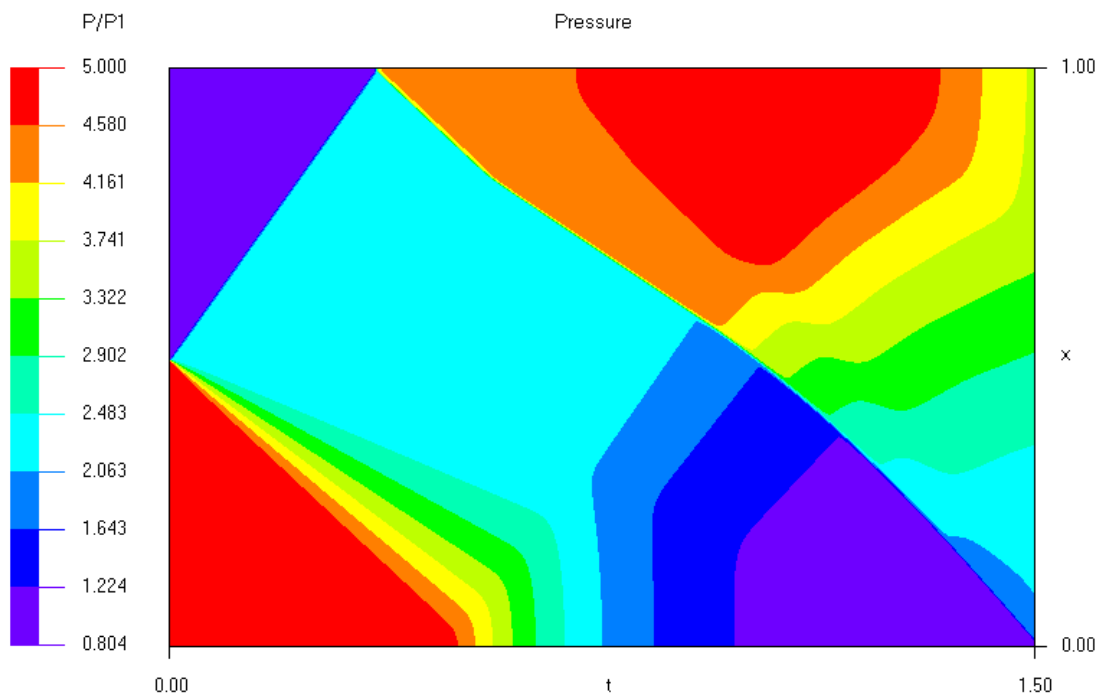
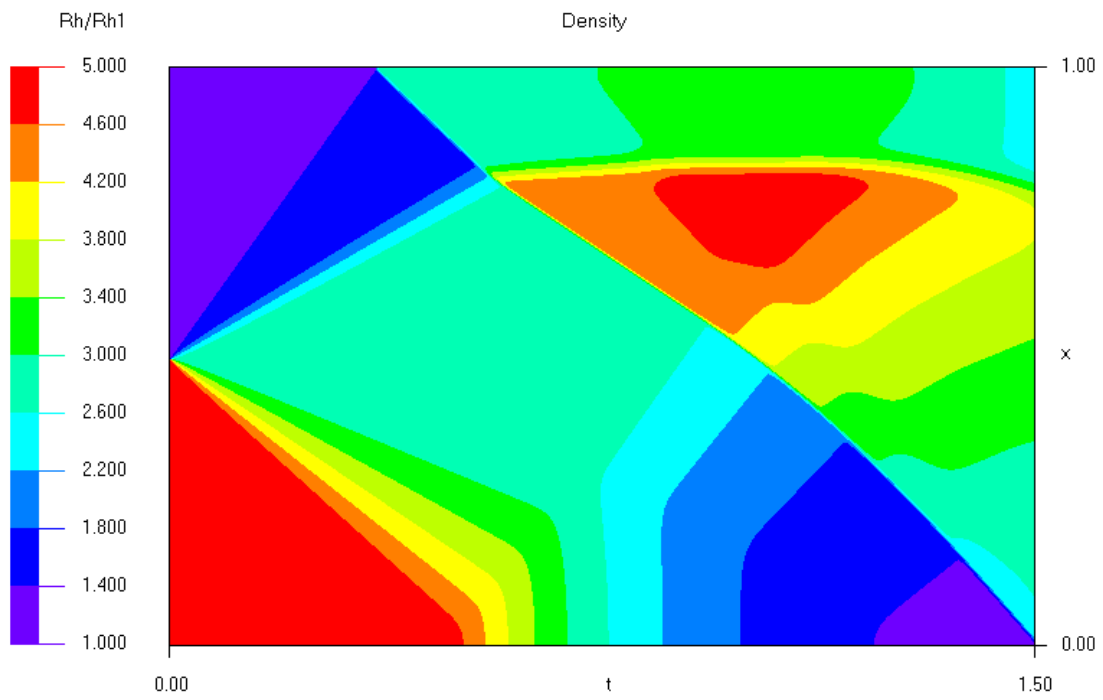


Figure 3-6 Continued—(ROE Solution)

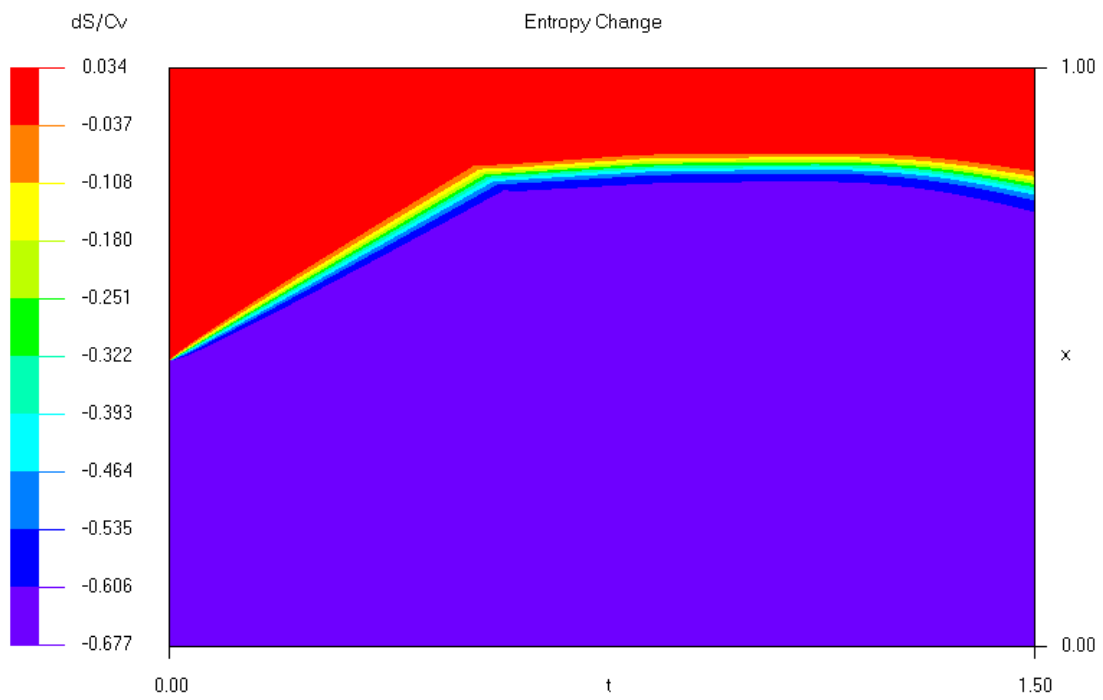
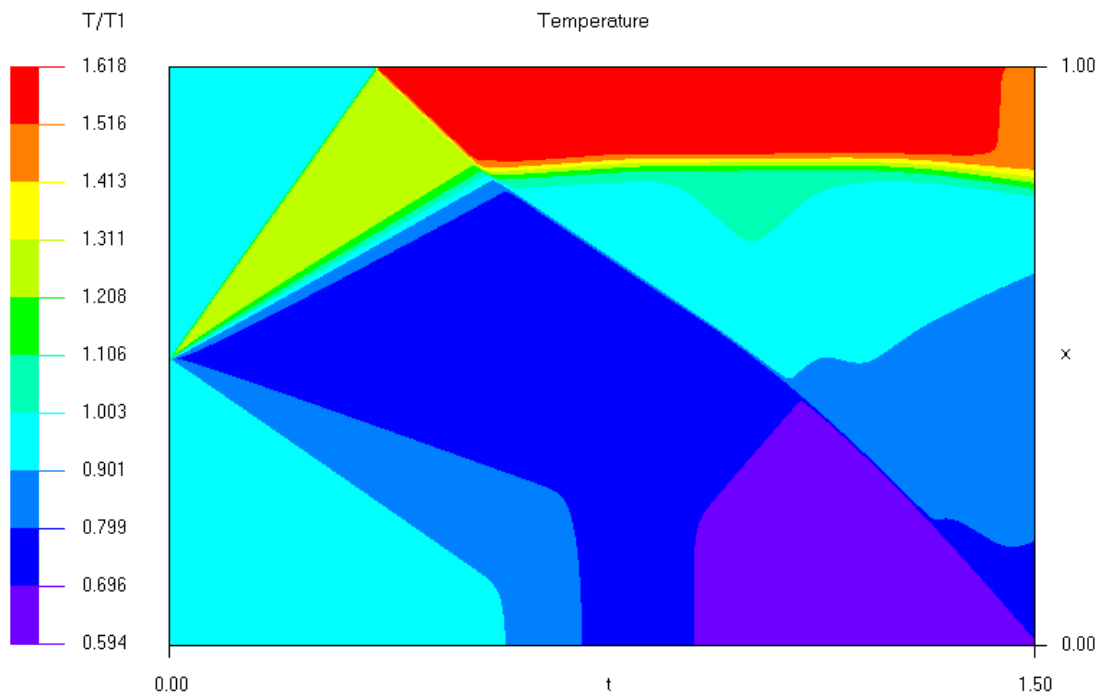


Figure 3-6 Continued—(ROE Solution)

3.3.2.2 TVD Scheme

In 1982, Ami Harten published a groundbreaking paper [7] that became the basis of CFD research for many years to come. Under the title “High Resolution Schemes for Hyperbolic Conservation Laws”, Harten introduced the term *total variation non-increasing* (TVNI), which was later shortened by other researchers to *total variation diminishing* (TVD). In essence, Harten was able to combine the stability of first-order schemes with the accuracy of second-order algorithms, without introducing their negative side effects of numerical diffusion and dispersion. The dispersive character of second-order algorithms causes spurious oscillations in the neighborhood of flow discontinuities such as shocks, a truly undesirable feature. Harten’s paper, which is developed in the most rigorous mathematical fashion, includes the derivation of every result, which shall not be repeated here. Instead, only the numerical algorithm will be stated, followed by a brief explanation of its rationale. According to Harten’s ULT1 scheme, renamed here as the TVD scheme, the vector \bar{b} is formed as follows,

$$\bar{b}_{i+1/2} = \text{Viscos}(\bar{l}_{i+1/2} + \bar{m}_{i+1/2}) \bar{a}_{i+1/2} - (\bar{u}_i + \bar{u}_{i+1}) \quad (3.61)$$

with \bar{l} and \bar{a} as previously defined in Equations (3.56) and (3.57). The flux correction \bar{u} and numerical viscosity modification \bar{m} are calculated in the following manner,

$$\begin{aligned} \bar{m}_{i+1/2} &= (\bar{u}_{i+1} - \bar{u}_i) / \bar{a}_{i+1/2} & \text{if } \bar{a}_{i+1/2} \neq 0 \\ &= 0 & \text{if } \bar{a}_{i+1/2} = 0 \end{aligned} \quad (3.62)$$

$$\begin{aligned} \bar{u}_i &= \tilde{\mathcal{G}}_w \text{Minmod}(|\bar{m}_{i+1/2}|, \bar{m}_{i-1/2}, \tilde{\mathcal{G}}_w) \\ \tilde{\mathcal{G}}_w &= \text{sgn}(\bar{m}_{i+1/2}) \end{aligned} \quad (3.63)$$

where,

$$\bar{m}_{i+1/2} = \frac{1}{2} (\text{Viscos}(\bar{l}_{i+1/2}) - (\bar{l}_{i+1/2})^2) \bar{a}_{i+1/2} \quad (3.64)$$

and,

$$\text{Minmod}(x, y) = \max[0, \min(x, y)] \quad (3.65)$$

The Minmod function acts as a *flux limiter* to the flux correction \bar{u} ; whenever the function returns a zero value, both \bar{u} and \bar{m} vanish, and Equation (3.61) reduces to the modified ROE scheme of Equation (3.59). Such is the case at points of local extrema within the flow, where the overall accuracy of the scheme is only first-order. Shocks and contact discontinuities are also treated by the TVD algorithm as if they were extrema. At points away from local extrema and discontinuities, the Minmod function allows either a *linear* or *limited* amount of flux correction, which renders the overall scheme second-order accurate in space. The flux correction \bar{u} is essentially a dispersive flux, which counteracts the diffusive flux of the underlying first-order scheme. Adding too much dispersive flux, however, could introduce oscillations into the flow field, which is prevented through the limitation imposed by the Minmod function.

The concept of a flux limiter can be better understood by rewriting the Minmod function in a slightly different form, which is known in neural networks as the threshold linear signal function [9, 21],

$$\mathcal{L}(r) = \text{Minmod}(1, r), \quad \text{where } r = y/x \quad (3.66)$$

The input signal r represents the ratio of neighboring gradients within a flow field, and its output signal determines the amount of dispersive flux that is sent depending on this ratio. As can be seen in Figure 3-7, the output signal is a piecewise linear function, which can be divided into three intervals: (1) If the ratio of consecutive gradients is negative, the flow field is undergoing a local maximum or minimum. The dispersive flux is zero, and the resulting scheme is first-order upwind. (2) If the ratio of gradients is between zero and one, their magnitude is increasing (they can both be negative), which means the flow field *steepens*. The dispersive flux is linear, and the resulting scheme is second-order upwind. (3) If the ratio of gradients is greater than one, their magnitude is decreasing, which means the flow field *flattens*. The dispersive flux is limited, and the overall scheme becomes second-order central. In summary, the TVD scheme is second-order accurate in space except at local extrema, where the accuracy reduces to first order.

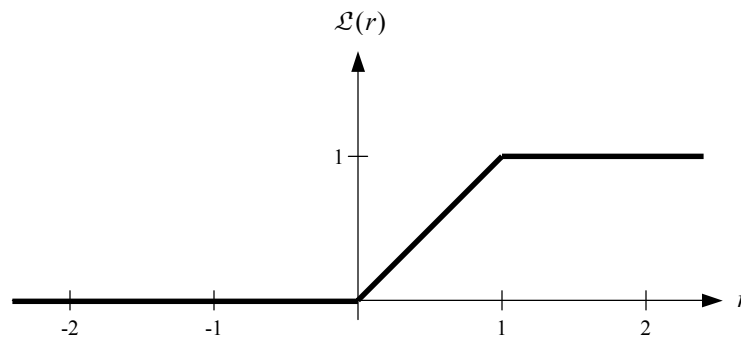


Figure 3-7: Flux Limiter Function

The computational results for the shock tube problem, based on the TVD scheme, are presented over the next pages in Figures 3-8 and 3-9. The non-dimensional scale of all profile plots and wave diagrams is again identical to the solutions presented earlier, such that an immediate comparison can be made. Overall, the profile plots for the TVD scheme are very similar to the ones computed by the ROE scheme. The wave fronts in each plot are somewhat sharper in comparison, yet there is no noticeable difference in the shock resolution between the two numerical schemes. The contact discontinuity is slightly steeper in the TVD profile plots, but there is still room for enhancement. The main improvement of the TVD scheme over the ROE scheme can be seen in the wave diagrams. The chevron patterns produced by the reflected waves are definitely crisper than they were before. Most striking is the time evolution of the contact wave when followed on the entropy wave diagram. In the ROE computation, the entropy wave became considerably smeared over time, which was attributed to the ubiquitous numerical viscosity of the first-order scheme. In the TVD computation, the contact discontinuity stays intact over a much longer time period, even after the reflected shock has traveled through the contact.

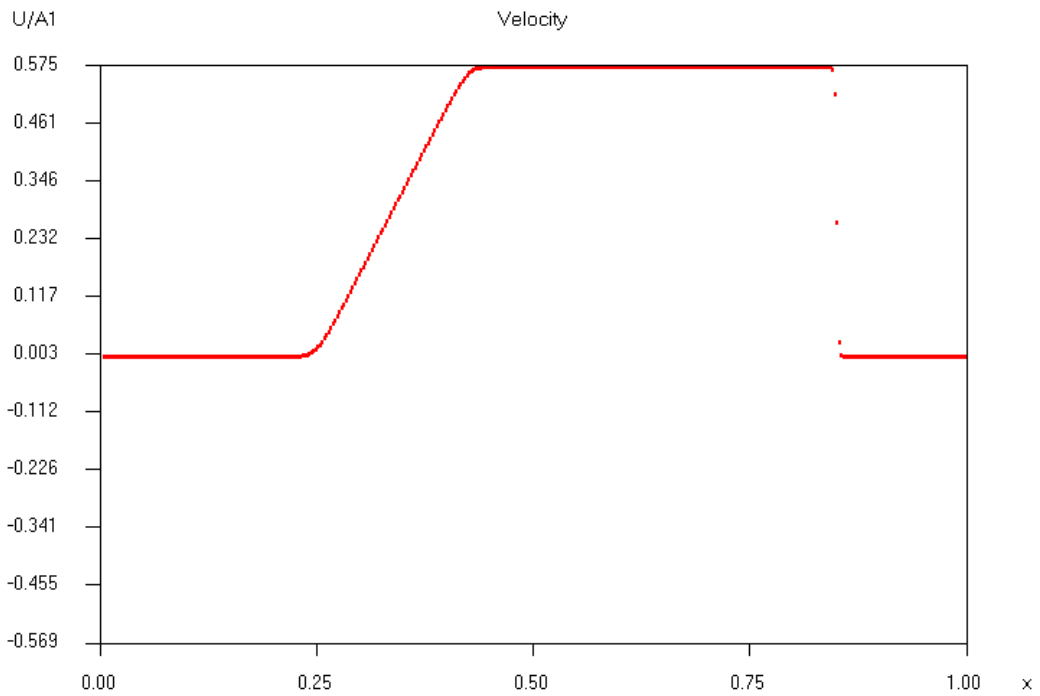
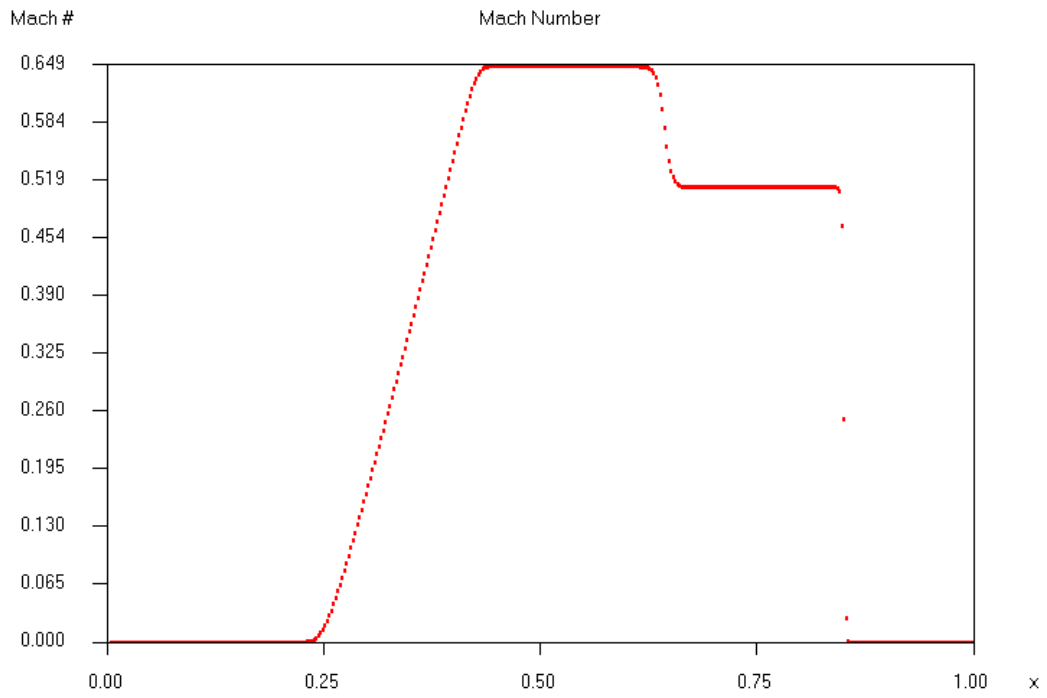


Figure 3-8: Shock Tube Flow at Time $t = 0.25$ (TVD Solution)

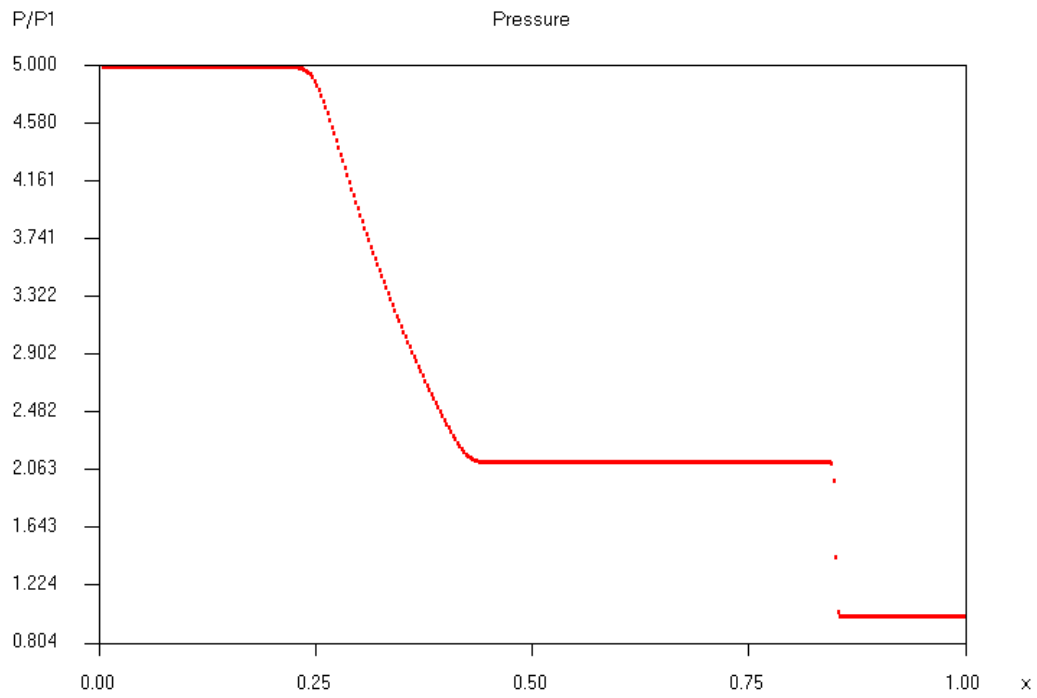
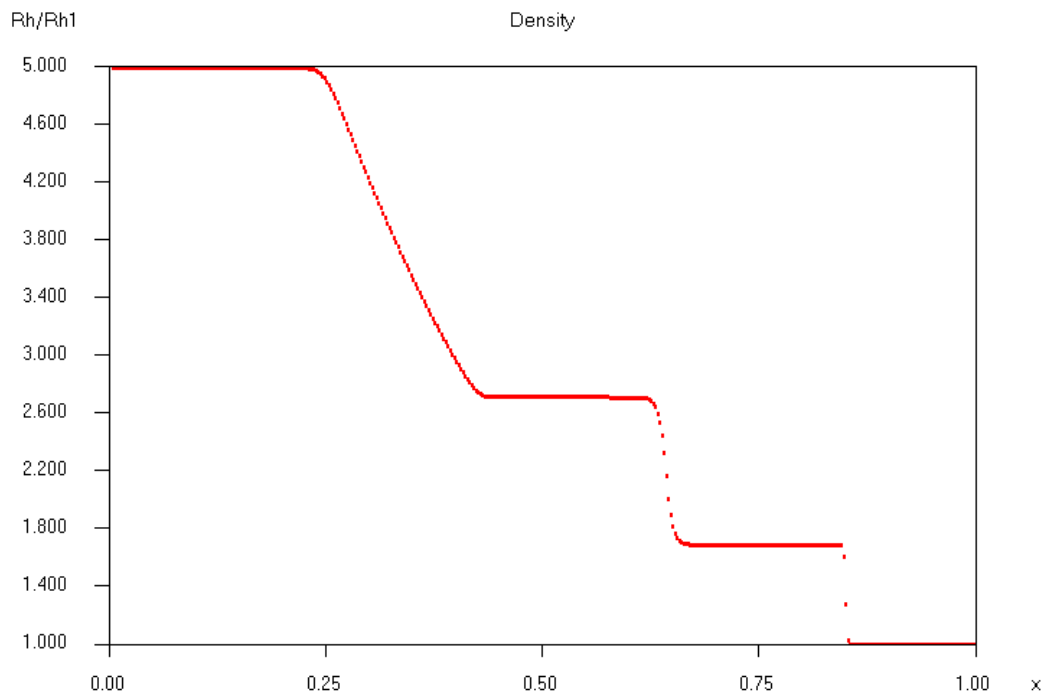


Figure 3-8 Continued—(TVD Solution)

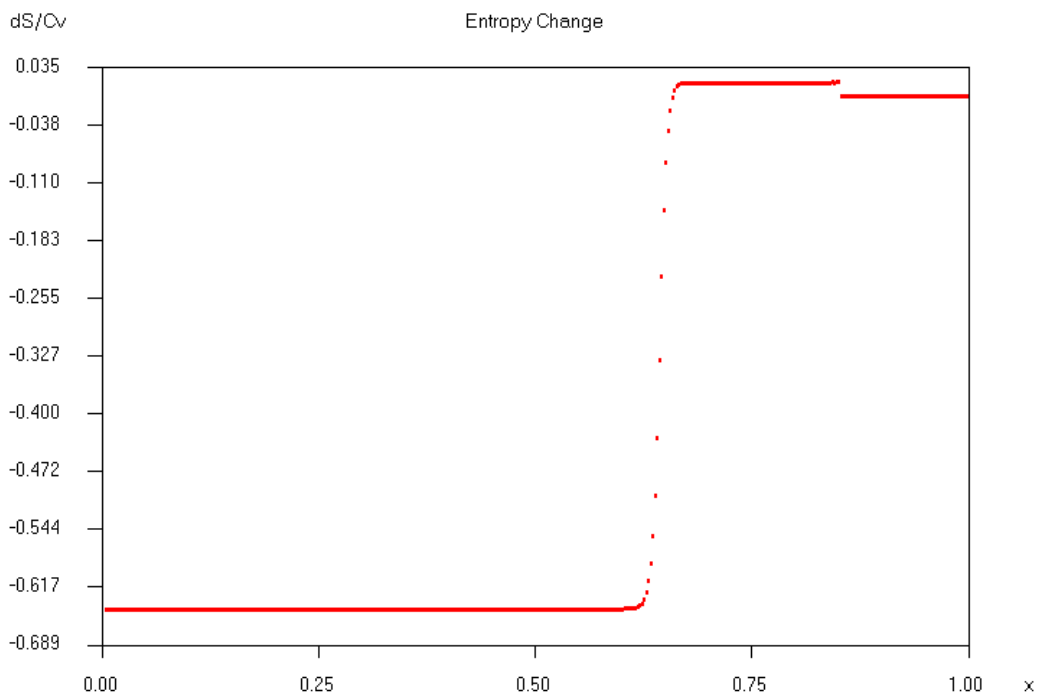
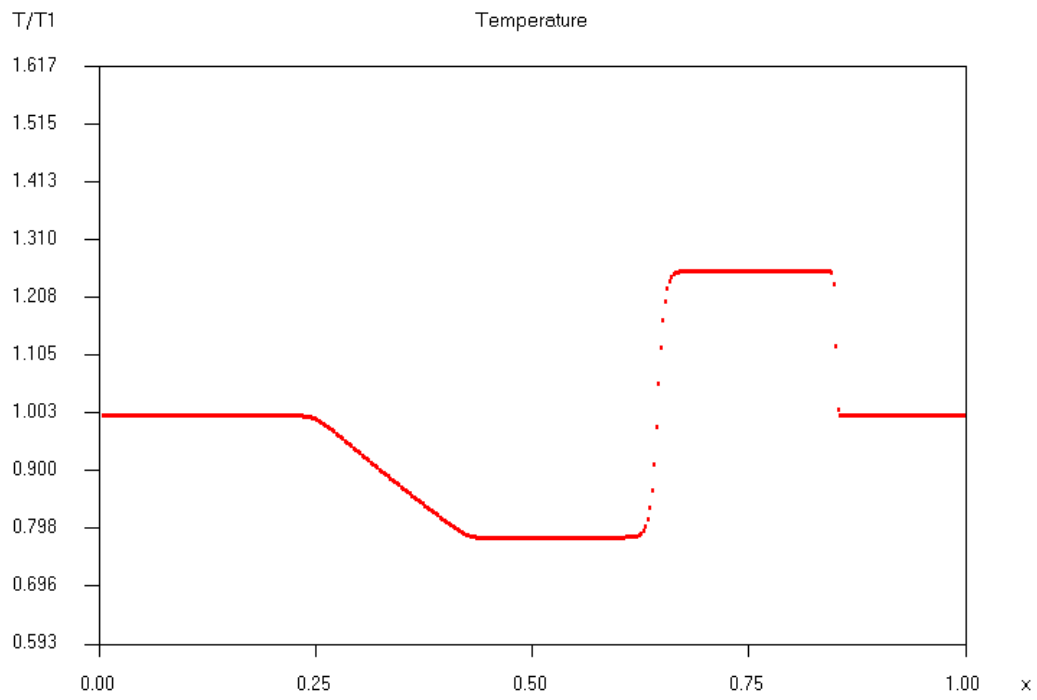


Figure 3-8 Continued—(TVD Solution)

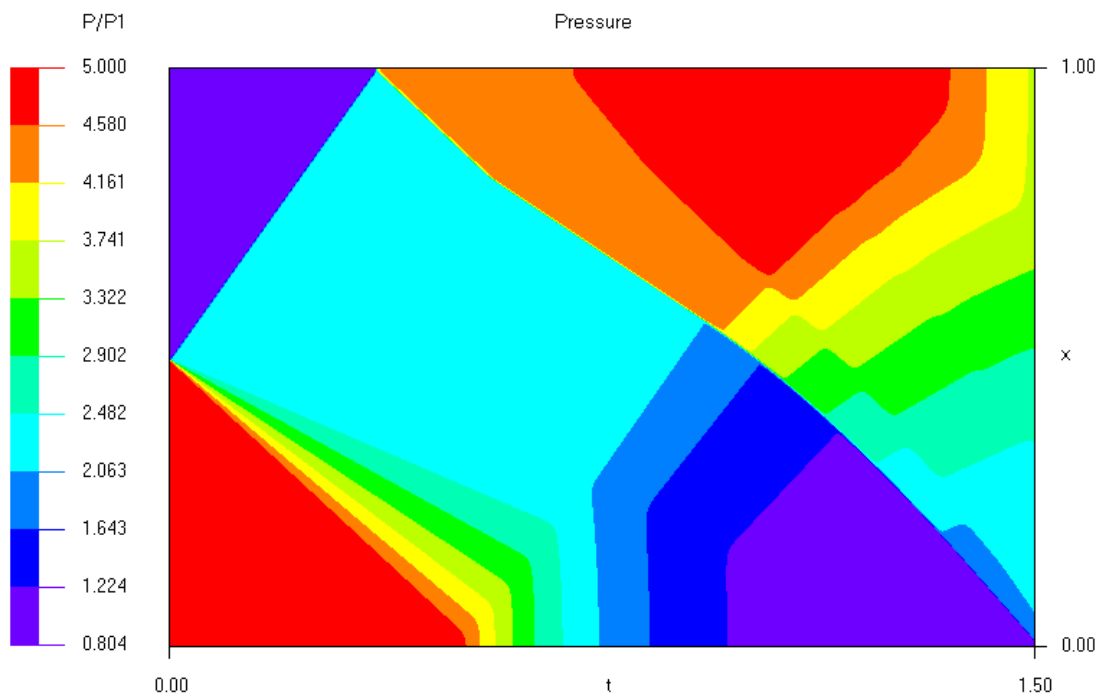
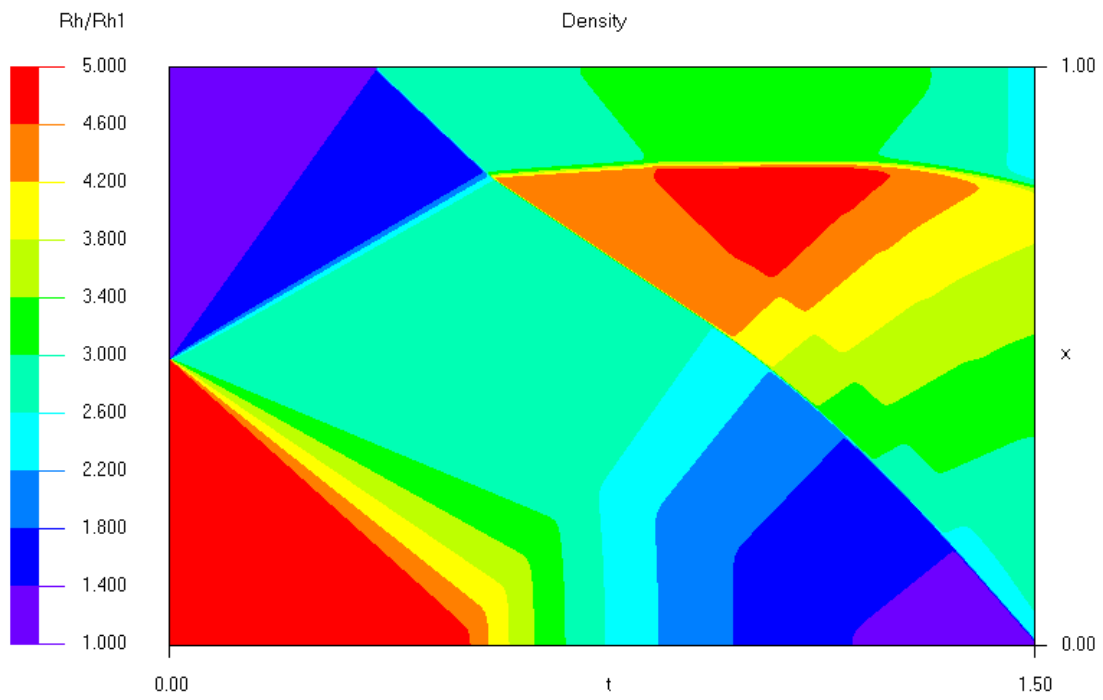


Figure 3-9 Continued—(TVD Solution)

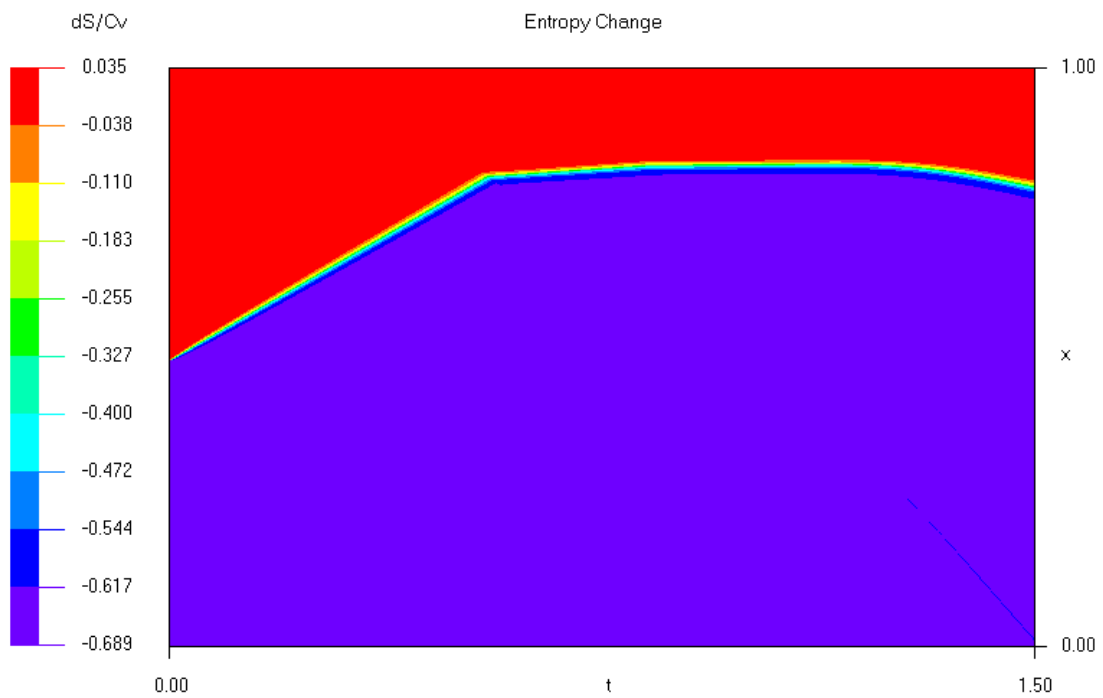
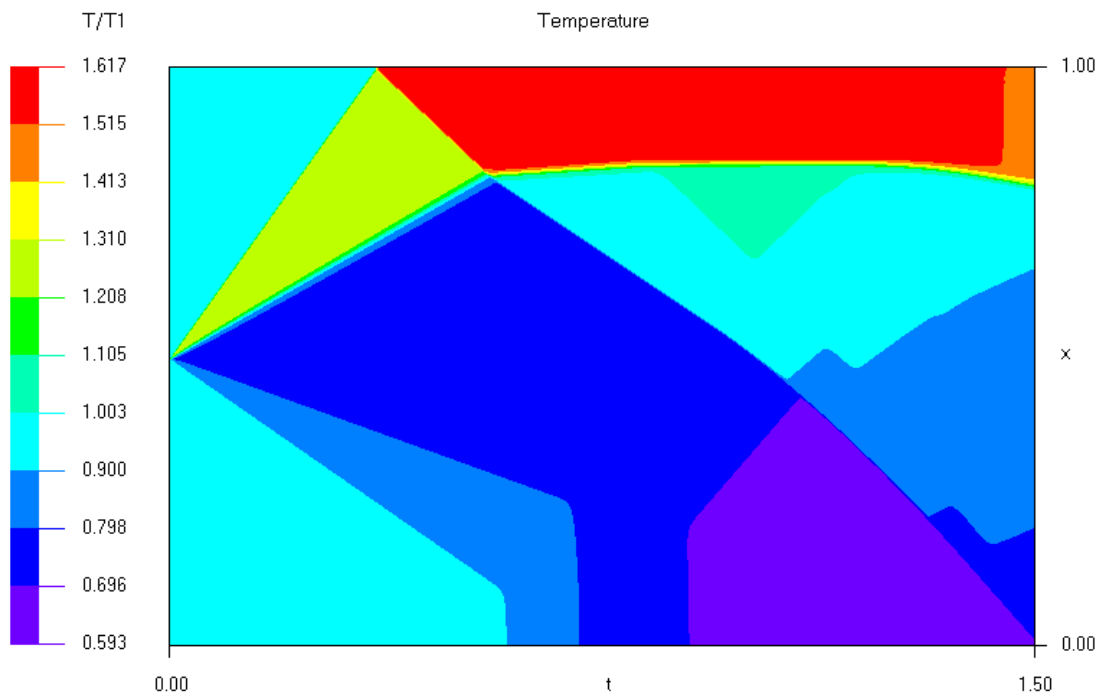


Figure 3-9 Continued—(TVD Solution)

3.3.2.3 ULT Scheme

The ULT scheme is more or less an extension of the TVD scheme presented in the last section and is mainly geared towards the preservation of the contact discontinuity. In Harten's original paper [7], the algorithm was presented as a variation to the ULT1 scheme. He labeled it ULT1C, the C standing for compressive, however the name adopted here shall simply be ULT, short for the *ultimate* TVD algorithm. TVD schemes come in different "flavors" depending on the exact form of the flux correction employed. Since only the two most popular schemes are of interest to us, the abbreviations TVD and ULT were chosen instead of ULT1 and ULT1C for ease of reference. Similar to the previous TVD scheme, the vector \bar{b} is formed as follows,

$$\bar{b}_{i+1/2} = \text{Viscos}(\bar{l}_{i+1/2} + \bar{n}_{i+1/2}) \bar{a}_{i+1/2} - (\bar{g}_i + \bar{g}_{i+1}) \quad (3.67)$$

again with \bar{l} and \bar{a} as previously defined in Equations (3.56) and (3.57). The new flux correction \bar{g} and numerical viscosity modification \bar{n} are calculated in the following manner,

$$\bar{n}_{i+1/2} = \begin{cases} (\bar{g}_{i+1} - \bar{g}_i) / \bar{a}_{i+1/2} & \text{if } \bar{a}_{i+1/2} \neq 0 \\ = 0 & \text{if } \bar{a}_{i+1/2} = 0 \end{cases} \quad (3.68)$$

$$\bar{g}_i = \bar{u}_i + \bar{c}_i \bar{v}_i \quad (3.69)$$

where,

$$\bar{c}_i = \frac{|\bar{a}_{i+1/2} - \bar{a}_{i-1/2}|}{|\bar{a}_{i+1/2}| + |\bar{a}_{i-1/2}|} \quad (3.70)$$

and,

$$\bar{v}_i = \bar{\mathcal{G}}_a \text{Minmod}(\bar{s}_{i+1/2} |\bar{a}_{i+1/2}|, \bar{s}_{i-1/2} \bar{a}_{i-1/2} \bar{\mathcal{G}}_a) \quad (3.71)$$

$$\bar{\mathcal{G}}_a = \text{sgn}(\bar{a}_{i+1/2})$$

$$\bar{s}_{i+1/2} = \frac{1}{2} (1 - \text{Viscos}(\bar{l}_{i+1/2})) \quad (3.72)$$

The vector \bar{u} is defined as before in Equations (3.63) and (3.64). The vector \bar{c} denotes the *artificial compression* introduced into the algorithm. Note that by setting \bar{c} equal to zero, i.e., using no artificial compression, the above algorithm is identical to the TVD scheme presented in the last section.

As before, the derivation of the algorithm shall be referred to Harten's paper [7], yet a few remarks will be made regarding its underlying rationale. Recall that the Euler equations carry three families of waves, each family traveling at a characteristic speed defined by its eigenvalue. Accordingly, an inviscid flow field can be divided into different *characteristic fields*, depending on the type of wave family dominant in the flow. Characteristic fields are recognized in wave diagrams by their *characteristic lines*, along which the wave speed (dx/dt) is constant. Graphically, characteristic lines separate the different colors in a wave diagram. Needless to say, the number of characteristic lines seen in a wave diagram depends on the size of the color palette being used, which is why we only talk about *families* of waves. Also, depending on the flow property being plotted, not all wave families can be identified at once. For example in a wave diagram showing either velocity or pressure, a contact or entropy wave is nowhere to be found.

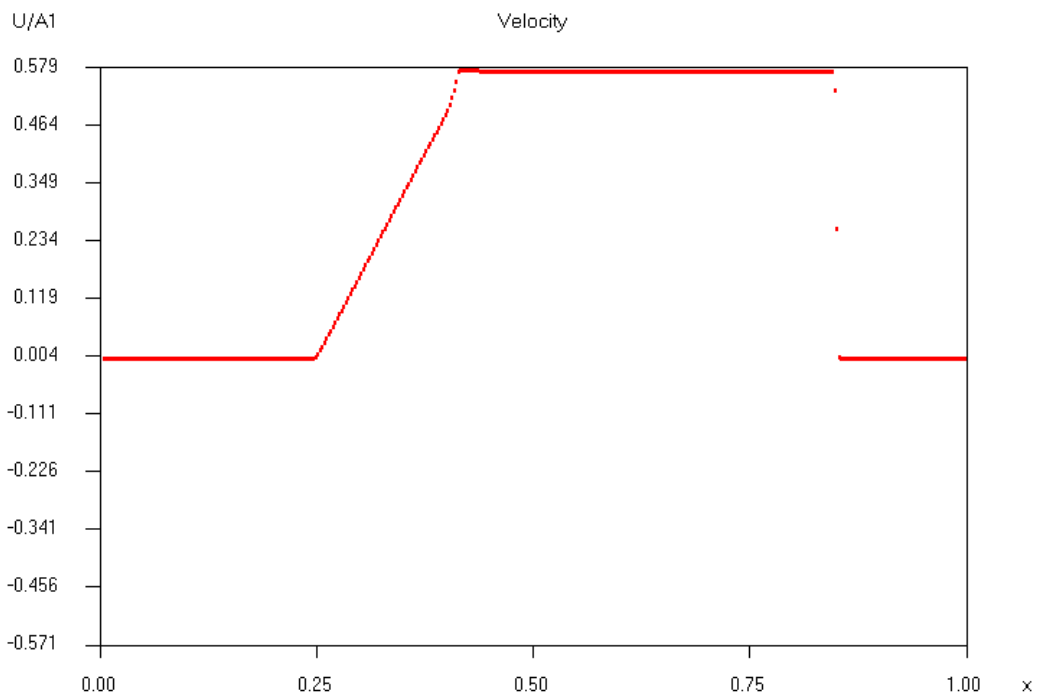
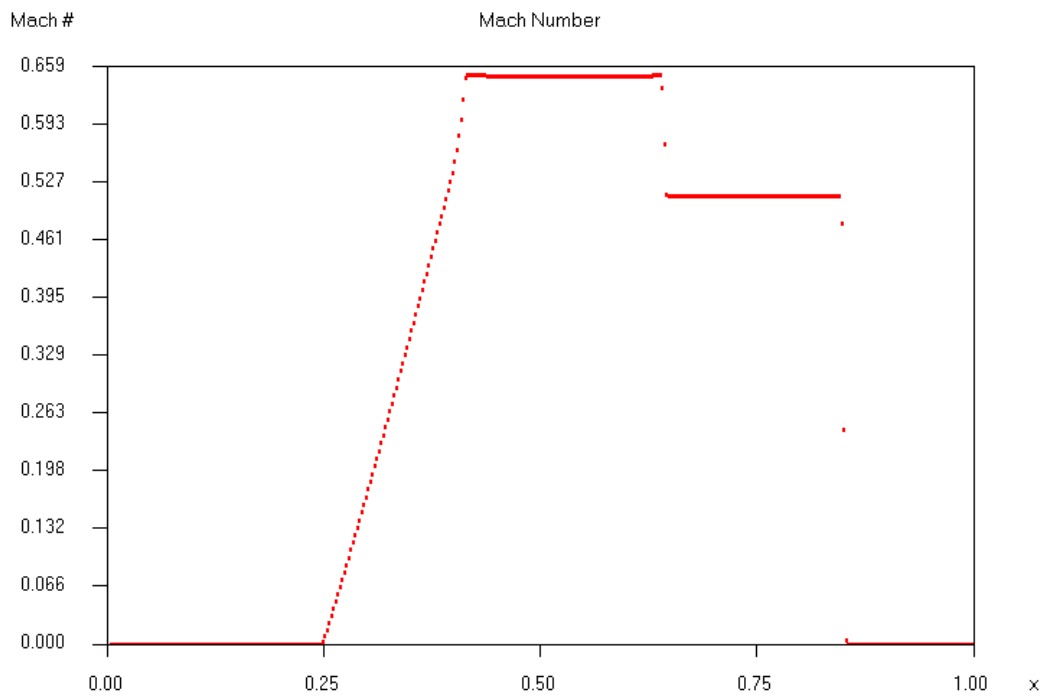


Figure 3-10: Shock Tube Flow at Time $t = 0.25$ (ULT Solution)

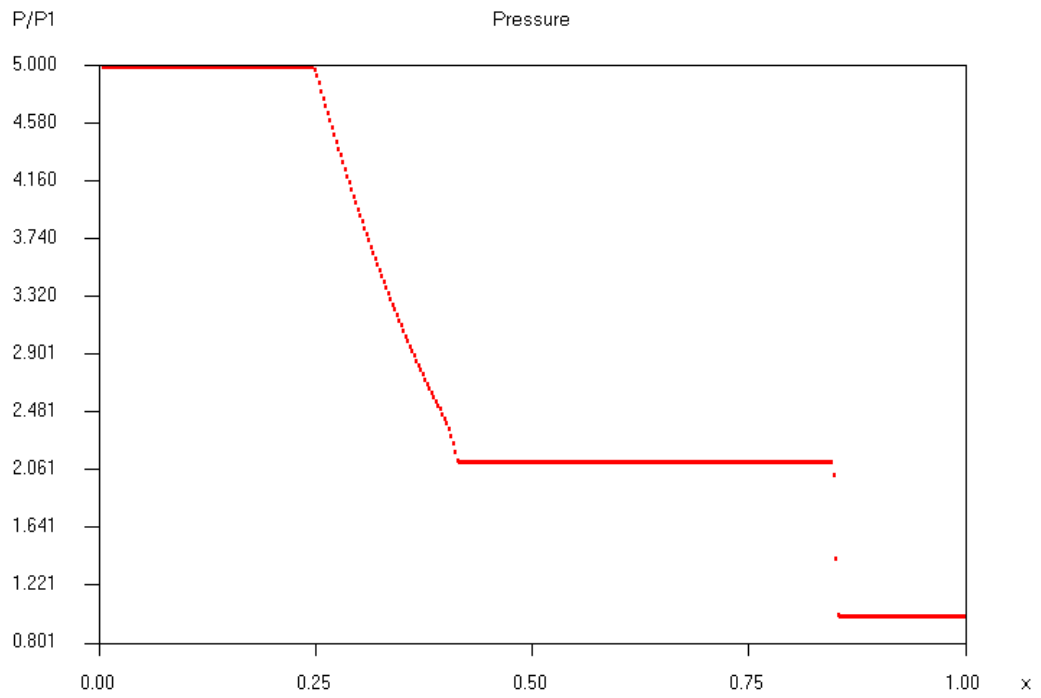
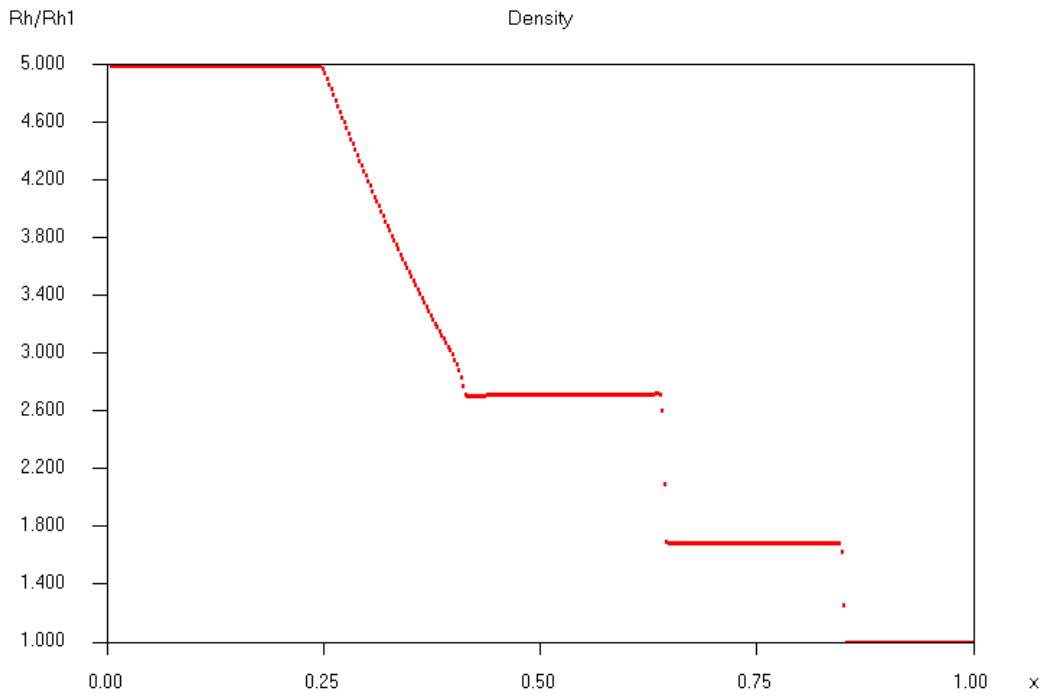


Figure 3-10 Continued—(ULT Solution)

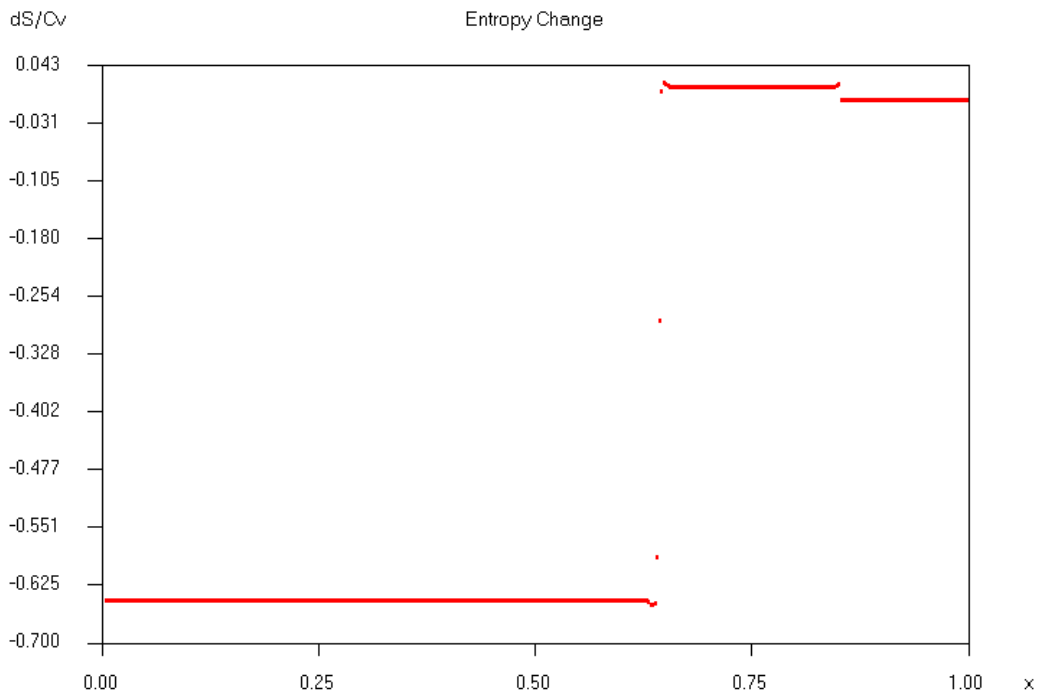
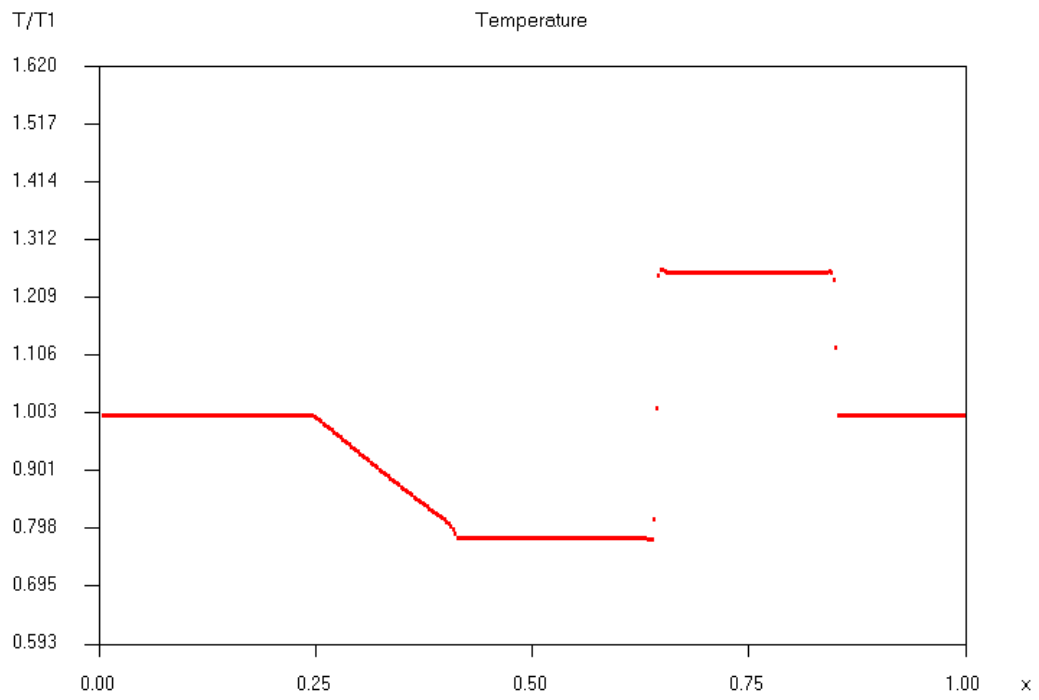


Figure 3-10 Continued—(ULT Solution)

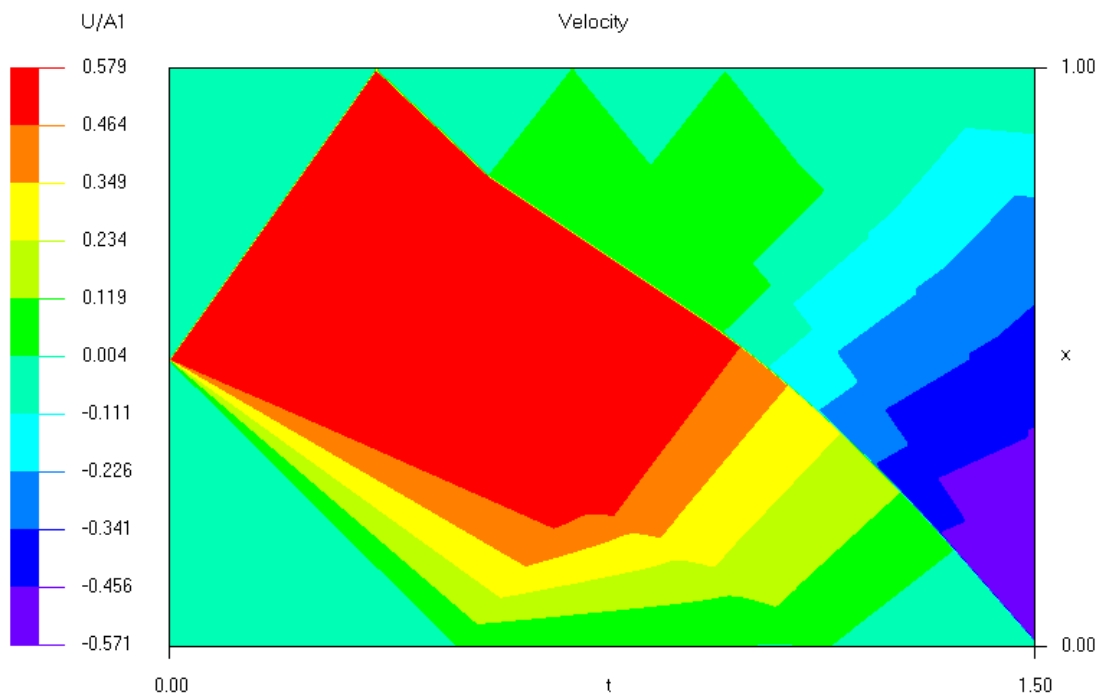
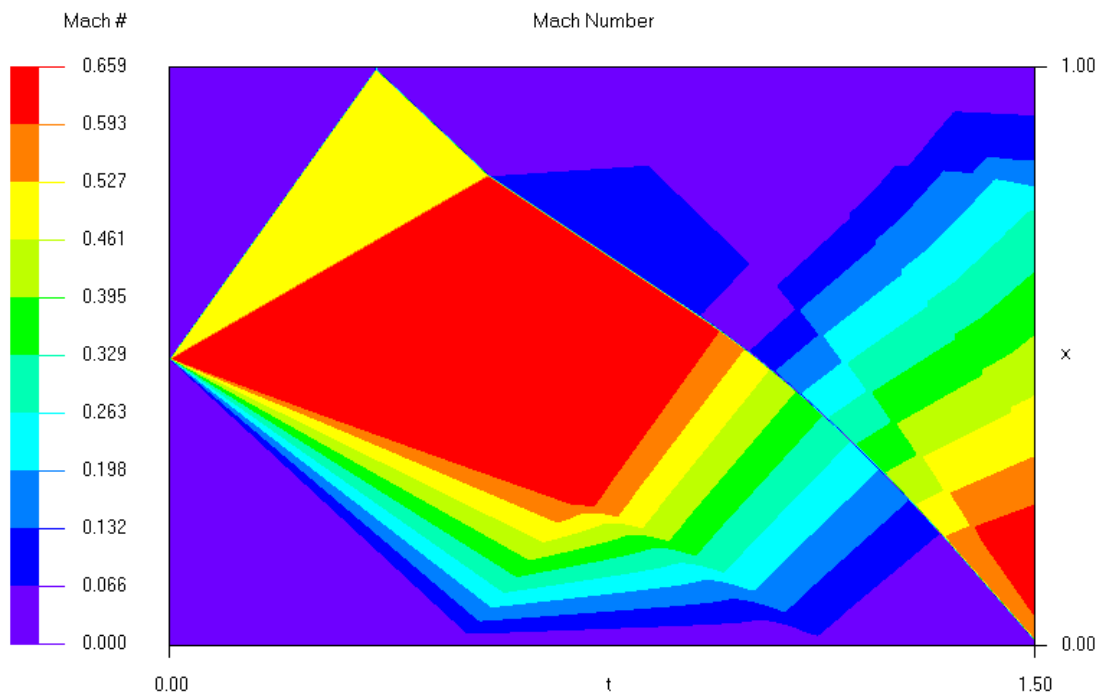


Figure 3-11: Shock Tube Flow – Wave Diagram (ULT Solution)

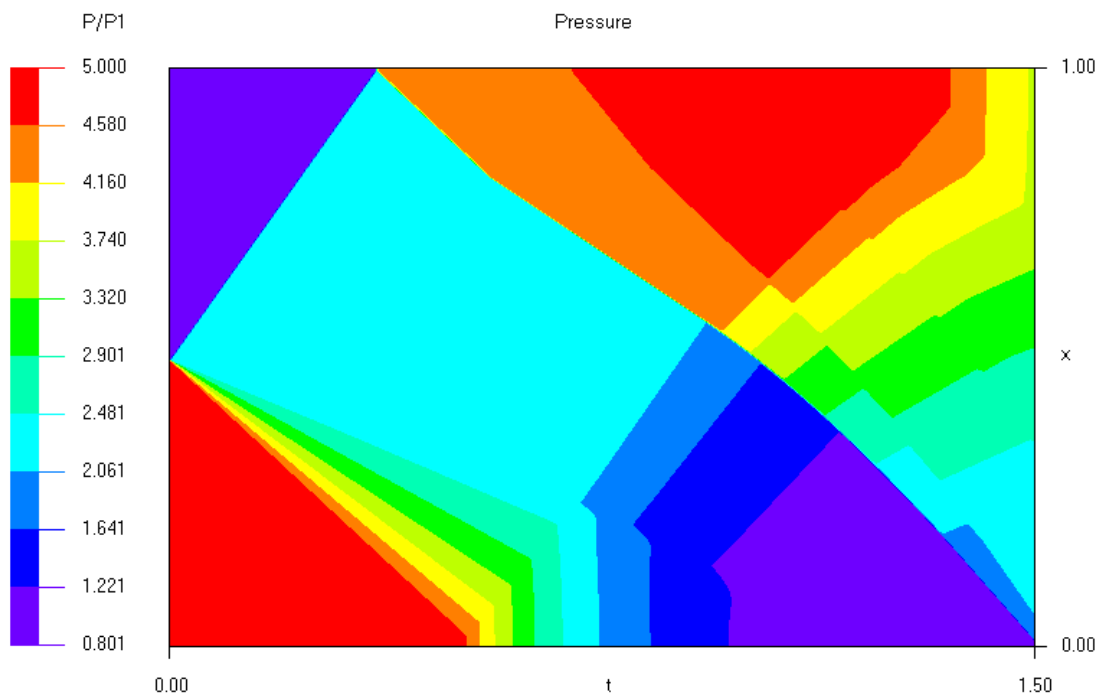
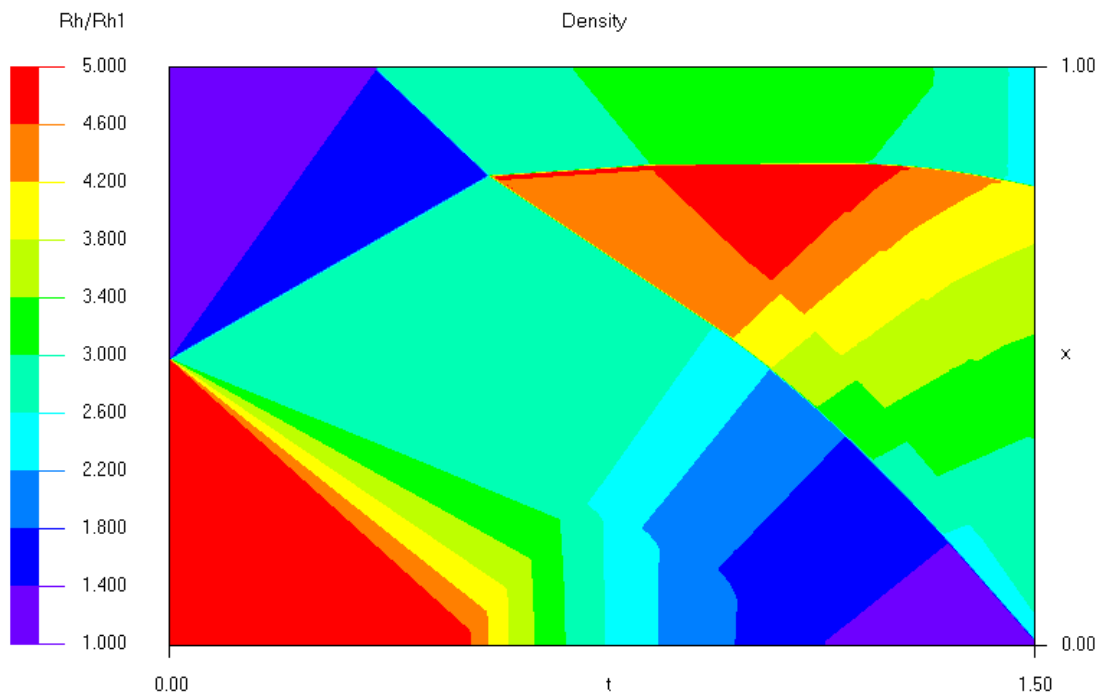


Figure 3-11 Continued—(ULT Solution)

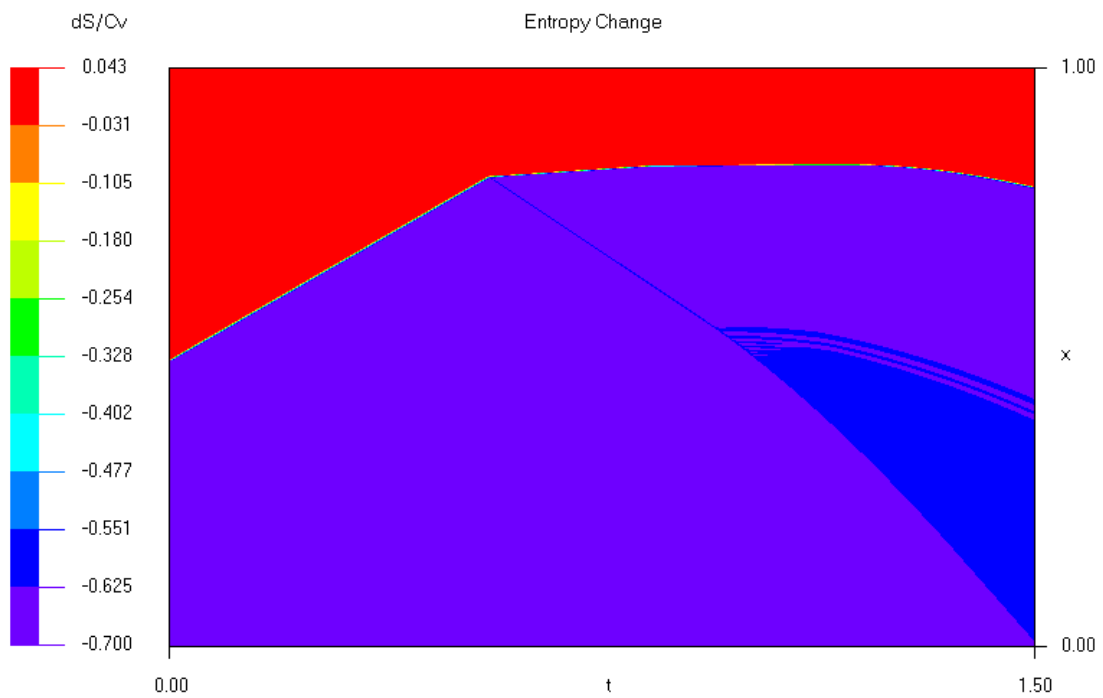
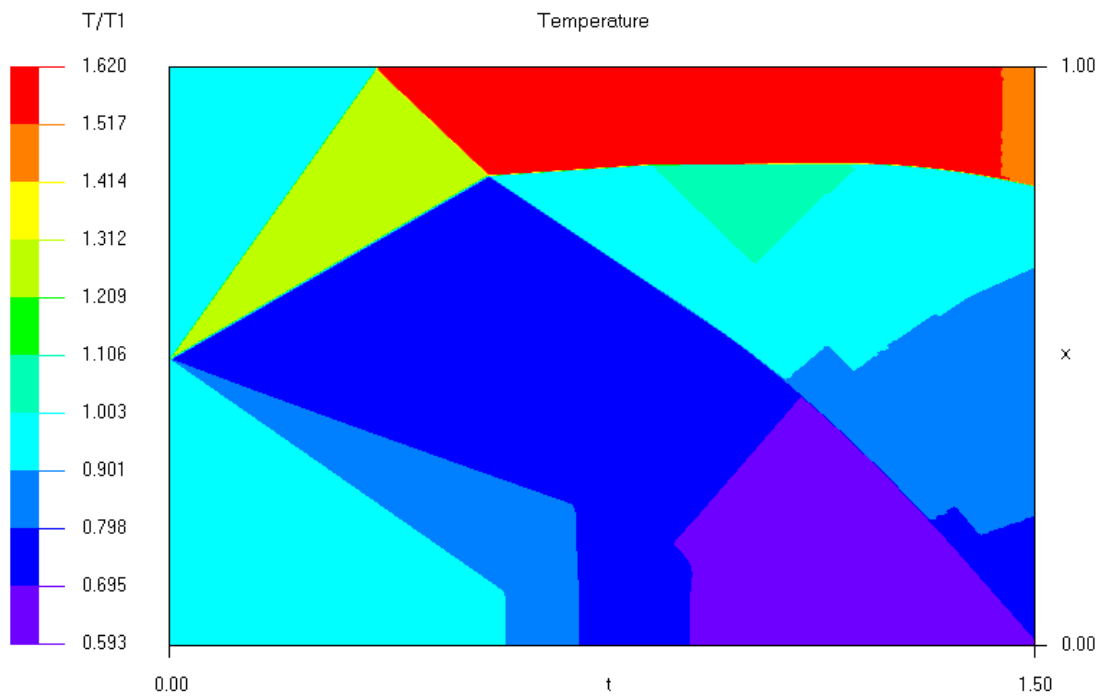


Figure 3-11 Continued—(ULT Solution)

For shocks, the characteristics $dx/dt = u + a$ all coalesce into a single line, whereas for expansion fans, the characteristics $dx/dt = u - a$ fan out between the head and the tail of the expansion. More generally, the characteristic lines of compression waves are convergent, whereas for rarefaction waves they are divergent. For contact discontinuities, which travel with the flow, the nearby characteristics $dx/dt = u$ are parallel. Even a slight numerical divergence of the characteristic lines near a contact, induced by a small amount of artificial viscosity, will result in considerable loss of resolution or *smearing*. On the other hand, a slight convergence of these characteristics, induced by an evenly small amount of artificial compression, will preserve a contact discontinuity almost indefinitely. Such is the rationale of the ULT scheme.

Although artificial compression is applied throughout the flow field, it is yet so small that its effect on shock and expansion fan can hardly be detected. Upon closer inspections of the computed results for the ULT scheme, presented in Figures 3-10 and 3-11 over the last pages, one will notice a minimal overshoot near the contact and around the head of the expansion fan. This effect was not seen before, and can thus be directly attributed to the artificial compression introduced into the algorithm. One should further notice that the scale on some of the graphs, which is dependent on the global range of variables for all times, has slightly increased. Recall that the scale in both the ROE and the TVD solution was identical to the scale of the analytical solution. So there is a bit of a trade-off when using artificial compression. The wave fronts are much better defined in the ULT scheme than they were before, at the same time the range of variables is no longer exact due to some of the overshoots.

When comparing the different wave diagrams of all three schemes (ROE, TVD and ULT) one can clearly observe that the artificial compression of the ULT algorithm has lent its graphs an extraordinary crispness. There is no noticeable deterioration in the contact discontinuity, not even after the shock wave has reflected and traveled through the contact, although a few entropy ripples can be seen in the reflected portion of the wave diagram, which should not be present. Overall, the ULT algorithm appears indeed as the *ultimate* numerical scheme for solving the shock tube problem.

BLANK PAGE

4. SOLUTION DETAIL

The full Navier Stokes (FNS) equations, originally presented in Section 2.2, were completely disassembled in Chapter 3 in order to demonstrate the solution methodology. After eliminating the viscous terms from the full set of conservation equations, an eigensystem analysis was carried out on the remaining Euler equations for 3-D inviscid flow. The wave character of the Euler equations was demonstrated, and the TVD concept was applied to the 1-D inviscid subset, the governing equations for shock tube flow. After taking the FNS equations apart and studying their underlying structure, we are now ready to reassemble them in order to solve the actual problem, the flow over a rotating disc in forward flight.

4.1 Equations for Viscous Flow (FNS)

The conservation equations for viscous flow, which are commonly referred to as the Navier Stokes equations, were introduced in Section 2.2 in a coordinate independent format, using a general notation of vectors and tensors. Based on a fixed Cartesian frame of reference, we shall now rewrite the FNS equations in the same column type format that was used in Section 3.1 for the Euler equations. Again, each column represents the full set of conserved properties—mass, momentum, and energy,

$$\frac{\partial}{\partial t} \int_{CV} \bar{Q} dV + \oint_{CS} \bar{F} dA = 0 \quad (4.1)$$

where,

$$\bar{Q} = \begin{bmatrix} \rho \\ \rho u \\ \rho v \\ \rho w \\ \rho e_o \end{bmatrix}, \quad \bar{F} = \begin{bmatrix} \rho v_n \\ \rho u v_n - f_x \\ \rho v v_n - f_y \\ \rho w v_n - f_z \\ \rho h_o v_n - e_n \end{bmatrix}$$

The velocity across a cell boundary is again defined as the dot product of local velocity vector and outward unit normal vector to the boundary,

$$v_n = \bar{v} \cdot \hat{n} = u n_x + v n_y + w n_z, \quad n_x^2 + n_y^2 + n_z^2 = 1 \quad (4.2)$$

The stagnation energy and enthalpy per unit mass are the sum of static and dynamic parts, respectively,

$$e_o = e + e_k, \quad h_o = h + e_k \quad (4.3)$$

$$e_k = \frac{1}{2} (u^2 + v^2 + w^2)$$

where e_k is the kinetic energy per unit mass. Static energy, enthalpy, and pressure shall now be expressed in terms of temperature,

$$e = c_v T, \quad h = c_p T, \quad p = \rho R T \quad (4.4)$$

The energy flux e_n across a cell boundary, which is due to heat exchange as well the work done by the viscous stress tensor, is defined as follows,

$$e_n = (\vec{\bar{\tau}} \cdot \vec{v} - \vec{q}) \cdot \hat{n} \quad (4.5)$$

where,

$$\vec{\bar{\tau}} = \begin{bmatrix} \tau_{xx} & \tau_{xy} & \tau_{xz} \\ \tau_{yx} & \tau_{yy} & \tau_{yz} \\ \tau_{zx} & \tau_{zy} & \tau_{zz} \end{bmatrix}, \quad \vec{q} = \begin{pmatrix} q_x \\ q_y \\ q_z \end{pmatrix} \quad (4.6)$$

The force vector \vec{f} , which appears in the momentum equation, is the dot product of the stress tensor $\vec{\bar{\sigma}}$ and the outward unit normal to the surface,

$$\vec{f} = \vec{\bar{\sigma}} \cdot \hat{n} = \begin{pmatrix} f_x \\ f_y \\ f_z \end{pmatrix} \quad (4.7)$$

where,

$$\vec{\bar{\sigma}} = \begin{bmatrix} \tau_{xx} - p & \tau_{xy} & \tau_{xz} \\ \tau_{yx} & \tau_{yy} - p & \tau_{yz} \\ \tau_{zx} & \tau_{zy} & \tau_{zz} - p \end{bmatrix} \quad (4.8)$$

The components of the viscous stress tensor $\vec{\bar{\tau}}$, based on a Cartesian frame of reference, are determined through local velocity gradients,

$$\begin{aligned} \tau_{xx} &= \frac{2}{3} \mu \left(2 \frac{\partial u}{\partial x} - \frac{\partial v}{\partial y} - \frac{\partial w}{\partial z} \right), & \tau_{xy} &= \mu \left(\frac{\partial v}{\partial x} + \frac{\partial u}{\partial y} \right) = \tau_{yx} \\ \tau_{yy} &= \frac{2}{3} \mu \left(2 \frac{\partial v}{\partial y} - \frac{\partial u}{\partial x} - \frac{\partial w}{\partial z} \right), & \tau_{yz} &= \mu \left(\frac{\partial w}{\partial y} + \frac{\partial v}{\partial z} \right) = \tau_{zy} \\ \tau_{zz} &= \frac{2}{3} \mu \left(2 \frac{\partial w}{\partial z} - \frac{\partial v}{\partial y} - \frac{\partial u}{\partial x} \right), & \tau_{zx} &= \mu \left(\frac{\partial u}{\partial z} + \frac{\partial w}{\partial x} \right) = \tau_{xz} \end{aligned} \quad (4.9)$$

Similarly, the components of the heat flux vector \vec{q} are determined through local temperature gradients according to Fourier's law of heat conduction,

$$q_x = -\kappa \frac{\partial T}{\partial x}, \quad q_y = -\kappa \frac{\partial T}{\partial y}, \quad q_z = -\kappa \frac{\partial T}{\partial z} \quad (4.10)$$

The local gradients of velocity and temperature are difficult to calculate unless the finite volume mesh is Cartesian. Determining the above partial derivatives on a curvilinear mesh is anything but a trivial task. One may attempt to come up with an interpolation algorithm, which realigns all flow properties with the major axes. Although such algorithms exist, which are widely used in flow visualization, there are more elegant ways of computing the gradients. The standard method is based on a mathematical transformation from local to global coordinates, which will be presented over the next sections.

4.2 Curvilinear Coordinate System

Before we introduce the mathematics of coordinate transformations, we shall first define the curvilinear coordinate system employed on our finite volume mesh. Recall from Figure 2-2 that the construction of the finite volume mesh becomes almost spherical as one moves further away from the surface of the ellipsoid. Therefore, the natural way of indexing the cells within the mesh is through an adaptation of the spherical coordinate system. Similar to longitude, latitude, and altitude around a globe, the cells around the ellipsoid are numbered according to their radial (I), polar (J), and circumferential (K) position, which is shown in Figure 4-1. Index i runs from the surface of the ellipsoid to the outer spherical boundary. Index j traverses 180 degrees from “north pole” to “south pole”. And index k sweeps 360 degrees counter-clockwise around the polar axis, when viewed from above, starting just to the left of the “date line” and ending to its right.

We shall distinguish between *local* (I, J, K) and *global* (x, y, z) coordinate systems. The global *Cartesian* coordinate system is fixed in space; its axes originate at the center of the ellipsoid, and they are orthogonal with respect to each other. The axes of the local coordinate system, however, are *nearly orthogonal* at most, and being located at the center of each cell—defined here to be the average of its corner points—their direction changes from one cell to another. Note that both local and global coordinate systems are right-handed, meaning that each set of axes can be visualized by thumb, index, and middle finger of the right hand. The right-handedness property is important for the metrics of the coordinate transformation. Although the indices (i, j, k) are discrete integers, the coordinates (I, J, K) are continuous, and at cell centers their values coincide ($I = i, J = j, K = k$). Therefore, the distance between adjacent cell centers measured along the local axes is always unity by construction.

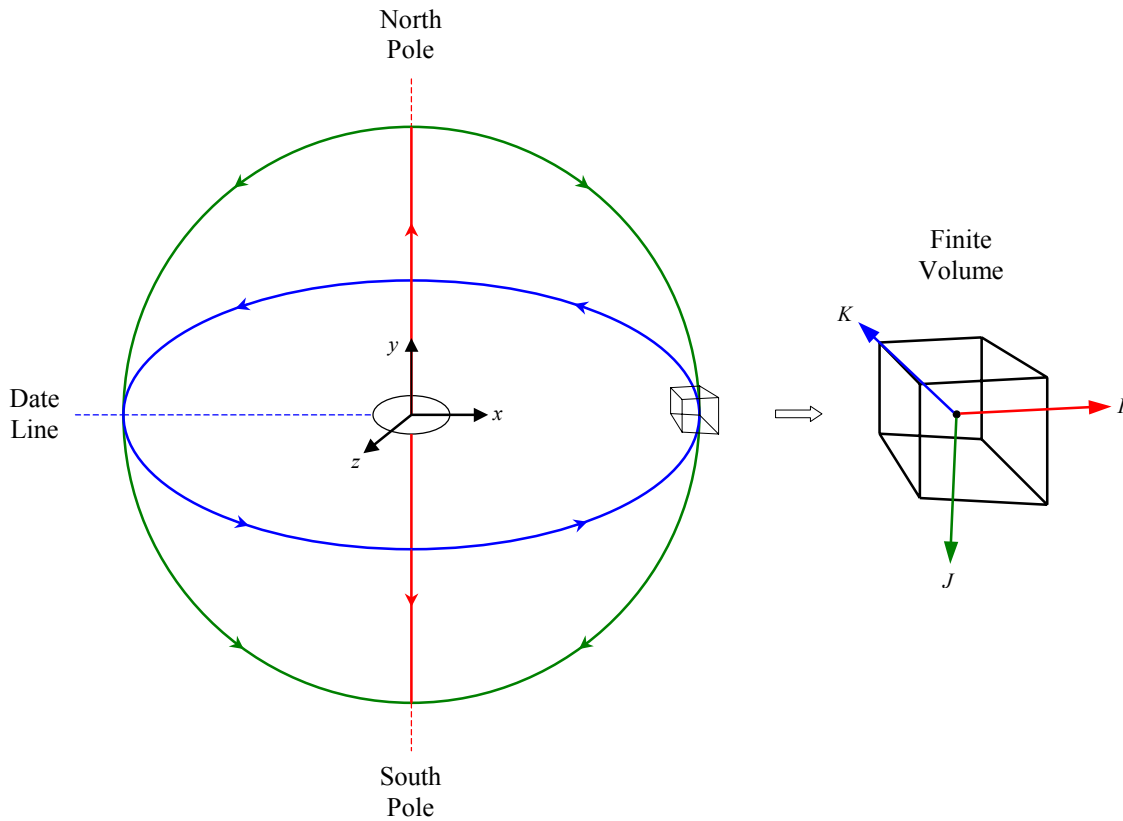


Figure 4-1: Local and Global Coordinate System

4.3 Coordinate Transformation

For the curvilinear coordinate system shown in Figure 4-1, each set of local coordinates (I, J, K) can be expressed as a function of global coordinates (x, y, z), which is known as the transformation,

$$I = I(x, y, z), \quad J = J(x, y, z), \quad K = K(x, y, z) \quad (4.11)$$

Using the chain rule of partial differentiation, the partial derivatives based on the fixed reference frame are,

$$\begin{aligned} \frac{\partial(\quad)}{\partial x} &= I_x \frac{\partial(\quad)}{\partial I} + J_x \frac{\partial(\quad)}{\partial J} + K_x \frac{\partial(\quad)}{\partial K} \\ \frac{\partial(\quad)}{\partial y} &= I_y \frac{\partial(\quad)}{\partial I} + J_y \frac{\partial(\quad)}{\partial J} + K_y \frac{\partial(\quad)}{\partial K} \\ \frac{\partial(\quad)}{\partial z} &= I_z \frac{\partial(\quad)}{\partial I} + J_z \frac{\partial(\quad)}{\partial J} + K_z \frac{\partial(\quad)}{\partial K} \end{aligned} \quad (4.12)$$

where

$$\begin{aligned} I_x &= \frac{\partial I}{\partial x}, \quad J_x = \frac{\partial J}{\partial x}, \quad K_x = \frac{\partial K}{\partial x} \\ I_y &= \frac{\partial I}{\partial y}, \quad J_y = \frac{\partial J}{\partial y}, \quad K_y = \frac{\partial K}{\partial y} \\ I_z &= \frac{\partial I}{\partial z}, \quad J_z = \frac{\partial J}{\partial z}, \quad K_z = \frac{\partial K}{\partial z} \end{aligned} \quad (4.13)$$

are known as the metrics of the transformation; we can write them in packets of three, using the gradient operator,

$$\nabla I = \begin{pmatrix} I_x \\ I_y \\ I_z \end{pmatrix}, \quad \nabla J = \begin{pmatrix} J_x \\ J_y \\ J_z \end{pmatrix}, \quad \nabla K = \begin{pmatrix} K_x \\ K_y \\ K_z \end{pmatrix} \quad (4.14)$$

These gradient vectors can be directly related to familiar finite volume terms, a heuristic result, which will become apparent over the next sections,

$$\begin{aligned} \nabla I_{i+1/2,j,k} &= \hat{n}_{i+1/2,j,k} \frac{\Delta A_{i+1/2,j,k}}{\frac{1}{2}(\Delta V_{i+1,j,k} + \Delta V_{i,j,k})} \\ \nabla J_{i,j+1/2,k} &= \hat{n}_{i,j+1/2,k} \frac{\Delta A_{i,j+1/2,k}}{\frac{1}{2}(\Delta V_{i,j+1,k} + \Delta V_{i,j,k})} \\ \nabla K_{i,j,k+1/2} &= \hat{n}_{i,j,k+1/2} \frac{\Delta A_{i,j,k+1/2}}{\frac{1}{2}(\Delta V_{i,j,k+1} + \Delta V_{i,j,k})} \end{aligned} \quad (4.15)$$

To apply Equations (4.12) and (4.13), we shall write out the finite difference expression for the temperature gradient along the x direction at a cell center. By definition, $\Delta I = \Delta J = \Delta K = 1$, which simplifies the terms,

$$\begin{aligned} \left(\frac{\partial T}{\partial x} \right)_{i,j,k} &= \frac{1}{2} (I_x)_{i+1/2,j,k} (T_{i+1,j,k} - T_{i,j,k}) + \frac{1}{2} (I_x)_{i-1/2,j,k} (T_{i,j,k} - T_{i-1,j,k}) \\ &+ \frac{1}{2} (J_x)_{i,j+1/2,k} (T_{i,j+1,k} - T_{i,j,k}) + \frac{1}{2} (J_x)_{i,j-1/2,k} (T_{i,j,k} - T_{i,j-1,k}) \\ &+ \frac{1}{2} (K_x)_{i,j,k+1/2} (T_{i,j,k+1} - T_{i,j,k}) + \frac{1}{2} (K_x)_{i,j,k-1/2} (T_{i,j,k} - T_{i,j,k-1}) \end{aligned} \quad (4.16)$$

Since the gradients at all six faces of the volume element are averaged equally, the above formula is *centrally differenced*, and its accuracy is second order. The temperature gradients along the y and z direction are computed analogously, by using the respective metrics.

One may wonder about the applicability of Equation (4.16) near the poles. After all, the polar axis is a mathematical singularity, which makes it difficult to define gradients. Consistent with our mathematical formulation, we shall approach this problem from a finite volume point of view. One can view the polar axis as a stack of cells that have all collapsed into a single line as their volume has shrunk to zero. Accordingly, the area of their cell faces is also zero, which implies that no flux can leave or enter them. This only makes sense, because a cell of zero volume would not be able to store anything anyway. Thus if no energy can be stored inside a collapsed *polar cell*, no heat flux can enter it, and therefore the temperature gradient towards the polar axis must vanish. This does not imply that we cannot have different temperatures at opposite sides of the pole; it only means that according to our finite volume model there is no direct heat exchange between such cells. Any heat exchange between two cells on opposite sides of the polar axis must travel *around* the axis, traversing all intermediate cells along the circumferential direction. By assigning zero volume and zero face area to these imaginary polar cells, we shall now demonstrate that Equation (4.16) is valid throughout the computational domain. For $j = 1, \dots, J_{\max}$ on the interior,

$$\begin{aligned} \Delta V_{i,0,k} &= 0, & \Delta A_{i,1/2,k} &= 0 & \text{(North Pole)} \\ \Delta V_{i,J_{\max}+1,k} &= 0, & \Delta A_{i,J_{\max}+1/2,k} &= 0 & \text{(South Pole)} \end{aligned} \quad (4.17)$$

which yields,

$$\nabla J_{i,1/2,k} = 0, \quad \nabla J_{i,J_{\max}+1/2,k} = 0 \quad (4.18)$$

according to Equation (4.15). When substituting this result into Equation (4.16), the temperature gradient into the pole does indeed vanish. Therefore, Equation (4.16) is applicable near the poles. It is needless to say that finite difference expressions for velocity gradients can be derived similar to Equation (4.16), which would also be valid throughout the computational domain, including near the poles. The above discussion was limited to temperature gradients and heat flux, which is physically more intuitive than velocity gradients and divergence.

Next to the poles, the circumferential cut or “date line” is another area of concern when taking derivatives or evaluating fluxes. The index k starts and ends with the dateline, running from $k = 1, \dots, K_{\max}$. Whenever $k = 1$ and a difference equation addresses a quantity labeled with $l = k - 1$, the computer program has to automatically fetch the quantity on the other side of the cut by replacing the address with $l = K_{\max}$. Likewise, whenever $k = K_{\max}$, an address $m = k + 1$ must be replaced with $m = 1$.

4.4 Finite Volume Approximation

In Equation (4.15) the transformation metrics were related to the more physical finite volume terms. Although the 2-D analogue to this equation is always exact, the 3-D version presented here is only a good approximation, largely depending on how the terms on either side of the equation are calculated and on the degree of distortion of each *hexahedral* element within the mesh. As seen in Figure 4-2, a *hexahedron* carries six faces (thus the name) and can be compared to a distorted cube, similar to a cardboard box that has somehow been bent out of shape. Depending on the level of distortion, none of the six faces may be planar. In other words, each face may experience some degree of curvature. Try to imagine an out-of-shape cardboard box that would not sit level on an even floor, and which could be rocked slightly back and forth. Since the area of a hexahedral face cannot be exactly defined, neither can its volume, which explains why Equation (4.15) is just a numerical approximation of terms and not an exact relation.

The approach taken here, in approximating the volume and face areas of a hexahedral cell, is graphically outlined in Figure 4-2. For simplicity, the local coordinate system was attached to the lower corner of the hexahedron instead of its center. Although this is inconsistent with our usual description of terms, the half-indexing was avoided for the sake of clarity. Based on the eight corner points of the hexahedron, which are defined in Cartesian coordinates via \vec{C} , the face areas are computed by diagonally spanning vectors across each face and taking their cross product. The magnitude of the resulting vector cross product yields twice the projected surface area; the direction of vector \vec{S} is normal to the plane of projection, pointing inward. One may ask, how the area is projected. Whenever there is curvature present within a face, the vectors spanning diagonal corners do not intersect. By shifting these vectors in space such that they do intersect diagonally, one moves them into a common plane, which is the plane of projection.

Notice that we only have to calculate the surface area to three orthogonal faces—nearly orthogonal to be precise—for each hexahedral cell. The remaining face areas are calculated via neighboring cells, as one sweeps the entire mesh along radial, polar, and circumferential direction. For this reason, it was decided to have all surface vectors point along the direction of the local coordinate system. After all, an inward normal to one cell is an outward normal to its neighboring cell.

The volume of the hexahedron is obtained by slicing it into three pyramids, such that the base of each pyramid coincides with one of the faces for which the surface area has already been calculated. It can be seen in Figure 4-1 that all three pyramids share a common edge, spanned by the \vec{H} vector, which points to the tip of each pyramid. By dotting the \vec{H} and \vec{S} vectors, one obtains the product of base area and height of each pyramid, which is three times its volume. The volume of the entire hexahedron is simply the sum of all pyramid volumes. Mathematically, this is equivalent to adding the base vectors first and then dotting them collectively with one-third of the “height” vector, which is the formula presented in Figure 4-2. Again, it should be emphasized that the volume computed is only an approximation based on the projected faces of the hexahedron.

$$\begin{aligned} \text{Physical Space Volume} &= \frac{\pi}{6} (7D)^3 - \frac{\pi}{6} (D)^3 (1/6) = 179.507D^3 \\ \text{Numerical Mesh Volume} &= \sum_{i=1}^{I_{\max}} \sum_{j=1}^{J_{\max}} \sum_{k=1}^{K_{\max}} \Delta V_{i,j,k} = 179.046D^3 \end{aligned} \quad (4.19)$$

An accuracy check of the volume approximation formula was carried out by computing the volume of the entire 60x40x80 mesh and comparing it to its “exact” value, the physical space occupied between the outer sphere and the inner ellipsoid. Although the error is only 0.257% with respect to the entire volume, it is equivalent to more than five times the volume of the ellipsoid.

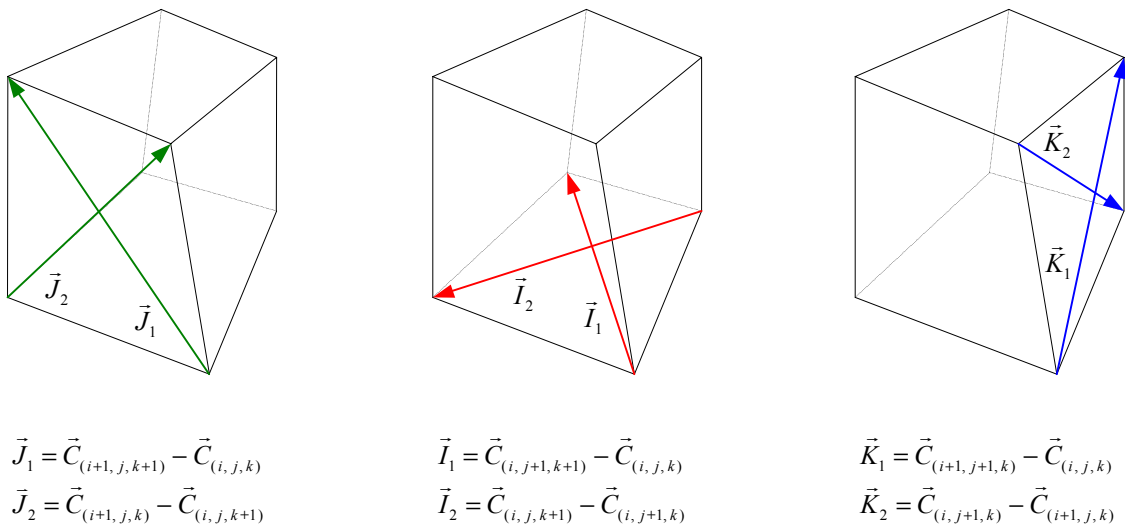
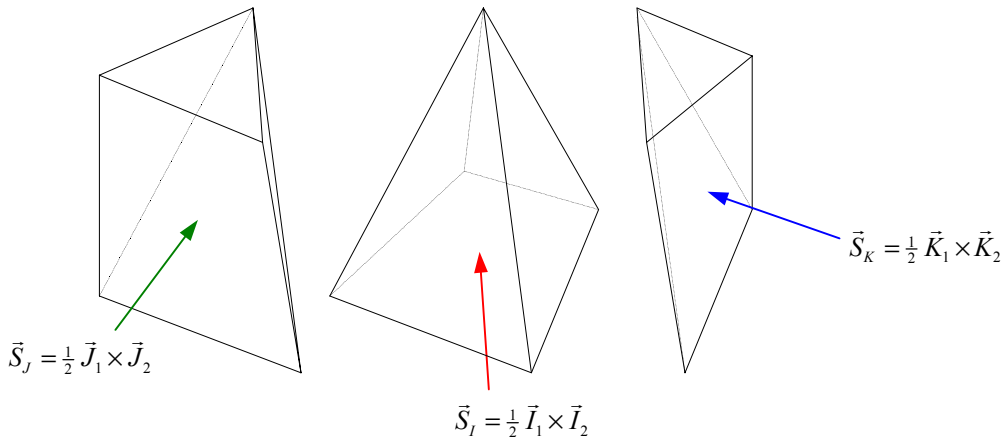
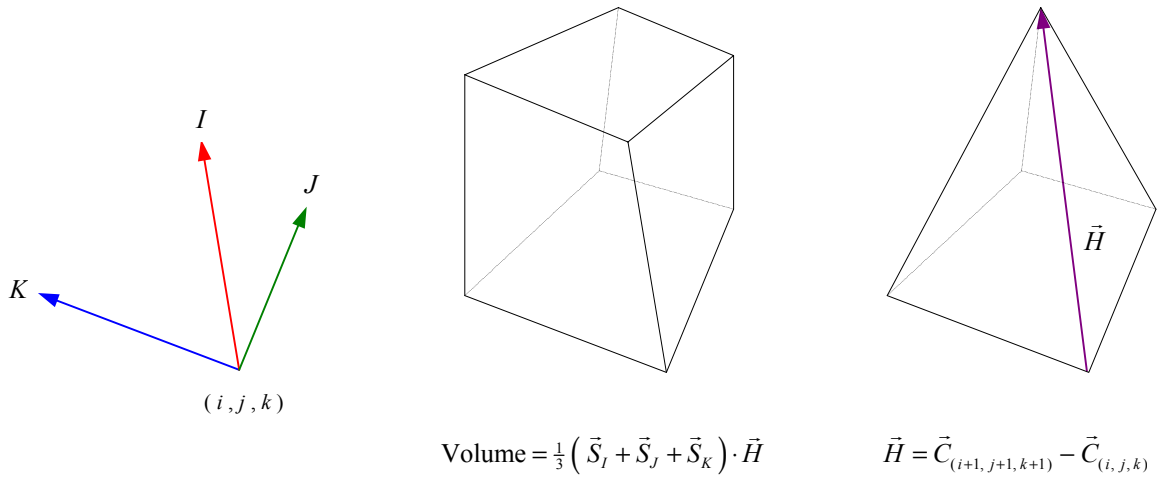


Figure 4-2: Volume of Hexahedron

4.5 Discretization Scheme

The numerical discretization of the 3-D Navier Stokes equations is simply an extension to the discretization of the 1-D Euler equations presented in Section 3.3.2. We are now summing fluxes over six faces instead of two, and each term in the discretized equation is identified via three indices instead of one. Using first-order accurate explicit time marching as before, the discretized set of viscous conservation equations is,

$$\begin{aligned} \bar{Q}_{i,j,k}^{p+1} = \bar{Q}_{i,j,k}^p - \frac{\Delta t}{\Delta V_{i,j,k}} & \left\{ (\bar{F}_{i+1/2,j,k} \Delta A_{i+1/2,j,k} + \bar{F}_{i,j+1/2,k} \Delta A_{i,j+1/2,k} + \bar{F}_{i,j,k+1/2} \Delta A_{i,j,k+1/2}) \right. \\ & \left. - (\bar{F}_{i-1/2,j,k} \Delta A_{i-1/2,j,k} + \bar{F}_{i,j-1/2,k} \Delta A_{i,j-1/2,k} + \bar{F}_{i,j,k-1/2} \Delta A_{i,j,k-1/2}) \right\} \\ & + \frac{1}{2} \left\{ (\bar{f}_{i+1/2,j,k} + \bar{f}_{i,j+1/2,k} + \bar{f}_{i,j,k+1/2}) - (\bar{f}_{i-1/2,j,k} + \bar{f}_{i,j-1/2,k} + \bar{f}_{i,j,k-1/2}) \right\} \end{aligned} \quad (4.20)$$

where,

$$\begin{aligned} \bar{F}_{i+1/2,j,k} &= \frac{1}{2} \bar{F}(\bar{Q}_{i,j,k}^p) + \frac{1}{2} \bar{F}(\bar{Q}_{i+1,j,k}^p) \\ \bar{F}_{i-1/2,j,k} &= \frac{1}{2} \bar{F}(\bar{Q}_{i,j,k}^p) + \frac{1}{2} \bar{F}(\bar{Q}_{i-1,j,k}^p) \end{aligned}$$

The flow vector \bar{Q} and flux vector \bar{F} were defined in Section 4.1, including all of their intrinsic terms. The evaluation of fluxes at cell interfaces along the polar (J) and circumferential (K) directions is carried out analogously. The discretization of the heat flux vector and viscous stress tensor inherent in \bar{F} has already been demonstrated in Section 4.3 and shall not be repeated here. The eigenfluxes \bar{f} are now based on the eigensystem of the 3-D Euler equations derived in Section 3.2. The 5x5 matrices of left and right eigenvectors used below are chosen from the set $\{(L-1), (L-2), (L-3)\}$ and $\{(R-1), (R-2), (R-3)\}$ each, depending on the direction of the unit normal vector to the cell face,

$$\bar{f}_{i+1/2,j,k} = \bar{\bar{R}}_{i+1/2,j,k} \cdot \bar{b}_{i+1/2,j,k} \quad (4.21)$$

where,

$$\bar{\bar{R}}_{i+1/2,j,k} = \bar{\bar{R}}(\bar{Q}_{i+1/2,j,k}^p), \quad \bar{Q}_{i+1/2,j,k}^p = \frac{1}{2} (\bar{Q}_{i,j,k}^p + \bar{Q}_{i+1,j,k}^p) \quad (4.22)$$

The formation of the vector \bar{b} shall be presented according to the modified ROE scheme, which uses the entropy fix of the numerical viscosity function that was defined in Equation (3.58). It has been demonstrated in Section 3.3.2 that the TVD and ULT scheme are merely an extension to the ROE scheme. For general 3-D flow, the discretized equations for the TVD and ULT scheme are identical to the ones presented in Section 3.3.2 except for the additional two indices in the subscript. According to the modified ROE scheme,

$$\bar{b}_{i+1/2,j,k} = \text{Viscos}(\bar{l}_{i+1/2,j,k}) \bar{a}_{i+1/2,j,k} \quad (4.23)$$

where,

$$\bar{a}_{i+1/2,j,k} = \bar{\bar{L}}_{i+1/2,j,k} \cdot \Delta \bar{Q}_{i+1/2,j,k}^p \quad (4.24)$$

$$\Delta \bar{Q}_{i+1/2,j,k}^p = \bar{Q}_{i+1,j,k}^p - \bar{Q}_{i,j,k}^p, \quad \bar{\bar{L}}_{i+1/2,j,k} = \bar{\bar{L}}(\bar{Q}_{i+1/2,j,k}^p)$$

and,

$$\bar{l}_{i+1/2,j,k} = \bar{\lambda}_{i+1/2,j,k} \tau_{i+1/2,j,k} \quad (4.25)$$

$$\tau_{i+1/2,j,k} = \frac{\Delta t \Delta A_{i+1/2,j,k}}{\frac{1}{2}(\Delta V_{i,j,k} + \Delta V_{i+1,j,k})}, \quad \bar{\lambda}_{i+1/2,j,k} = \bar{\lambda}(\bar{Q}_{i+1/2,j,k}^p) = \begin{bmatrix} v_n - a \\ v_n \\ v_n + a \\ v_n \\ v_n \end{bmatrix}_{i+1/2,j,k}$$

4.5.1 Boundary Conditions

The discretized Navier Stokes equations only describe the numerical relation between flow properties of adjacent volume elements. What drives the flow and sets one flow solution apart from another are the boundary conditions. By taking a second look at Figure 4-1, the depiction of local and global coordinate systems, we can identify three mathematical and two physical boundaries. The mathematical boundaries are the north pole, south pole, and date line, which have already been addressed in Section 4.3 as part of the coordinate transformation. No special flow properties are assigned at any of the mathematical boundaries. The two physical boundaries are the *surface* of the ellipsoid as well as the *far field* or *outer* boundary, the latter being represented by an imaginary sphere. In reality, the outer boundary is at infinity, but for all practical purposes we have to set it at a finite distance. The outer boundary should be far enough away from the ellipsoid such that its shape, which is arbitrary, does not influence the flow field solution. Thus we could have chosen a large rectangular box instead of a sphere, however, this would have unnecessarily complicated our meshing.

4.5.1.1 Surface Boundary

In Section 2.2, the surface boundary condition was expressed in two parts, a *no-slip* condition for the velocity components and a *no-flux* condition for the energy exchange. Although these are both necessary conditions for adiabatic viscous flow, they are not sufficient, neither from a physical nor from a computational viewpoint. Recall that we have a system of five integral equations solving for five unknowns, three velocity components and two thermodynamic state variables. The no-slip condition specifies the three velocity components, whereas the no-flux condition indirectly determines the temperature at the surface by requiring that its gradient is zero. So far, we have only four boundary conditions. To complete the set, we need one more, which specifies another thermodynamic state variable, either directly or indirectly.

We saw in Section 3.3.2 how the boundary conditions for shock tube flow were implemented through *ghost cells*, imaginary cells outside the physical domain, which reflected the flow conditions of the interior. The reflection boundary condition prescribed at the end walls of the shock tube was stated in Equation (3.54), which essentially maps the interior flow properties into the ghost cells and reverses the momentum by putting a minus sign in front of it. Note that reversing the momentum does not change the kinetic energy, and by setting the mass and energy equal on both sides of the wall boundary, Equation (3.54) indirectly implies that the temperature and density gradients are both zero at the wall. A zero temperature gradient is consistent with the adiabatic wall condition, but what about the density gradient? It turns out that in one-dimensional inviscid flow the pressure gradient vanishes at any wall, a result that can be derived directly from the momentum equation. As a consequence, the density gradient must also vanish, which can be seen by differentiating the equation of state for a perfect gas with respect to a direction normal to the wall,

$$\frac{\partial \rho}{\partial n} = \rho \left(\frac{1}{p} \frac{\partial p}{\partial n} - \frac{1}{T} \frac{\partial T}{\partial n} \right) \quad (4.26)$$

In multidimensional flow, things are not quite as simple! Although the temperature gradient can always be forced to zero through an adiabatic condition, the pressure gradient at the surface is a direct function of the centrifugal force felt by a fluid particle. A centrifugal force field is present whenever fluid particles travel along a curved path, which is almost always the case in multi-dimensional flow. In addition, a centrifugal force field can become particularly strong when the surface itself is rotating, which accelerates fluid particles radially outward. Such is the case in our flow simulation, and therefore the pressure, or density gradient cannot be neglected in the surface boundary formulation. On the contrary, an expression for the surface density gradient serves as a fifth boundary condition, which is needed to close the set.

Although an approximate analytical expression for the surface density gradient can be derived, whether or not the body is rotating, it is just as accurate to simply measure the density gradient above the surface and use this value when extrapolating into the ghost cell. By doing so, we are essentially setting the gradient of the gradient equal to zero, which is equivalent to saying that the second partial derivative of density with respect to the surface must vanish. Together with the adiabatic surface condition we can thus write,

$$\frac{\partial^2 \rho}{\partial n^2} = 0, \quad \frac{\partial T}{\partial n} = 0 \quad (4.27)$$

Strictly speaking, the numerical evaluation of any derivative should be based on the full set of metrics as stated in Equation (4.16). However, since the hexahedral cells near the surface are highly compressed along the radial direction, one can neglect the density and temperature variations along the polar and circumferential directions, even if the radial direction is not normal to the surface as depicted in Figure 4-3.

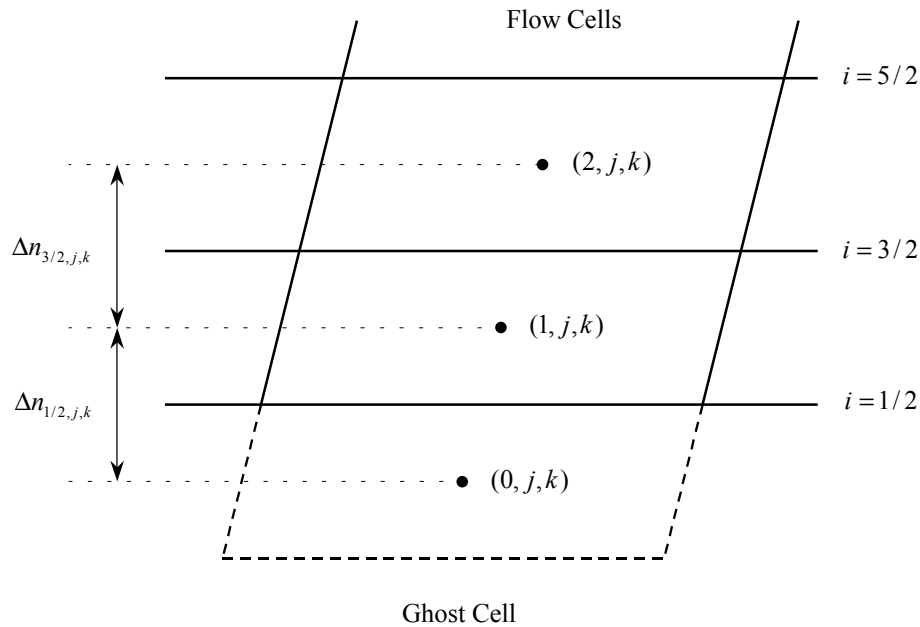


Figure 4-3: Surface Boundary

Therefore, the temperature gradient at the surface may be approximated as follows,

$$\frac{T_{1,j,k} - T_{0,j,k}}{\Delta n_{1/2,j,k}} = 0 \quad (4.28)$$

which yields,

$$T_{0,j,k} = T_{1,j,k} \quad (4.29)$$

The difference Δn is the separation distance between cell centers measured along the interface normal, which is equal to the reciprocal magnitude of the metrics vector defined in Equation (4.15),

$$\Delta n_{i+1/2,j,k} = \left(\nabla I_{i+1/2,j,k} \cdot \nabla I_{i+1/2,j,k} \right)^{-1/2} = \frac{\frac{1}{2} (\Delta V_{i+1,j,k} + \Delta V_{i,j,k})}{\Delta A_{i+1/2,j,k}} \quad (4.30)$$

The variation of the face normal is minimal between the surface and the cell face just above, $\hat{n}_{3/2,j,k} \approx \hat{n}_{1/2,j,k}$, since the lines $i = 3/2$ and $i = 1/2$ are virtually parallel. Therefore, the density gradient at the surface can be extrapolated as follows,

$$\frac{\rho_{1,j,k} - \rho_{0,j,k}}{\Delta n_{1/2,j,k}} = \frac{\rho_{2,j,k} - \rho_{1,j,k}}{\Delta n_{3/2,j,k}} \quad (4.31)$$

and rearranged,

$$\rho_{0,j,k} = \rho_{1,j,k} + \frac{\Delta n_{1/2,j,k}}{\Delta n_{3/2,j,k}} (\rho_{1,j,k} - \rho_{2,j,k}) \quad (4.32)$$

Strictly speaking, the second derivative of density with respect to the surface normal does not vanish exactly at the surface, but rather at the cell center just above the surface according to Equation (4.31). Since our initial intent was a mere gradient extrapolation, this should come as no surprise.

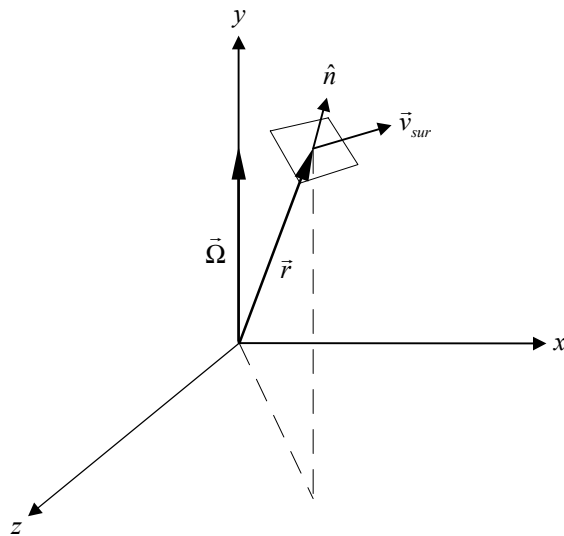


Figure 4-4: Surface Velocity

Equation (4.29) and (4.32) take care of the two thermodynamic state variables needed to fill the ghost cells. We still have to address the velocity vector at the surface to cover the remaining three surface boundary conditions. For a non-rotating surface, the no-slip condition simply dictates that the velocity at the surface vanishes, $\vec{v}_{sur} = \vec{0}$. For a rotating surface, however, there is a non-zero tangential velocity component, which depends on rotation rate $\vec{\Omega}$ and radius vector \vec{r} . For counter-clockwise rotation around the y -axis, as shown in Figure 4-4, the surface velocity is simply the cross product of rotation and radius vector,

$$\vec{v}_{sur} = \vec{\Omega} \times \vec{r} = \begin{pmatrix} 0 \\ \Omega \\ 0 \end{pmatrix} \times \begin{pmatrix} r_x \\ r_y \\ r_z \end{pmatrix} = \begin{pmatrix} \Omega r_z \\ 0 \\ -\Omega r_x \end{pmatrix} \quad (4.33)$$

The vector \vec{r} does not describe a radius in the true sense, unless we have a rotating sphere. Due to the lack of a better term, and because of the similarity between the spherical and the ellipsoidal coordinate system, the expression “radius vector” was yet adopted here. Although not immediately apparent, the tangency of the surface velocity is guaranteed, because the radius vector \vec{r} , the rotation vector $\vec{\Omega}$, and the local surface normal \hat{n} always lie in the same plane. Therefore,

$$\hat{n} \cdot \vec{v}_{sur} = \hat{n} \cdot (\vec{r} \times \vec{\Omega}) = (\hat{n} \times \vec{r}) \cdot \vec{\Omega} = 0 \quad (4.34)$$

Numerically, the no-slip condition is implemented such that the arithmetic average of the ghost cell velocity below the surface and the adjacent flow cell velocity above is equal to the surface velocity prescribed by Equation (4.33). Solving for the ghost cell velocity,

$$\vec{v}_{0,j,k} = 2\vec{v}_{sur} - \vec{v}_{1,j,k} \quad (4.35)$$

The arithmetic average embedded in Equation (4.35) only yields the exact rotational velocity at the surface, if each ghost cell has the same volume as its adjacent flow cell. Therefore,

$$\Delta V_{0,j,k} = \Delta V_{1,j,k} \quad (4.36)$$

is an auxiliary requirement to the no-slip condition prescribed by Equation (4.35). Combined with Equations (4.29) and (4.32), we now have five boundary conditions—for five unknowns—and the physical set is complete. Computationally, however, we are not quite done! Recall that the flux vector \vec{F} requires values for the heat flux vector and viscous stress tensor at cell centers, which are centrally differenced with respect to all six faces. A ghost cell, however, has only one neighbor, which means the central difference formula of Equation (4.16) clearly would not apply. The heat flux vector can be mirrored with respect to the surface, because its arithmetic average vanishes by the volume condition of Equation (4.36),

$$\vec{q}_{0,j,k} = -\vec{q}_{1,j,k} \quad (4.37)$$

Simply mapping the components of the viscous stress tensor from flow cell to ghost cell would be incorrect, since the state of viscous stress near the surface is a strong function of normal distance. Therefore, it was decided to extrapolate the viscous stress tensor components based on their gradients just above the surface. Similar to Equation (4.32), the following formula was employed,

$$\vec{\tau}_{0,j,k} = \vec{\tau}_{1,j,k} + \frac{\Delta n_{1/2,j,k}}{\Delta n_{3/2,j,k}} (\vec{\tau}_{1,j,k} - \vec{\tau}_{2,j,k}) \quad (4.38)$$

Again, it should be emphasized that Equations (4.37) and (4.38) are computational requirements rather than physical boundary conditions. The viscous stress and heat flux at the surface are already determined through Equations (4.29) and (4.35), and adding two more equations is somewhat an over-specification to the physical problem. Nonetheless, Equations (4.37) and (4.38) are essential to the solution algorithm, and it seemed appropriate to present them within the context of boundary conditions.

It is remarkable that many textbooks on CFD do not discuss the possibility of a pressure or density gradient near the surface, except for some of the most recent sources [3, 11]. The classical texts only mention the reflection boundary condition for inviscid flow, but simply omit a proper boundary treatment when presenting the FNS equations [1]. Therefore it seems, as if the standard practice in CFD is to use the reflection boundary condition whenever an adiabatic surface is present, which indirectly enforces a zero gradient for both density and pressure. It has been the author's experience that neglecting the surface density gradient when solving inviscid flow only has a minimal effect, whereas for a viscous flow solution, the point of boundary layer separation can be delayed by as much as 20% chord when using the above extrapolation scheme. Apparently, a compressible viscous boundary layer is very susceptible to even the slightest density gradients near the surface, and therefore such gradients should not be neglected.

4.5.1.2 Outer Boundary

Since the flow at the outer boundary is assumed to be undisturbed, we must accordingly enforce the conditions of free stream flow there, which are specified by two thermodynamic state variables, typically pressure and temperature, as well as a wind direction and wind speed. Denoting free stream values with the infinity symbol, we can construct the following flow vector of conserved properties,

$$\bar{Q}_\infty = \begin{bmatrix} \rho_\infty \\ \rho_\infty \bar{v}_\infty \\ \rho_\infty (c_v T_\infty + \frac{1}{2} \bar{v}_\infty \cdot \bar{v}_\infty) \end{bmatrix} \quad (4.39)$$

where,

$$\rho_\infty = \frac{P_\infty}{RT_\infty}, \quad \bar{v}_\infty = M a_\infty \begin{pmatrix} \cos \alpha \\ \sin \alpha \\ 0 \end{pmatrix}, \quad a_\infty = \sqrt{\gamma RT_\infty}$$

Thus \bar{Q}_∞ is completely specified by free stream pressure and temperature, p_∞ and T_∞ , as well as flow Mach number and angle of attack, M and α . Although a general wind direction can include a cross wind component, specified by a possible cross wind angle β , such a generalization is not necessary, because the flow over any body of revolution can always be reduced to a single angle with respect to its axis. The same is true when the body is rotating around its axis, which can be visualized by shifting the wind vector in space until both the axis of rotation and the wind vector fall within the same plane.

Another condition that must be met at the outer boundary is the vanishing of any gradients, which is generally guaranteed as long as the outer boundary is at a far enough distance. Although pressure and density gradients are supposed to fade away naturally, the vanishing of temperature and velocity gradients can be enforced by setting the components of viscous stress tensor and heat flux vector equal to zero,

$$\bar{q}_\infty = \bar{0}, \quad \bar{\tau}_\infty = \bar{0} \quad (4.40)$$

The numerical implementation of Equations (4.39) and (4.40) is straightforward. Similar to the surface boundary, ghost cells are attached just outside the physical domain and are set to free stream conditions,

$$\bar{Q}_{I_{\max}+1,j,k} = \bar{Q}_{\infty}, \quad \bar{q}_{I_{\max}+1,j,k} = \bar{0}, \quad \bar{\tau}_{I_{\max}+1,j,k} = \bar{0} \quad (4.41)$$

Each ghost cell is assigned the same volume as its adjacent flow cell, mainly to ensure that fluxes leaving and entering the outer boundary are properly computed, since gradients are supposed to vanish anyway,

$$\Delta V_{I_{\max}+1,j,k} = \Delta V_{I_{\max},j,k} \quad (4.42)$$

It can be argued that the downstream portion of the outer boundary is too close to the disc, being only four disc diameters away from its center, and enforcing Equations (4.39) and (4.40) limits the proper development of a wake. After all, a wake generally extends over hundreds of (disc) diameters before it completely dissipates. However, since the flow over the disc is computed in the compressible range ($M = 0.5$), much more information is propagated downstream than upstream, and thus the influence of the downstream boundary on the upstream flow field is weak. Nonetheless, a loss in accuracy does occur by cutting the wake short, which shall be tolerated here.

4.5.2 Initial Condition

The initial flow condition is somewhat arbitrary, since a steady state or asymptotic solution of a subsonic flow field depends solely on boundary conditions. For faster convergence, one may want to use an approximate solution as a starting point, if such a solution exists. For example, the flow over the spinning disc was computed from the converged solution of the non-spinning case. However, time savings are not always guaranteed when starting with an existing solution. Such is the case for separated flow that wants to reattach after a change in parameters has been made. The author's experience has been that the simulation time required for a boundary layer reattachment and subsequent convergence is roughly the same as it is for starting the flow impulsively from rest. An impulsive start is numerically equivalent to initializing all flow cells with the free stream flow vector of conserved properties, which was defined in Equation (4.39),

$$\bar{Q}_{i,j,k}^0 = \bar{Q}_{\infty} \quad (4.43)$$

When accelerating an aerodynamic body impulsively, the initial velocity gradients normal to the surface are infinitely steep. The boundary layer grows over time as the surrounding flow field develops, which all happens within fractions of a second for any subsonic flow in air. Although this may seem a small time frame for an observer, it is fairly long compared to the time it takes for acoustic waves to set up within the flow. The development of a boundary layer is a viscous process governed by the time scale of molecular diffusion, which is generally very large compared to the time it takes for sound waves to travel the same distance. For example, imagine one is working in a lab that contains a small balloon filled with a highly poisonous gas. Accidentally, the balloon pops, a sound that can be heard “immediately” throughout the lab. The time it takes for the gas to diffuse and reach lethal levels is yet long enough for anyone to get out of the lab—unless the diffusion process is aided by ceiling fans.

As a general rule, one could say that the development, or adjustment, of a boundary layer always takes its time, regardless of the initial condition present. Therefore, one might as well start “fresh” with every new computation and initialize the flow field according to free stream conditions.

4.5.3 Boundary Layer Resolution

The boundary layer is the thin layer of fluid flow surrounding an aerodynamic body in which viscous forces are significant. It is characterized by strong velocity gradients, as fluid particles accelerate from a zero velocity on the surface to the velocity of the nearby flow. A boundary layer originates at the forward stagnation point and grows in thickness up to the point of separation, where the local direction of flow reverses itself. For a slender body at small angles of attack, the boundary layer thickness δ is a function of flow Reynolds number and downstream location along the surface. Experimental and numerical data suggest [17] that the boundary layer thickness along a slender aerodynamic shape grows about an order of magnitude between the leading and trailing edges. For a non-rotating disc of diameter D , the following “rule of thumb” applies,

$$\text{(near leading edge)} \quad 0.5 Re^{-1/2} < \frac{\delta}{D} < 5 Re^{-1/2} \quad \text{(near trailing edge)} \quad (4.44)$$

Thus for a Reynolds number of 30,000 based on diameter, the non-dimensional boundary layer thickness near the leading edge is approximately 3/1000, which is quite small. The spatial discretization was carried out such that the average cell spacing normal to the surface is roughly one-third of that scale,

$$\frac{\text{ave}(\Delta n_{1/2,j,k})}{D} \approx \frac{1}{1000} \quad (4.45)$$

In other words, the boundary layer near the leading edge is captured within three cells only, and is therefore considered minimally resolved. A higher resolution would require further subdivision of the cells near the surface, which would directly affect the integration time step and ultimately increase the overall computation time.

4.5.4 Integration Time Step

An important aspect of the discretization, which has not been addressed yet, is how to choose a proper integration time step Δt . A time step too large will result in failure of the computation as the numbers become unstable and eventually “blow up”, whereas an integration time step well below the stable limit will result in extra iterations, an unnecessary computational expense. For an explicit time marching scheme, such as the one presented in Equation (4.20), the limit for numerical stability is dictated by the well-known CFL condition, after a 1928 paper published by Courant, Friedrichs and Lewy [4],

$$\Delta t < \frac{\Delta n}{v_n + a} \quad \text{(local)} \quad (4.46)$$

The CFL condition is based on the physical principle that flow disturbances can travel no faster than the local speed of sound and flow speed combined, and thus information should advance by no more than one cell spacing in a single time step. Since all these parameters vary throughout the discretized flow field, the global stability of the computation is limited by the smallest time step based on local conditions. One can devise a conservative estimate for a global integration time step as follows: From the spatial discretization, we know that the cell spacing right at the surface is closest, in order to capture the boundary layer. Since temperature variations are small in subsonic flow—for $M = 0.5$ the stagnation temperature is only 5% above the free stream static temperature—the speed of sound is nearly constant throughout the flow. From experience, one could say that the local flow speed is generally no greater than twice the wind speed. Therefore, a conservative global integration time step, expressed in terms of flow Mach number, the free stream speed of sound, and the smallest cell spacing found anywhere along the surface, would be,

$$\Delta t = \frac{\min(\Delta n_{1/2,j,k})}{a_\infty (2M + 1)} \quad (\text{global}) \quad (4.47)$$

For a compressible viscous flow of moderate Reynolds number, the integration time step has to be very small to assure stability. Generally, thousands of iteration time steps are needed before an impulsively accelerated flow converges to its steady or asymptotic state. It should be mentioned that the computation of aerodynamic flow at low Reynolds numbers ($Re < 100$) is even more restricted. High altitude flight falls into this regime. When the ambient air density is very low, molecular diffusion and acoustic waves propagate signals at comparable speeds, since intermolecular collision is rare.

4.6 Aerodynamic Coefficients

Once the flow field is computed, the prime quantities of interest are the aerodynamic forces and moments acting on the disc, which are obtained by integrating the stress tensor over the entire surface,

$$\begin{aligned} \text{(Net Force)} \quad \vec{F} &= \sum_{j=1}^{J_{\max}} \sum_{k=1}^{K_{\max}} \vec{f}_{1/2,j,k} \Delta A_{1/2,j,k} \\ \text{(Net Moment)} \quad \vec{M} &= \sum_{j=1}^{J_{\max}} \sum_{k=1}^{K_{\max}} \vec{r}_{1/2,j,k} \times \vec{f}_{1/2,j,k} \Delta A_{1/2,j,k} \end{aligned} \quad (4.48)$$

where,

$$\vec{f}_{1/2,j,k} = \vec{\sigma}_{1/2,j,k} \cdot \hat{n}_{1/2,j,k}$$

Both \vec{F} and \vec{M} are calculated with respect to the Cartesian reference frame (x, y, z) , which we shall refer to as the *body axes*, since they are attached to the center of the disc. Generally, the components of the force vector are expressed with respect to a rotated reference frame (I, J, K) , which we shall call the *wind axes*.

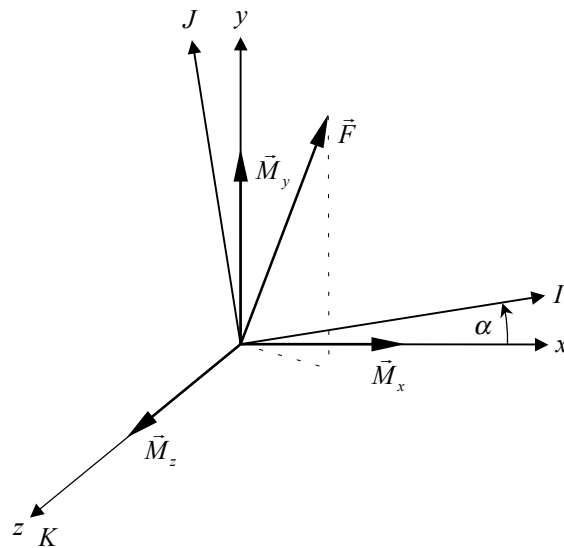


Figure 4-5: Net Force and Moments

The wind axes are rotated as shown in Figure 4-5 such that one axis is aligned with the wind direction. The force components with respect to the rotated reference frame are obtained through the following transformation of coordinates,

$$\begin{pmatrix} F_I \\ F_J \\ F_K \end{pmatrix} = \begin{bmatrix} I_x & I_y & I_z \\ J_x & J_y & J_z \\ K_x & K_y & K_z \end{bmatrix} \begin{pmatrix} F_x \\ F_y \\ F_z \end{pmatrix} \quad (4.49)$$

where,

$$\begin{pmatrix} I_x \\ I_y \\ I_z \end{pmatrix} = \begin{pmatrix} \cos \alpha \\ \sin \alpha \\ 0 \end{pmatrix}, \quad \begin{pmatrix} J_x \\ J_y \\ J_z \end{pmatrix} = \begin{pmatrix} -\sin \alpha \\ \cos \alpha \\ 0 \end{pmatrix}, \quad \begin{pmatrix} K_x \\ K_y \\ K_z \end{pmatrix} = \begin{pmatrix} 0 \\ 0 \\ 1 \end{pmatrix}$$

One can think of Equation (4.49) as a special case of the more general coordinate transformation described in Section 4.3. A general transformation changes both direction and length scale, whereas a rotation only changes direction but preserves length scale. In Equation (4.49), the gradient vectors ∇I , ∇J , and ∇K all have unit length and are mutually orthogonal, and therefore they can be viewed as face vectors to a unit cube, centered at the origin, that was rotated through an angle α around the z -axis.

Although the components of the net moment vector \vec{M} could also be transformed according to Equation (4.49), it was decided to leave them in body coordinates for better visualization. The following nomenclature for aerodynamic forces and moments shall be adopted here:

$$\begin{pmatrix} F_x \\ F_y \\ F_z \end{pmatrix} = \begin{pmatrix} Aft \\ Up \\ Left \end{pmatrix}, \quad \begin{pmatrix} F_I \\ F_J \\ F_K \end{pmatrix} = \begin{pmatrix} Drag \\ Lift \\ Left \end{pmatrix}, \quad \begin{pmatrix} M_x \\ M_y \\ M_z \end{pmatrix} = \begin{pmatrix} Roll \\ Yaw \\ Pitch \end{pmatrix} \quad (4.50)$$

Notice that the *left* force—which steers the disc to the left, thus the name—is the same with respect to wind and body axes, $F_K = F_z$, because the K -axis and z -axis coincide. By definition, the drag is always measured along the wind direction and the lift being normal to it, which is why the wind axes were introduced.

It is common practice in engineering to present data in non-dimensional form. Aerodynamic forces and moments are turned into coefficients by dividing them by reference quantities that can easily be measured. The product of free stream dynamic pressure,

$$q_\infty = \frac{1}{2} \rho_\infty (\vec{v}_\infty \cdot \vec{v}_\infty) = \frac{1}{2} \gamma p_\infty M^2 \quad (4.51)$$

and planform area,

$$A_{ref} = \frac{\pi}{4} D^2 \quad (4.52)$$

yields a reference force. A reference moment is obtained by multiplying this force by the disc diameter D . For example, the lift and pitching moment coefficients for a disc are defined as follows,

$$C_{Lift} = \frac{F_J}{q_\infty A_{ref}}, \quad C_{Pitch} = \frac{M_z}{q_\infty A_{ref} D} \quad (4.53)$$

Also of interest are the coefficients of local surface pressure,

$$c_p = \frac{p_{1/2,j,k} - p_\infty}{q_\infty} \quad (4.54)$$

and local traction vector, including its magnitude,

$$\vec{c}_t = \frac{\sqrt{Re}}{q_\infty} \vec{t}_{1/2,j,k}, \quad c_t = (\vec{c}_t \cdot \vec{c}_t)^{1/2} \quad (4.55)$$

where,

$$\vec{t}_{1/2,j,k} = \vec{\tau}_{1/2,j,k} \cdot \hat{n}_{1/2,j,k}$$

The viscous stress is generally orders of magnitude smaller than the pressure, which is why the square root of the Reynolds number is used as a scaling factor. The local traction is similar to the more commonly used skin friction coefficient when presenting viscous forces along a surface. Skin friction is based on shear stress, which is usually measured tangential to a surface. Viscous stress, on the other hand, does not always act tangentially unless the flow is nearly steady, or incompressible. For example, when the disc was impulsively accelerated, the local traction vector pointed normal to the surface in the neighborhood of stagnating fluid. This effect can be attributed to compressibility, and as the flow field reached equilibrium the component of viscous stress normal to any surface was absorbed by local pressure. For that matter, it was decided to also monitor the coefficient of normal traction, as an indication of local equilibrium,

$$c_{t-n} = \vec{c}_t \cdot \hat{n}_{1/2,j,k} \quad (4.56)$$

5. RESULTS

The full Navier Stokes (FNS) flow solver was first developed for 2-D flow and tested on a number of cases such as the flow over a cylinder and the flow over an elliptical airfoil at zero and non-zero angle of attack. At a Mach number of 0.5 and Reynolds number of 30,000, a 3-D flow computation over a sphere or ellipsoidal disc took nearly two weeks on a 1GHz Pentium PC, whereas a similar 2-D flow computation generally converged in less than six hours, a more reasonable time frame. The primary purpose of developing a 2-D flow solver was to evaluate the different inviscid algorithms, ROE, TVD, and ULT, which form the core of the FNS code.

When computing subsonic viscous flow on a curvilinear mesh, the artificial compression of the ULT algorithm turned out an undesirable feature, which only enhanced the reflection of transient waves at the far field boundary and as a result slowed down convergence. Undoubtedly, the ULT algorithm would be highly suitable for supersonic flow computations, where far field wave reflection is not an issue. For fully subsonic flow, employing the ULT algorithm within a FNS flow solver was therefore ruled out.

The TVD algorithm, although second-order accurate, did not always yield physically valid results when computing without entropy enforcement ($\epsilon = 0$). For example, using the TVD scheme to solve the 2-D viscous flow over a cylinder produced a large recirculation region in the wake, the size of several diameters, with a reversed flow speed that was nearly equal to the wind speed. Upon adding a small amount of numerical viscosity ($\epsilon = 0.005$) to the entropy function, the flow field corrected itself to a physically reasonable solution, but at the same time the wake lost most of its structure, and the entire flow field appeared “washed out”.

In comparison, the original ROE scheme without the entropy fix ($\epsilon = 0$) seemed the best algorithm for solving subsonic flow. Although viscous solutions based on the ROE scheme are only first-order accurate, for the cases being tested, they were always physically valid and at the same time appeared reasonably resolved. The 2-D flow over a cylinder ($M = 0.5$; $Re = 10,000$) was computed based on Roe’s scheme and appears in very good agreement with experimental data obtained by Anatol Roshko [16]. Roshko used a splitter plate in the wake of his cylinder, which is the only way to obtain a steady symmetric flow field in the laminar regime with two stable vortices. Unlike a numerical wind tunnel, a physical wind tunnel is never 100% turbulence free, which creates vortex instability and causes the periodic vortex shedding in the wake of a cylinder that is generally observed in experiments.

Since the ROE scheme is an upwind scheme, transient wave reflection at the far field boundary was a minor issue, which enhanced the convergence of the computation. In addition, the ROE scheme is also the computationally least expensive of the three algorithms, which yielded an additional time saving. For all the above reasons, it was therefore decided to exclusively use the ROE scheme—as part of the FNS solver—for computing the 3-D viscous flow over the ellipsoidal disc.

In all computations, the size of the disc as well as the ambient conditions and wind speed were chosen such that the resulting flow Mach number and flow Reynolds number would match $M = 0.5$ and $Re = 30,000$. The angle of attack was held fixed at 5 degrees, while the spin ratio was varied between 0, 0.5, 1, and 1.5. In the subsequent discussion, the following terms shall be used to distinguish between different solutions based on varying spin ratio: *non-rotational* ($SR = 0$), *sub-rotational* ($SR = 0.5$), *equi-rotational* ($SR = 1$), and *super-rotational* ($SR = 1.5$). Aerodynamic data such as force and moment coefficients were compiled for all four cases, which are tabulated in Section 5.4. Due to space limitations, however, only the non-rotational and equi-rotational case is presented in form of contour-, vector-, and surface plots. The majority of these plots are full-page color graphs, and in view of their large number—about thirty for each case—they are listed in separate Appendices, A and B. Reference will be made by page numbers.

5.1 Flow Field

The flow field is plotted in terms of Mach number, pressure, and density for the three mutually perpendicular coordinate planes: *side view* (x - y plane), *front view* (y - z plane), and *top view* (x - z plane). Collectively, we shall refer to them as *contour plots*, because their coloring indirectly reveals the contours, i.e. lines, of constant Mach number, pressure, and density within each plane of view. Pressure and density were non-dimensionalized by their free-stream values. Other thermodynamic properties, such as temperature and entropy were also available from the plot menu, however, these graphs were not as colorful at ordinary magnification ($Zoom = 3$), because their range of values was mainly confined to the thin boundary layer. Therefore, these plots were not included. In order to show the computational mesh in each plot, the flow cells were not filled with solid color, but were simply crossed out.

We shall first discuss the non-rotational case. The contour plots of Mach number, pressure, and density all show symmetry with respect to the x - y plane, which is expected due to symmetric boundary conditions. Asymmetry, introduced by the non-zero angle of attack, can only be seen within the side views (85-93).

Recall that in subsonic flow temperature variations are small, and thus the speed of sound is nearly uniform throughout the flow field. Accordingly, the Mach number plots directly display the speed of the local flow. In all three views one can identify the thin boundary layer surrounding the disc, in which fluid particles decelerate to zero as they approach the surface. Outside the boundary layer the flow behaves as if it were inviscid. Just below the forward rim, the flow comes to a complete rest as it impinges normal to the surface, which is known as the *forward stagnation point*. As the flow moves over and around the disc, it accelerates due to the fact that it is displaced. Once the flow reaches the rearward rim, it again decelerates and comes to rest at the *rearward stagnation point*. There is considerably more stagnant fluid at the rear compared to the front because of the wake of the disc, which is a result of *boundary layer separation*, a phenomenon that will be explained in the next section.

As the flow decelerates, the local static pressure increases; and as it accelerates, static pressure drops again, an observation that can be made when comparing Mach number and pressure plots. Due to the non-zero angle of attack, the flow over the top is slightly faster than over the bottom, and as a result we have a small pressure differential which creates *aerodynamic lift*. Near the rearward stagnation point, the flow decelerates again, however, the pressure rise is not as dramatic compared to the forward stagnation point. This lack of pressure recovery can directly be attributed to the frictional losses within the boundary layer. The gradual drop in stagnation pressure as well as the frictional forces along the surface is what creates *aerodynamic drag*.

Density behaves similar to pressure. The density rises as the flow reaches the forward stagnation point, where the air is being compressed. As the air accelerates over the top and bottom, it expands, and the local density decreases. An additional expansion of air can be seen close to the surface, which is due to frictional heating within the boundary layer. The lowest density can be found right around the rearward rim, where frictional losses are greatest. As can be seen in the graphs, the rearward stagnation point does not see any density rise, unlike the pressure recovery, and the lower than ambient density extends far into the wake.

Having discussed the non-rotational case, we shall now review the contour plots of the equi-rotational case for comparison (115-123). The most obvious change can be seen in the top view of the Mach number plot. The stagnant fluid around the rearward rim has separated from the surface and is now dragging behind the disc similar to the tail of a comet. Due to the disc's rotation, the rearward stagnation "bubble" can no longer be found on the surface, and when comparing all three Mach number views, one can visualize an entire sheet of zero-velocity fluid that is loosely wrapped around the right rear quarter of the disc. The velocity vector plots for the boundary layer, discussed in the next section, will shed further light on this phenomenon.

The pressure contour plots only display a minimal change compared to the non-rotational case. The side views for both flow scenarios are almost identical except for an enhanced pressure recovery at the rearward rim for the rotating disc. The top view shows a slight opposite rotation of the pressure field at the right and rear rim, with an improved pressure recovery. Both side view and top view indicate a bubble of elevated pressure in the immediate wake that has detached itself from the rear surface. The pressure distribution along the front rim appears to be unaffected by the rotation. The front view for the rotational case reveals a weak shift in the pressure pattern towards the left (with respect to the body axes). It is this minor shift in the pressure field which gives the disc a small left steering force. A shift in pressure due to rotation is known as the *Magnus effect* [14].

When comparing the density contour plots, the first thing one will notice is a shift in the color spectrum, which is due to a minor change in density range. Although the upper density limit is virtually unaffected, the lower limit for the equi-rotational case has jumped up almost 5% compared to the density field of the non-spinning disc. This change can be attributed to the increased frictional heating that takes place in the boundary layer over the advancing surface of the disc. The top view and side view clearly demonstrate this effect. The side view of the rotational density field lacks the density drop around the rearward rim, which can be explained by the suppressed boundary layer separation, as we shall find out later.

5.2 Boundary Layer

The boundary layer has been completely mapped throughout the three orthogonal coordinate planes in form of *vector plots* (94). Strictly speaking, we are only looking at the 2-D components of the local velocity vector within each plane. Since the direction of the vectors can generally be identified from the context, arrow-heads were omitted to avoid clutter. The color of the 2-D vectors specifies the local flow Mach number and directly indicates the magnitude of the respective 3-D velocity vector. A common magnification factor was used in all plots ($Zoom = 25$) such that a direct comparison can be made between different views. The coordinates given at the lower right-hand corner of each graph (*X-view* & *Y-view*) are with respect to the page and do not reflect the body axes. Setting both page coordinates to zero always centers the view. Navigating within each plane based on page coordinates turned out more intuitive than using body axes, which do not always point to the right and up depending on the view selected. All page coordinates are scaled with respect to the disc's diameter.

Again, we shall address the non-rotational case first. The side view vector plots (94-97) clearly show the boundary layer growth along the top and bottom surface, starting at the forward stagnation point just below the rim. As the boundary layer grows in thickness, it loses momentum, and due to the adverse pressure gradient, which sets in about midsection, the flow near the surface eventually stops and reverses itself, which is referred to as *boundary layer*-, or *flow separation*. On the upper surface, this occurs at about 70% of the centerline chord. (*Chord* is the streamwise length of an aerodynamic surface and is measured from the leading edge; for a disc, the centerline chord length is equal to its diameter). Along the lower surface, the adverse pressure gradient is less severe, and the flow along the centerline does not separate until about 90% chord. Past the point of separation, the local flow near the surface recirculates, which can be observed in the rearward section of the side view plot. The separated boundary layers from the top and bottom surface form the wake of the disc.

The top view vector plots (98-103) cover the boundary layer profile from forward to rearward stagnation point for the left half of the disc. Since the flow field is symmetric with respect to the x - y plane, the right half was omitted. Along the front rim, the boundary layer grows slowly because the pressure gradient is favorable. Once the flow passes the lateral axis, the pressure gradient becomes adverse, and the boundary layer grows quickly. Separation at the rim starts at about 50 degrees measured from the rear centerline.

Recirculation within the top view plane is minimal near the rim, yet clearly visible in the wake portion. The flow around the rearward rim is highly three-dimensional and difficult to capture in any projected view. The front view (104-105) confirms this notion and demonstrates that there is an upward flow component that curls around the rim of the disc due to the non-zero angle of attack. Towards the vertical axis, the front view shows a diminishing lateral flow. The red dots represent flow vectors of large magnitude that point into the plane of view, along the downstream direction.

Keeping the above boundary layer discussion in mind, we shall now examine the vector plots for the equi-rotational case, first inspecting the side view plane (124-127). At a first glance, the boundary layer profile around the forward rim looks identical in shape compared to the non-rotational case, with one minor difference: the colors near the surface do not show the familiar red-blue shift. Although the 2-D vectors diminish in length the closer they get to the surface, their color indicates that the actual 3-D velocity vector increases in magnitude. This seems contradictory, yet it does make perfect sense. Very close to the surface, fluid particles move according to the disc's rotation, and the further one moves towards the front rim, the larger becomes the vector component that points out of the side view plane. The same is true for the velocity near the rearward rim, as seen in the same color reversal, although the third velocity component now points into the page. Near the axis of rotation, the angular velocity component is small and the boundary layer profiles look virtually identical, in shape and color, when comparing the side views of both cases. The most striking difference of the equi-rotational case is the absence of flow reversal along the upper rear surface. Apparently, the centrifugal force imparted on the fluid near the surface has delayed boundary layer separation all the way to the rearward rim judging from the graph, or may have even eliminated separation entirely depending on the magnitude of the circumferential traction component.

To further demonstrate the centrifugal force effect, we shall now turn to the front view vector plots (140-143). Outside the boundary layer, there is an upward flow around each rim similar to the non-rotating case. Along the upper surface though, one will notice a radially outward flow induced by rotation, which opposes the inward flow further above. This effect is slightly more enhanced on the receding side, and judging from the biased boundary layer profile near the axis of rotation, one could say that there is a net flow from the advancing to the receding rim. The radial boundary layer profiles of upper and lower surface meet somewhere close to the rim, which may result in flow separation if the streamwise surface traction is weak. Such is definitely the case along the receding side, and as we shall find out in the next section, a line of separation can be located near the left rim.

The top view vector plots are by far the most interesting, and because of the completely asymmetric flow field of the equi-rotational case, the boundary layer was mapped along the entire circumference (128-139). Starting at the forward rim, one will immediately notice the very steep velocity gradient, as the flow wants to impinge normal to the surface but is redirected tangentially. Traveling around the rim counterclockwise, i.e. with the rotation, this gradient slowly diminishes as the local surface tangential aligns itself with the wind. After a quarter turn, the boundary layer has completely disappeared, since the relative wind seen by the left rim is zero. Along the leeward side of the receding rim the velocity gradient redevelops, yet the boundary layer profile is much wider compared to the windward side, which is to be expected. Although the flow field is highly three-dimensional within the wake, one can clearly identify the large circulation region behind the disc, as the rim rotates through the centerline. This circulation field tightens as the leeward side advances into the wind, and at the right rim the reversal of boundary layer flow follows a nearly parabolic profile. The advancing rim sees exactly twice the wind speed at the three-quarter turn, which explains the strong frictional effects felt in this region. As the rim completes the 360-degree turn, the boundary layer profile quickly steepens to the point where it essentially becomes under-resolved. The velocity vector just above the surface already shows a significant normal component, a somewhat undesirable feature, which gives the graph a "pick-a-stick" appearance. Frictional forces reach a maximum at a circumferential angle of about 315 degrees, which is revealed by a surface traction plot presented in the next section (Figure 5-3).

5.3 Surface Forces

There are two kinds of surface forces. One is due to the thermodynamic pressure and always acts normal to the local surface. The other force is due to the viscous stress tensor and generally acts tangential to the surface, unless the flow goes through unsteady compression. The complete surface force field has been plotted in a three-dimensional view of the disc, using both color and *tufts*. The color specifies the local pressure, whereas the tufts indicate the direction of the local traction. Although the traction magnitude was originally communicated through the length of the tufts, it turned out more practical to make them all the same length for better visualization. Regions of boundary layer separation were difficult to determine, because the scaled tufts often reduced to a mere dot on the surface due to the large overall range in traction magnitude. Similar to tufts placed on an actual wind tunnel model, they also indicate the direction of the relative wind just above the surface.

Again, we shall start with the 3-D surface plots of the non-spinning disc, for which six rotated views are provided (106-111). The orientation of the disc is indicated by a set of translated body axes at the lower left corner of each graph. The colors red, green, and blue correspond to the x -, y -, and z -axis, respectively. In almost every view, the orientation of the disc can be identified by the red colored rim, which marks the forward stagnation point. It turns out that most of the disc is painted in three colors, which implies that the only major pressure changes occur along the forward rim, where the flow stagnates. The tufts show exactly how the air parts at the front rim and evenly flows over the forward half of the disc with a slight upward curl around the side rims. Once past the lateral plane, the air seems to slightly steer away from the disc's centerline resulting in a fork of two separation lines at about 70% center chord. The two lines of boundary layer separation veer symmetrically outward over the remainder of the upper surface, somewhat resembling an unzipped neck collar. A similar separation pattern can be found on the lower surface, although the lines of separation are much closer to the aft rim, and the area of reversed flow is significantly smaller compared to the top surface.

The 3-D surface plots for the equi-rotational case (144-151) reveal a much different picture, which should not be too surprising after having studied the earlier vector plots in great detail. The disc's rotation has dramatically altered the surface traction, and the tufts along the upper and lower rear surface verify previous indications that the flow remains attached over the entire aft portion of the disc, even along the rearward rim! Apparently, the centrifugal force felt within the boundary layer has prevented the flow from separating, and along the aft rim, the circumferential traction component kept the boundary layer attached despite the adverse pressure gradient. The only line of separating flow that can be found on the entire disc is wrapped around the left receding rim. Indicated by the presence of crossing tufts, the line of separation extends from about 70 degrees above the rim to about 120 degrees below, the angle being measured circumferentially with respect to the "dateline". The forward impingement point, which was originally located just below the centerline, has moved about 55 degrees counterclockwise, i.e. with the rotation, and can be identified by the outward pointing tufts just below the rim. Although the tufts show the direction of the local surface traction, they do not reveal their relative magnitude. For that matter, the traction magnitude has been plotted for selected circumferential cross sections, which are presented in Figures 5-2 and 5-3. Also included is a 2-D traction plot along the centerline of the non-spinning disc for comparison.

Despite the drastic alteration in traction, the change in surface pressure due to rotation is less severe. The windward pressure region has remained in place, despite the movement of the impingement point itself. Next to the Magnus effect, the only major difference between the two cases can be seen along the upper surface, where the region of lowest pressure has spread just past the lateral plane, by about 10% chord near the centerline. Overall, the disc's rotation had a minor effect on the surface pressure distribution, which is mainly governed by the inviscid flow field. To better illustrate the subtle changes in surface pressure induced by rotation, the pressure coefficient along the longitudinal cross section has been plotted for both cases and is compared in Figure 5-1.

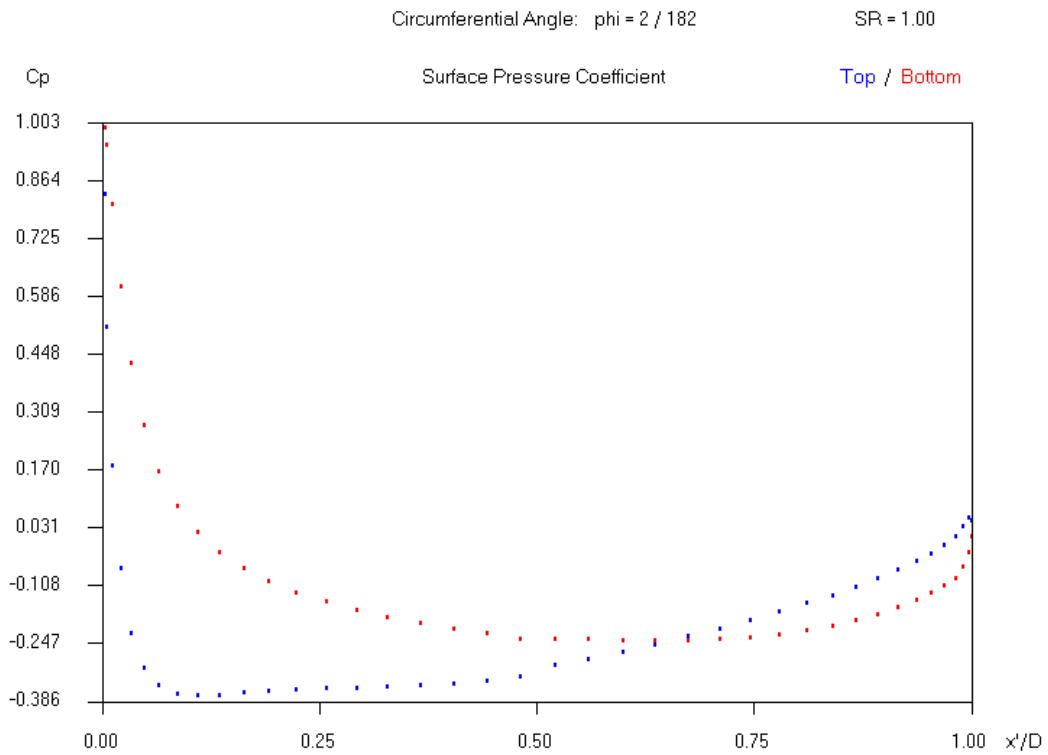
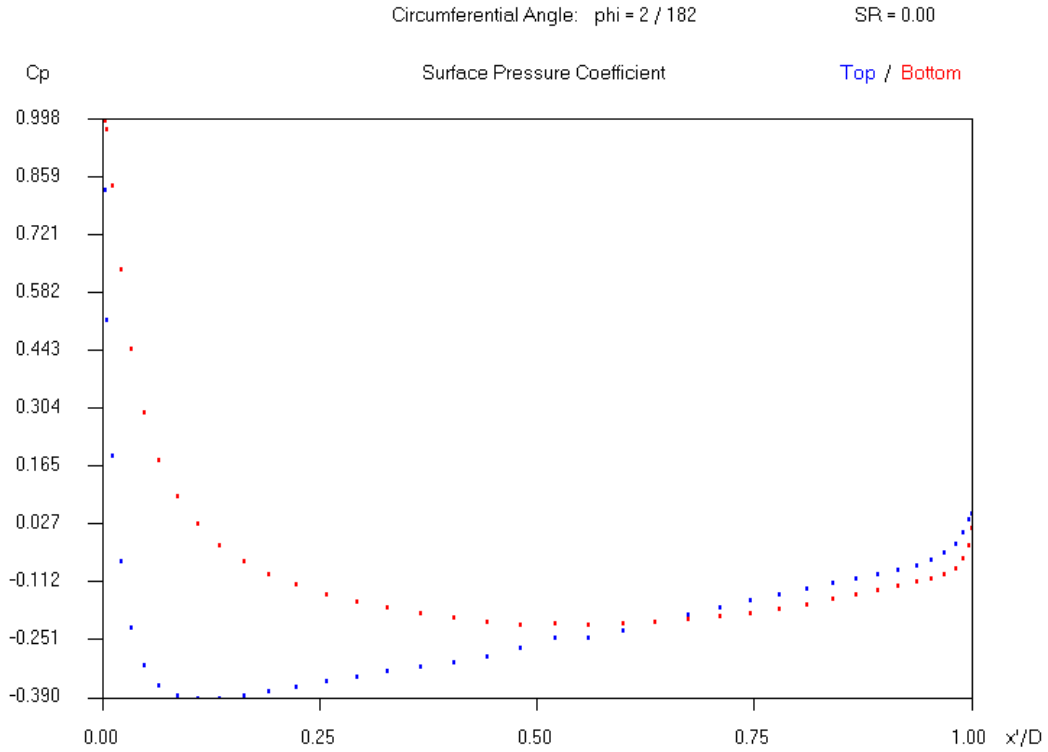


Figure 5-1: Longitudinal Pressure Comparison

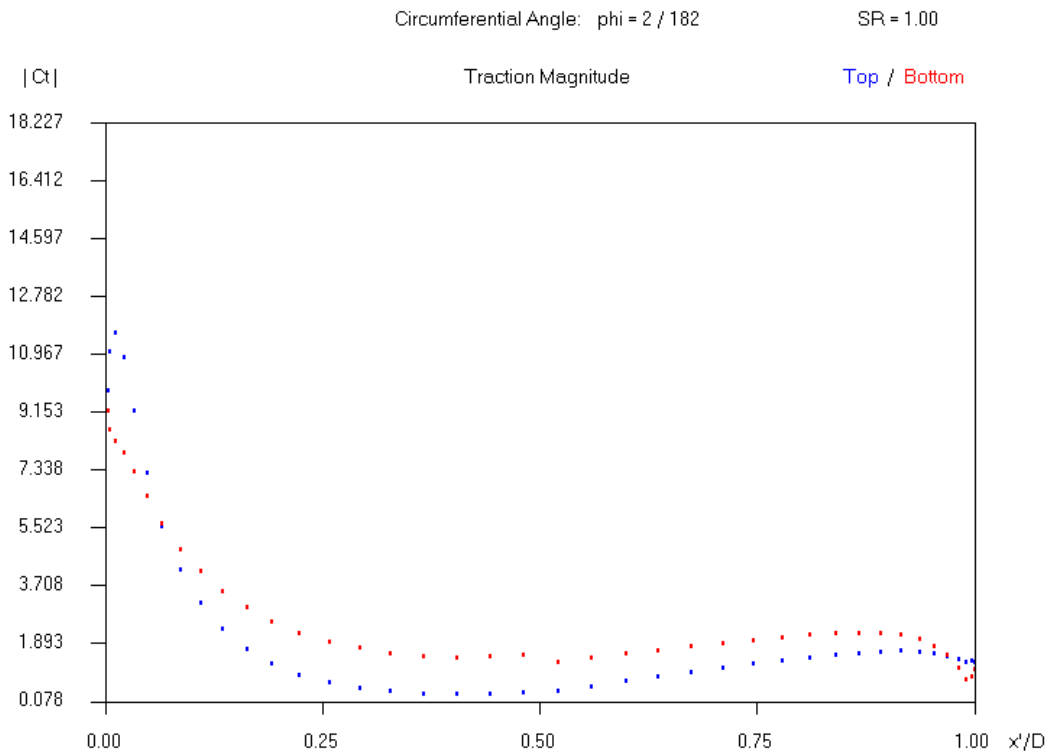
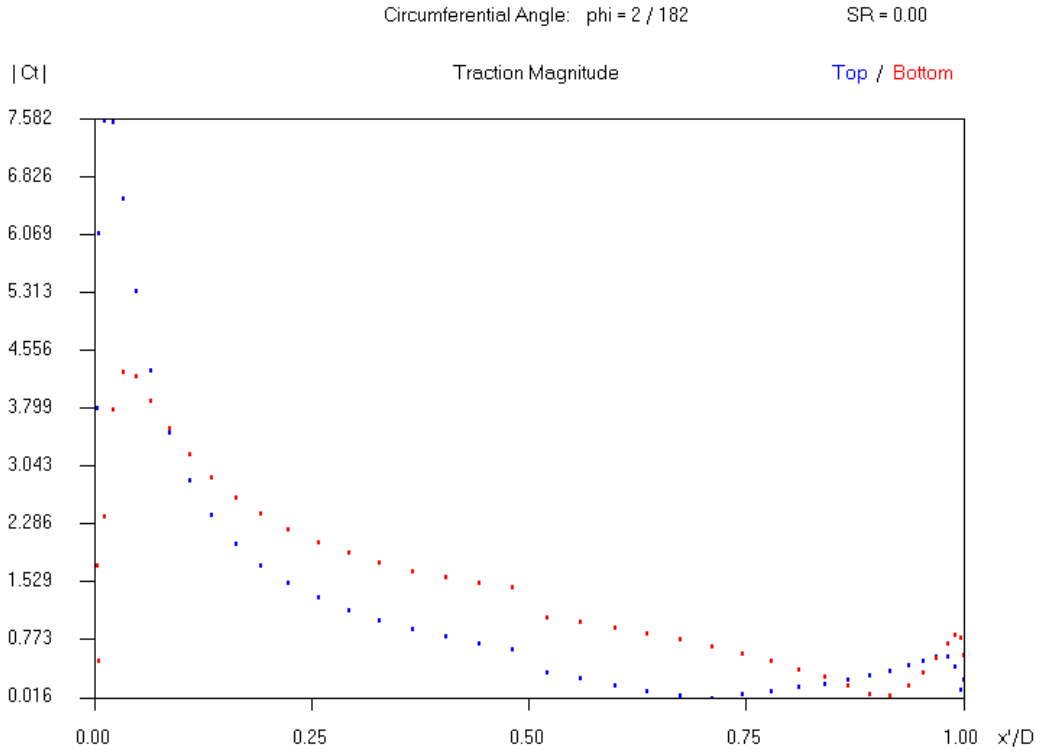


Figure 5-2: Longitudinal Traction Comparison

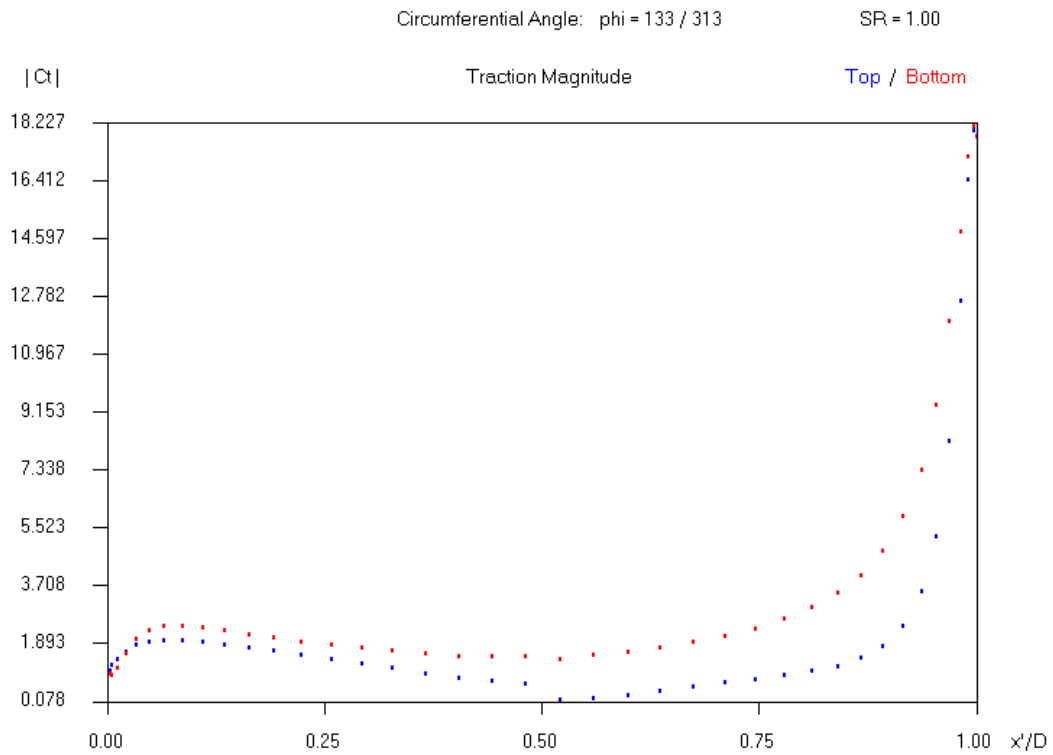
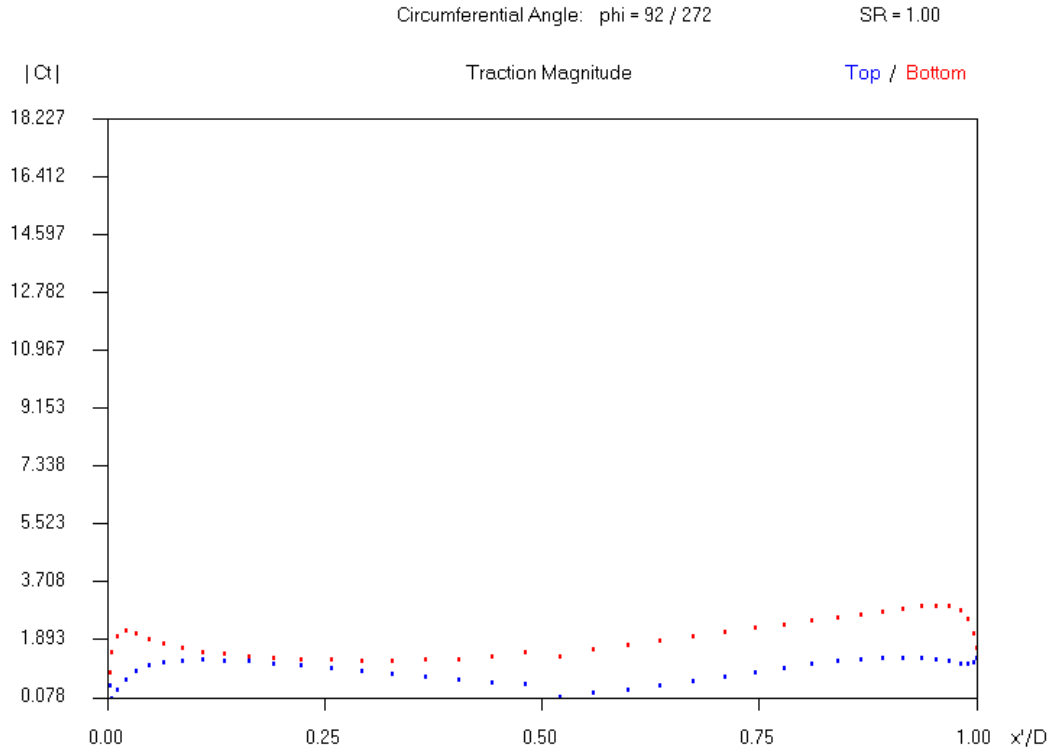


Figure 5-3: Traction in Lateral and Oblique Plane

The traction plots show slight jumps across the polar axis ($x/D = 0.5$), particularly the non-rotational case, which can be attributed to the mathematical modeling. Recall that cells on opposite sides of the pole are only connected circumferentially, and what may appear as a jump is actually a smooth variation. Although one may be inclined to employ an averaging technique of some sort, such practice would not be consistent with first principles.

5.4 Aerodynamic Data

As mentioned earlier, aerodynamic data were compiled for all four cases of varying spin ratio, which are tabulated below. Recall that the coefficients of lift and drag are computed with respect to the wind axes, whereas other force and moment coefficients are relative to the body axes (x, y, z). All recorded moment coefficients turn out negative, which implies right roll, pitch up, and clockwise yaw according to the sign convention established in Figure 4-5. Needless to say, gyroscopic effects have to be taken into consideration whenever the disc is spinning, in order to predict which way it will turn.

As expected, the yawing moment opposes rotation, and it appears that the functional relationship between yawing moment and rotation rate closely resembles a cubic polynomial. The pitching moment is virtually unaffected by rotation, and is the only moment acting when the disc is not spinning. The rolling moment is very small in comparison to both pitching and yawing moment, yet shows an increase with rotation rate. An exact aerodynamic center can only be calculated for the non-rotational case and is located along the negative x -axis, around 16.6% center chord,

$$x_{A.C.} = \frac{C_{Pitch}}{C_{Up}} = \frac{-0.03964}{0.11878} = -0.33373 \quad (5.1)$$

For the spinning disc, the flow field is completely asymmetric, and the resulting forces and moments can no longer be represented by a single force acting away from the center of gravity.

<i>SR</i>	0.000	0.500	1.000	1.500
C_{Aft}	0.04352	0.04483	0.04866	0.05734
C_{Up}	0.11878	0.12140	0.11547	0.10126
C_{Left}	0.00000	0.00313	0.00371	0.00215
C_{Roll}	0.00000	-0.00038	-0.00068	-0.00126
C_{Yaw}	0.00000	-0.00330	-0.00792	-0.01505
C_{Pitch}	-0.03964	-0.03887	-0.03916	-0.04066
C_{Drag}	0.05370	0.05524	0.05854	0.06595
C_{Lift}	0.11454	0.11703	0.11079	0.09588
C_{Left}	0.00000	0.00313	0.00371	0.00215
L/D	2.133	2.119	1.893	1.454
γ	25.1°	25.3°	27.8°	34.5°

Table 5-1: Aerodynamic Data

The data suggest a slow increase of drag with rotation rate. The lift shows a small peak in the sub-rotational range followed by a drop-off as rotation is further increased. The lift-to-drag ratio displays a shallow parabolic decline, and the corresponding glide angle γ —defined in Equation (1.3)—steepens accordingly. The left steering force seems to peak at equi-rotational spin, although one might have expected a steady increase with rotation rate based on experience with rotating cylinders.

5.5 Conclusion

In contrast to the major change in boundary layer and immediate flow field surrounding a spinning disc, the overall aerodynamics were minimally affected, if one excludes the gyroscopic stability benefit of rotation. The aerodynamic center, although not precisely defined for a rotating disc, did not move significantly in view of the minimal change in pitching moment and upward force, compared to the non-rotational case. The subtle increase in lift in the sub-rotational range was accompanied by an equally small increase in drag, such that the lift-to-drag ratio, and consequently the glide angle, remained more or less unchanged.

Judging from the aerodynamic data collected, the ellipsoid would make an unlikely candidate for a sports disc of any kind. The relatively large pitching moment, combined with gyroscopic precession, would result in considerable banking and quickly turn the disc upside down. Next to the problem of stability, the low lift-to-drag ratio of the ellipsoid would only yield a mediocre flight range.

Despite its undesirable aerodynamics, the ellipsoid was perfectly suited for a numerical flow simulation. Compared to a Frisbee, the shape of an ellipsoid is much more streamlined, and thus turbulence played a lesser role in the analysis. The extra computational expense of turbulence modeling was not an option in light of the extensive run time of a single simulation.

Although the numerical simulations were limited to a single shape and only one variation in flight parameters, the overall CFD analysis was able to unveil most of the “big picture” in disc aerodynamics. The influence of rotation on boundary layer growth and flow separation was anything but expected, and trying to obtain the same level of documentation in an actual wind tunnel test would be next to impossible. Although the number of graphs generated from the computational data may have been overwhelming, collectively they mapped out the flow field and thus told the “complete story”.

The major findings of this research can be summarized as follows: For an ellipsoidal disc at a small angle of attack, the onset of rotation accelerated fluid particles within the boundary layer radially outward. Combined with the rotational traction near the aft rim, flow separation could be eliminated along the entire rear surface. The only line of separation that was observed on the equi-rotational ellipsoid was curled around the left receding rim, where the relative wind vanishes and the surface traction is minimal. The forward impingement point, which is equivalent to the forward stagnation point for a non-rotating disc, was displaced circumferentially in the direction of the spin. The influence of rotation on the surrounding pressure field was weak, and the overall aerodynamic forces acting on the ellipsoid only experienced minor changes, such as the addition of a small left-steering force.

Being limited by computational resources, this work can only be considered a small first step towards the better understanding of disc aerodynamics. Future research on this topic should include the testing of different aerodynamic shapes, under a larger set of flight parameters. It should also address the turbulent aspect of the flow, which may have considerable impact on the overall aerodynamic behavior.

REFERENCES

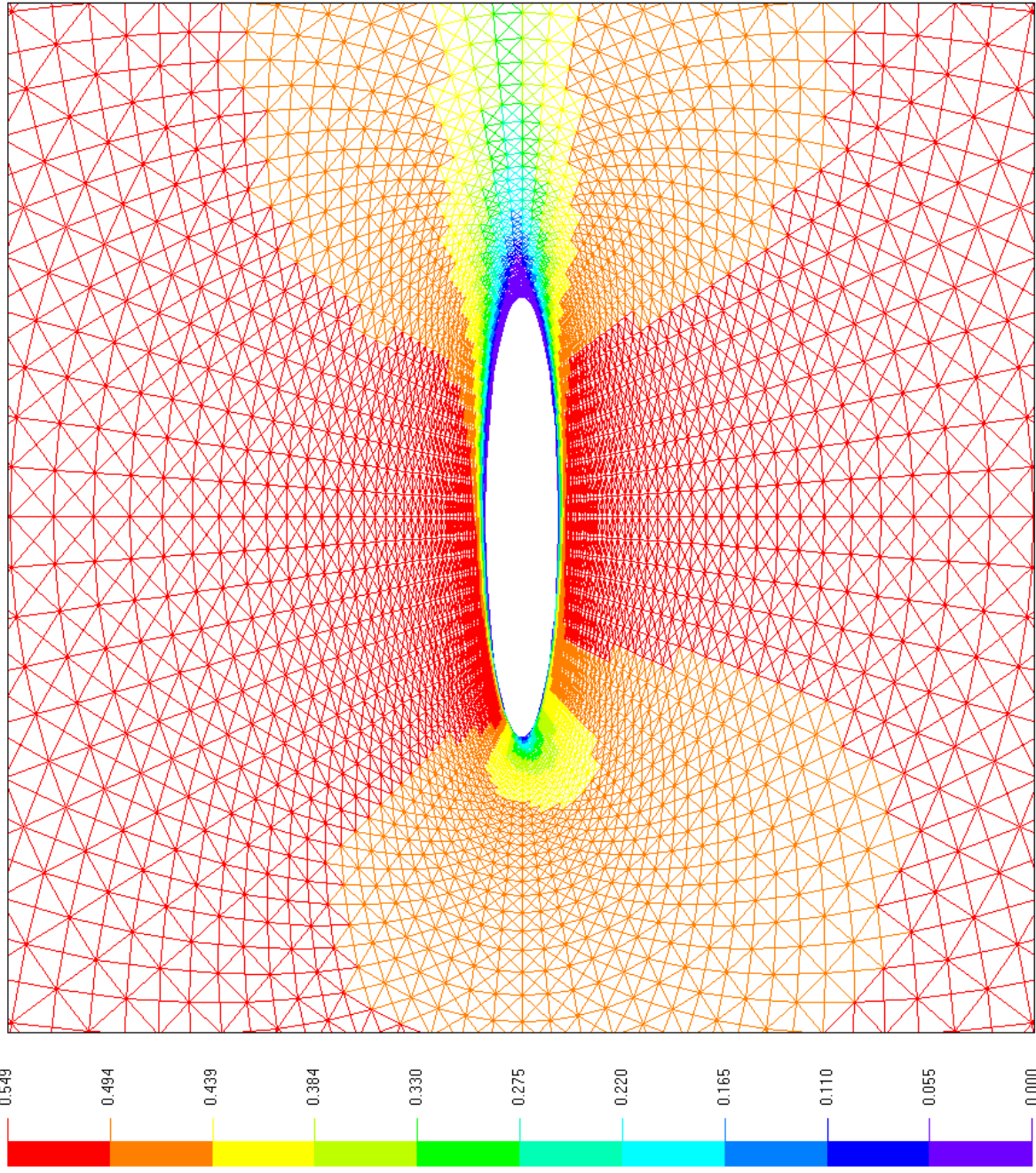
- [1] Anderson, Dale Arden, John C. Tannehill, and Richard H. Pletcher.
Computational Fluid Mechanics and Heat Transfer.
Hemisphere Publishing, New York, NY, 1984.
- [2] Anderson, John David, Jr.
Modern Compressible Flow, With Historical Perspective, Second Edition.
McGraw-Hill, New York, NY, 1990.
- [3] Anderson, John David, Jr.
Computational Fluid Dynamics: The Basics with Applications.
McGraw-Hill, New York, NY, 1995.
- [4] Courant, R., O. Friedrichs, and H. Lewy.
Über die Differenzgleichungen der Mathematischen Physik.
Mathematische Annalen, Volume 100, 1928, p. 32.
- [5] Fox, Robert W., and Alan T. McDonald.
Introduction to Fluid Mechanics, Third Edition.
John Wiley & Sons, New York, NY, 1985.
- [6] Hale, Francis J.
Introduction to Aircraft Performance, Selection, and Design.
John Wiley & Sons, New York, NY, 1984.
- [7] Harten, Ami.
High Resolution Schemes for Hyperbolic Conservation Laws.
Journal of Computational Physics, Volume 49, 1983, pp. 357-393.
- [8] Hoerner, Sighard F.
Fluid-Dynamic Lift, Practical Information on Aerodynamic and Hydrodynamic Lift.
Published by the Author, 1965.
- [9] Jeng, Yih Nen, and Uon Jan Payne.
An Adaptive TVD Limiter.
Journal of Computational Physics, Volume 118, 1995, pp. 229-241.
- [10] Katz, Paul.
The Free Flight of a Rotating Disc.
Israel Journal of Technology, Volume 6, No.1-2, 1968, pp. 150-155.
- [11] Laney, Culbert B.
Computational Gasdynamics.
Cambridge University Press, Cambridge, UK, 1998.
- [12] Mugler, John P., Jr., and Walter B. Olstad.
Static Longitudinal Aerodynamic Characteristics at Transonic Speeds of a Lenticular-Shaped Reentry Vehicle.
NASA Technical Memorandum, X-423, 1960.
- [13] Nakamura, Y., and N. Fukamachi.
Visualization of the flow past a Frisbee.
Fluid Dynamics Research, Volume 7, No.1, January 1991, pp. 31-35.

- [14] Panton, Ronald L.
Incompressible Flow, Second Edition.
John Wiley & Sons, New York, NY, 1996.
- [15] Roe, Philip L.
Approximate Riemann Solvers, Parameter Vectors, and Difference Schemes.
Journal of Computational Physics, Volume 43, 1981, pp. 357-372.
- [16] Roshko, Anatol.
On the Drag and Shedding Frequency of Cylinders.
NACA Technical Note, TN-3169, 1954.
- [17] Schlichting, Hermann.
Boundary Layer Theory, Seventh Edition.
McGraw-Hill, New York, NY, 1987.
- [18] Schuurmans, Macé.
Flight of the Frisbee.
New Scientist, Volume 127, No.1727, 28 July 1990, pp. 37-40.
- [19] Shelton, Jay.
The Physics of Frisbee Flight, from the book,
Frisbee: a practitioner's manual and definitive treatise, by Stancil Johnson, 1975.
- [20] Simon, Craig.
Frisbee, Beyond Catch and Throw.
Craig Simon, 1982.
- [21] Smithwick, Quinn, and Scott Eberhardt.
Fuzzy Controller and Neuron Models of Harten's Second-Order TVD Scheme.
AIAA Journal, Volume 32, No. 10, 1994, pp. 2122-2124.
- [22] Vincenti, Walter Guido, and Charles H. Kruger, Jr.
Introduction to Physical Gas Dynamics.
Krieger Publishing Company, Malabar, FL, 1975.
- [23] Wang, J.C.T., and G.F. Widhopf.
A High-Resolution TVD Finite Volume Scheme for the Euler Equations in Conservation Form.
Journal of Computational Physics, Volume 84, 1989, pp. 145-173.
- [24] Wang, Z., and B.E. Richards.
High Resolution Schemes for Steady Flow Computation.
Journal of Computational Physics, Volume 97, 1991, pp. 53-72.
- [25] Yee, Helen C., and P. Kutler.
Application of Second-Order-Accurate TVD Schemes to the Euler Equations in General Geometries.
NASA Technical Memorandum, TM 85845, 1983.
- [26] Yee, Helen C., R.F. Warming, and Ami Harten.
"On a Class of TVD Schemes for Gas Dynamic Calculations",
Numerical Methods of the Euler Equations of Fluid Dynamics.
Edited by F. Angrand, A. Dervieux, J.A. Desideri, and R. Glowinski.
Society for Industrial and Applied Mathematics, Philadelphia, PA, 1985, pp. 84-107.

APPENDIX A

Computational Results for Non-Rotational Disc

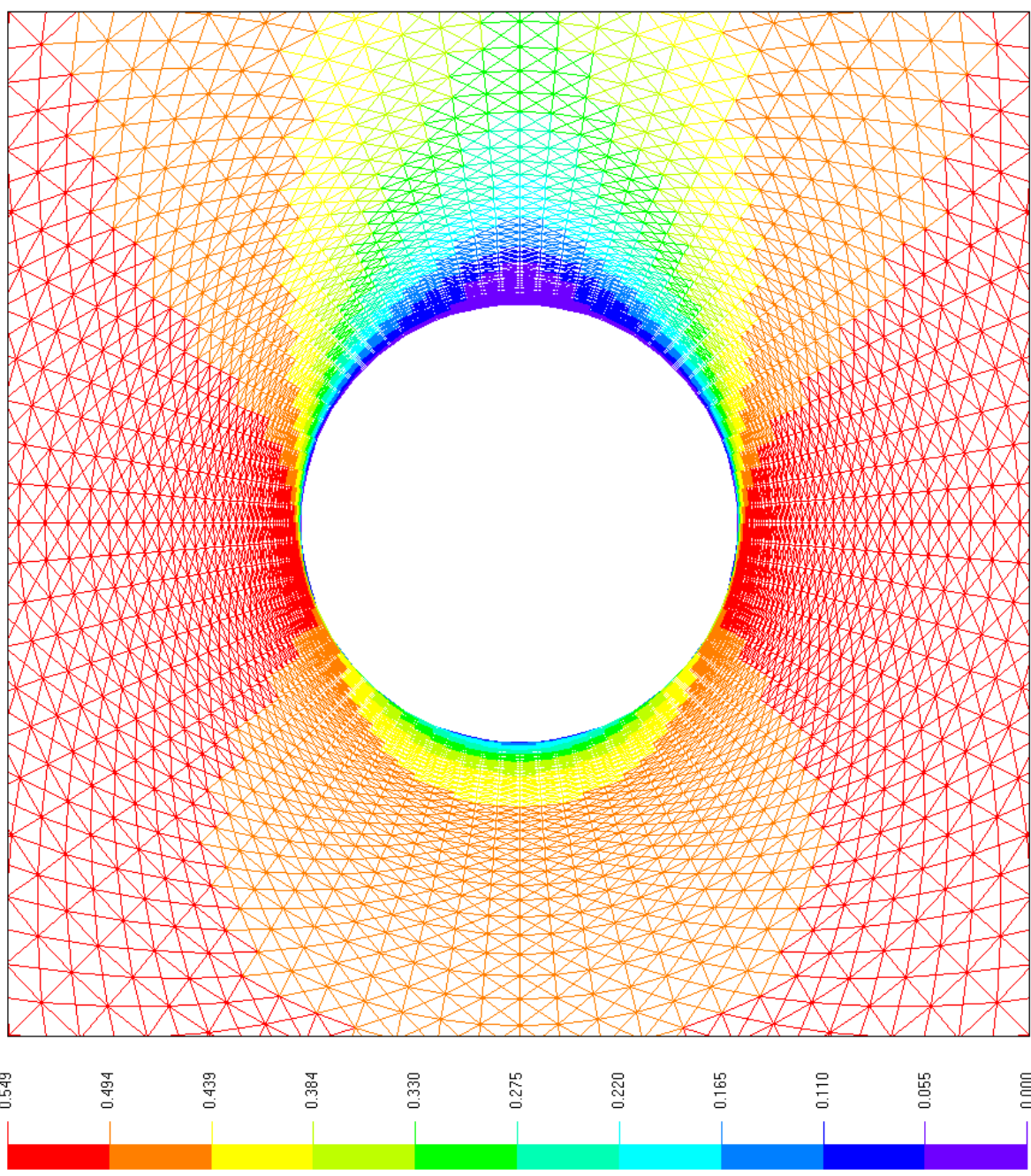
BLANK PAGE



Side View: Mach Number

Test ID: ELL000.tst
 Mesh Resolution: 60 x 40 x 80
 Spin Ratio: SR = 0.00
 Reynolds Number: Re = 3.00E4
 Mach Number: M = 0.50
 Diameter (m): D = 0.010
 Angle of Attack (deg): $\alpha = 5$
 Static Pressure (hPa): P = 270
 Static Temperature (K): T = 296
 Gas Constant (J/kgK): R = 287
 Specific Heats Ratio: k = 1.40
 Run Time (s): t = 0.001000
 Time Step (ms): dt = 0.025
 Stop Time (s): T = 0.001000
 Drag Coefficient: Cd = 0.054
 Lift Coefficient: Cl = 0.115
 Left Coefficient: Ce = 0.000
 Lift-to-Drag Ratio: L/D = 2.133
 X-view: 0.00
 Y-view: 0.00
 Zoom: 3.00

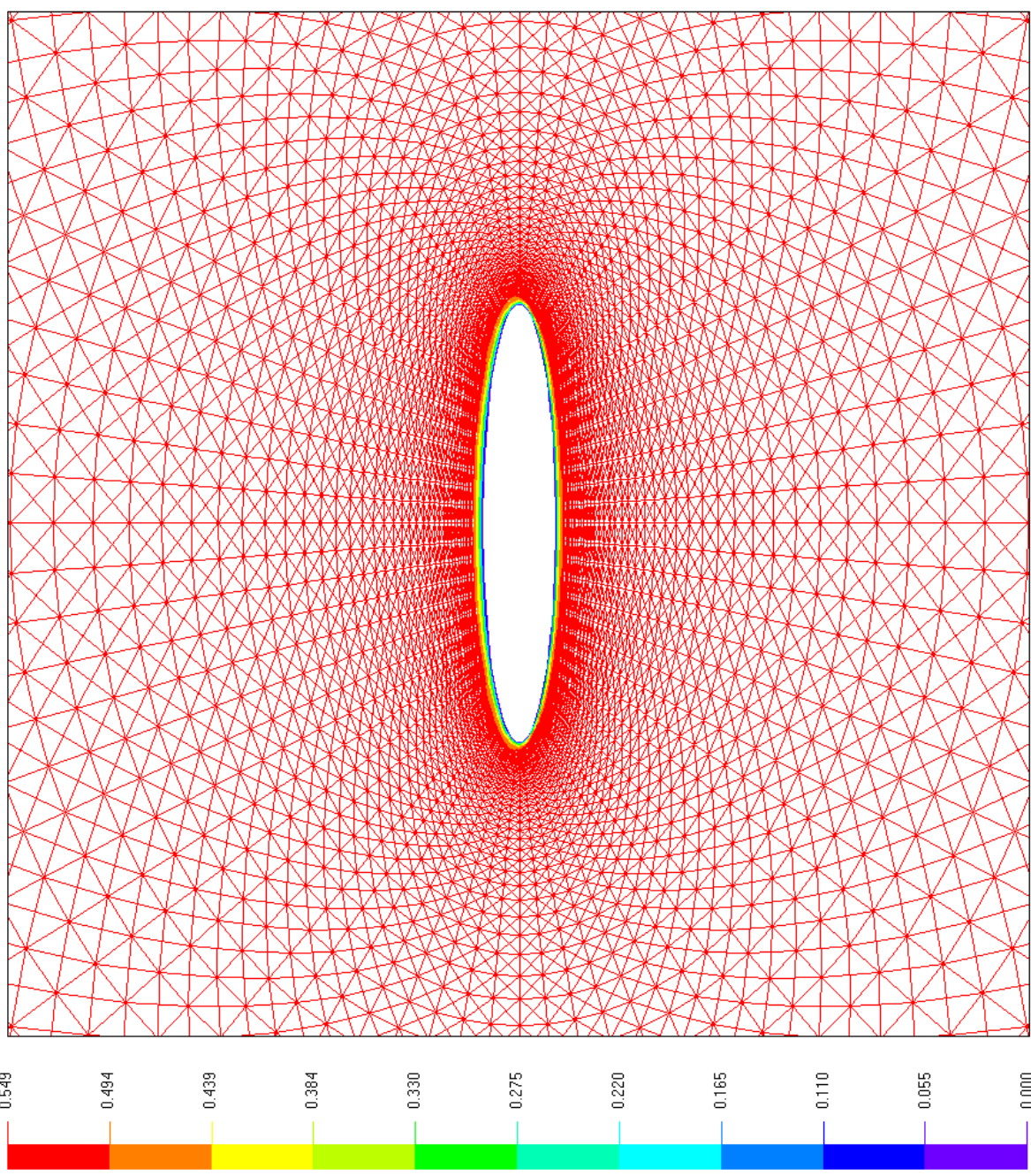
Test ID: ELL000.tst
 Mesh Resolution: 60 x 40 x 80
 Spin Ratio: SR = 0.00
 Reynolds Number: Re = 3.00E4
 Mach Number: M = 0.50
 Diameter (m): D = 0.010
 Angle of Attack (deg): $\alpha = 5$
 Static Pressure (hPa): P = 270
 Static Temperature (K): T = 296
 Gas Constant (J/kgK): R = 287
 Specific Heats Ratio: k = 1.40
 Run Time (s): t = 0.001000
 Time Step (ms): dt = 0.025
 Stop Time (s): T = 0.001000
 Drag Coefficient: Cd = 0.054
 Lift Coefficient: Cl = 0.115
 Left Coefficient: Ce = 0.000
 Lift-to-Drag Ratio: L/D = 2.133
 X-view: 0.00
 Y-view: 0.00
 Zoom: 3.00



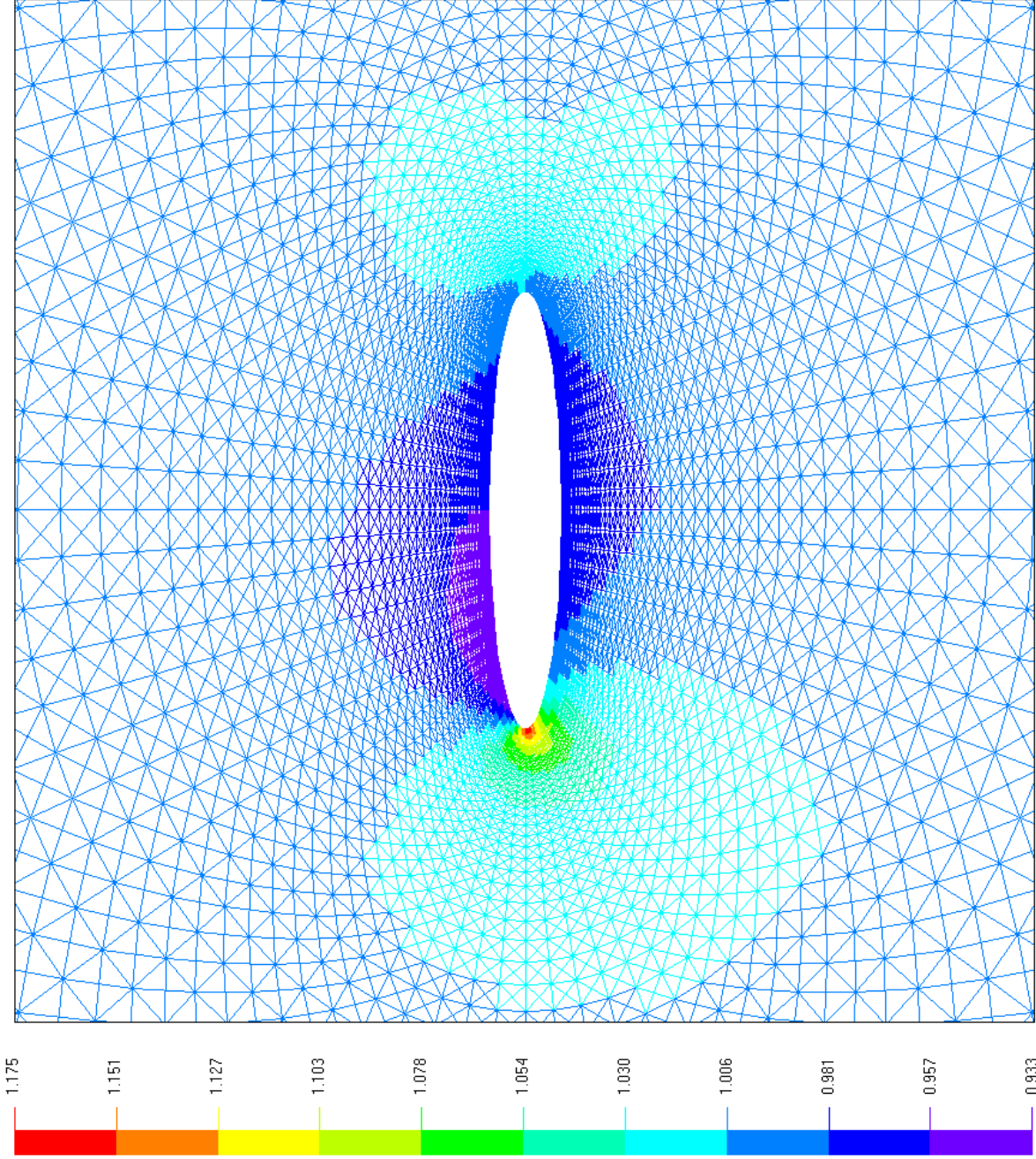
Top View: Mach Number

Mach #

Test ID: ELL000.tst
 Mesh Resolution: 60 x 40 x 80
 Spin Ratio: SR = 0.00
 Reynolds Number: Re = 3.00E4
 Mach Number: M = 0.50
 Diameter (m): D = 0.010
 Angle of Attack (deg): $\alpha = 5$
 Static Pressure (hPa): P = 270
 Static Temperature (K): T = 296
 Gas Constant (J/kgK): R = 287
 Specific Heats Ratio: k = 1.40
 Run Time (s): t = 0.001000
 Time Step (ms): dt = 0.025
 Stop Time (s): T = 0.001000
 Drag Coefficient: Cd = 0.054
 Lift Coefficient: Cl = 0.115
 Left Coefficient: Ce = 0.000
 Lift-to-Drag Ratio: L/D = 2.133
 X-view: 0.00
 Y-view: 0.00
 Zoom: 3.00



Front View: Mach Number



Test ID: ELL000.tst

Mesh Resolution: 60 x 40 x 80

Spin Ratio: SR = 0.00

Reynolds Number: Re = 3.00E4

Mach Number: M = 0.50

Diameter (m): D = 0.010

Angle of Attack (deg): $\alpha = 5$

Static Pressure (hPa): P = 270

Static Temperature (K): T = 296

Gas Constant (J/kgK): R = 287

Specific Heats Ratio: k = 1.40

Run Time (s): t = 0.001000

Time Step (ms): dt = 0.025

Stop Time (s): T = 0.001000

Drag Coefficient: Cd = 0.054

Lift Coefficient: Cl = 0.115

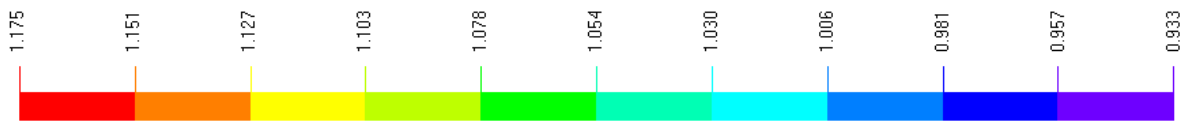
Left Coefficient: Ce = 0.000

Lift-to-Drag Ratio: L/D = 2.133

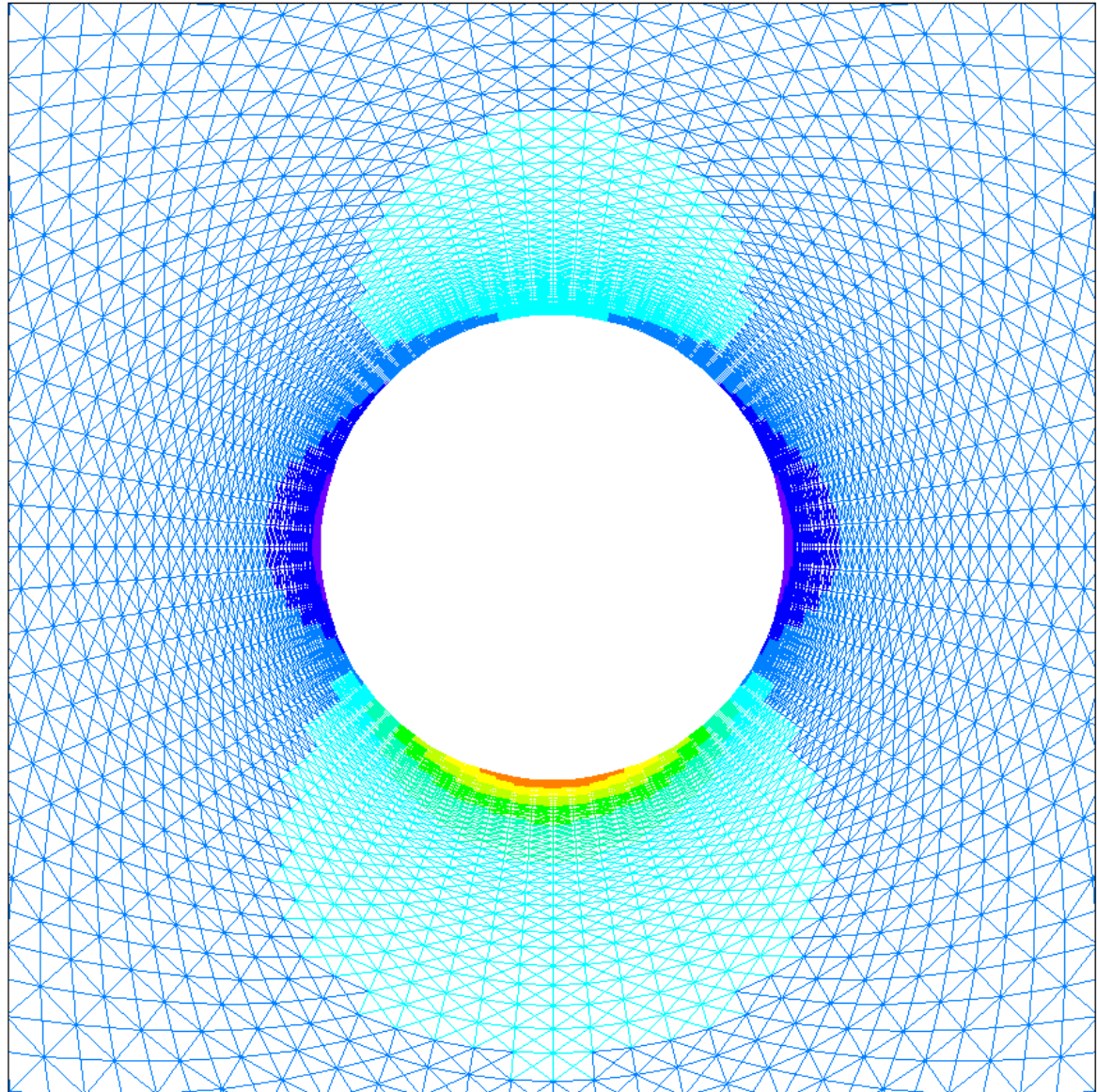
X-view: 0.00

Y-view: 0.00

Zoom: 3.00

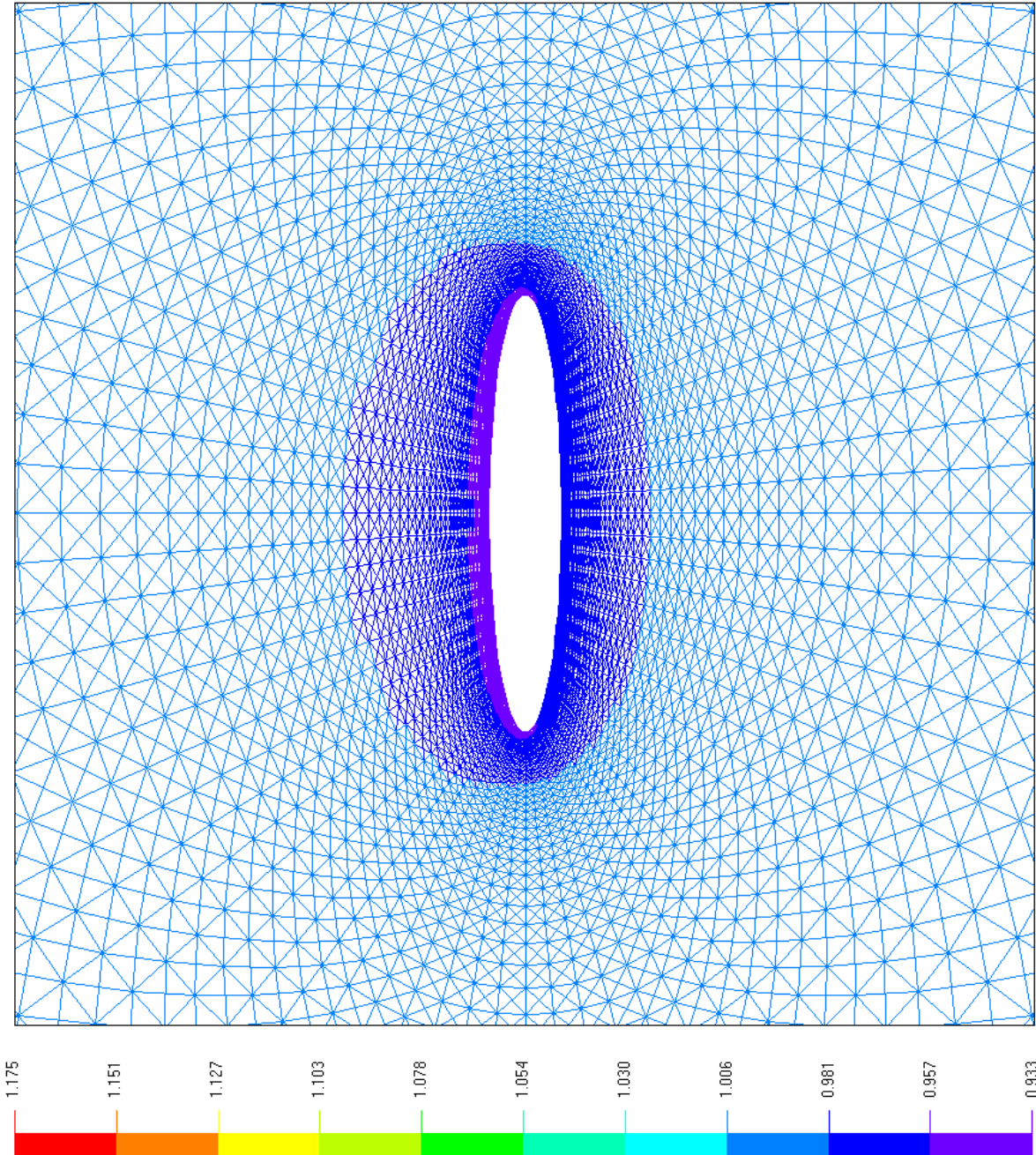


Test ID: ELL000.tst
 Mesh Resolution: 60 x 40 x 80
 Spin Ratio: SR = 0.00
 Reynolds Number: Re = 3.00E4
 Mach Number: M = 0.50
 Diameter (m): D = 0.010
 Angle of Attack (deg): $\alpha = 5$
 Static Pressure (hPa): P = 270
 Static Temperature (K): T = 296
 Gas Constant (J/kgK): R = 287
 Specific Heats Ratio: k = 1.40
 Run Time (s): t = 0.001000
 Time Step (ms): dt = 0.025
 Stop Time (s): T = 0.001000
 Drag Coefficient: Cd = 0.054
 Lift Coefficient: Cl = 0.115
 Left Coefficient: Ce = 0.000
 Lift-to-Drag Ratio: L/D = 2.133
 X-view: 0.00
 Y-view: 0.00
 Zoom: 3.00



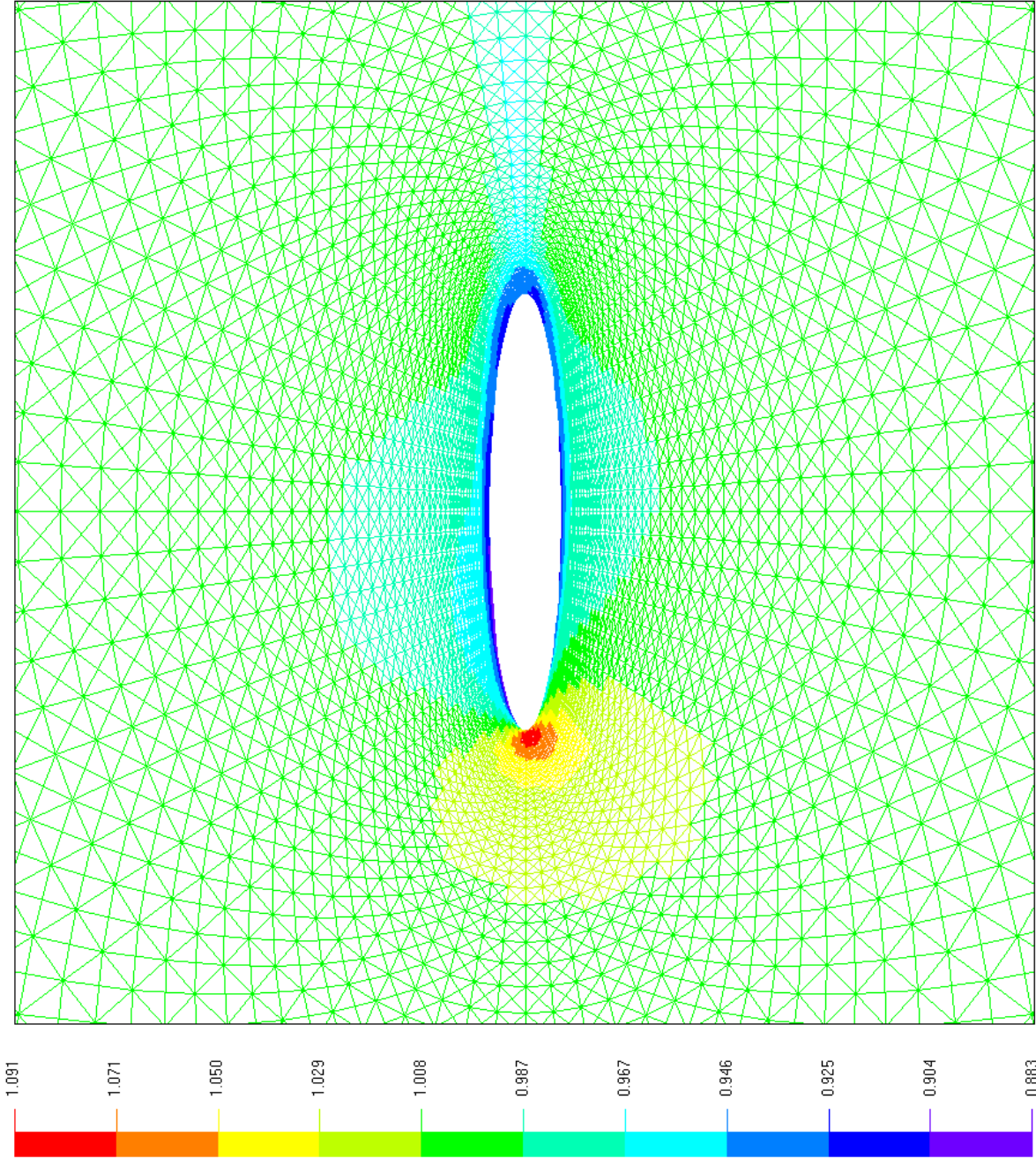
Top View: Pressure

P/Pt



Front View: Pressure

Test ID: ELL000.tst
 Mesh Resolution: 60 x 40 x 80
 Spin Ratio: SR = 0.00
 Reynolds Number: Re = 3.00E4
 Mach Number: M = 0.50
 Diameter (m): D = 0.010
 Angle of Attack (deg): $\alpha = 5$
 Static Pressure (hPa): P = 270
 Static Temperature (K): T = 296
 Gas Constant (J/kgK): R = 287
 Specific Heats Ratio: k = 1.40
 Run Time (s): t = 0.001000
 Time Step (ms): dt = 0.025
 Stop Time (s): T = 0.001000
 Drag Coefficient: Cd = 0.054
 Lift Coefficient: Cl = 0.115
 Left Coefficient: Ce = 0.000
 Lift-to-Drag Ratio: L/D = 2.133
 X-view: 0.00
 Y-view: 0.00
 Zoom: 3.00



Side View: Density

Rh/Rinf

Test ID: ELL000.tst

Mesh Resolution: 60 x 40 x 80

Spin Ratio: SR = 0.00

Reynolds Number: Re = 3.00E4

Mach Number: M = 0.50

Diameter (m): D = 0.010

Angle of Attack (deg): $\alpha = 5$

Static Pressure (hPa): P = 270

Static Temperature (K): T = 296

Gas Constant (J/kgK): R = 287

Specific Heats Ratio: k = 1.40

Run Time (s): t = 0.001000

Time Step (ms): dt = 0.025

Stop Time (s): T = 0.001000

Drag Coefficient: Cd = 0.054

Lift Coefficient: Cl = 0.115

Left Coefficient: Ce = 0.000

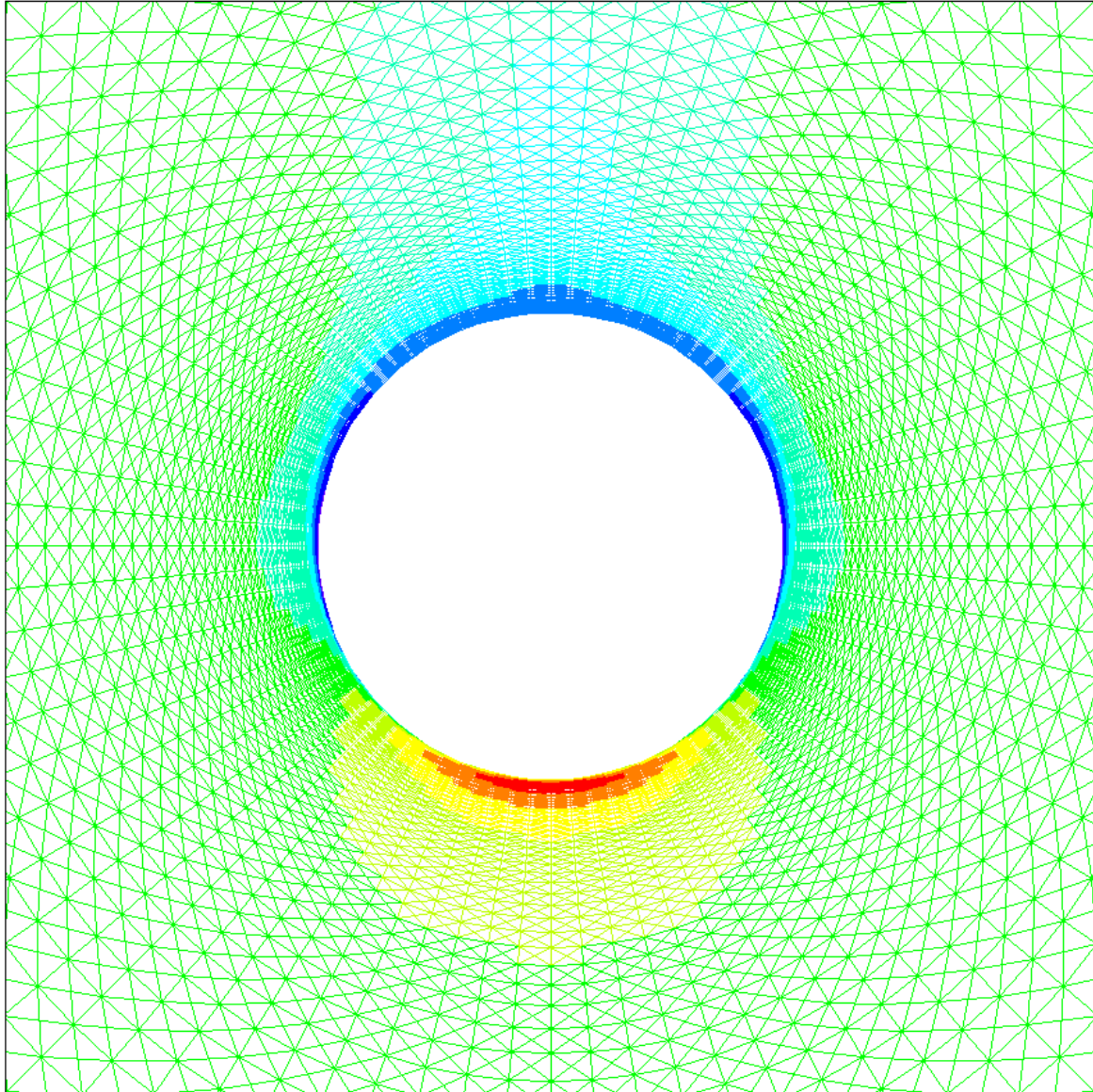
Lift-to-Drag Ratio: L/D = 2.133

X-view: 0.00

Y-view: 0.00

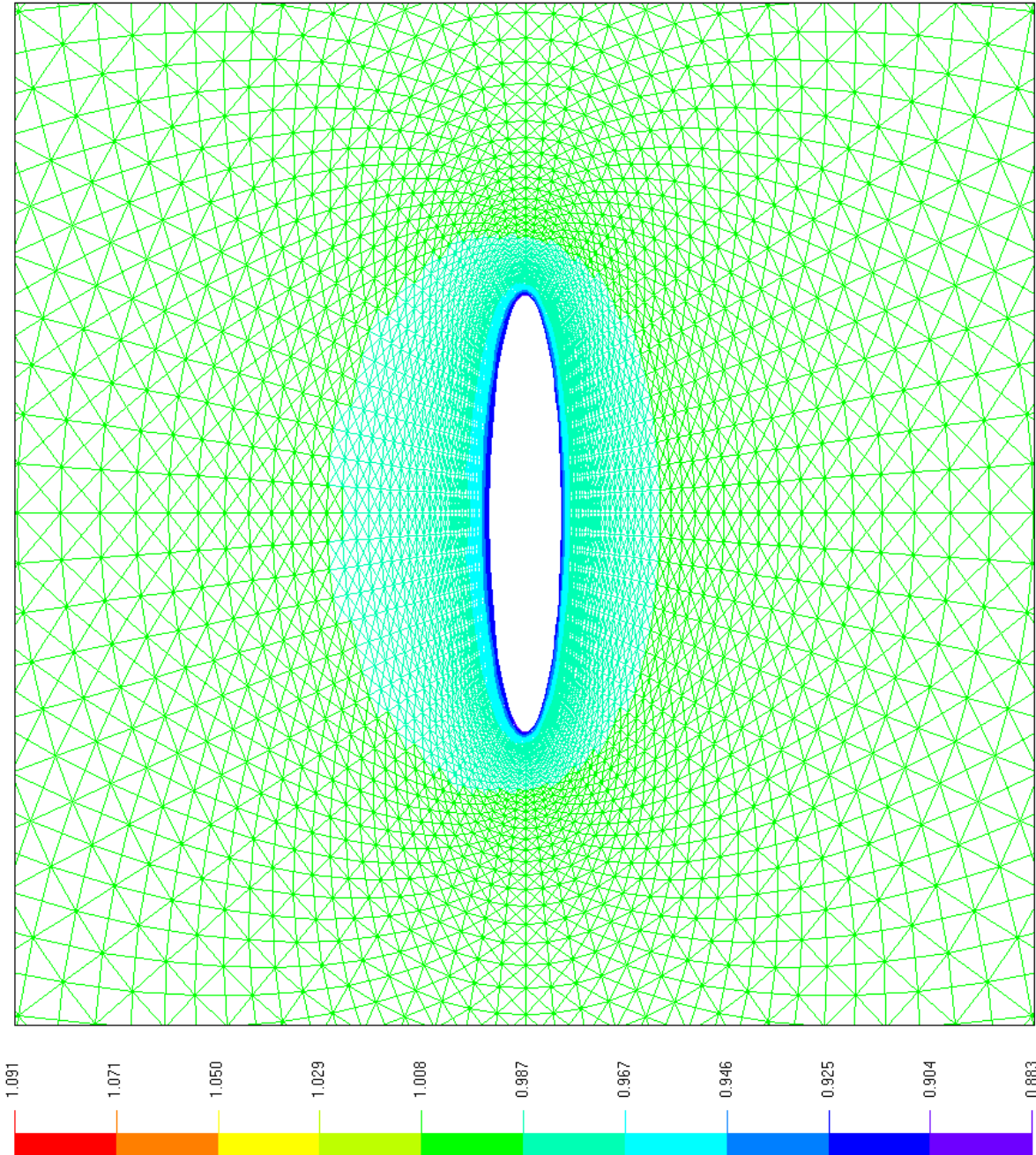
Zoom: 3.00

Test ID: ELL000.tst
 Mesh Resolution: 60 x 40 x 80
 Spin Ratio: SR = 0.00
 Reynolds Number: Re = 3.00E4
 Mach Number: M = 0.50
 Diameter (m): D = 0.010
 Angle of Attack (deg): $\alpha = 5$
 Static Pressure (hPa): P = 270
 Static Temperature (K): T = 296
 Gas Constant (J/kgK): R = 287
 Specific Heats Ratio: $k = 1.40$
 Run Time (s): t = 0.001000
 Time Step (ms): dt = 0.025
 Stop Time (s): T = 0.001000
 Drag Coefficient: Cd = 0.054
 Lift Coefficient: Cl = 0.115
 Left Coefficient: Ce = 0.000
 Lift-to-Drag Ratio: L/D = 2.133
 X-view: 0.00
 Y-view: 0.00
 Zoom: 3.00

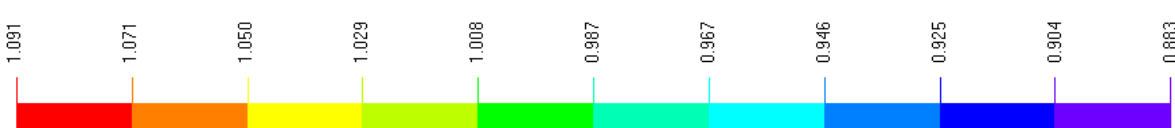


Top View: Density



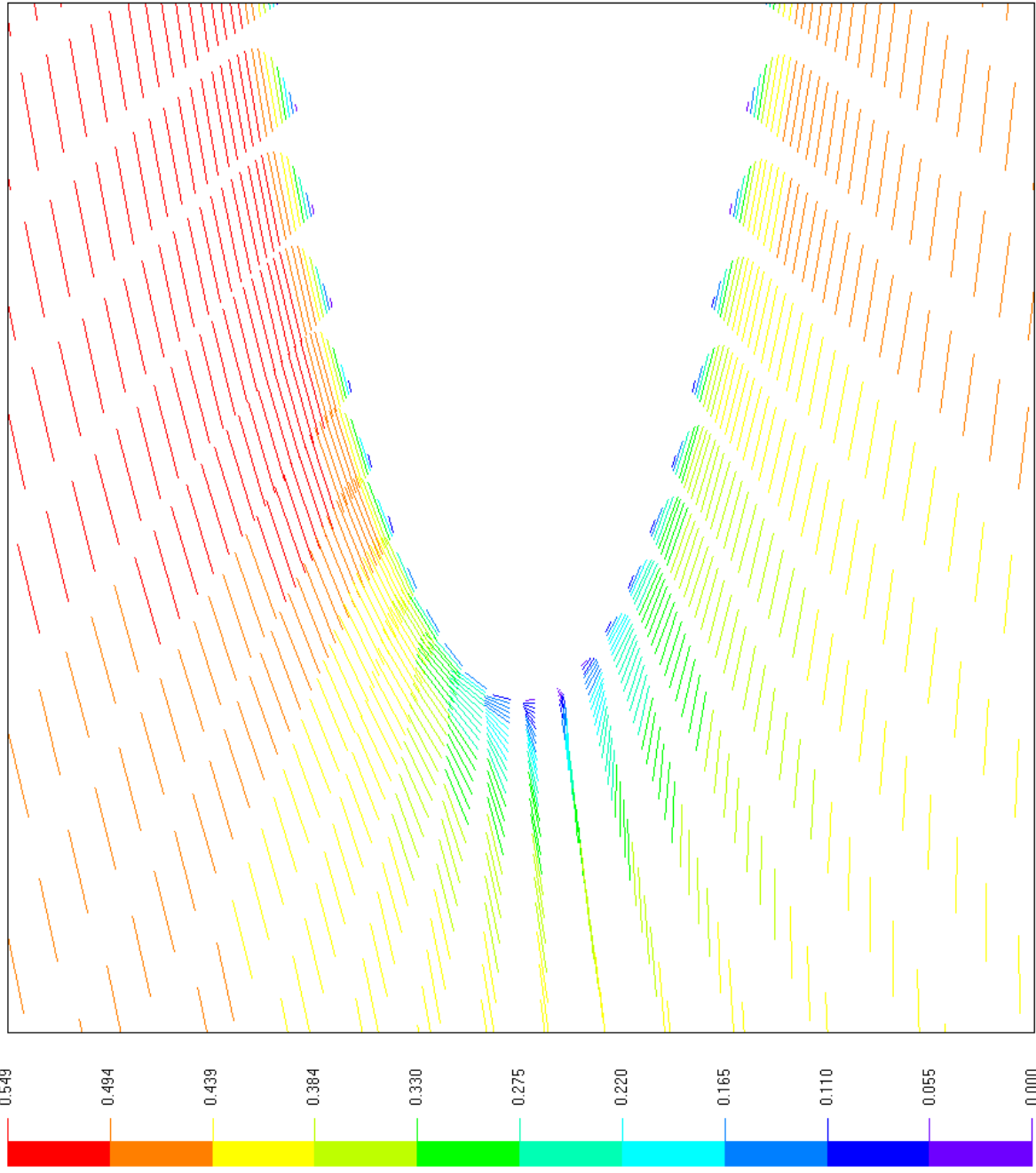


Front View: Density



Rh/Rinf

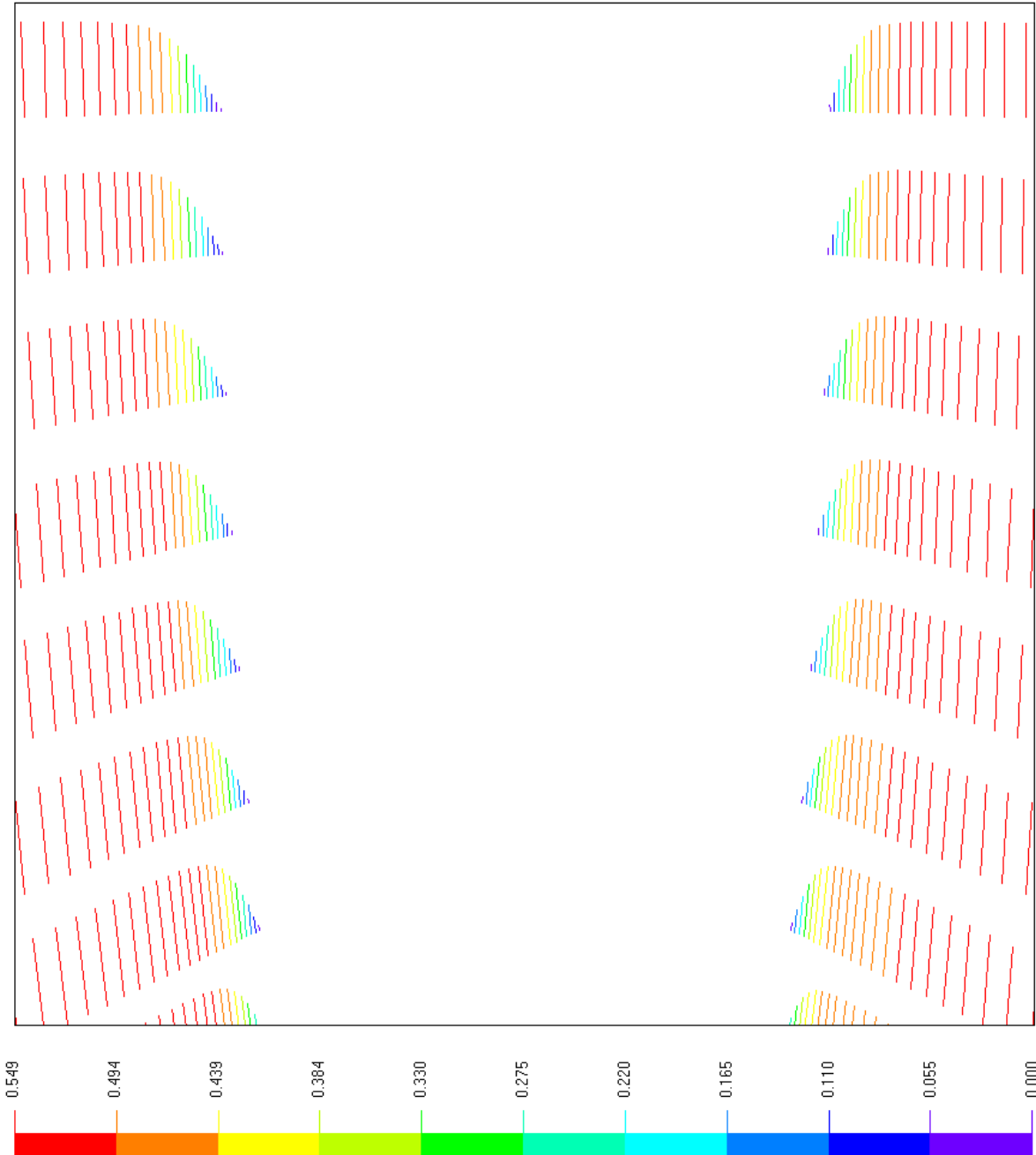
Test ID: ELL000.tst
 Mesh Resolution: 60 x 40 x 80
 Spin Ratio: SR = 0.00
 Reynolds Number: Re = 3.00E4
 Mach Number: M = 0.50
 Diameter (m): D = 0.010
 Angle of Attack (deg): $\alpha = 5$
 Static Pressure (hPa): P = 270
 Static Temperature (K): T = 296
 Gas Constant (J/kgK): R = 287
 Specific Heats Ratio: k = 1.40
 Run Time (s): t = 0.001000
 Time Step (ms): dt = 0.025
 Stop Time (s): T = 0.001000
 Drag Coefficient: Cd = 0.054
 Lift Coefficient: Cl = 0.115
 Left Coefficient: Ce = 0.000
 Lift-to-Drag Ratio: L/D = 2.133
 X-view: 0.00
 Y-view: 0.00
 Zoom: 3.00



Side View: Mach Number

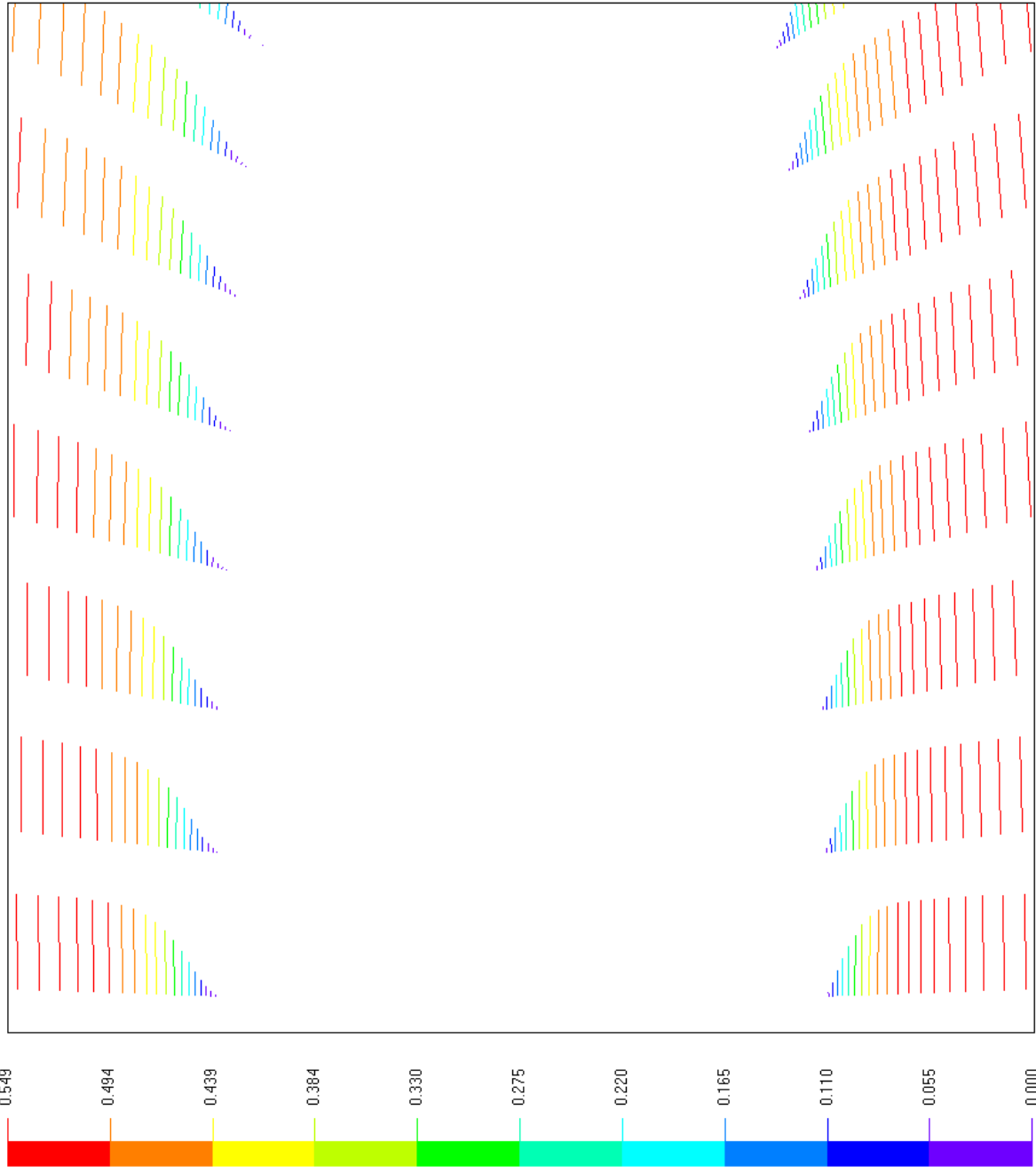


Test ID: ELL000.tst
 Mesh Resolution: 60 x 40 x 80
 Spin Ratio: SR = 0.00
 Reynolds Number: Re = 3.00E4
 Mach Number: M = 0.50
 Diameter (m): D = 0.010
 Angle of Attack (deg): $\alpha = 5$
 Static Pressure (hPa): P = 270
 Static Temperature (K): T = 296
 Gas Constant (J/kgK): R = 287
 Specific Heats Ratio: k = 1.40
 Run Time (s): t = 0.001000
 Time Step (ms): dt = 0.025
 Stop Time (s): T = 0.001000
 Drag Coefficient: Cd = 0.054
 Lift Coefficient: Cl = 0.115
 Left Coefficient: Ce = 0.000
 Lift-to-Drag Ratio: L/D = 2.133
 X-view: -0.45
 Y-view: 0.00
 Zoom: 25.00



Side View: Mach Number

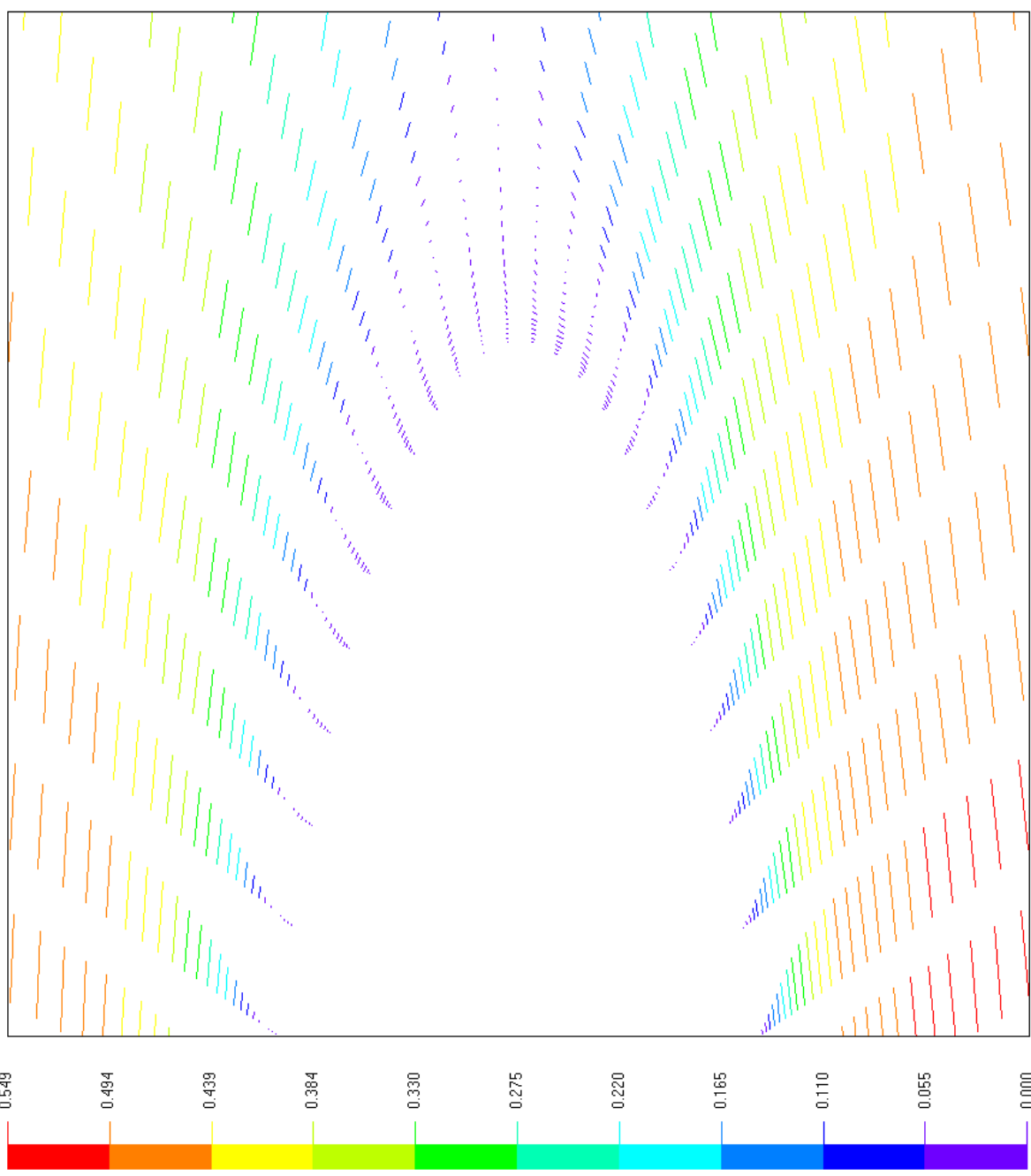
Test ID: ELL000.tst
 Mesh Resolution: 60 x 40 x 80
 Spin Ratio: SR = 0.00
 Reynolds Number: Re = 3.00E4
 Mach Number: M = 0.50
 Diameter (m): D = 0.010
 Angle of Attack (deg): $\alpha = 5$
 Static Pressure (hPa): P = 270
 Static Temperature (K): T = 296
 Gas Constant (J/kgK): R = 287
 Specific Heats Ratio: k = 1.40
 Run Time (s): t = 0.001000
 Time Step (ms): dt = 0.025
 Stop Time (s): T = 0.001000
 Drag Coefficient: Cd = 0.054
 Lift Coefficient: Cl = 0.115
 Left Coefficient: Ce = 0.000
 Lift-to-Drag Ratio: L/D = 2.133
 X-view: -0.13
 Y-view: 0.00
 Zoom: 25.00



Side View: Mach Number

Test ID: ELL000.tst
 Mesh Resolution: 60 x 40 x 80
 Spin Ratio: SR = 0.00
 Reynolds Number: Re = 3.00E4
 Mach Number: M = 0.50
 Diameter (m): D = 0.010
 Angle of Attack (deg): $\alpha = 5$
 Static Pressure (hPa): P = 270
 Static Temperature (K): T = 296
 Gas Constant (J/kgK): R = 287
 Specific Heats Ratio: $k = 1.40$
 Run Time (s): $t = 0.001000$
 Time Step (ms): $dt = 0.025$
 Stop Time (s): T = 0.001000
 Drag Coefficient: Cd = 0.054
 Lift Coefficient: Cl = 0.115
 Left Coefficient: Ce = 0.000
 Lift-to-Drag Ratio: L/D = 2.133
 X-view: 0.15
 Y-view: 0.00
 Zoom: 25.00

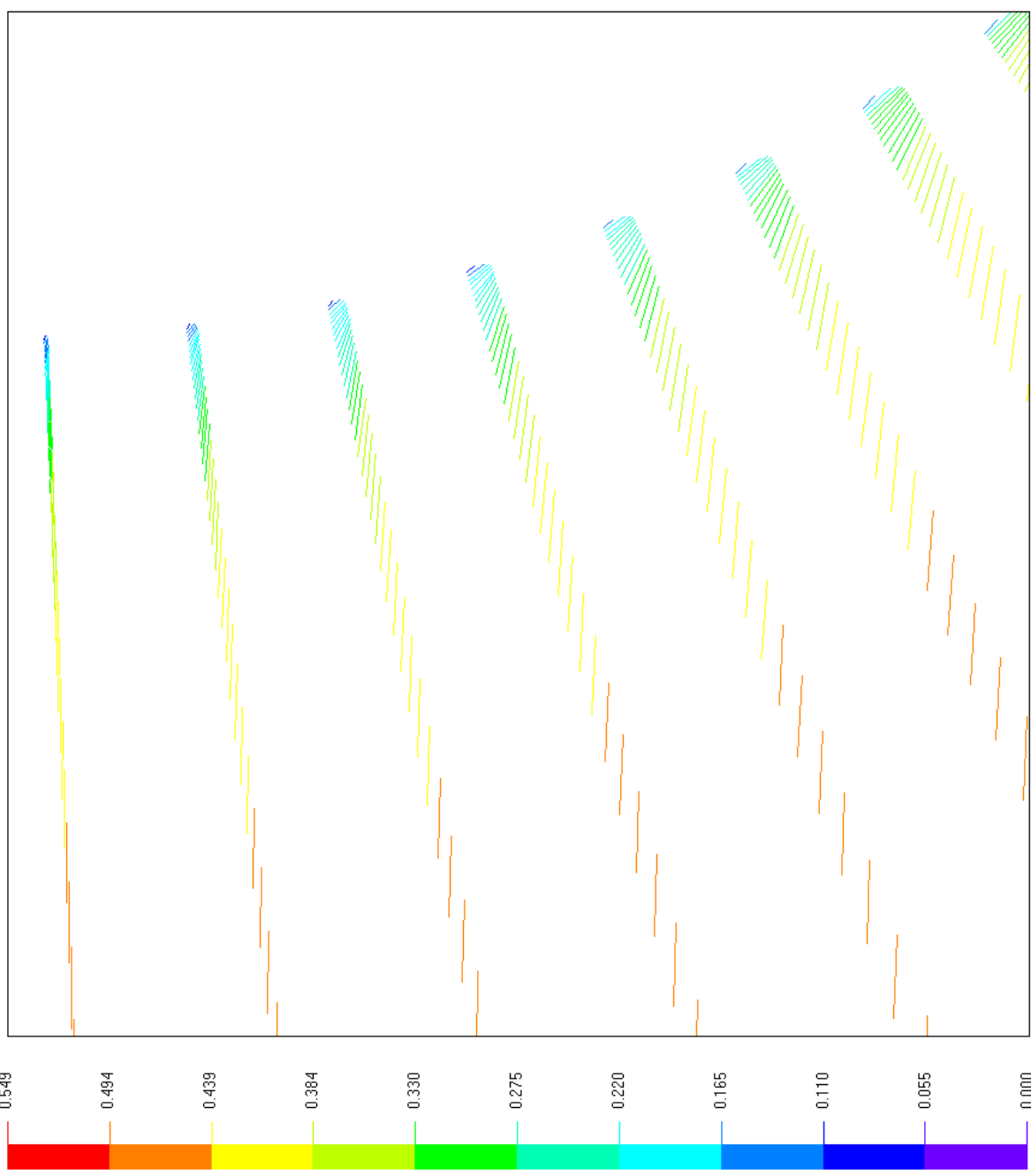
Test ID: ELL000.tst
 Mesh Resolution: 60 x 40 x 80
 Spin Ratio: SR = 0.00
 Reynolds Number: Re = 3.00E4
 Mach Number: M = 0.50
 Diameter (m): D = 0.010
 Angle of Attack (deg): $\alpha = 5$
 Static Pressure (hPa): P = 270
 Static Temperature (K): T = 296
 Gas Constant (J/kgK): R = 287
 Specific Heats Ratio: k = 1.40
 Run Time (s): t = 0.001000
 Time Step (ms): dt = 0.025
 Stop Time (s): T = 0.001000
 Drag Coefficient: Cd = 0.054
 Lift Coefficient: Cl = 0.115
 Left Coefficient: Ce = 0.000
 Lift-to-Drag Ratio: L/D = 2.133
 X-view: 0.45
 Y-view: 0.00
 Zoom: 25.00

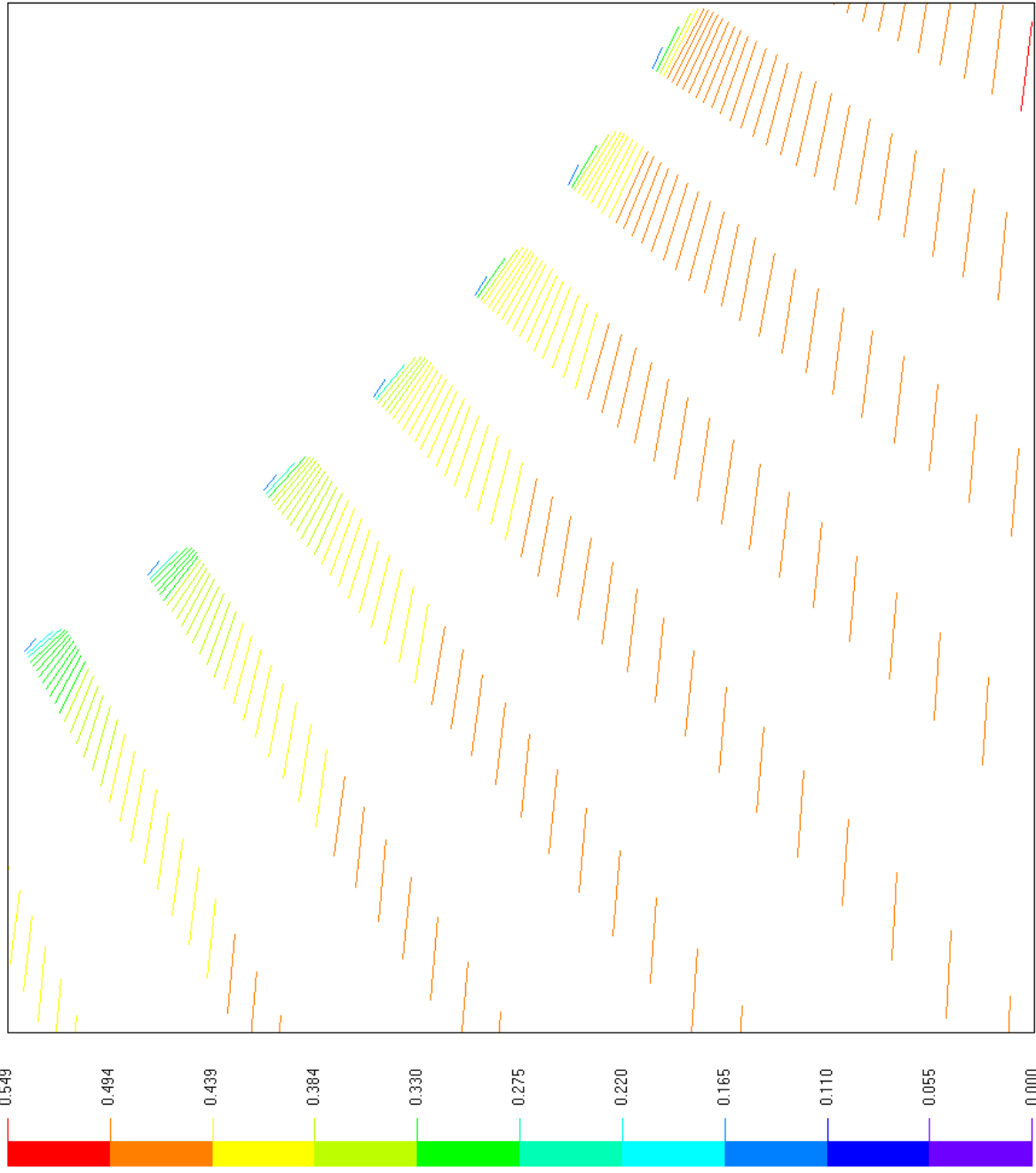


Side View: Mach Number

Mach #

Test ID: ELL000.tst
 Mesh Resolution: 60 x 40 x 80
 Spin Ratio: SR = 0.00
 Reynolds Number: Re = 3.00E4
 Mach Number: M = 0.50
 Diameter (m): D = 0.010
 Angle of Attack (deg): $\alpha = 5$
 Static Pressure (hPa): P = 270
 Static Temperature (K): T = 296
 Gas Constant (J/kgK): R = 287
 Specific Heats Ratio: k = 1.40
 Run Time (s): t = 0.001000
 Time Step (ms): dt = 0.025
 Stop Time (s): T = 0.001000
 Drag Coefficient: Cd = 0.054
 Lift Coefficient: Cl = 0.115
 Left Coefficient: Ce = 0.000
 Lift-to-Drag Ratio: L/D = 2.133
 X-view: -0.55
 Y-view: -0.15
 Zoom: 25.00





Top View: Mach Number

Test ID: ELL000.tst
 Mesh Resolution: 60 x 40 x 80
 Spin Ratio: SR = 0.00
 Reynolds Number: Re = 3.00E4
 Mach Number: M = 0.50
 Diameter (m): D = 0.010
 Angle of Attack (deg): $\alpha = 5$
 Static Pressure (hPa): P = 270
 Static Temperature (K): T = 296
 Gas Constant (J/kgK): R = 287
 Specific Heats Ratio: $k = 1.40$
 Run Time (s): t = 0.001000
 Time Step (ms): dt = 0.025
 Stop Time (s): T = 0.001000
 Drag Coefficient: Cd = 0.054
 Lift Coefficient: Cl = 0.115
 Left Coefficient: Ce = 0.000
 Lift-to-Drag Ratio: L/D = 2.133
 X-view: -0.40
 Y-view: -0.38
 Zoom: 25.00

Test ID: ELL000.tst

Mesh Resolution: 60 x 40 x 80

Spin Ratio: SR = 0.00

Reynolds Number: Re = 3.00E4

Mach Number: M = 0.50

Diameter (m): D = 0.010

Angle of Attack (deg): $\alpha = 5$

Static Pressure (hPa): P = 270

Static Temperature (K): T = 296

Gas Constant (J/kgK): R = 287

Specific Heats Ratio: k = 1.40

Run Time (s): t = 0.001000

Time Step (ms): dt = 0.025

Stop Time (s): T = 0.001000

Drag Coefficient: Cd = 0.054

Lift Coefficient: Cl = 0.115

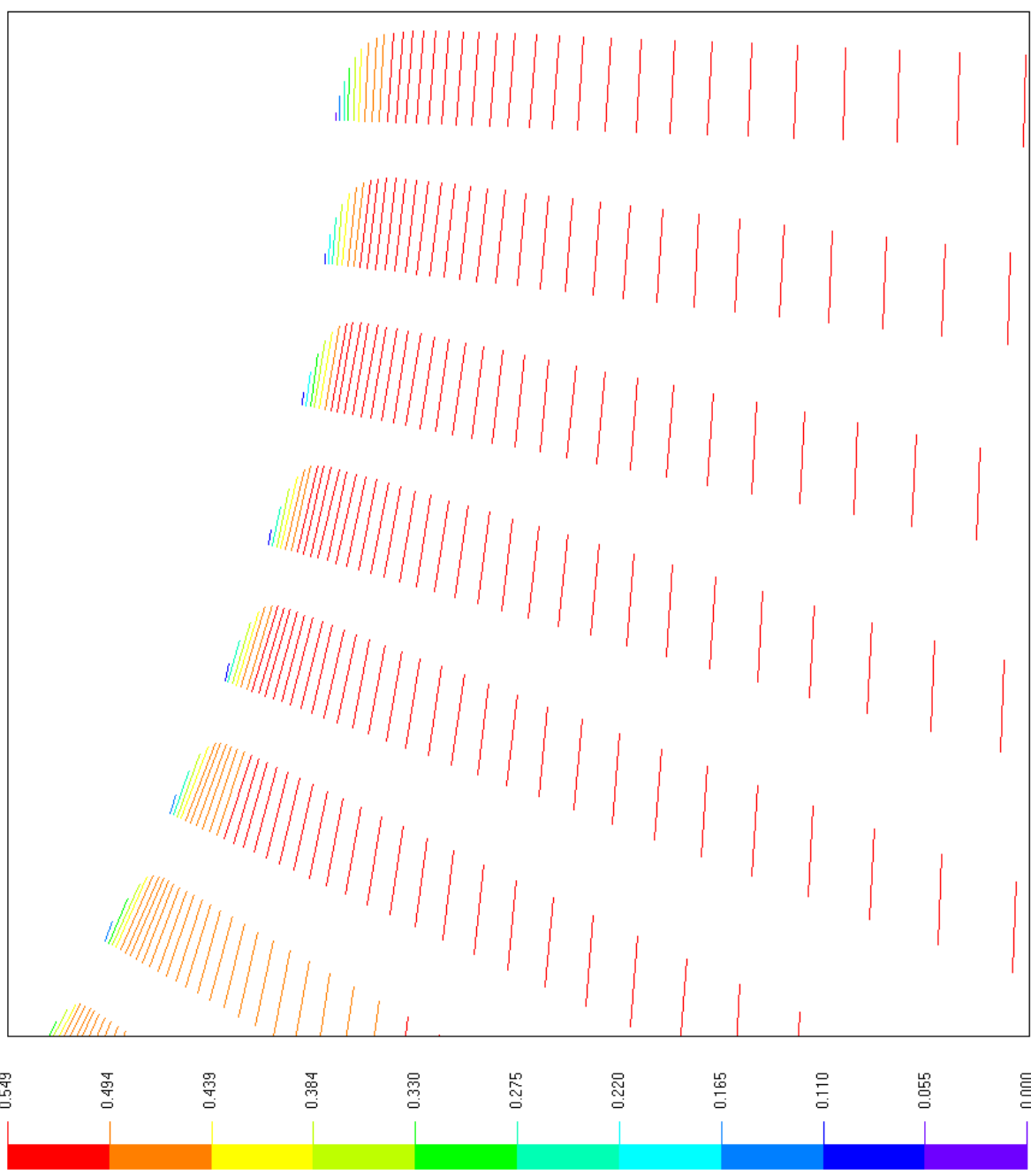
Left Coefficient: Ce = 0.000

Lift-to-Drag Ratio: L/D = 2.133

X-view: -0.13

Y-view: -0.55

Zoom: 25.00



Test ID: ELL000.tst

Mesh Resolution: 60 x 40 x 80

Spin Ratio: SR = 0.00

Reynolds Number: Re = 3.00E4

Mach Number: M = 0.50

Diameter (m): D = 0.010

Angle of Attack (deg): $\alpha = 5$

Static Pressure (hPa): P = 270

Static Temperature (K): T = 296

Gas Constant (J/kgK): R = 287

Specific Heats Ratio: k = 1.40

Run Time (s): t = 0.001000

Time Step (ms): dt = 0.025

Stop Time (s): T = 0.001000

Drag Coefficient: Cd = 0.054

Lift Coefficient: Cl = 0.115

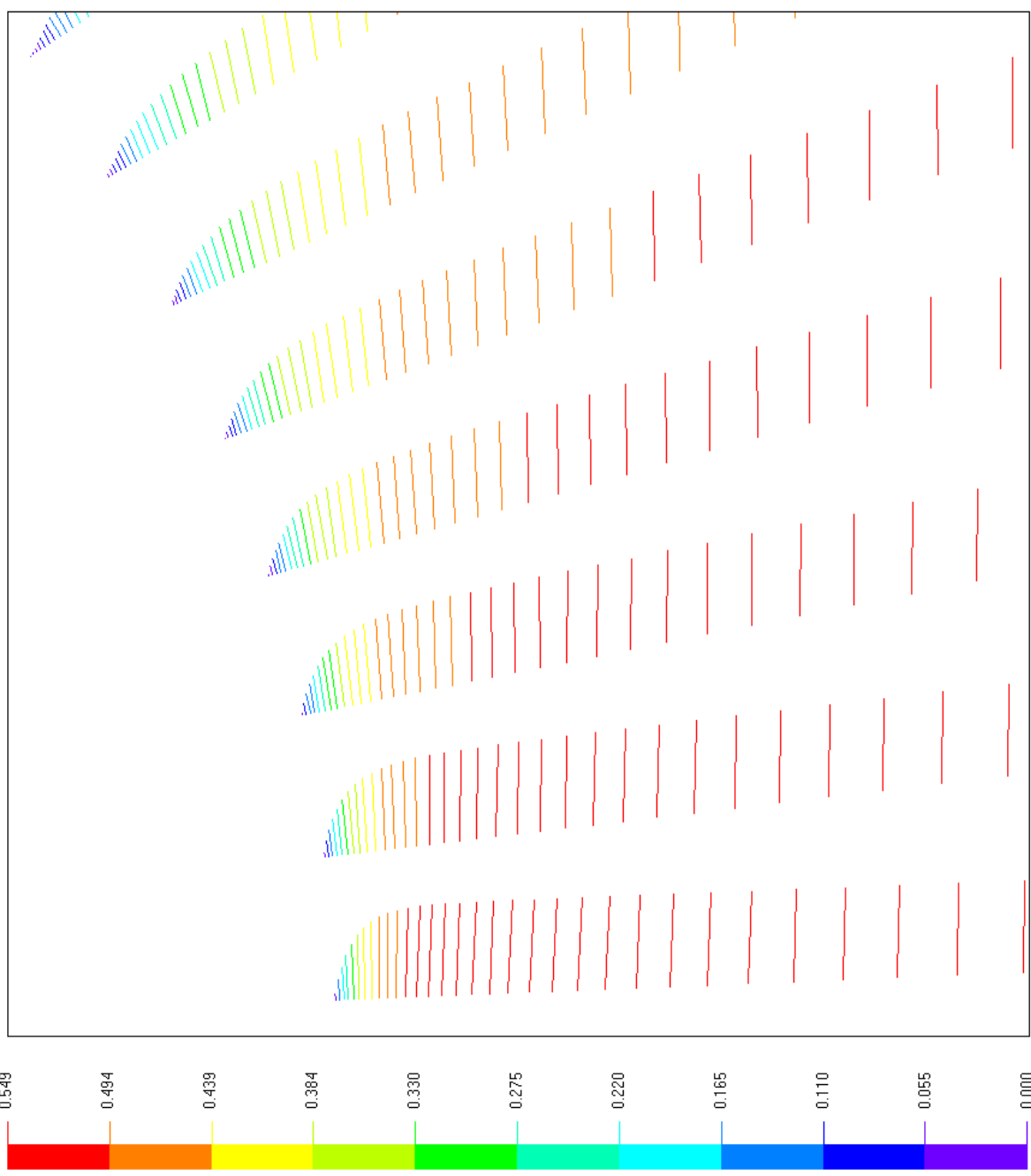
Left Coefficient: Ce = 0.000

Lift-to-Drag Ratio: L/D = 2.133

X-view: 0.15

Y-view: -0.55

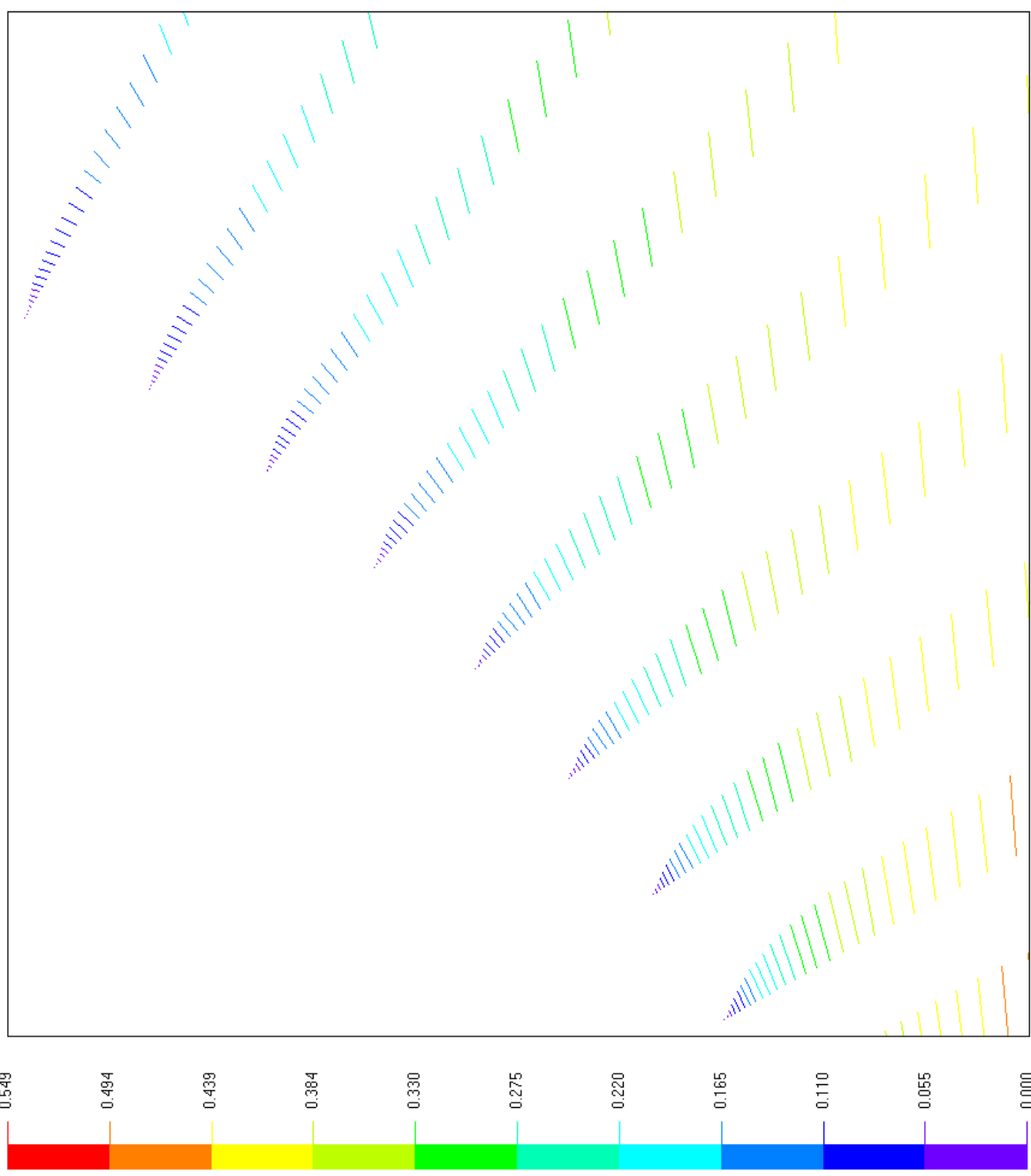
Zoom: 25.00



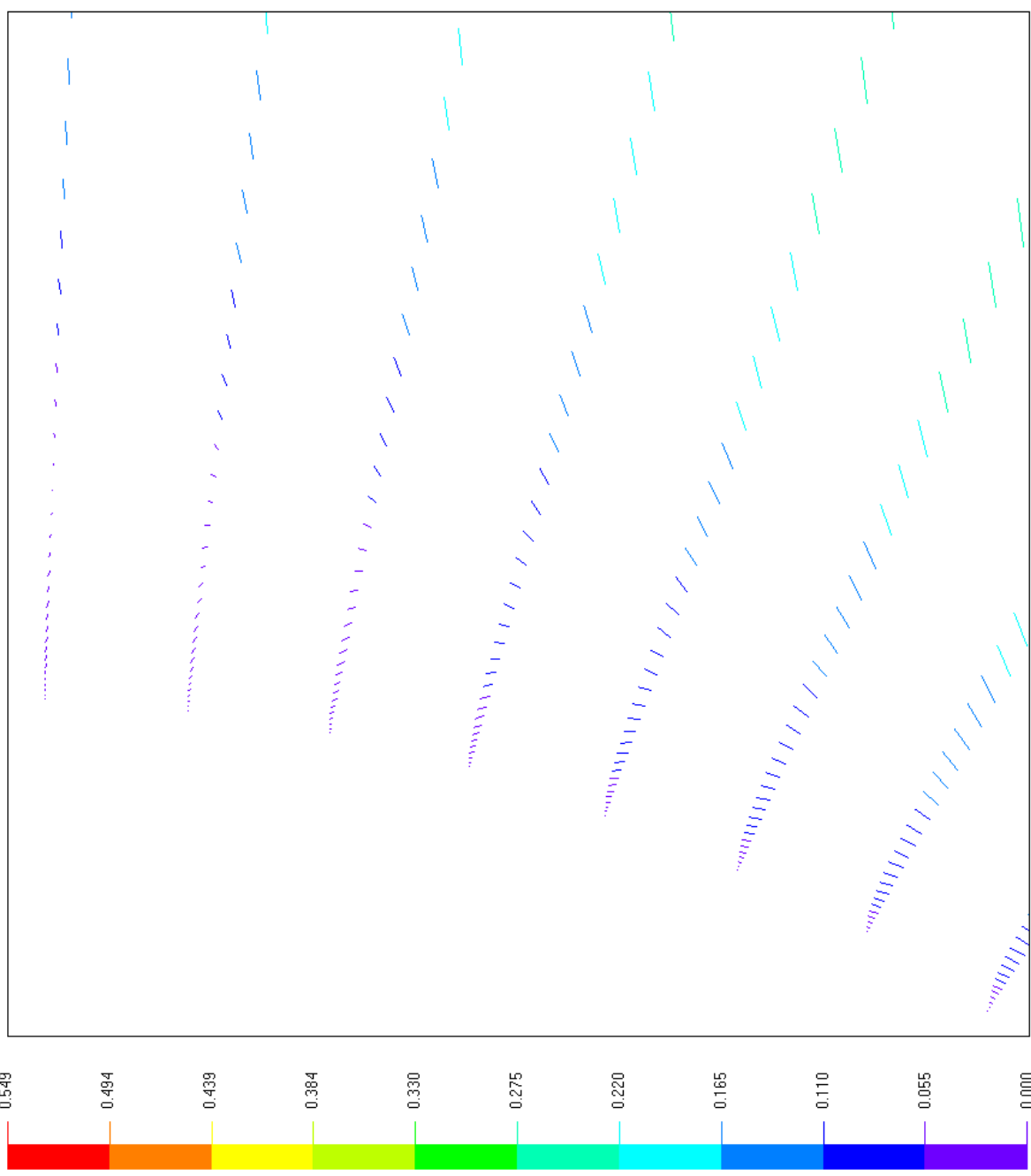
Top View: Mach Number

Mach #

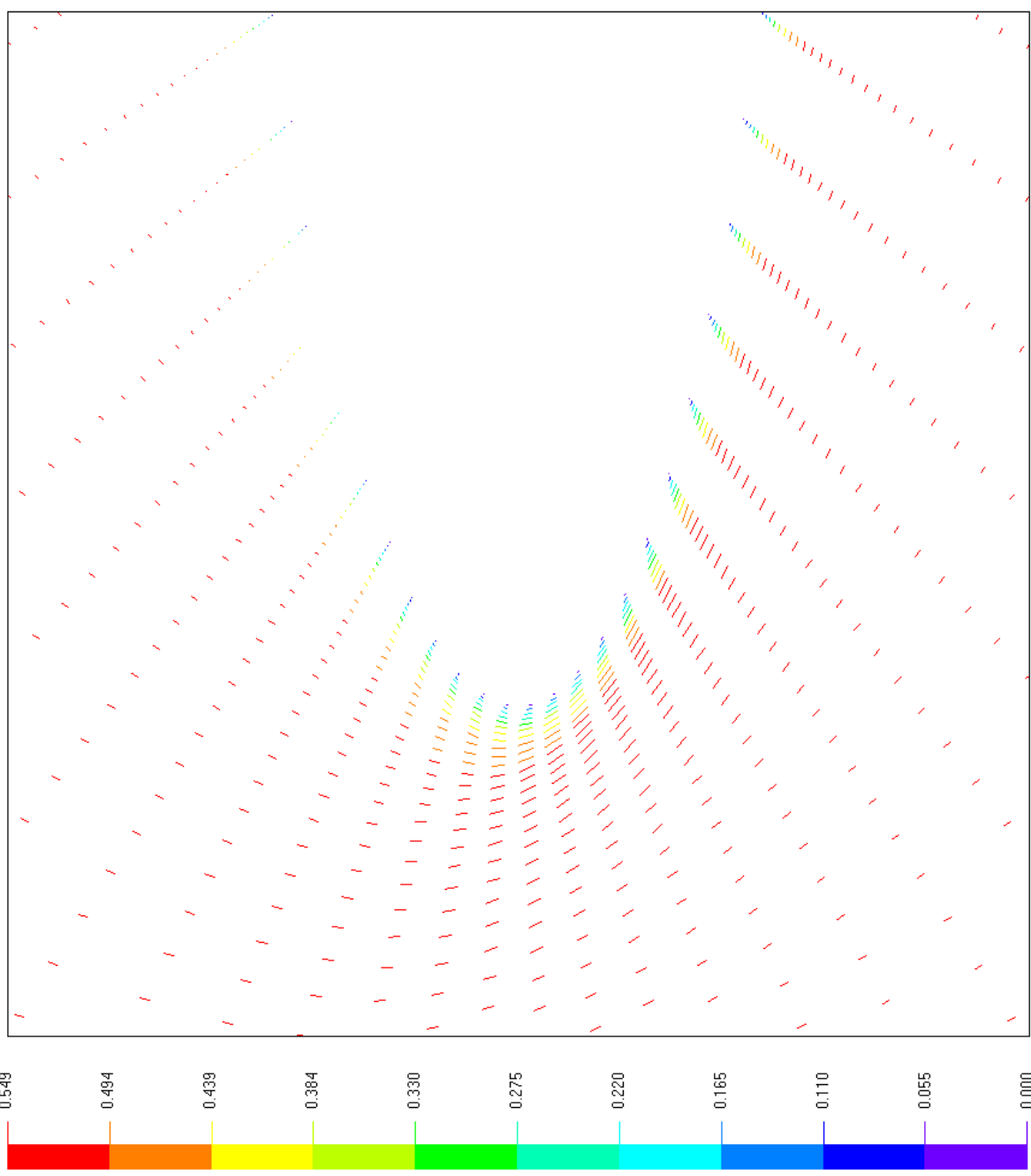
Test ID: ELL000.tst
 Mesh Resolution: 60 x 40 x 80
 Spin Ratio: SR = 0.00
 Reynolds Number: Re = 3.00E4
 Mach Number: M = 0.50
 Diameter (m): D = 0.010
 Angle of Attack (deg): $\alpha = 5$
 Static Pressure (hPa): P = 270
 Static Temperature (K): T = 296
 Gas Constant (J/kgK): R = 287
 Specific Heats Ratio: k = 1.40
 Run Time (s): t = 0.001000
 Time Step (ms): dt = 0.025
 Stop Time (s): T = 0.001000
 Drag Coefficient: Cd = 0.054
 Lift Coefficient: Cl = 0.115
 Left Coefficient: Ce = 0.000
 Lift-to-Drag Ratio: L/D = 2.133
 X-view: 0.38
 Y-view: -0.38
 Zoom: 25.00

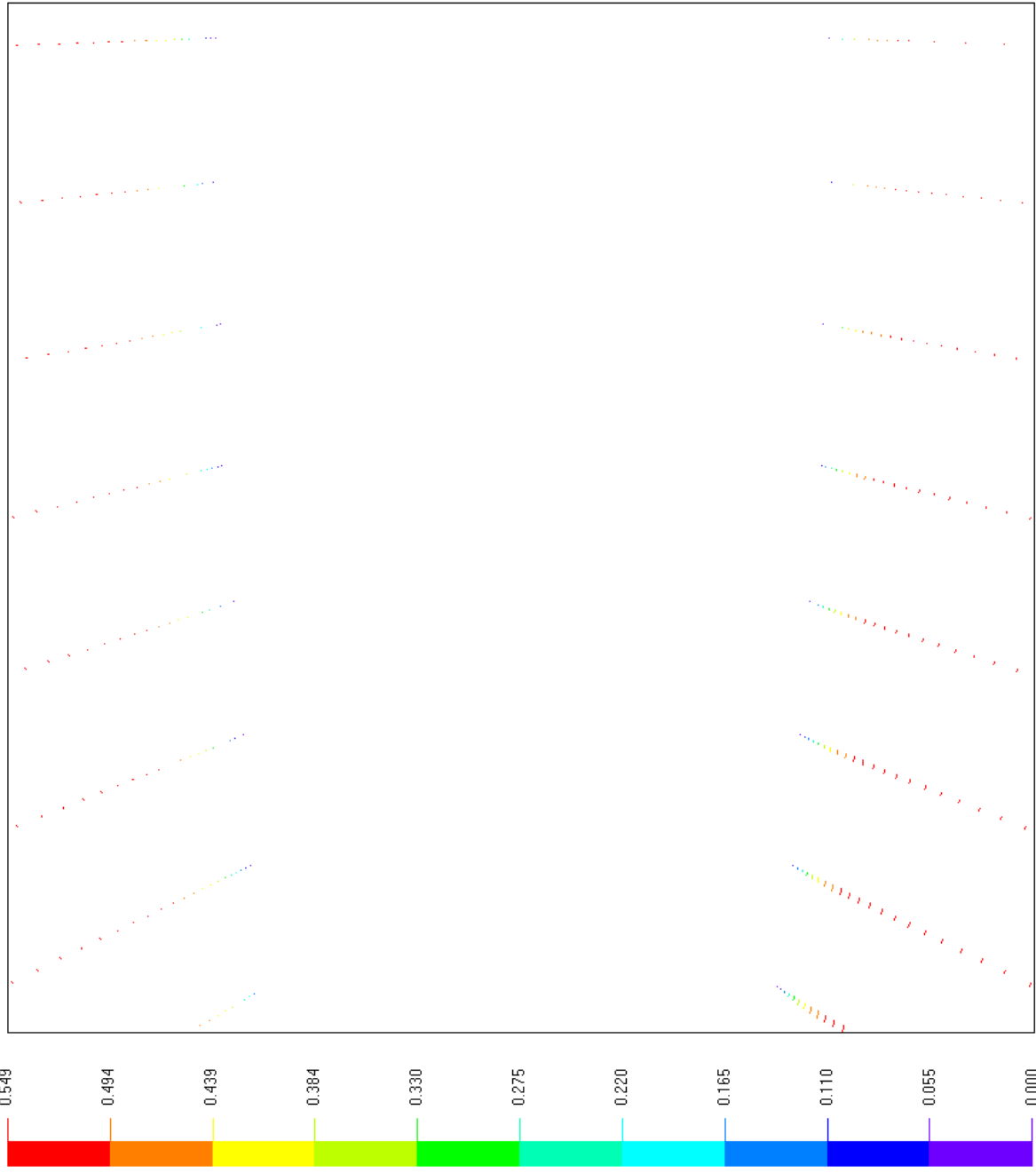


Test ID: ELL000.tst
 Mesh Resolution: 60 x 40 x 80
 Spin Ratio: SR = 0.00
 Reynolds Number: Re = 3.00E4
 Mach Number: M = 0.50
 Diameter (m): D = 0.010
 Angle of Attack (deg): $\alpha = 5$
 Static Pressure (hPa): P = 270
 Static Temperature (K): T = 296
 Gas Constant (J/kgK): R = 287
 Specific Heats Ratio: k = 1.40
 Run Time (s): t = 0.001000
 Time Step (ms): dt = 0.025
 Stop Time (s): T = 0.001000
 Drag Coefficient: Cd = 0.054
 Lift Coefficient: Cl = 0.115
 Left Coefficient: Ce = 0.000
 Lift-to-Drag Ratio: L/D = 2.133
 X-view: 0.55
 Y-view: -0.15
 Zoom: 25.00



Test ID: ELL000.tst
 Mesh Resolution: 60 x 40 x 80
 Spin Ratio: SR = 0.00
 Reynolds Number: Re = 3.00E4
 Mach Number: M = 0.50
 Diameter (m): D = 0.010
 Angle of Attack (deg): $\alpha = 5$
 Static Pressure (hPa): P = 270
 Static Temperature (K): T = 296
 Gas Constant (J/kgK): R = 287
 Specific Heats Ratio: k = 1.40
 Run Time (s): t = 0.001000
 Time Step (ms): dt = 0.025
 Stop Time (s): T = 0.001000
 Drag Coefficient: Cd = 0.054
 Lift Coefficient: Cl = 0.115
 Left Coefficient: Ce = 0.000
 Lift-to-Drag Ratio: L/D = 2.133
 X-view: -0.45
 Y-view: 0.00
 Zoom: 25.00





Front View: Mach Number

Test ID: ELL000.tst
 Mesh Resolution: 60 x 40 x 80
 Spin Ratio: SR = 0.00
 Reynolds Number: Re = 3.00E4
 Mach Number: M = 0.50
 Diameter (m): D = 0.010
 Angle of Attack (deg): $\alpha = 5$
 Static Pressure (hPa): P = 270
 Static Temperature (K): T = 296
 Gas Constant (J/kgK): R = 287
 Specific Heats Ratio: $k = 1.40$
 Run Time (s): $t = 0.001000$
 Time Step (ms): dt = 0.025
 Stop Time (s): T = 0.001000
 Drag Coefficient: Cd = 0.054
 Lift Coefficient: Cl = 0.115
 Left Coefficient: Ce = 0.000
 Lift-to-Drag Ratio: L/D = 2.133
 X-view: -0.15
 Y-view: 0.00
 Zoom: 25.00

Test ID: ELL000.tst

Mesh Resolution: 60 x 40 x 80

Spin Ratio: SR = 0.00

Reynolds Number: Re = 3.00E4

Mach Number: M = 0.50

Diameter (m): D = 0.010

Angle of Attack (deg): $\alpha = 5$

Static Pressure (hPa): P = 270

Static Temperature (K): T = 296

Gas Constant (J/kgK): R = 287

Specific Heats Ratio: k = 1.40

Run Time (s): t = 0.001000

Time Step (ms): dt = 0.025

Stop Time (s): T = 0.001000

Drag Coefficient: Cd = 0.054

Lift Coefficient: Cl = 0.115

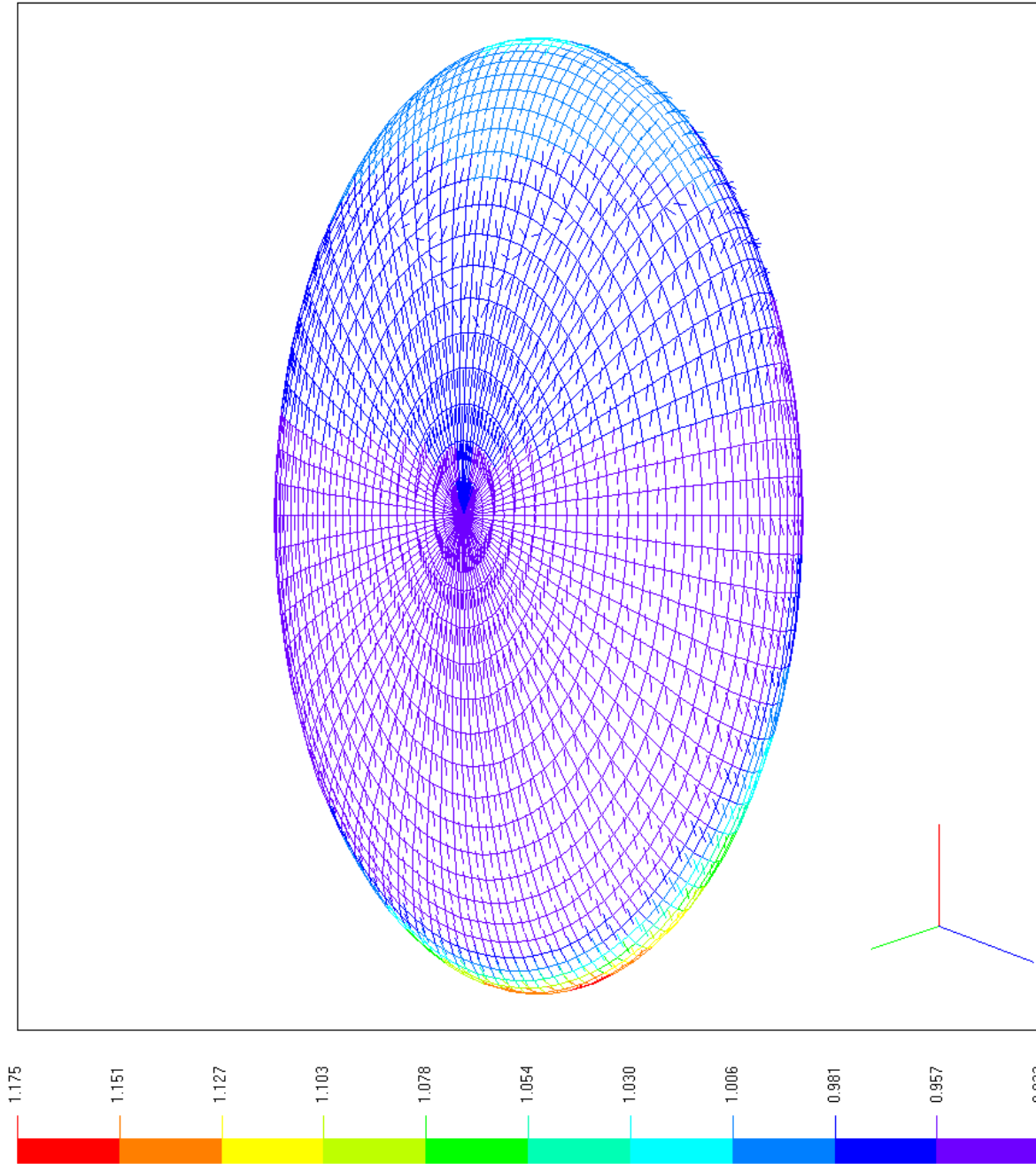
Left Coefficient: Ce = 0.000

Lift-to-Drag Ratio: L/D = 2.133

X-view: 0.00

Y-view: 0.00

Zoom: 1.00



Test ID: ELL000.tst

Mesh Resolution: 60 x 40 x 80

Spin Ratio: SR = 0.00

Reynolds Number: Re = 3.00E4

Mach Number: M = 0.50

Diameter (m): D = 0.010

Angle of Attack (deg): $\alpha = 5$

Static Pressure (hPa): P = 270

Static Temperature (K): T = 296

Gas Constant (J/kgK): R = 287

Specific Heats Ratio: k = 1.40

Run Time (s): t = 0.001000

Time Step (ms): dt = 0.025

Stop Time (s): T = 0.001000

Drag Coefficient: Cd = 0.054

Lift Coefficient: Cl = 0.115

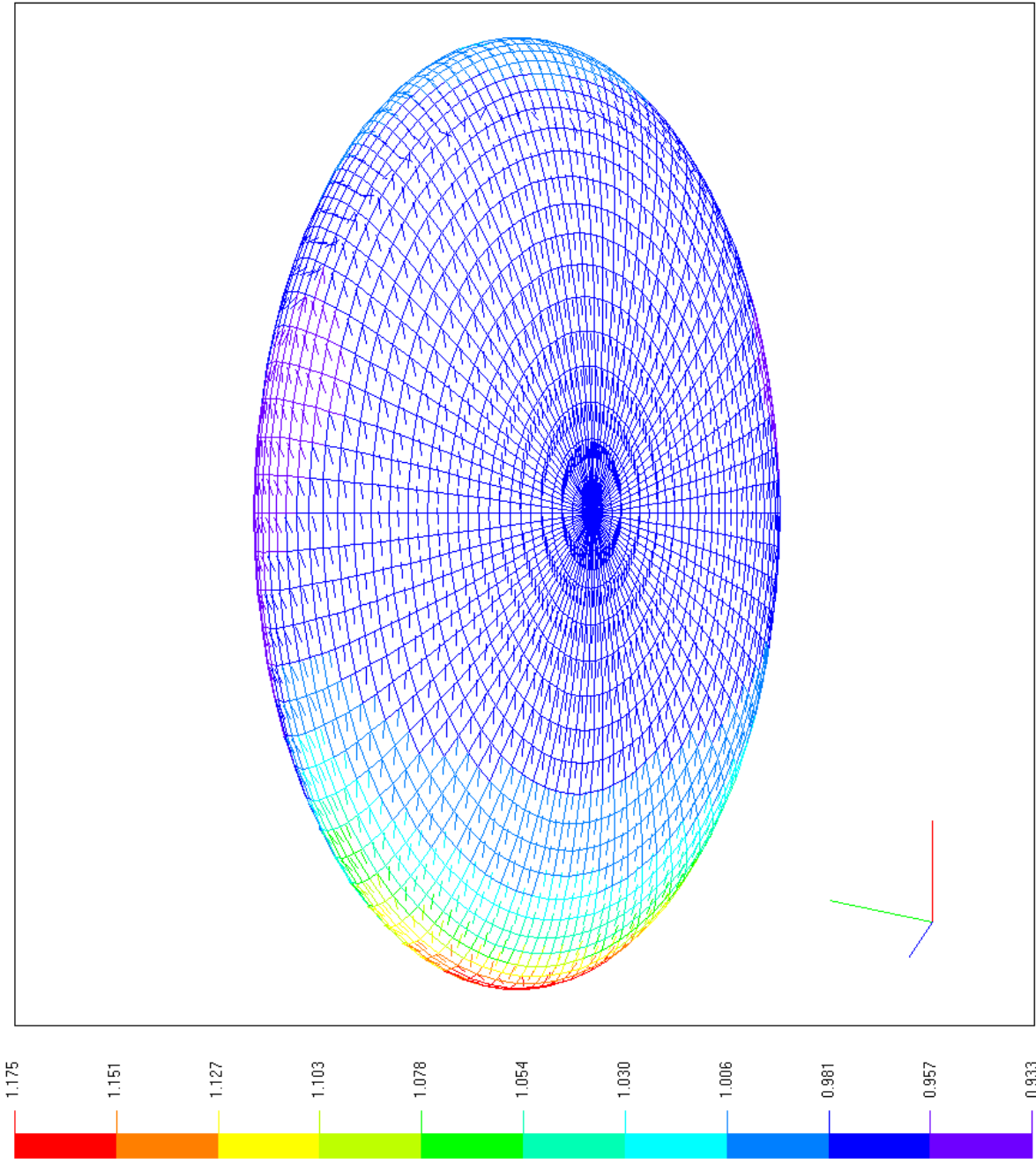
Left Coefficient: Ce = 0.000

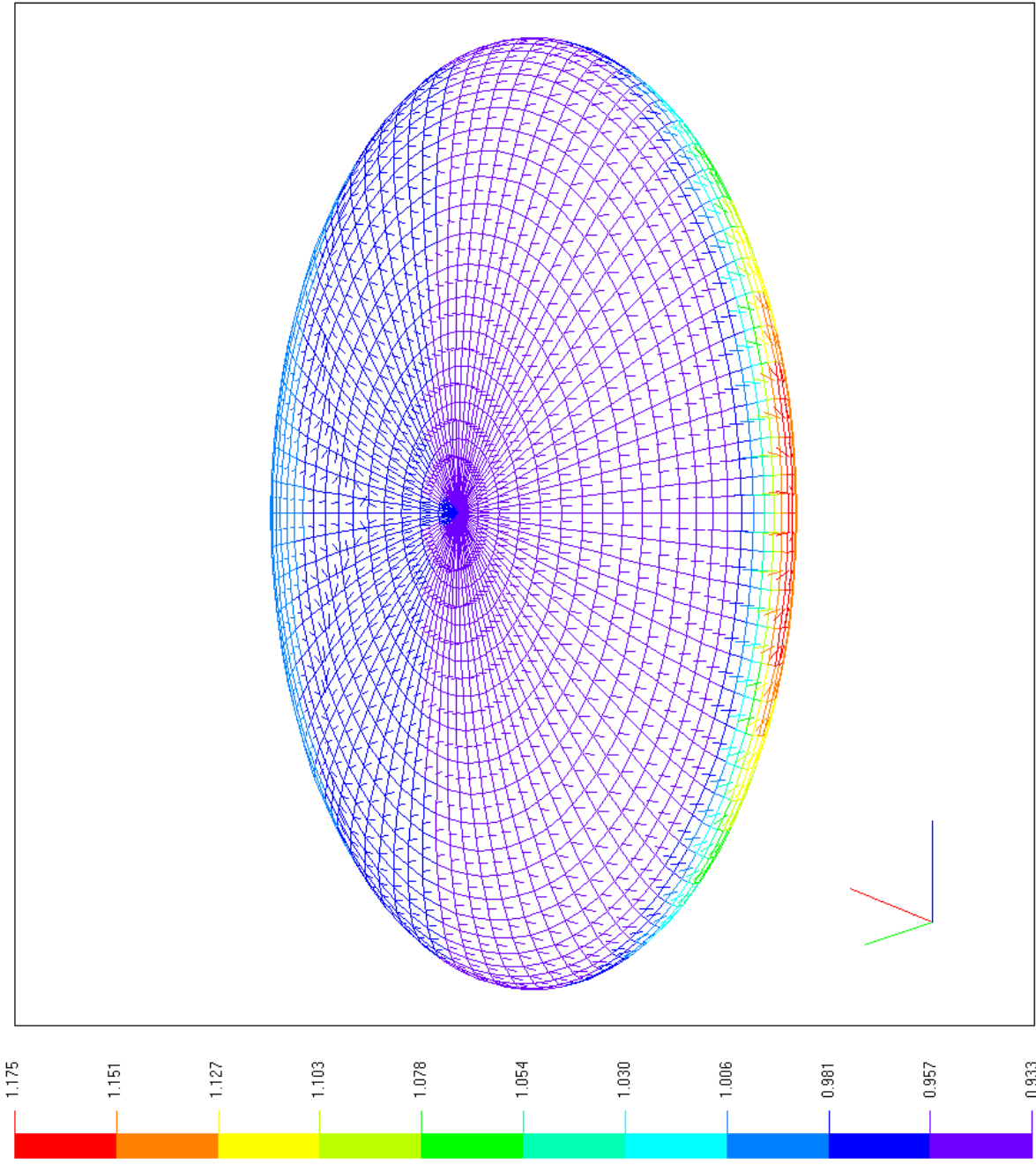
Lift-to-Drag Ratio: L/D = 2.133

X-view: 0.00

Y-view: 0.00

Zoom: 1.00





Test ID: ELL000.tst

Mesh Resolution: 60 x 40 x 80

Spin Ratio: SR = 0.00

Reynolds Number: Re = 3.00E4

Mach Number: M = 0.50

Diameter (m): D = 0.010

Angle of Attack (deg): $\alpha = 5$

Static Pressure (hPa): P = 270

Static Temperature (K): T = 296

Gas Constant (J/kgK): R = 287

Specific Heats Ratio: k = 1.40

Run Time (s): t = 0.001000

Time Step (ms): dt = 0.025

Stop Time (s): T = 0.001000

Drag Coefficient: Cd = 0.054

Lift Coefficient: Cl = 0.115

Left Coefficient: Ce = 0.000

Lift-to-Drag Ratio: L/D = 2.133

X-view: 0.00

Y-view: 0.00

Zoom: 1.00

Test ID: ELL000.tst

Mesh Resolution: 60 x 40 x 80

Spin Ratio: SR = 0.00

Reynolds Number: Re = 3.00E4

Mach Number: M = 0.50

Diameter (m): D = 0.010

Angle of Attack (deg): $\alpha = 5$

Static Pressure (hPa): P = 270

Static Temperature (K): T = 296

Gas Constant (J/kgK): R = 287

Specific Heats Ratio: k = 1.40

Run Time (s): t = 0.001000

Time Step (ms): dt = 0.025

Stop Time (s): T = 0.001000

Drag Coefficient: Cd = 0.054

Lift Coefficient: Cl = 0.115

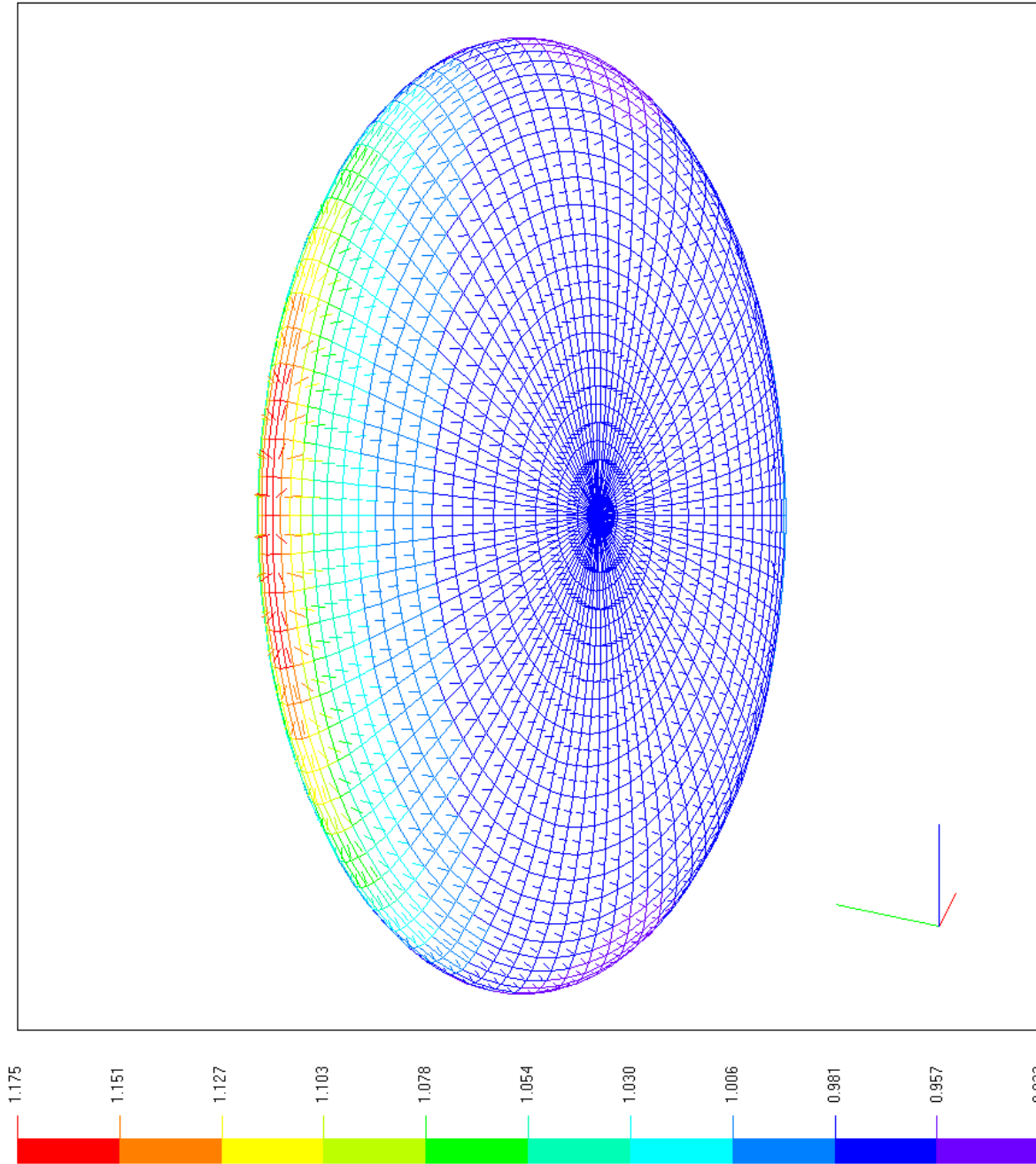
Left Coefficient: Ce = 0.000

Lift-to-Drag Ratio: L/D = 2.133

X-view: 0.00

Y-view: 0.00

Zoom: 1.00



Test ID: ELL000.tst

Mesh Resolution: 60 x 40 x 80

Spin Ratio: SR = 0.00

Reynolds Number: Re = 3.00E4

Mach Number: M = 0.50

Diameter (m): D = 0.010

Angle of Attack (deg): $\alpha = 5$

Static Pressure (hPa): P = 270

Static Temperature (K): T = 296

Gas Constant (J/kgK): R = 287

Specific Heats Ratio: k = 1.40

Run Time (s): t = 0.001000

Time Step (ms): dt = 0.025

Stop Time (s): T = 0.001000

Drag Coefficient: Cd = 0.054

Lift Coefficient: Cl = 0.115

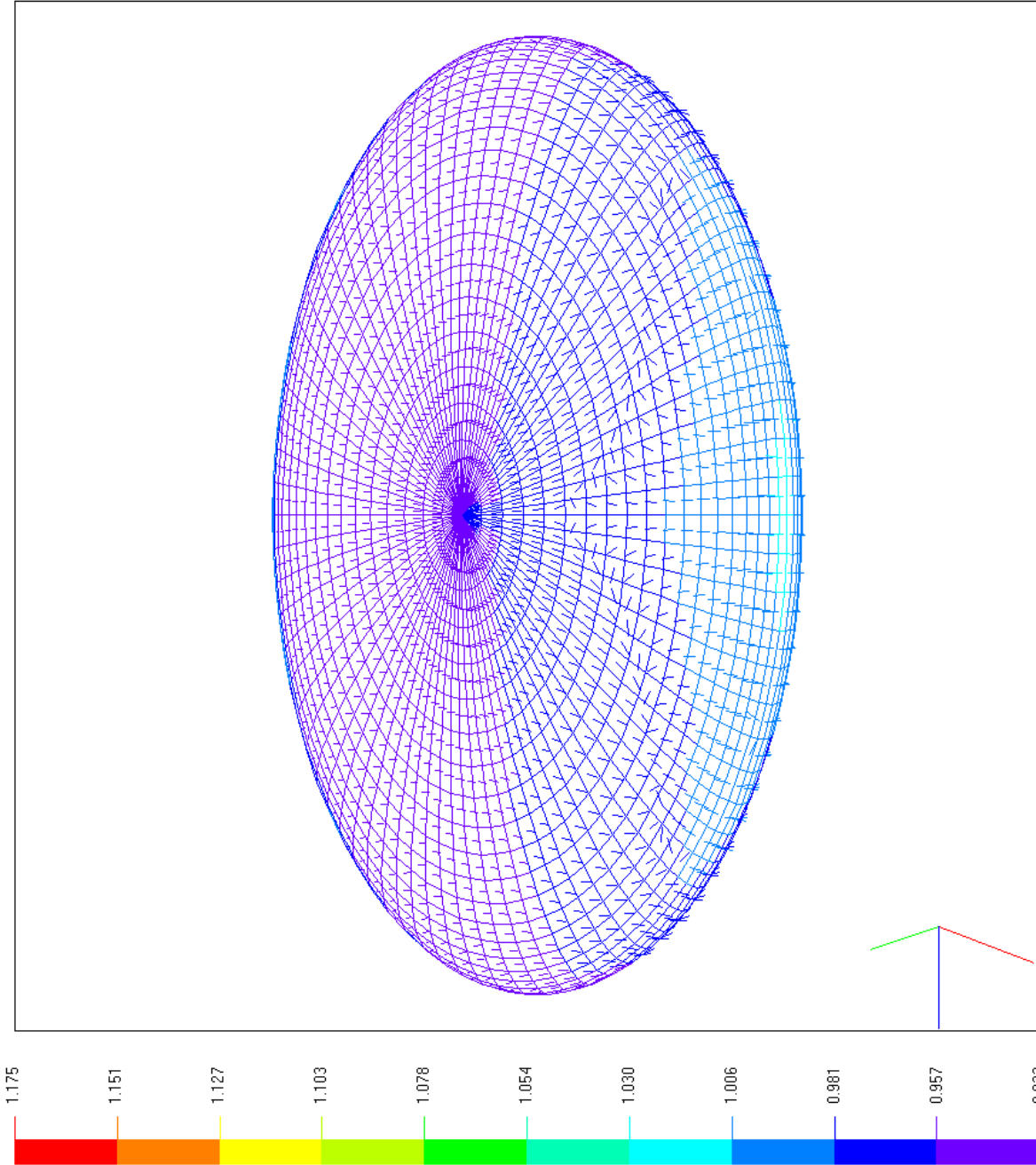
Left Coefficient: Ce = 0.000

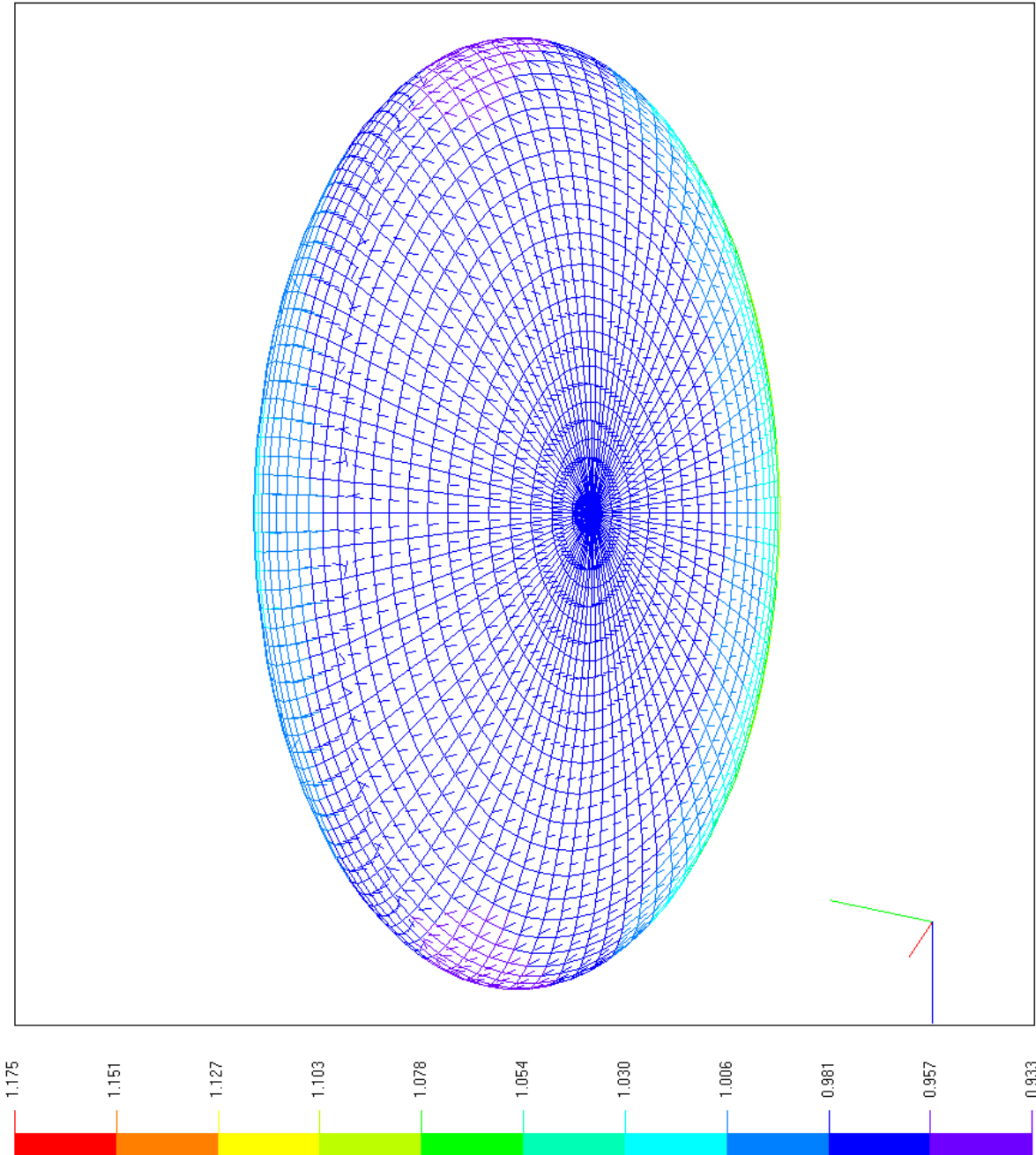
Lift-to-Drag Ratio: L/D = 2.133

X-view: 0.00

Y-view: 0.00

Zoom: 1.00





3D View: Pressure

Test ID: ELL000.tst

Mesh Resolution: 60 x 40 x 80

Spin Ratio: SR = 0.00

Reynolds Number: Re = 3.00E4

Mach Number: M = 0.50

Diameter (m): D = 0.010

Angle of Attack (deg): $\alpha = 5$

Static Pressure (hPa): P = 270

Static Temperature (K): T = 296

Gas Constant (J/kgK): R = 287

Specific Heats Ratio: k = 1.40

Run Time (s): t = 0.001000

Time Step (ms): dt = 0.025

Stop Time (s): T = 0.001000

Drag Coefficient: Cd = 0.054

Lift Coefficient: Cl = 0.115

Left Coefficient: Ce = 0.000

Lift-to-Drag Ratio: L/D = 2.133

X-view: 0.00

Y-view: 0.00

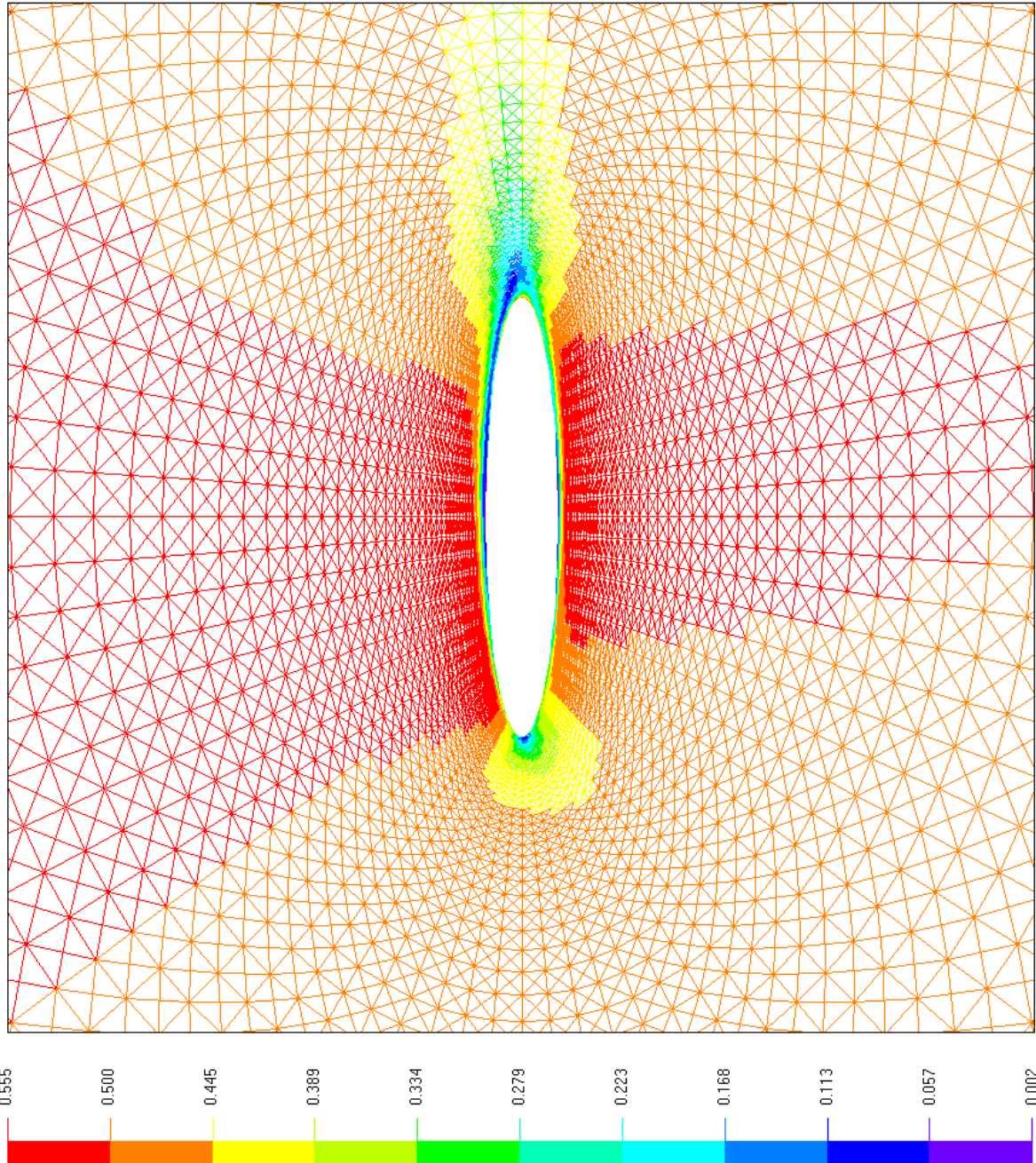
Zoom: 1.00

BLANK PAGE

APPENDIX B

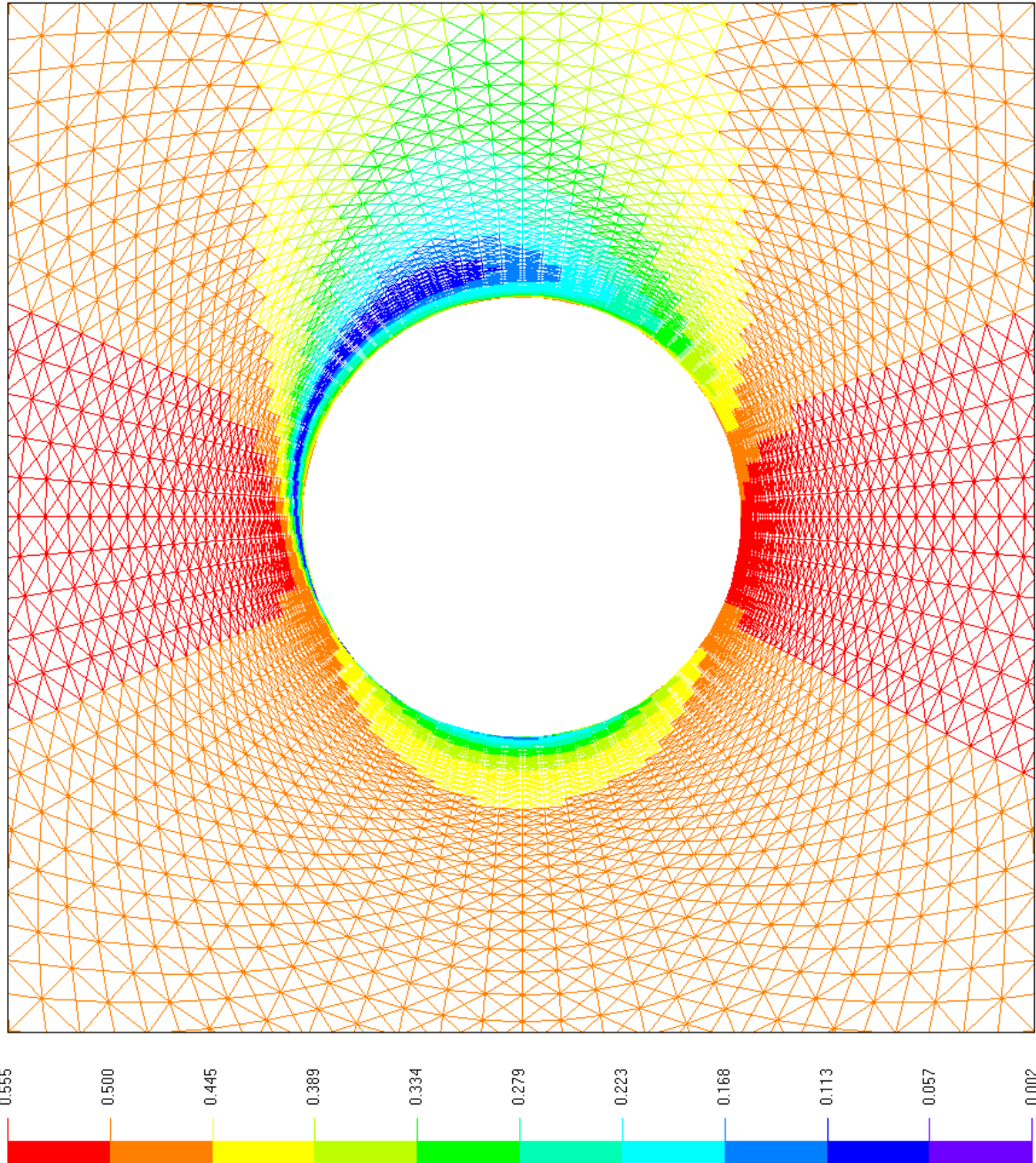
Computational Results for Equi-Rotational Disc

BLANK PAGE



Side View: Mach Number

Test ID: ELL100.tst
 Mesh Resolution: 60 x 40 x 80
 Spin Ratio: SR = 1.00
 Reynolds Number: Re = 3.00E4
 Mach Number: M = 0.50
 Diameter (m): D = 0.010
 Angle of Attack (deg): $\alpha = 5$
 Static Pressure (hPa): P = 270
 Static Temperature (K): T = 296
 Gas Constant (J/kgK): R = 287
 Specific Heats Ratio: k = 1.40
 Run Time (s): t = 0.001000
 Time Step (ms): dt = 0.025
 Stop Time (s): T = 0.001000
 Drag Coefficient: Cd = 0.059
 Lift Coefficient: Cl = 0.111
 Left Coefficient: Ce = 0.004
 Lift-to-Drag Ratio: L/D = 1.893
 X-view: 0.00
 Y-view: 0.00
 Zoom: 3.00

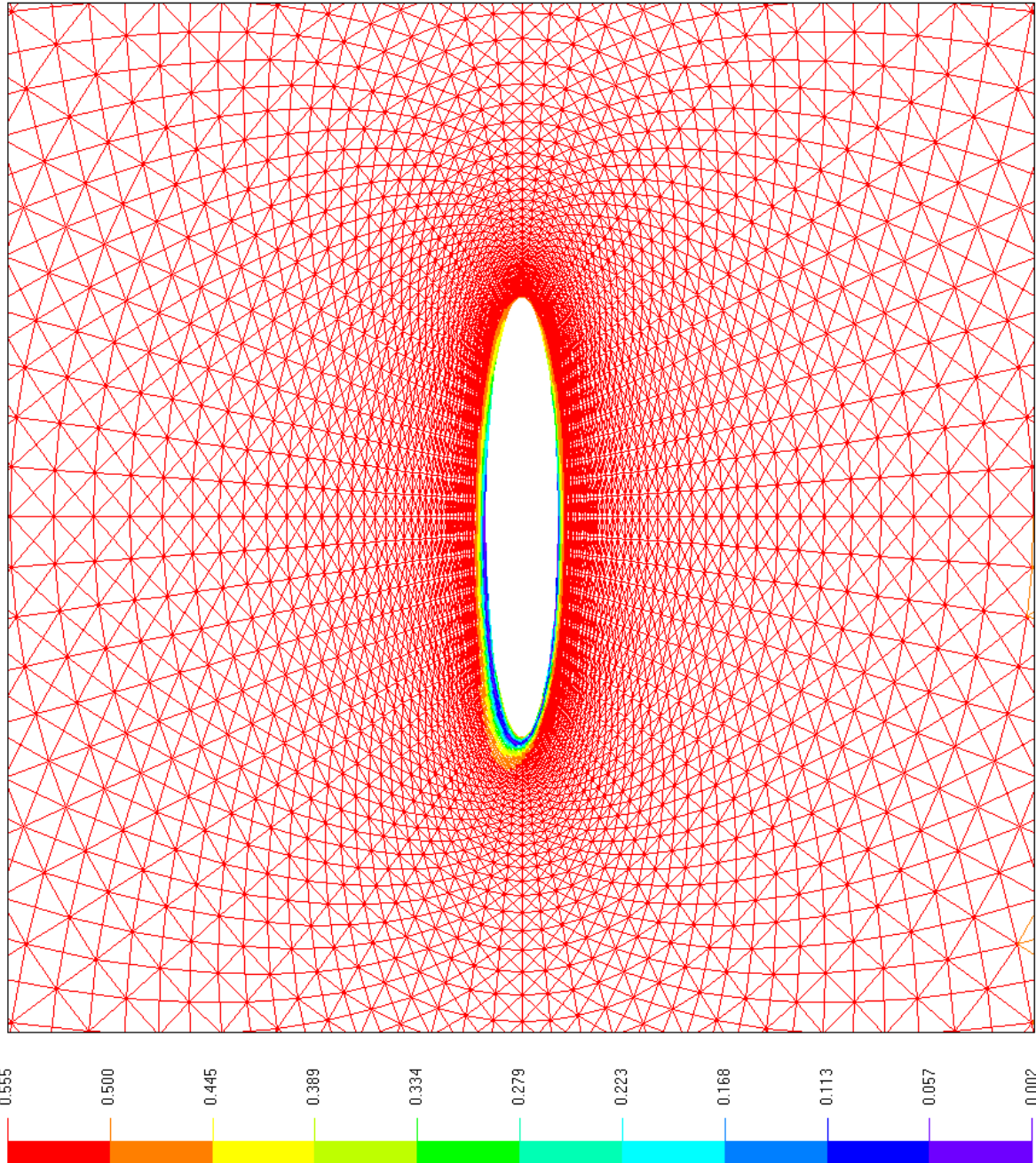


0.555
0.500
0.445
0.389
0.334
0.279
0.223
0.168
0.113
0.057
0.002

Mach #

Top View: Mach Number

Test ID: ELL100.tst
 Mesh Resolution: 60 x 40 x 80
 Spin Ratio: SR = 1.00
 Reynolds Number: Re = 3.00E4
 Mach Number: M = 0.50
 Diameter (m): D = 0.010
 Angle of Attack (deg): $\alpha = 5$
 Static Pressure (hPa): P = 270
 Static Temperature (K): T = 296
 Gas Constant (J/kgK): R = 287
 Specific Heats Ratio: k = 1.40
 Run Time (s): t = 0.001000
 Time Step (ms): dt = 0.025
 Stop Time (s): T = 0.001000
 Drag Coefficient: Cd = 0.059
 Lift Coefficient: Cl = 0.111
 Left Coefficient: Ce = 0.004
 Lift-to-Drag Ratio: L/D = 1.893
 X-view: 0.00
 Y-view: 0.00
 Zoom: 3.00



Test ID: ELL100.tst

Mesh Resolution: 60 x 40 x 80

Spin Ratio: SR = 1.00

Reynolds Number: Re = 3.00E4

Mach Number: M = 0.50

Diameter (m): D = 0.010

Angle of Attack (deg): $\alpha = 5$

Static Pressure (hPa): P = 270

Static Temperature (K): T = 296

Gas Constant (J/kgK): R = 287

Specific Heats Ratio: k = 1.40

Run Time (s): t = 0.001000

Time Step (ms): dt = 0.025

Stop Time (s): T = 0.001000

Drag Coefficient: Cd = 0.059

Lift Coefficient: Cl = 0.111

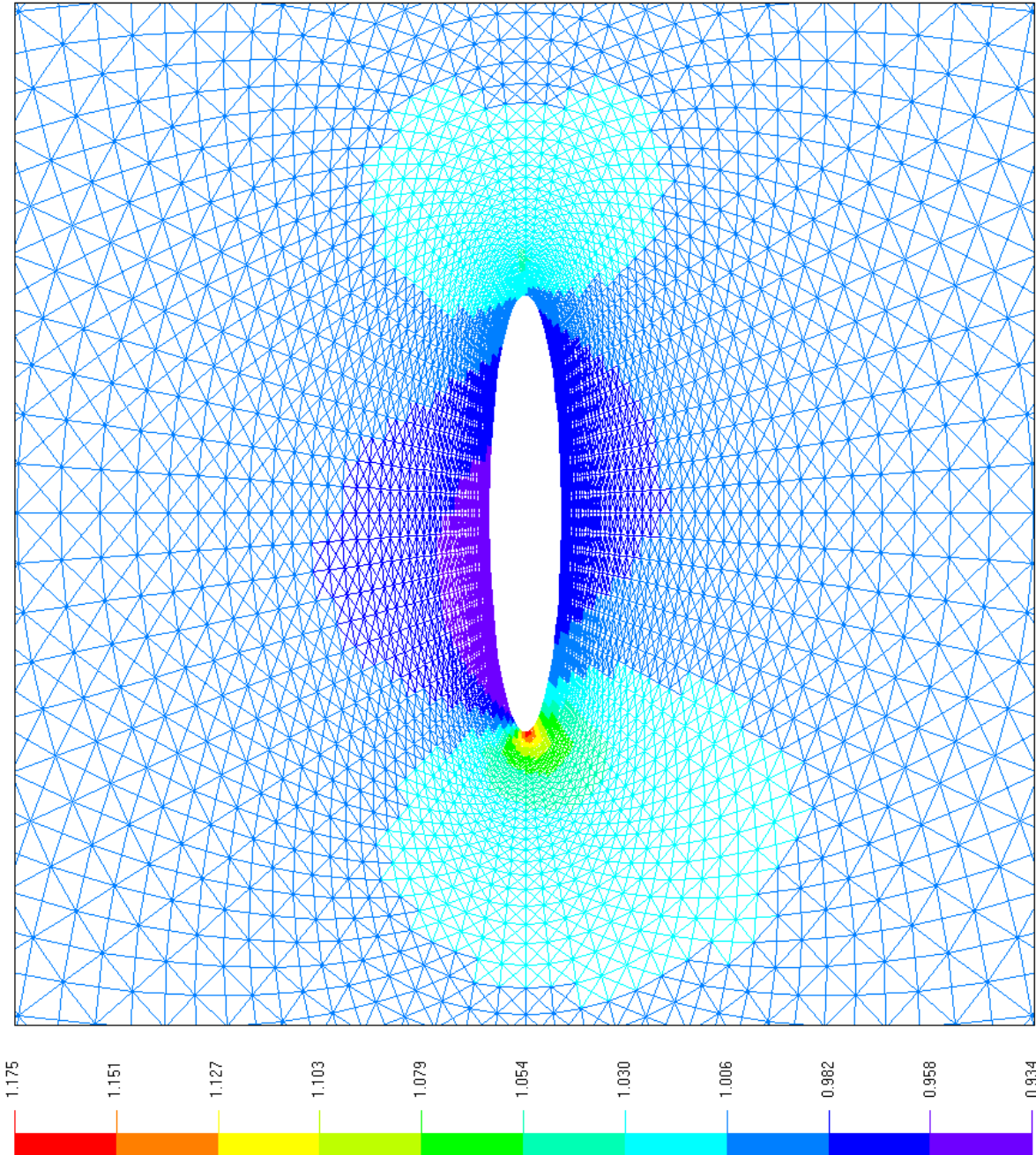
Left Coefficient: Ce = 0.004

Lift-to-Drag Ratio: L/D = 1.893

X-view: 0.00

Y-view: 0.00

Zoom: 3.00



Test ID: ELL100.tst
 Mesh Resolution: 60 x 40 x 80
 Spin Ratio: SR = 1.00
 Reynolds Number: Re = 3.00E4
 Mach Number: M = 0.50
 Diameter (m): D = 0.010
 Angle of Attack (deg): $\alpha = 5$
 Static Pressure (hPa): P = 270
 Static Temperature (K): T = 296
 Gas Constant (J/kgK): R = 287
 Specific Heats Ratio: k = 1.40
 Run Time (s): t = 0.001000
 Time Step (ms): dt = 0.025
 Stop Time (s): T = 0.001000
 Drag Coefficient: Cd = 0.059
 Lift Coefficient: Cl = 0.111
 Left Coefficient: Ce = 0.004
 Lift-to-Drag Ratio: L/D = 1.893
 X-view: 0.00
 Y-view: 0.00
 Zoom: 3.00

Test ID: ELL100.tst

Mesh Resolution: 60 x 40 x 80

Spin Ratio: SR = 1.00

Reynolds Number: Re = 3.00E4

Mach Number: M = 0.50

Diameter (m): D = 0.010

Angle of Attack (deg): $\alpha = 5$

Static Pressure (hPa): P = 270

Static Temperature (K): T = 296

Gas Constant (J/kgK): R = 287

Specific Heats Ratio: k = 1.40

Run Time (s): t = 0.001000

Time Step (ms): dt = 0.025

Stop Time (s): T = 0.001000

Drag Coefficient: Cd = 0.059

Lift Coefficient: Cl = 0.111

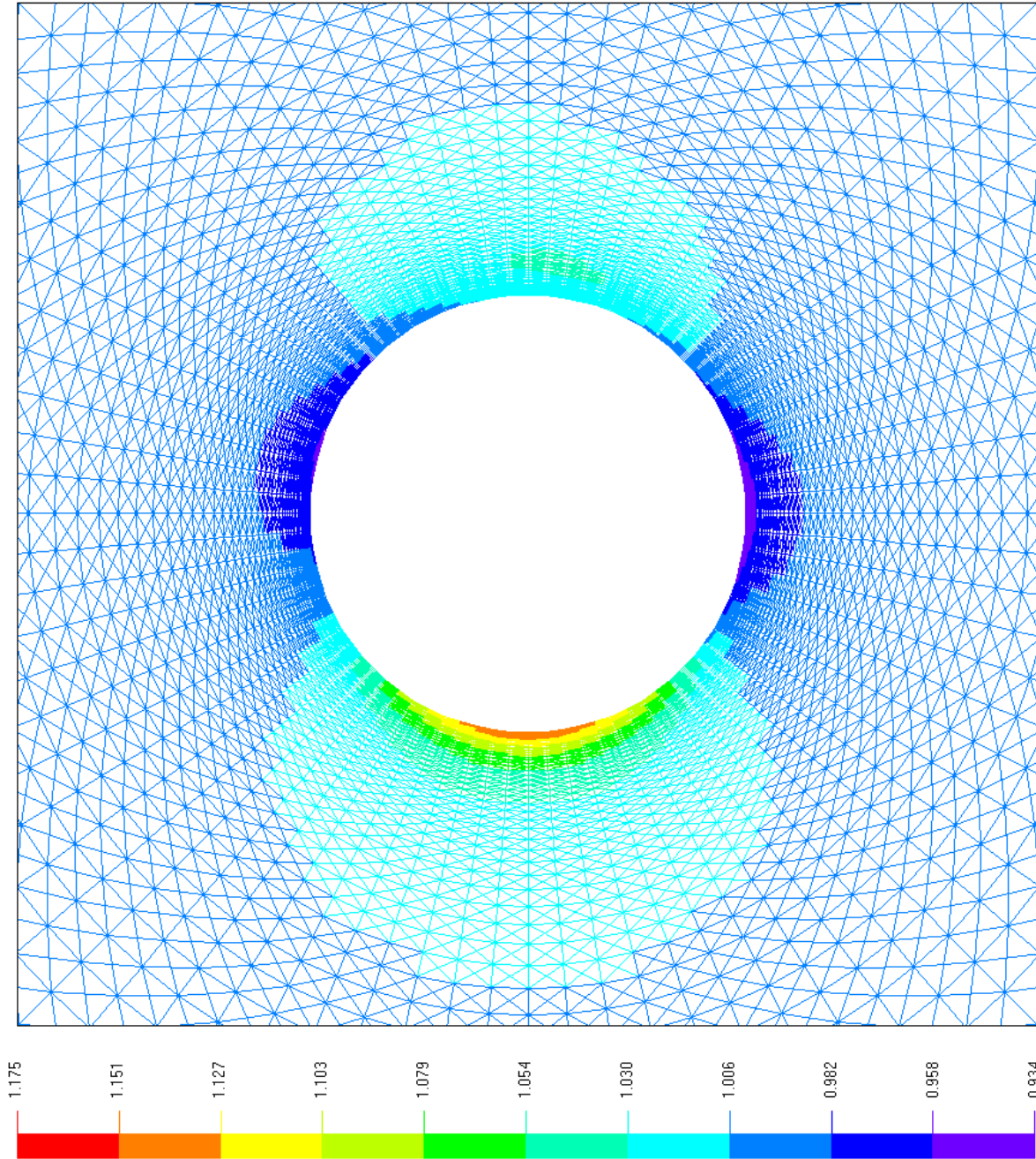
Left Coefficient: Ce = 0.004

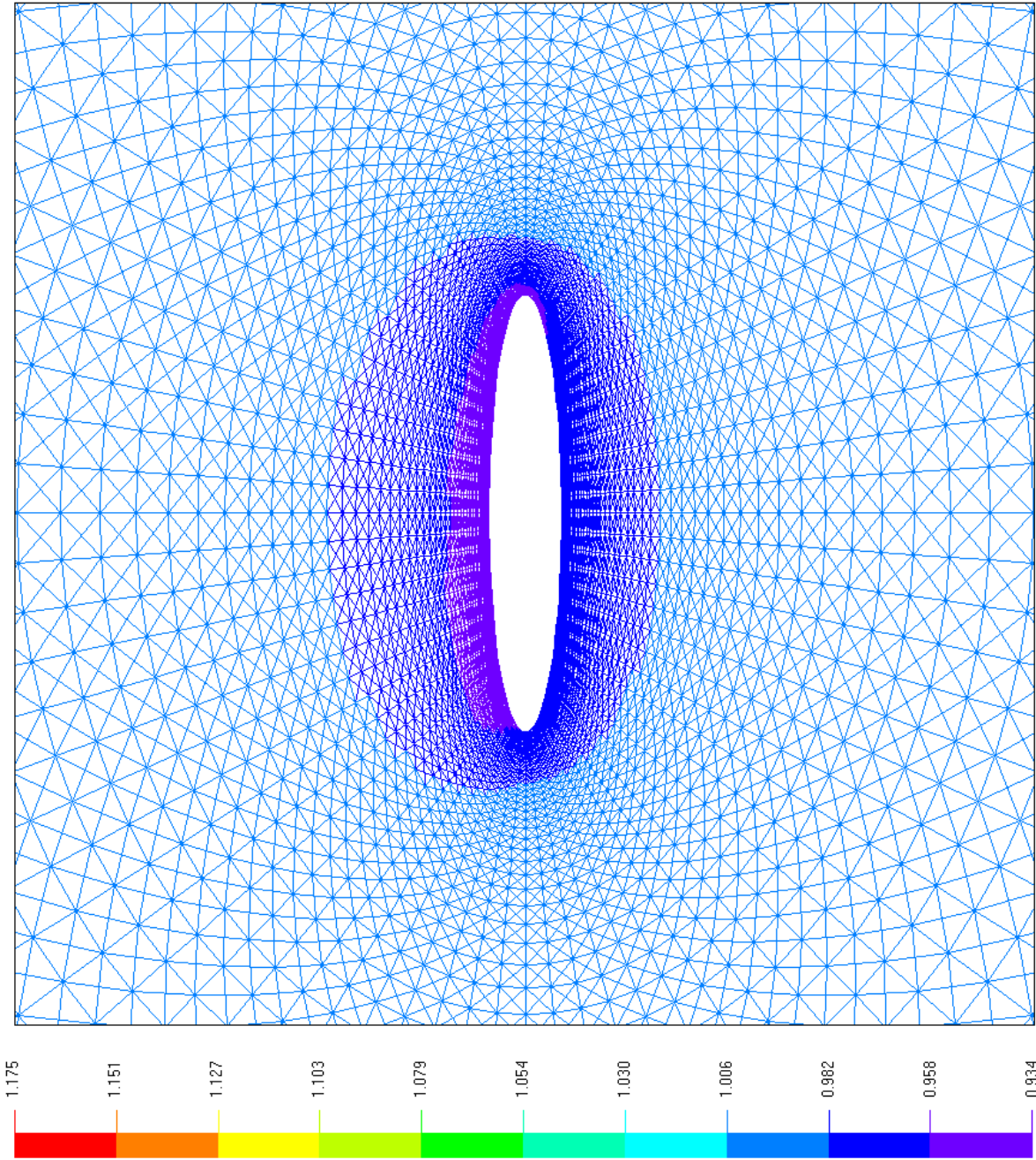
Lift-to-Drag Ratio: L/D = 1.893

X-view: 0.00

Y-view: 0.00

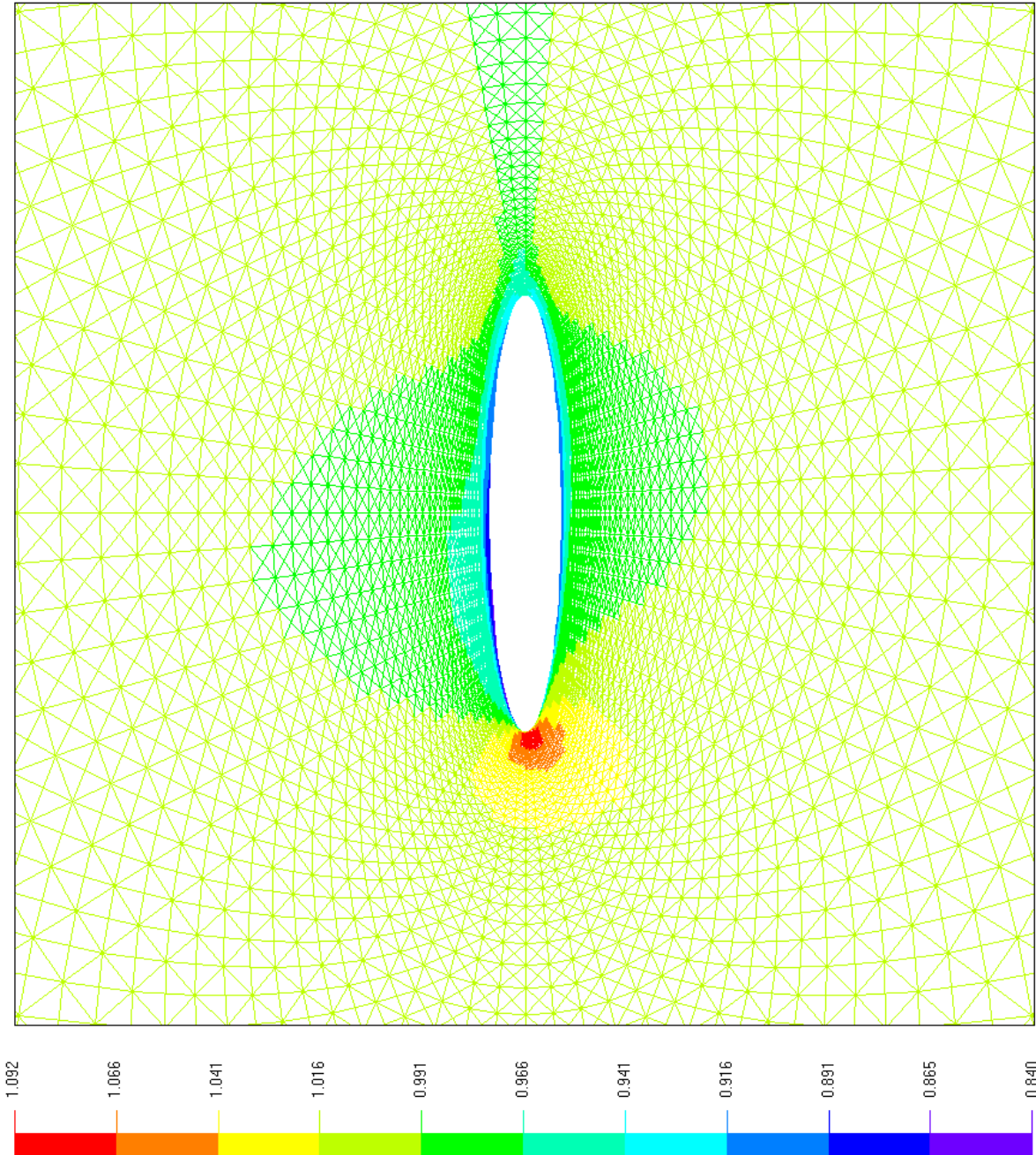
Zoom: 3.00





Front View: Pressure

Test ID: ELL100.tst
 Mesh Resolution: 60 x 40 x 80
 Spin Ratio: SR = 1.00
 Reynolds Number: Re = 3.00E4
 Mach Number: M = 0.50
 Diameter (m): D = 0.010
 Angle of Attack (deg): $\alpha = 5$
 Static Pressure (hPa): P = 270
 Static Temperature (K): T = 296
 Gas Constant (J/kgK): R = 287
 Specific Heats Ratio: k = 1.40
 Run Time (s): t = 0.001000
 Time Step (ms): dt = 0.025
 Stop Time (s): T = 0.001000
 Drag Coefficient: Cd = 0.059
 Lift Coefficient: Cl = 0.111
 Left Coefficient: Ce = 0.004
 Lift-to-Drag Ratio: L/D = 1.893
 X-view: 0.00
 Y-view: 0.00
 Zoom: 3.00



Test ID: ELL100.tst

Mesh Resolution: 60 x 40 x 80

Spin Ratio: SR = 1.00

Reynolds Number: Re = 3.00E4

Mach Number: M = 0.50

Diameter (m): D = 0.010

Angle of Attack (deg): $\alpha = 5$

Static Pressure (hPa): P = 270

Static Temperature (K): T = 296

Gas Constant (J/kgK): R = 287

Specific Heats Ratio: $k = 1.40$

Run Time (s): $t = 0.001000$

Time Step (ms): $dt = 0.025$

Stop Time (s): T = 0.001000

Drag Coefficient: Cd = 0.059

Lift Coefficient: Cl = 0.111

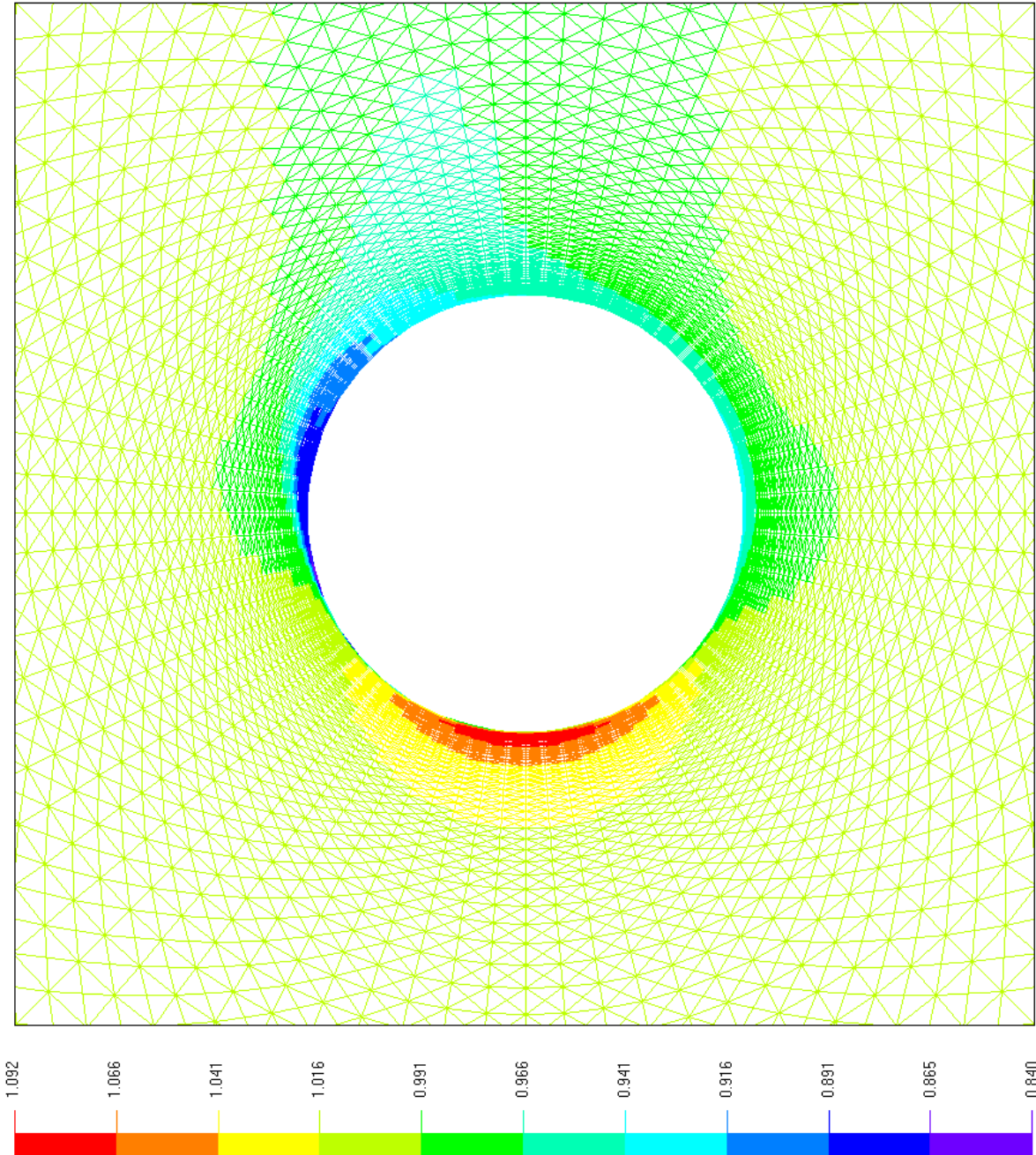
Left Coefficient: Ce = 0.004

Lift-to-Drag Ratio: L/D = 1.893

X-view: 0.00

Y-view: 0.00

Zoom: 3.00



Test ID: ELL100.tst

Mesh Resolution: 60 x 40 x 80

Spin Ratio: SR = 1.00

Reynolds Number: Re = 3.00E4

Mach Number: M = 0.50

Diameter (m): D = 0.010

Angle of Attack (deg): $\alpha = 5$

Static Pressure (hPa): P = 270

Static Temperature (K): T = 296

Gas Constant (J/kgK): R = 287

Specific Heats Ratio: k = 1.40

Run Time (s): t = 0.001000

Time Step (ms): dt = 0.025

Stop Time (s): T = 0.001000

Drag Coefficient: Cd = 0.059

Lift Coefficient: Cl = 0.111

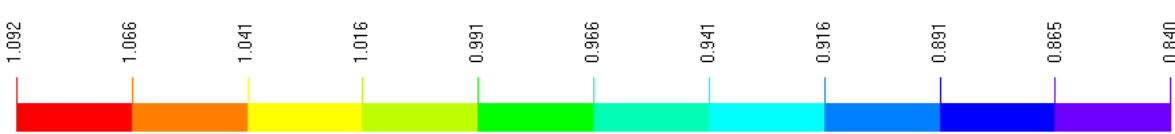
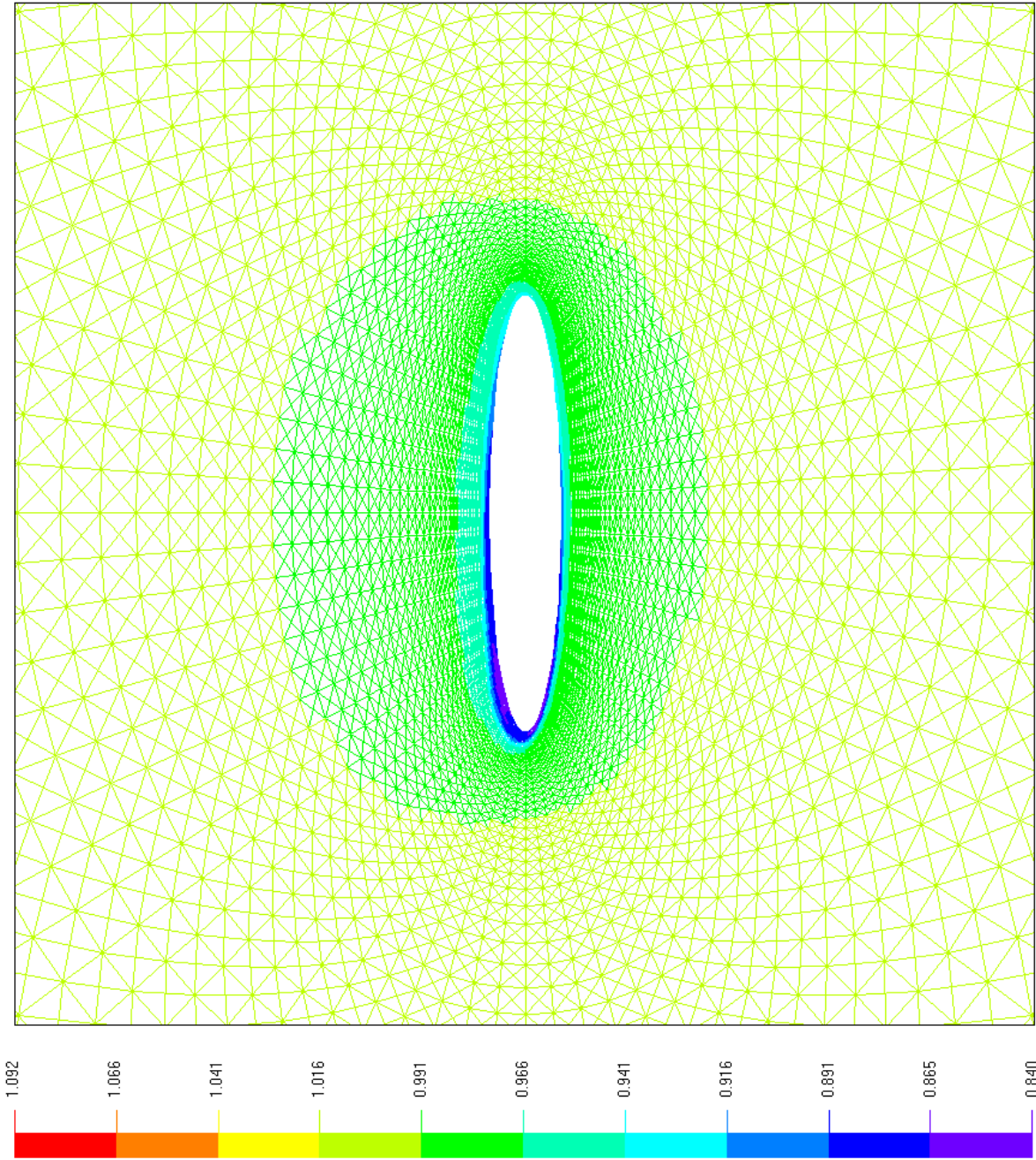
Left Coefficient: Ce = 0.004

Lift-to-Drag Ratio: L/D = 1.893

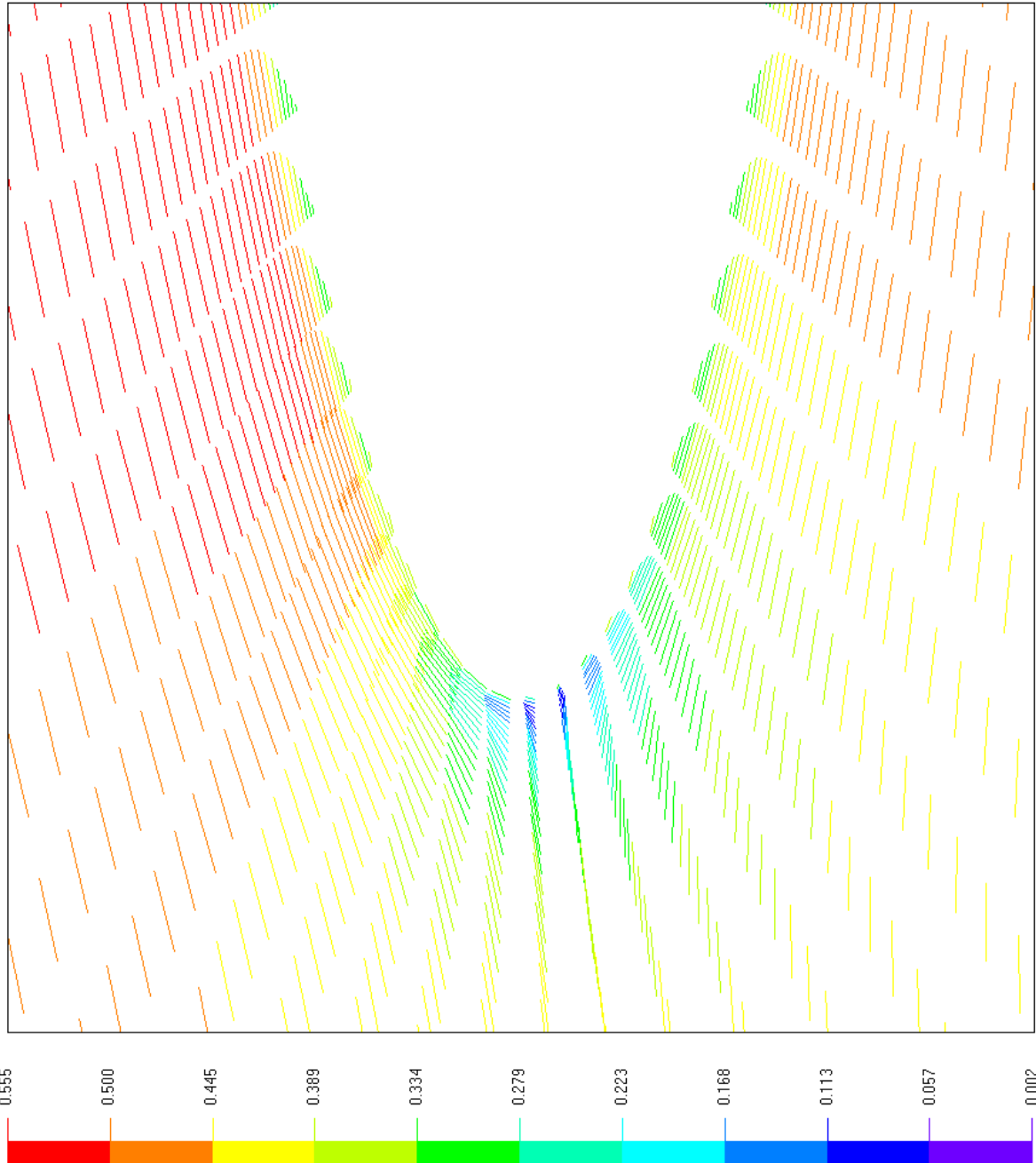
X-view: 0.00

Y-view: 0.00

Zoom: 3.00

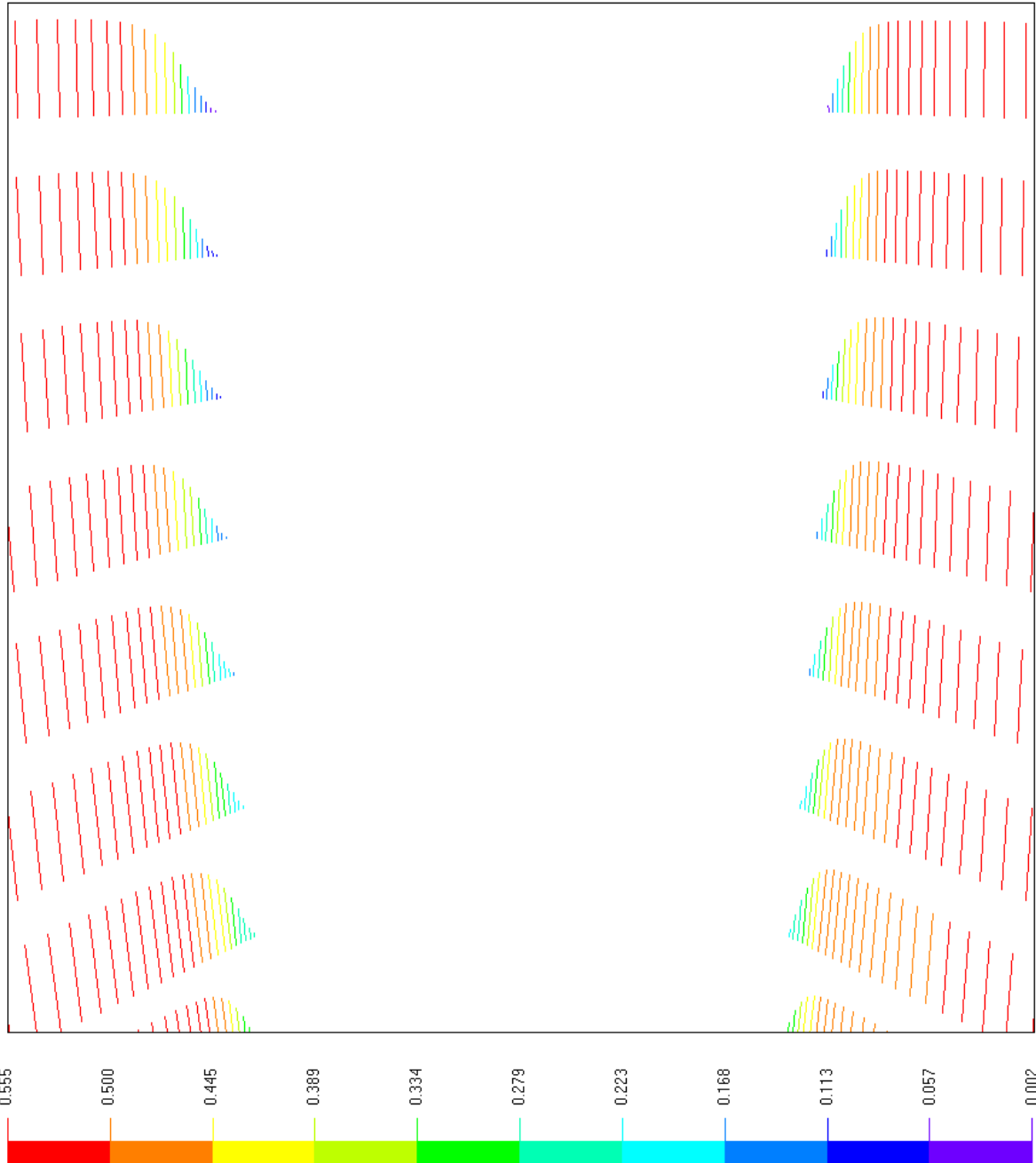


Test ID: ELL100.tst
 Mesh Resolution: 60 x 40 x 80
 Spin Ratio: SR = 1.00
 Reynolds Number: Re = 3.00E4
 Mach Number: M = 0.50
 Diameter (m): D = 0.010
 Angle of Attack (deg): $\alpha = 5$
 Static Pressure (hPa): P = 270
 Static Temperature (K): T = 296
 Gas Constant (J/kgK): R = 287
 Specific Heats Ratio: k = 1.40
 Run Time (s): t = 0.001000
 Time Step (ms): dt = 0.025
 Stop Time (s): T = 0.001000
 Drag Coefficient: Cd = 0.059
 Lift Coefficient: Cl = 0.111
 Left Coefficient: Ce = 0.004
 Lift-to-Drag Ratio: L/D = 1.893
 X-view: 0.00
 Y-view: 0.00
 Zoom: 3.00



Side View: Mach Number

Test ID: ELL100.tst
 Mesh Resolution: 60 x 40 x 80
 Spin Ratio: SR = 1.00
 Reynolds Number: Re = 3.00E4
 Mach Number: M = 0.50
 Diameter (m): D = 0.010
 Angle of Attack (deg): $\alpha = 5$
 Static Pressure (hPa): P = 270
 Static Temperature (K): T = 296
 Gas Constant (J/kgK): R = 287
 Specific Heats Ratio: k = 1.40
 Run Time (s): t = 0.001000
 Time Step (ms): dt = 0.025
 Stop Time (s): T = 0.001000
 Drag Coefficient: Cd = 0.059
 Lift Coefficient: Cl = 0.111
 Left Coefficient: Ce = 0.004
 Lift-to-Drag Ratio: L/D = 1.893
 X-view: -0.45
 Y-view: 0.00
 Zoom: 25.00



Test ID: ELL100.tst

Mesh Resolution: 60 x 40 x 80

Spin Ratio: SR = 1.00

Reynolds Number: Re = 3.00E4

Mach Number: M = 0.50

Diameter (m): D = 0.010

Angle of Attack (deg): $\alpha = 5$

Static Pressure (hPa): P = 270

Static Temperature (K): T = 296

Gas Constant (J/kgK): R = 287

Specific Heats Ratio: k = 1.40

Run Time (s): t = 0.001000

Time Step (ms): dt = 0.025

Stop Time (s): T = 0.001000

Drag Coefficient: Cd = 0.059

Lift Coefficient: Cl = 0.111

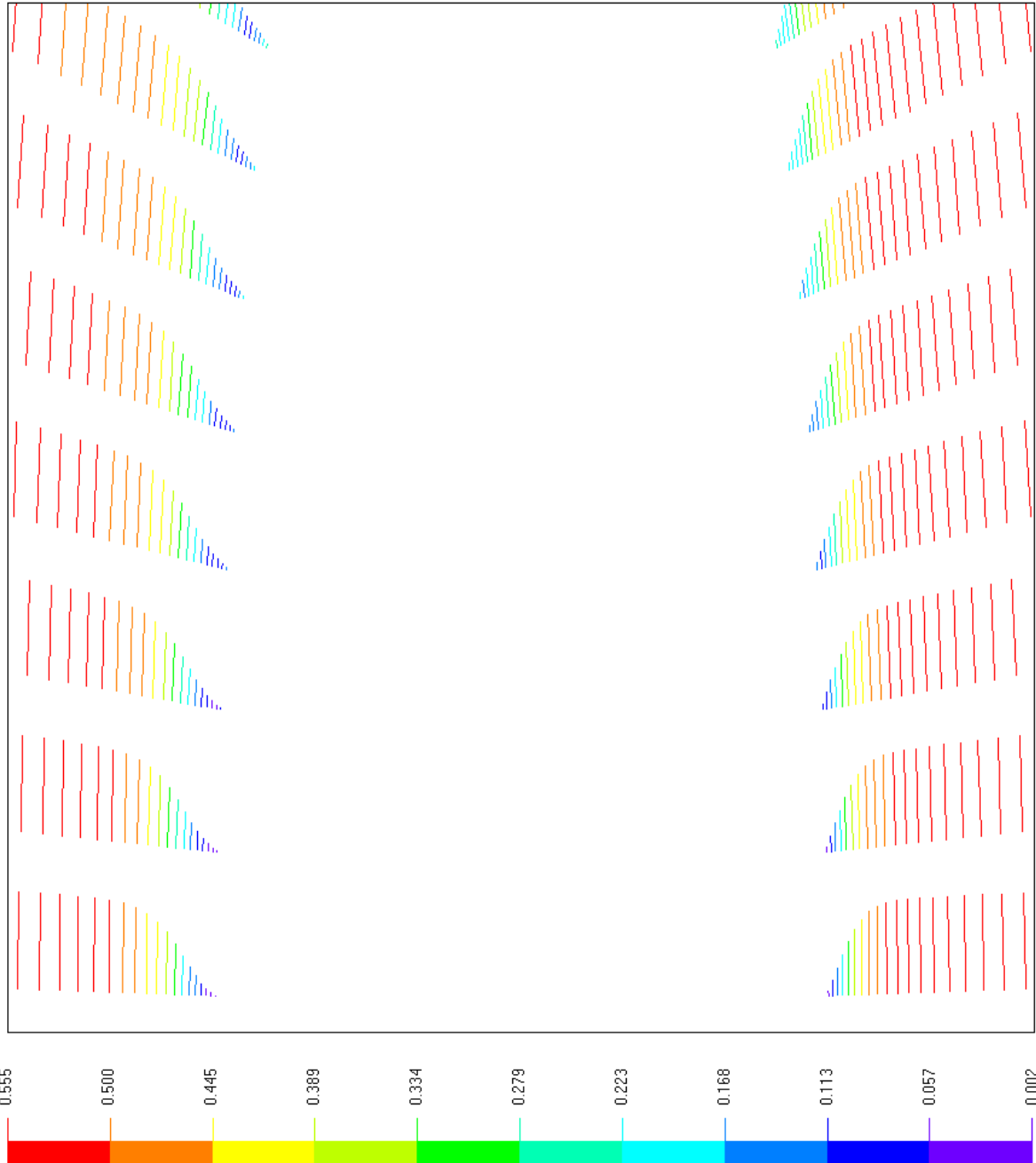
Left Coefficient: Ce = 0.004

Lift-to-Drag Ratio: L/D = 1.893

X-view: -0.13

Y-view: 0.00

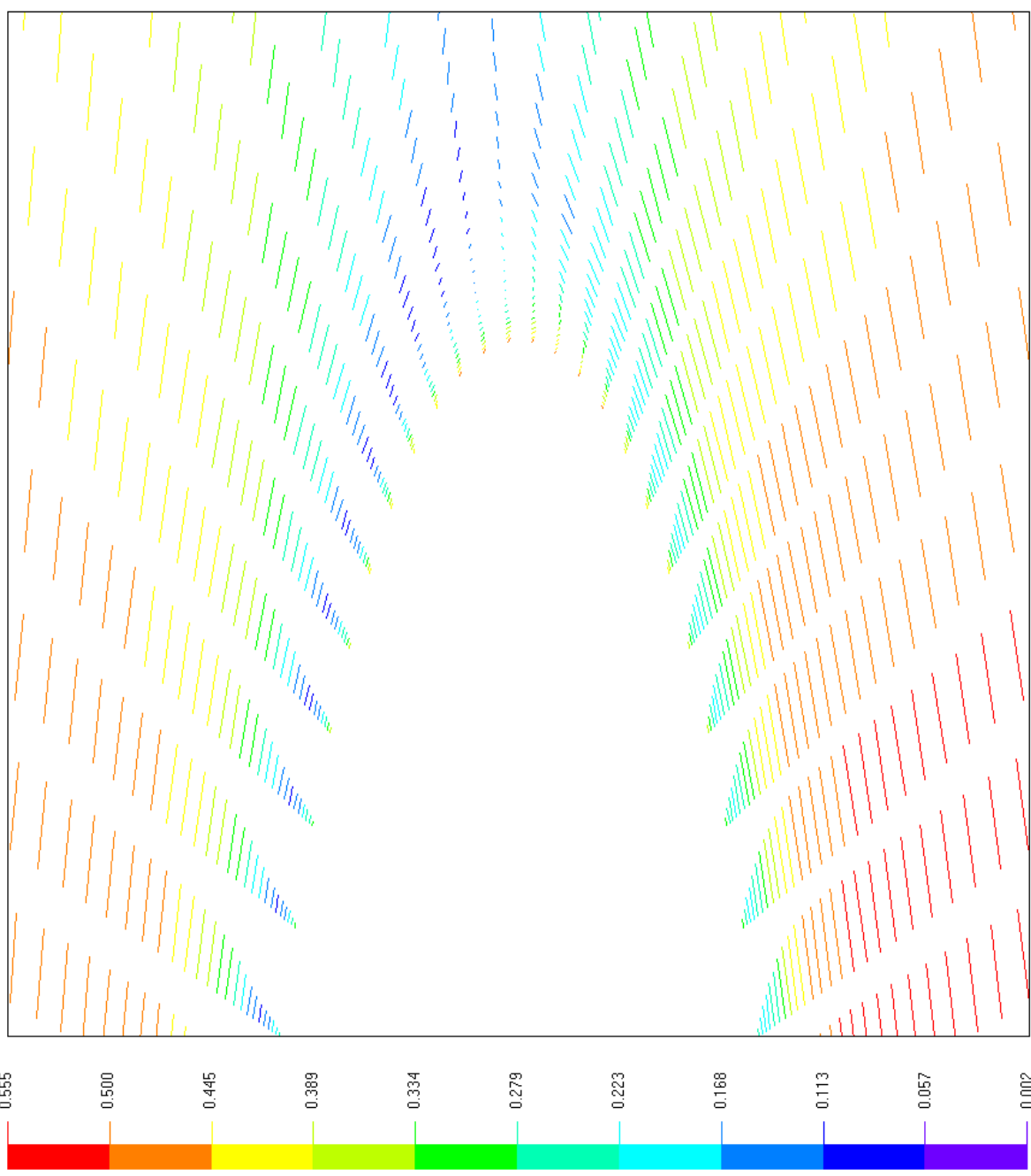
Zoom: 25.00



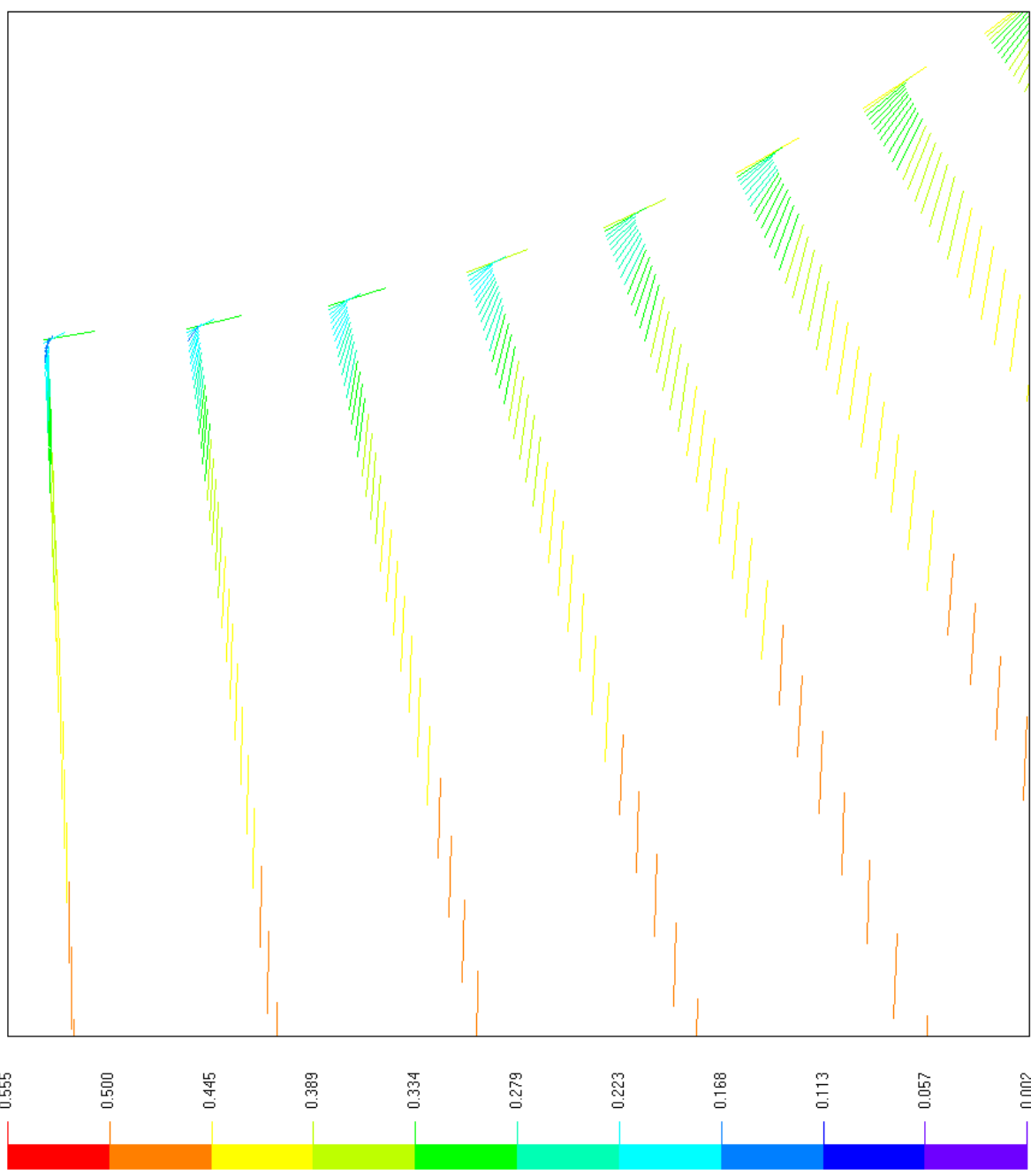
Side View: Mach Number

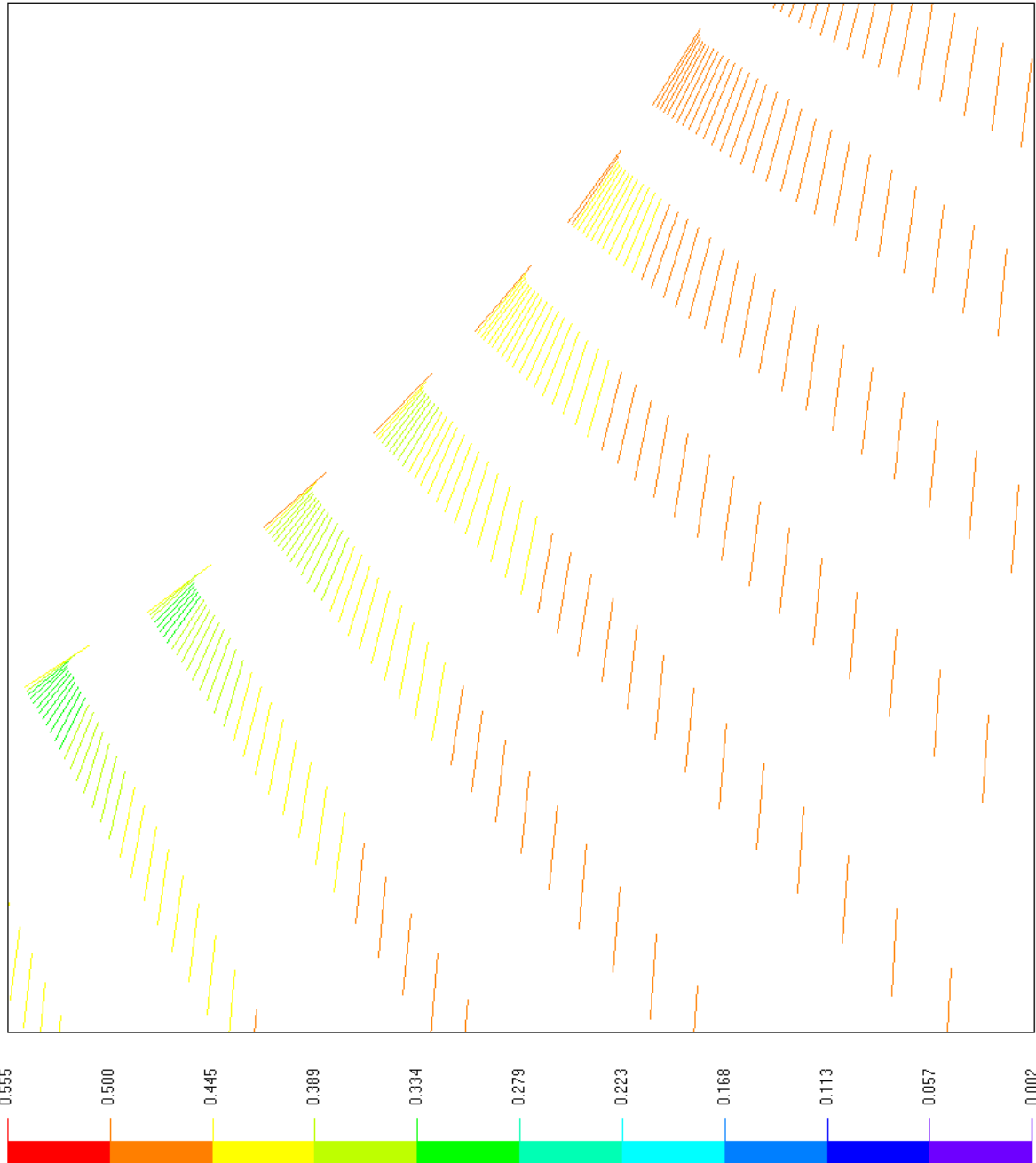
Test ID: ELL100.tst
 Mesh Resolution: 60 x 40 x 80
 Spin Ratio: SR = 1.00
 Reynolds Number: Re = 3.00E4
 Mach Number: M = 0.50
 Diameter (m): D = 0.010
 Angle of Attack (deg): $\alpha = 5$
 Static Pressure (hPa): P = 270
 Static Temperature (K): T = 296
 Gas Constant (J/kgK): R = 287
 Specific Heats Ratio: $k = 1.40$
 Run Time (s): $t = 0.001000$
 Time Step (ms): $dt = 0.025$
 Stop Time (s): T = 0.001000
 Drag Coefficient: Cd = 0.059
 Lift Coefficient: Cl = 0.111
 Left Coefficient: Ce = 0.004
 Lift-to-Drag Ratio: L/D = 1.893
 X-view: 0.15
 Y-view: 0.00
 Zoom: 25.00

Test ID: ELL100.tst
 Mesh Resolution: 60 x 40 x 80
 Spin Ratio: SR = 1.00
 Reynolds Number: Re = 3.00E4
 Mach Number: M = 0.50
 Diameter (m): D = 0.010
 Angle of Attack (deg): $\alpha = 5$
 Static Pressure (hPa): P = 270
 Static Temperature (K): T = 296
 Gas Constant (J/kgK): R = 287
 Specific Heats Ratio: k = 1.40
 Run Time (s): t = 0.001000
 Time Step (ms): dt = 0.025
 Stop Time (s): T = 0.001000
 Drag Coefficient: Cd = 0.059
 Lift Coefficient: Cl = 0.111
 Left Coefficient: Ce = 0.004
 Lift-to-Drag Ratio: L/D = 1.893
 X-view: 0.45
 Y-view: 0.00
 Zoom: 25.00



Test ID: ELL100.tst
 Mesh Resolution: 60 x 40 x 80
 Spin Ratio: SR = 1.00
 Reynolds Number: Re = 3.00E4
 Mach Number: M = 0.50
 Diameter (m): D = 0.010
 Angle of Attack (deg): $\alpha = 5$
 Static Pressure (hPa): P = 270
 Static Temperature (K): T = 296
 Gas Constant (J/kgK): R = 287
 Specific Heats Ratio: k = 1.40
 Run Time (s): t = 0.001000
 Time Step (ms): dt = 0.025
 Stop Time (s): T = 0.001000
 Drag Coefficient: Cd = 0.059
 Lift Coefficient: Cl = 0.111
 Left Coefficient: Ce = 0.004
 Lift-to-Drag Ratio: L/D = 1.893
 X-view: -0.55
 Y-view: -0.15
 Zoom: 25.00

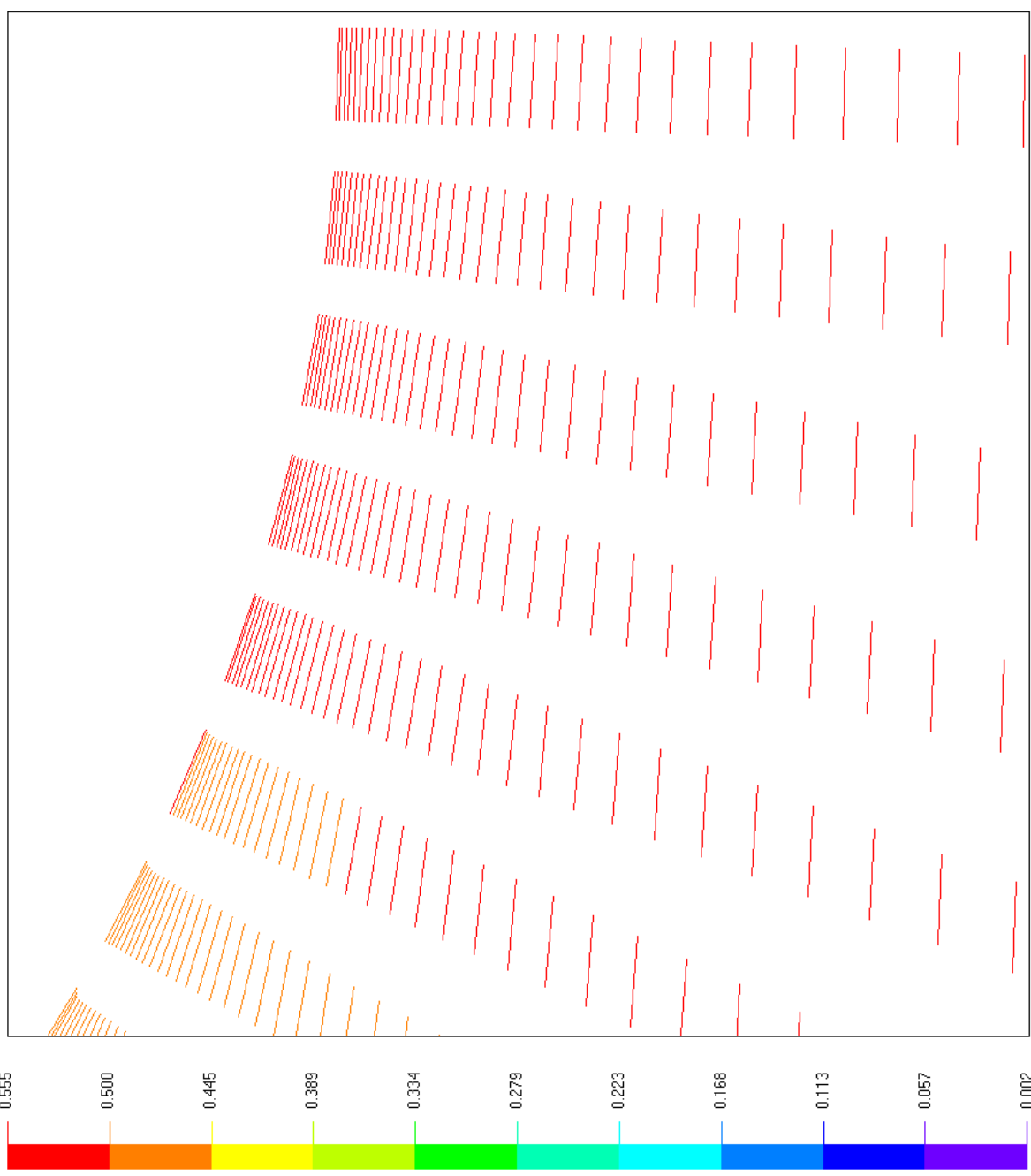




Top View: Mach Number

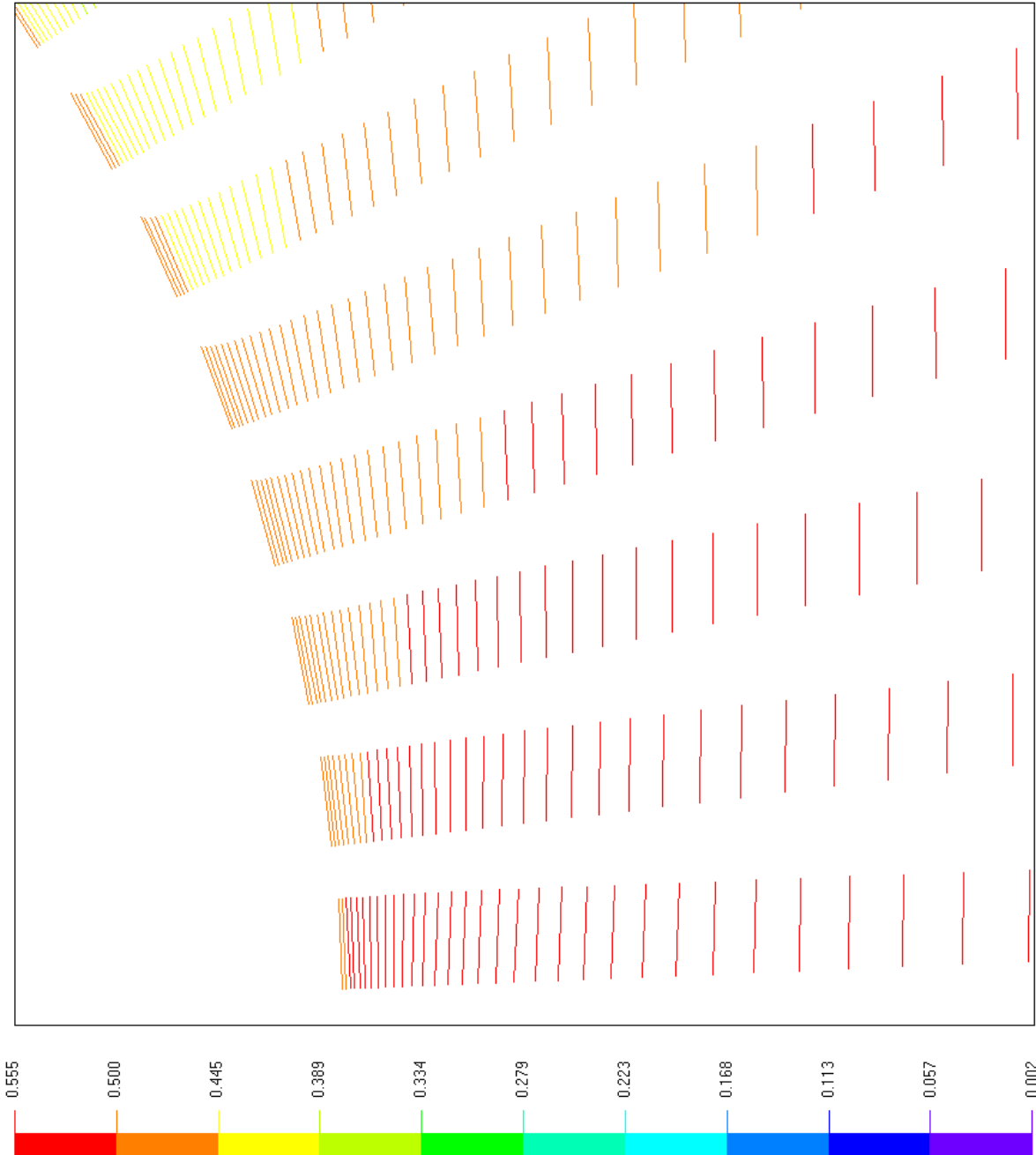
Test ID: ELL100.tst
 Mesh Resolution: 60 x 40 x 80
 Spin Ratio: SR = 1.00
 Reynolds Number: Re = 3.00E4
 Mach Number: M = 0.50
 Diameter (m): D = 0.010
 Angle of Attack (deg): $\alpha = 5$
 Static Pressure (hPa): P = 270
 Static Temperature (K): T = 296
 Gas Constant (J/kgK): R = 287
 Specific Heats Ratio: k = 1.40
 Run Time (s): t = 0.001000
 Time Step (ms): dt = 0.025
 Stop Time (s): T = 0.001000
 Drag Coefficient: Cd = 0.059
 Lift Coefficient: Cl = 0.111
 Left Coefficient: Ce = 0.004
 Lift-to-Drag Ratio: L/D = 1.893
 X-view: -0.39
 Y-view: -0.38
 Zoom: 25.00

Test ID: ELL100.tst
 Mesh Resolution: 60 x 40 x 80
 Spin Ratio: SR = 1.00
 Reynolds Number: Re = 3.00E4
 Mach Number: M = 0.50
 Diameter (m): D = 0.010
 Angle of Attack (deg): $\alpha = 5$
 Static Pressure (hPa): P = 270
 Static Temperature (K): T = 296
 Gas Constant (J/kgK): R = 287
 Specific Heats Ratio: k = 1.40
 Run Time (s): t = 0.001000
 Time Step (ms): dt = 0.025
 Stop Time (s): T = 0.001000
 Drag Coefficient: Cd = 0.059
 Lift Coefficient: Cl = 0.111
 Left Coefficient: Ce = 0.004
 Lift-to-Drag Ratio: L/D = 1.893
 X-view: -0.13
 Y-view: -0.55
 Zoom: 25.00

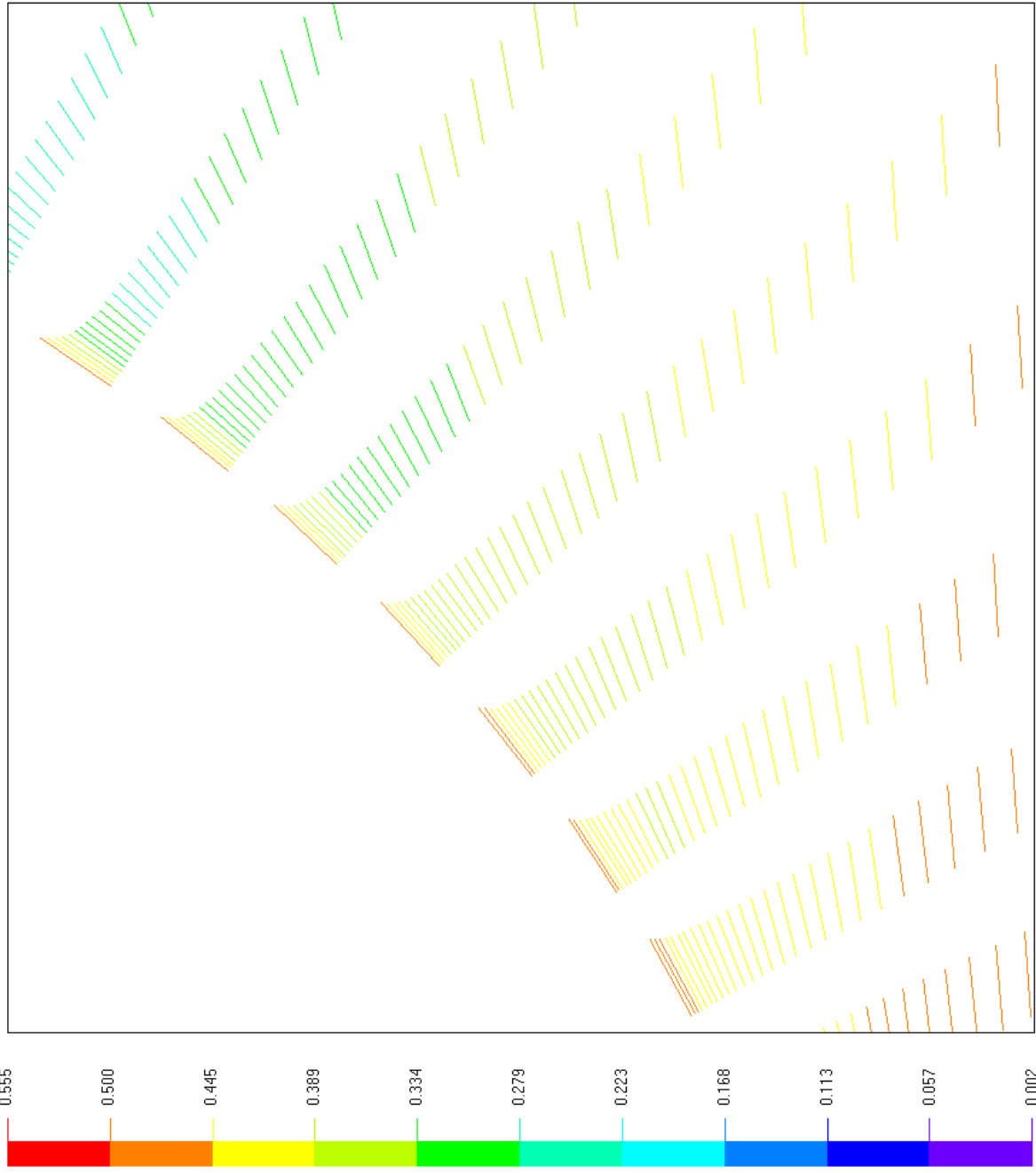


Top View: Mach Number

Mach #



Test ID: ELL100.tst
 Mesh Resolution: 60 x 40 x 80
 Spin Ratio: SR = 1.00
 Reynolds Number: Re = 3.00E4
 Mach Number: M = 0.50
 Diameter (m): D = 0.010
 Angle of Attack (deg): $\alpha = 5$
 Static Pressure (hPa): P = 270
 Static Temperature (K): T = 296
 Gas Constant (J/kgK): R = 287
 Specific Heats Ratio: $k = 1.40$
 Run Time (s): $t = 0.001000$
 Time Step (ms): $dt = 0.025$
 Stop Time (s): T = 0.001000
 Drag Coefficient: Cd = 0.059
 Lift Coefficient: Cl = 0.111
 Left Coefficient: Ce = 0.004
 Lift-to-Drag Ratio: L/D = 1.893
 X-view: 0.15
 Y-view: -0.55
 Zoom: 25.00



Test ID: ELL100.tst

Mesh Resolution: 60 x 40 x 80

Spin Ratio: SR = 1.00

Reynolds Number: Re = 3.00E4

Mach Number: M = 0.50

Diameter (m): D = 0.010

Angle of Attack (deg): $\alpha = 5$

Static Pressure (hPa): P = 270

Static Temperature (K): T = 296

Gas Constant (J/kgK): R = 287

Specific Heats Ratio: k = 1.40

Run Time (s): t = 0.001000

Time Step (ms): dt = 0.025

Stop Time (s): T = 0.001000

Drag Coefficient: Cd = 0.059

Lift Coefficient: Cl = 0.111

Left Coefficient: Ce = 0.004

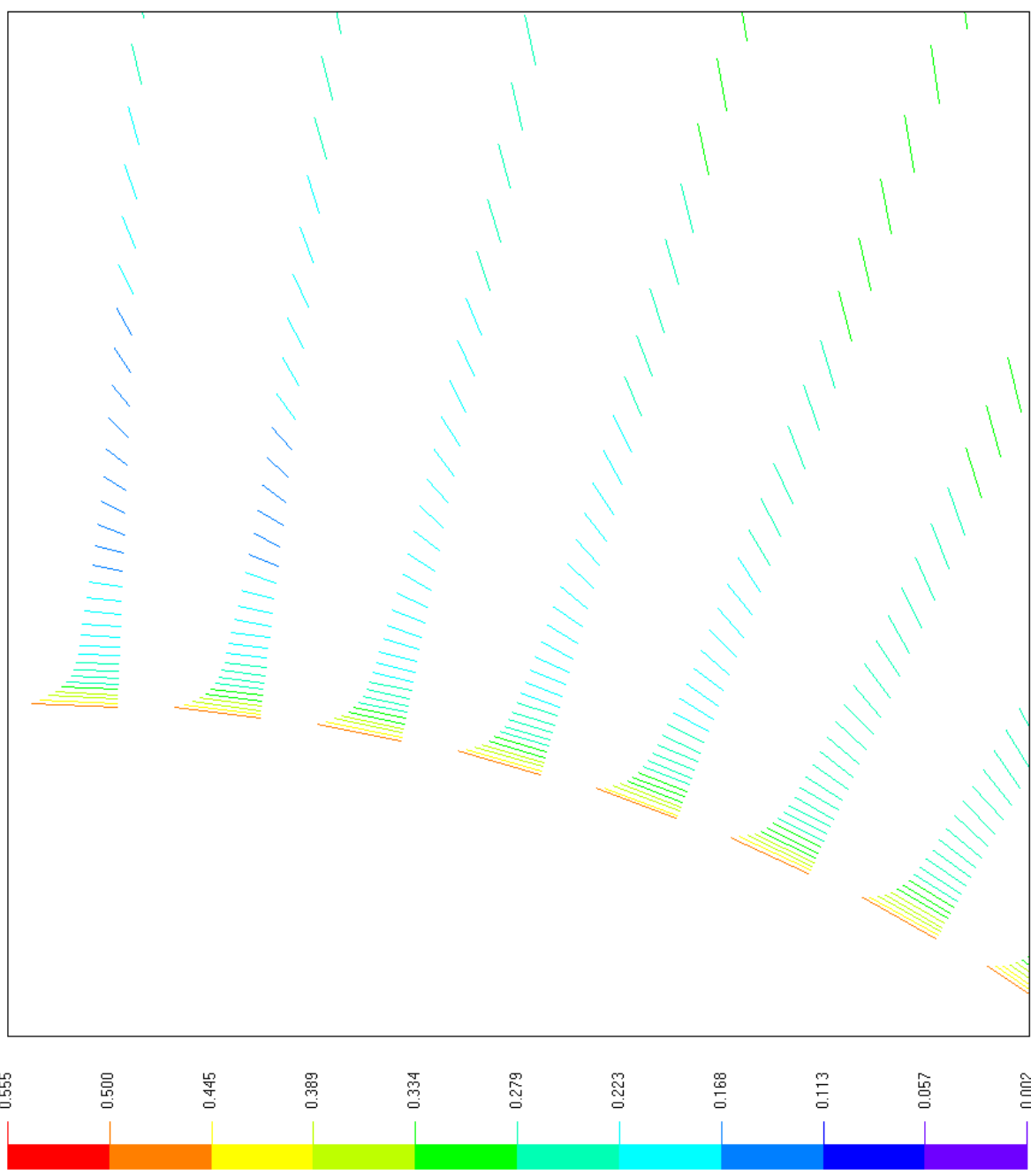
Lift-to-Drag Ratio: L/D = 1.893

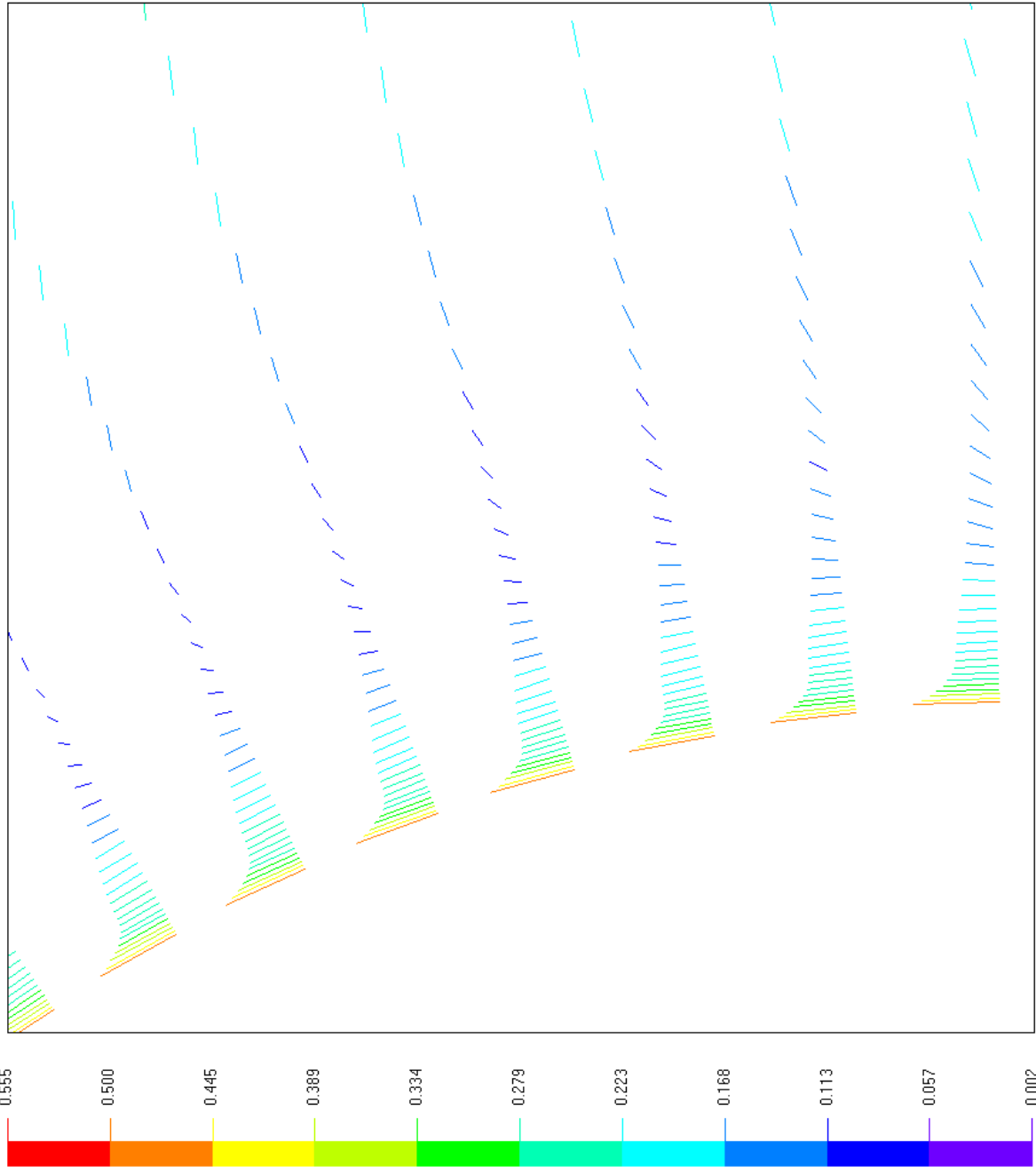
X-view: 0.38

Y-view: -0.39

Zoom: 25.00

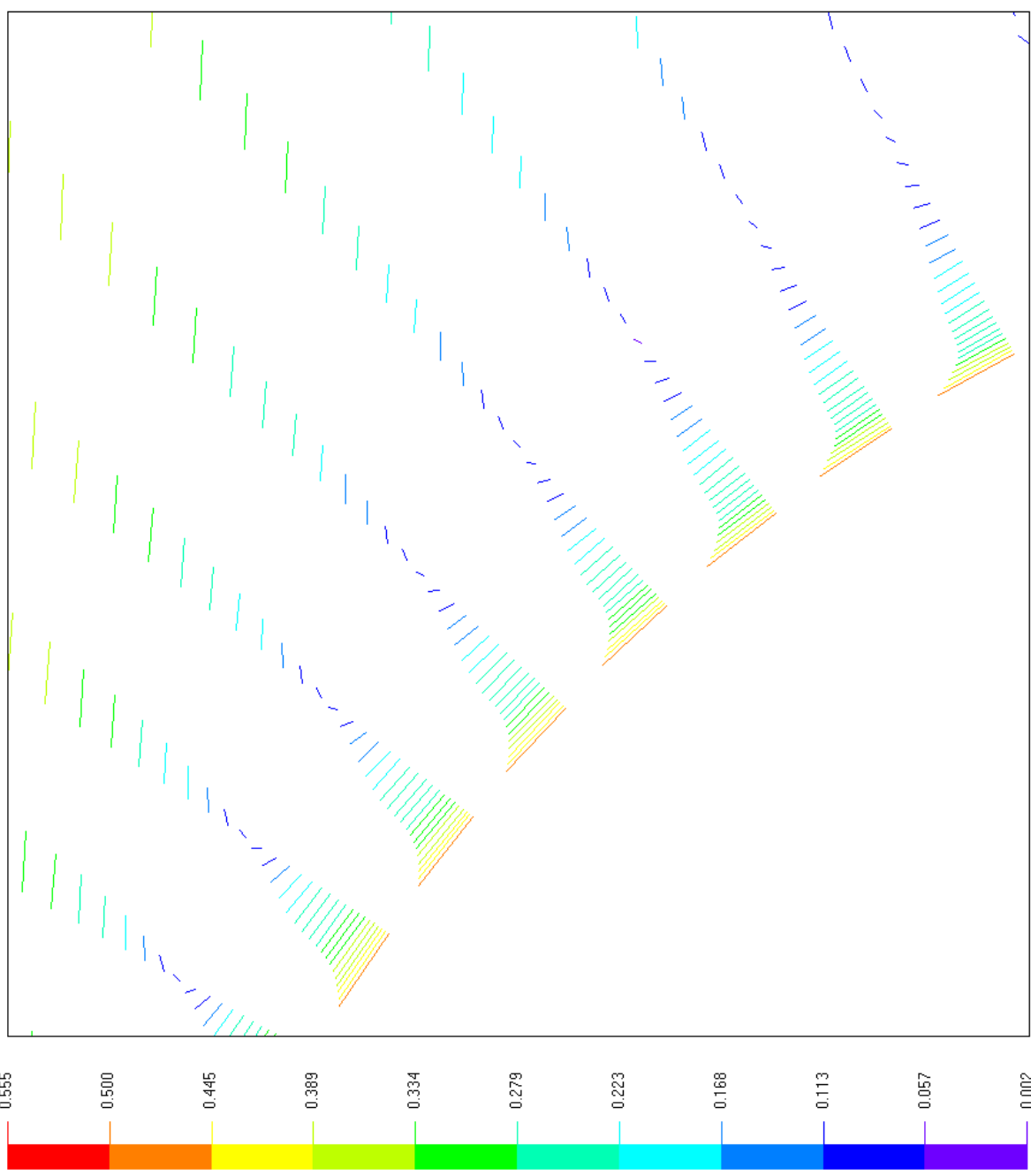
Test ID: ELL100.tst
 Mesh Resolution: 60 x 40 x 80
 Spin Ratio: SR = 1.00
 Reynolds Number: Re = 3.00E4
 Mach Number: M = 0.50
 Diameter (m): D = 0.010
 Angle of Attack (deg): $\alpha = 5$
 Static Pressure (hPa): P = 270
 Static Temperature (K): T = 296
 Gas Constant (J/kgK): R = 287
 Specific Heats Ratio: k = 1.40
 Run Time (s): t = 0.001000
 Time Step (ms): dt = 0.025
 Stop Time (s): T = 0.001000
 Drag Coefficient: Cd = 0.059
 Lift Coefficient: Cl = 0.111
 Left Coefficient: Ce = 0.004
 Lift-to-Drag Ratio: L/D = 1.893
 X-view: 0.55
 Y-view: -0.13
 Zoom: 25.00



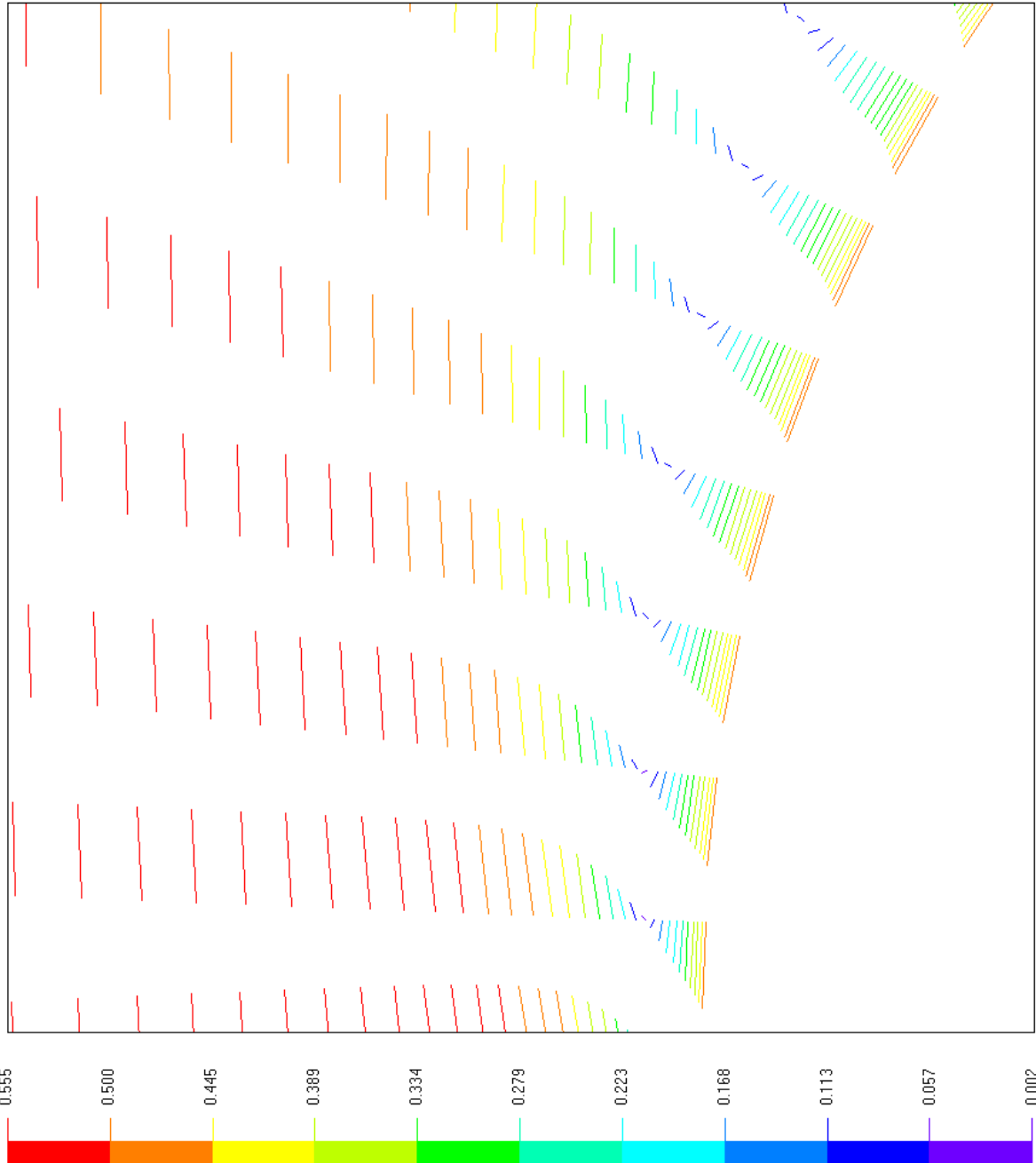


Test ID: ELL100.tst
 Mesh Resolution: 60 x 40 x 80
 Spin Ratio: SR = 1.00
 Reynolds Number: Re = 3.00E4
 Mach Number: M = 0.50
 Diameter (m): D = 0.010
 Angle of Attack (deg): $\alpha = 5$
 Static Pressure (hPa): P = 270
 Static Temperature (K): T = 296
 Gas Constant (J/kgK): R = 287
 Specific Heats Ratio: k = 1.40
 Run Time (s): t = 0.001000
 Time Step (ms): dt = 0.025
 Stop Time (s): T = 0.001000
 Drag Coefficient: Cd = 0.059
 Lift Coefficient: Cl = 0.111
 Left Coefficient: Ce = 0.004
 Lift-to-Drag Ratio: L/D = 1.893
 X-view: 0.55
 Y-view: 0.15
 Zoom: 25.00

Test ID: ELL100.tst
 Mesh Resolution: 60 x 40 x 80
 Spin Ratio: SR = 1.00
 Reynolds Number: Re = 3.00E4
 Mach Number: M = 0.50
 Diameter (m): D = 0.010
 Angle of Attack (deg): $\alpha = 5$
 Static Pressure (hPa): P = 270
 Static Temperature (K): T = 296
 Gas Constant (J/kgK): R = 287
 Specific Heats Ratio: $k = 1.40$
 Run Time (s): t = 0.001000
 Time Step (ms): dt = 0.025
 Stop Time (s): T = 0.001000
 Drag Coefficient: Cd = 0.059
 Lift Coefficient: Cl = 0.111
 Left Coefficient: Ce = 0.004
 Lift-to-Drag Ratio: L/D = 1.893
 X-view: 0.39
 Y-view: 0.38
 Zoom: 25.00



Top View: Mach Number



Test ID: ELL100.tst

Mesh Resolution: 60 x 40 x 80

Spin Ratio: SR = 1.00

Reynolds Number: Re = 3.00E4

Mach Number: M = 0.50

Diameter (m): D = 0.010

Angle of Attack (deg): $\alpha = 5$

Static Pressure (hPa): P = 270

Static Temperature (K): T = 296

Gas Constant (J/kgK): R = 287

Specific Heats Ratio: k = 1.40

Run Time (s): t = 0.001000

Time Step (ms): dt = 0.025

Stop Time (s): T = 0.001000

Drag Coefficient: Cd = 0.059

Lift Coefficient: Cl = 0.111

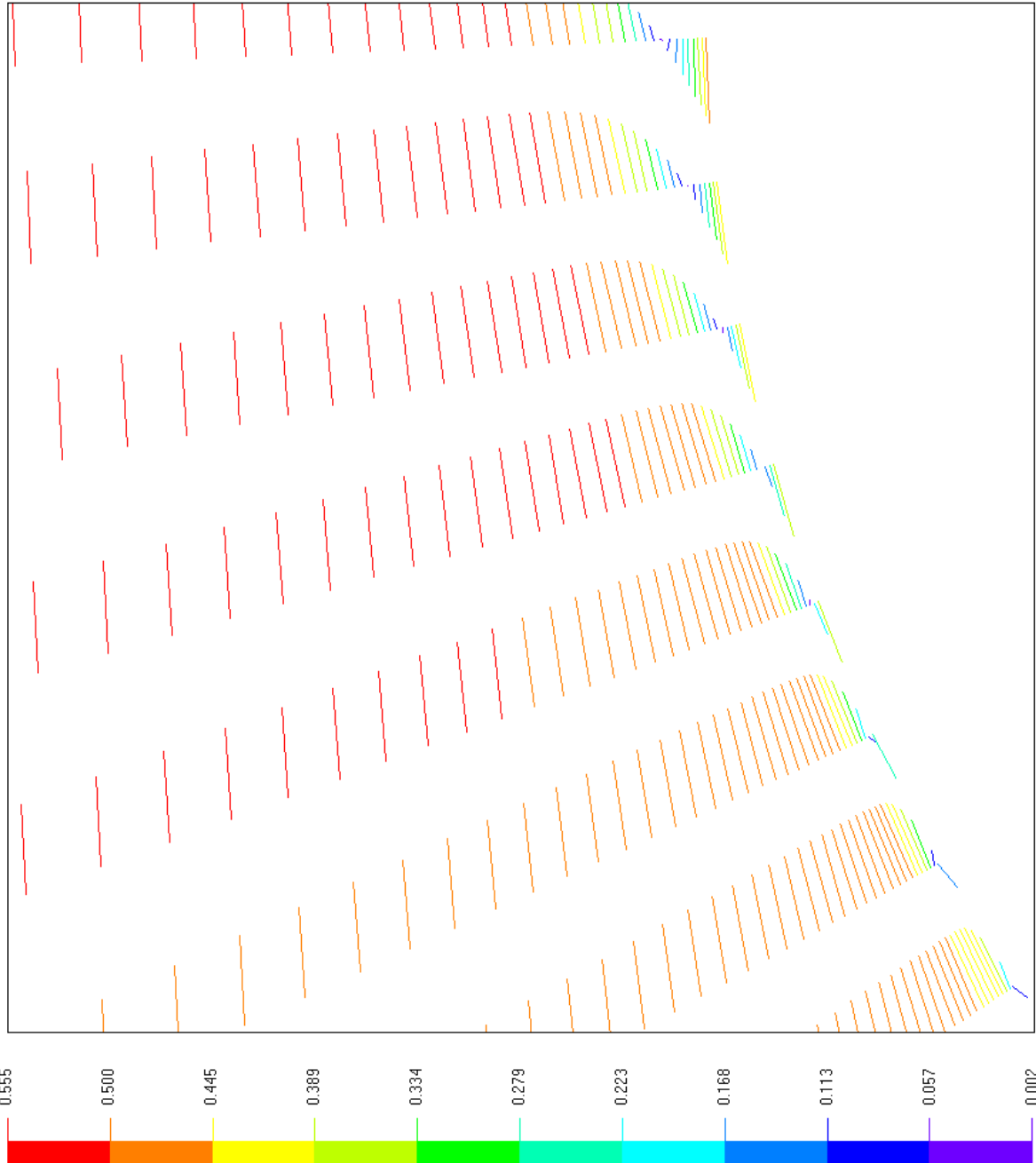
Left Coefficient: Ce = 0.004

Lift-to-Drag Ratio: L/D = 1.893

X-view: 0.13

Y-view: 0.55

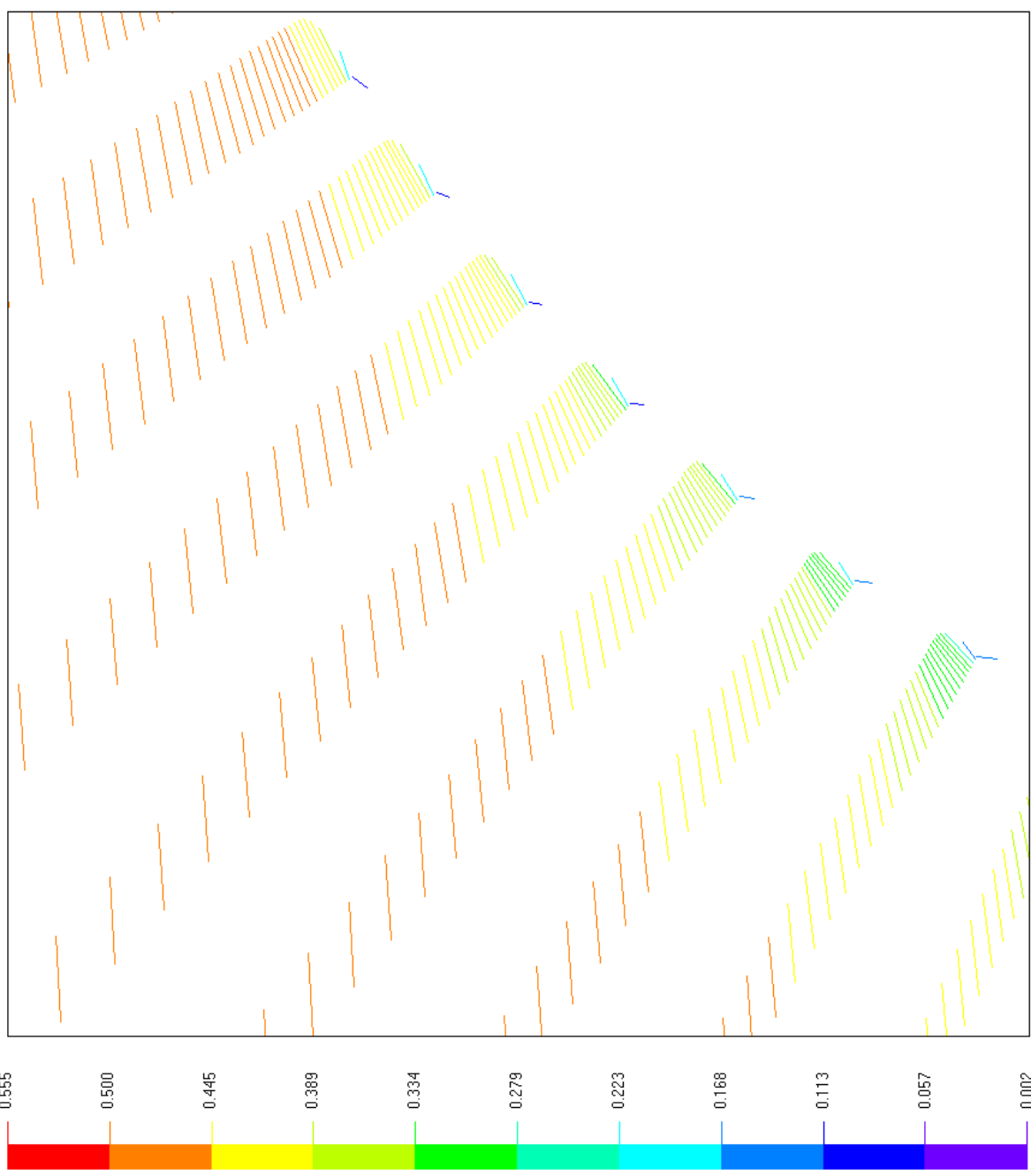
Zoom: 25.00



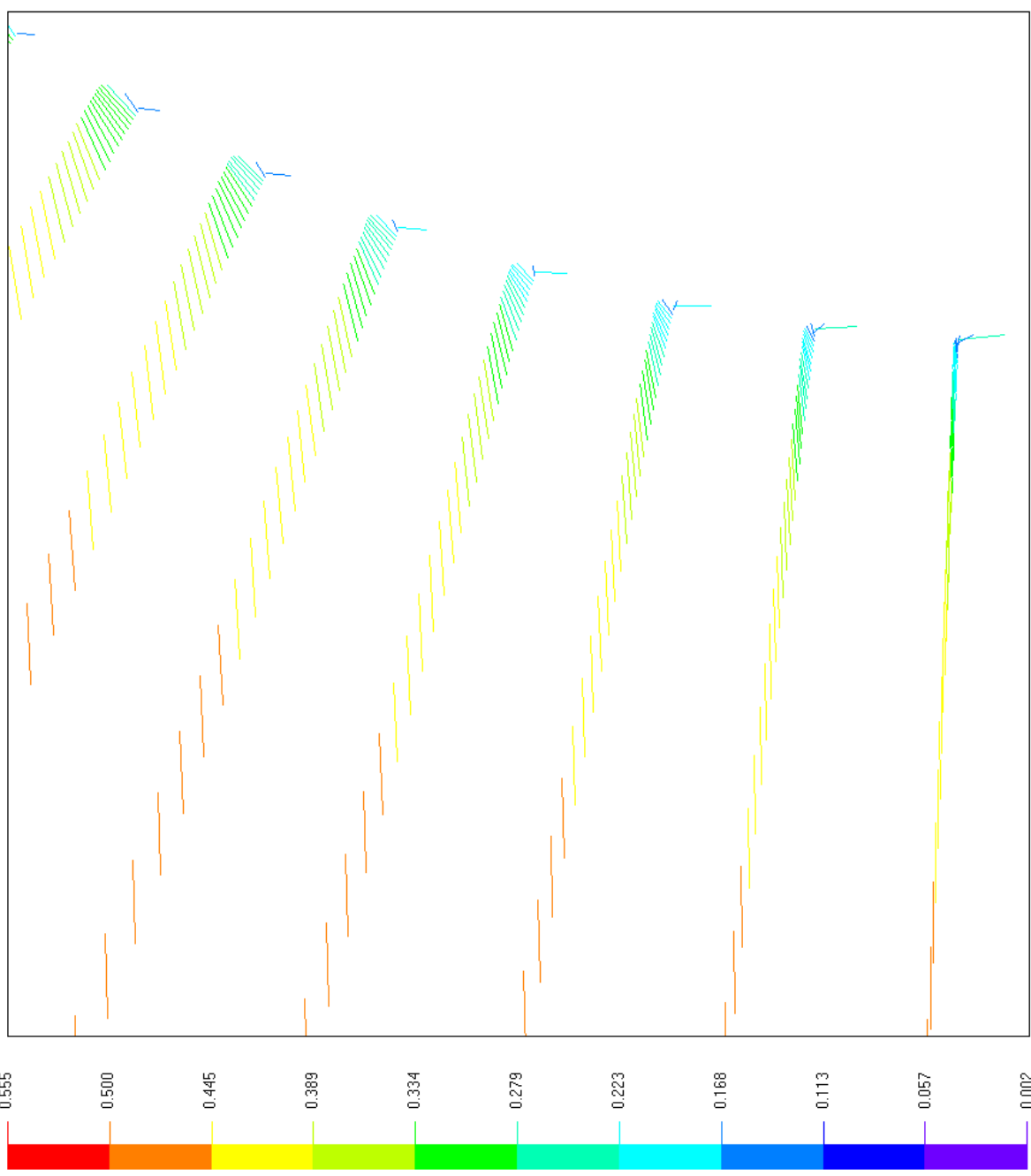
Top View: Mach Number

Test ID: ELL100.tst
 Mesh Resolution: 60 x 40 x 80
 Spin Ratio: SR = 1.00
 Reynolds Number: Re = 3.00E4
 Mach Number: M = 0.50
 Diameter (m): D = 0.010
 Angle of Attack (deg): $\alpha = 5$
 Static Pressure (hPa): P = 270
 Static Temperature (K): T = 296
 Gas Constant (J/kgK): R = 287
 Specific Heats Ratio: k = 1.40
 Run Time (s): t = 0.001000
 Time Step (ms): dt = 0.025
 Stop Time (s): T = 0.001000
 Drag Coefficient: Cd = 0.059
 Lift Coefficient: Cl = 0.111
 Left Coefficient: Ce = 0.004
 Lift-to-Drag Ratio: L/D = 1.893
 X-view: -0.15
 Y-view: 0.55
 Zoom: 25.00

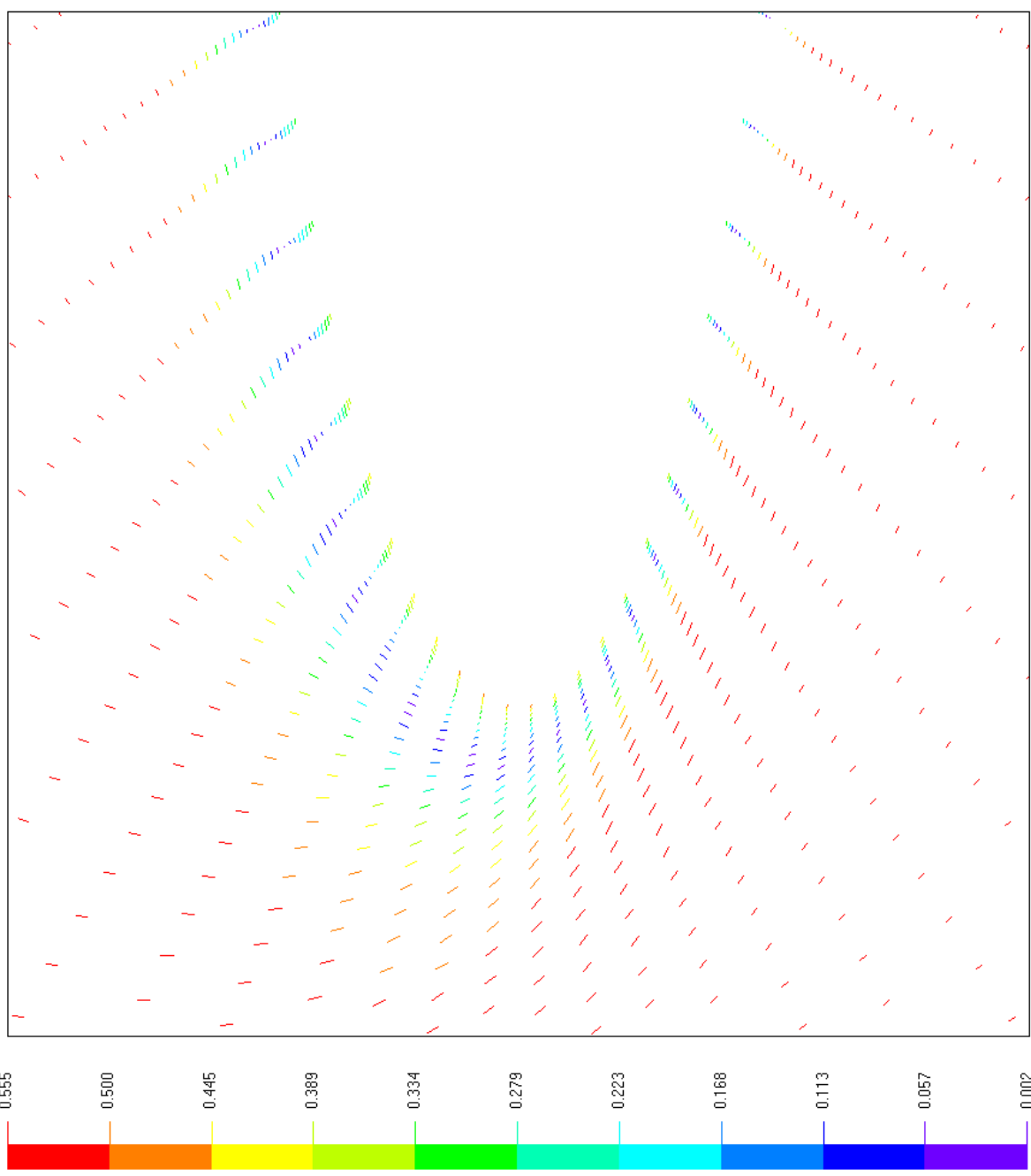
Test ID: ELL100.tst
 Mesh Resolution: 60 x 40 x 80
 Spin Ratio: SR = 1.00
 Reynolds Number: Re = 3.00E4
 Mach Number: M = 0.50
 Diameter (m): D = 0.010
 Angle of Attack (deg): $\alpha = 5$
 Static Pressure (hPa): P = 270
 Static Temperature (K): T = 296
 Gas Constant (J/kgK): R = 287
 Specific Heats Ratio: k = 1.40
 Run Time (s): t = 0.001000
 Time Step (ms): dt = 0.025
 Stop Time (s): T = 0.001000
 Drag Coefficient: Cd = 0.059
 Lift Coefficient: Cl = 0.111
 Left Coefficient: Ce = 0.004
 Lift-to-Drag Ratio: L/D = 1.893
 X-view: -0.40
 Y-view: 0.37
 Zoom: 25.00



Test ID: ELL100.tst
 Mesh Resolution: 60 x 40 x 80
 Spin Ratio: SR = 1.00
 Reynolds Number: Re = 3.00E4
 Mach Number: M = 0.50
 Diameter (m): D = 0.010
 Angle of Attack (deg): $\alpha = 5$
 Static Pressure (hPa): P = 270
 Static Temperature (K): T = 296
 Gas Constant (J/kgK): R = 287
 Specific Heats Ratio: k = 1.40
 Run Time (s): t = 0.001000
 Time Step (ms): dt = 0.025
 Stop Time (s): T = 0.001000
 Drag Coefficient: Cd = 0.059
 Lift Coefficient: Cl = 0.111
 Left Coefficient: Ce = 0.004
 Lift-to-Drag Ratio: L/D = 1.893
 X-view: -0.55
 Y-view: 0.14
 Zoom: 25.00

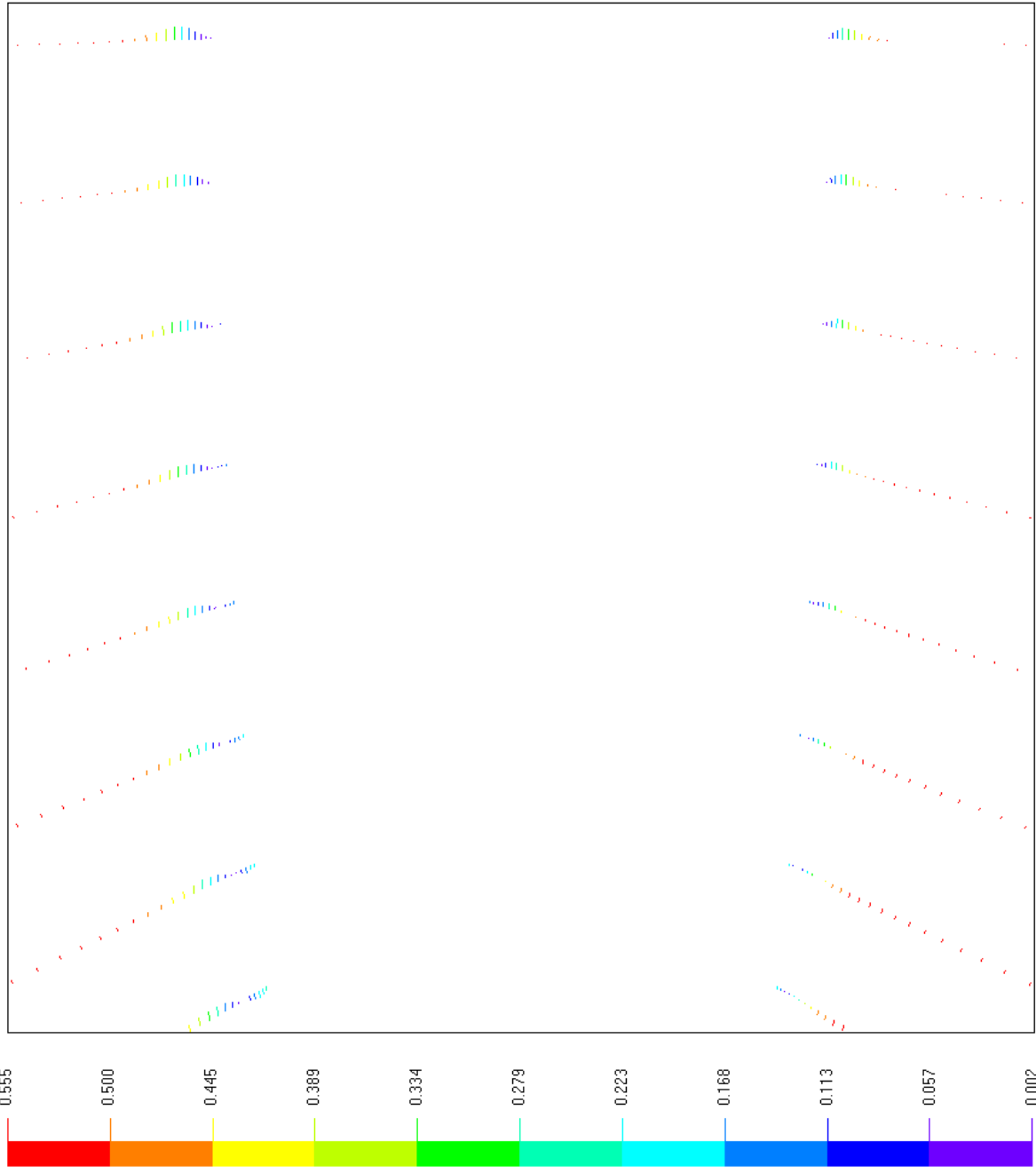


Test ID: ELL100.tst
 Mesh Resolution: 60 x 40 x 80
 Spin Ratio: SR = 1.00
 Reynolds Number: Re = 3.00E4
 Mach Number: M = 0.50
 Diameter (m): D = 0.010
 Angle of Attack (deg): $\alpha = 5$
 Static Pressure (hPa): P = 270
 Static Temperature (K): T = 296
 Gas Constant (J/kgK): R = 287
 Specific Heats Ratio: k = 1.40
 Run Time (s): t = 0.001000
 Time Step (ms): dt = 0.025
 Stop Time (s): T = 0.001000
 Drag Coefficient: Cd = 0.059
 Lift Coefficient: Cl = 0.111
 Left Coefficient: Ce = 0.004
 Lift-to-Drag Ratio: L/D = 1.893
 X-view: -0.45
 Y-view: 0.00
 Zoom: 25.00



Front View: Mach Number

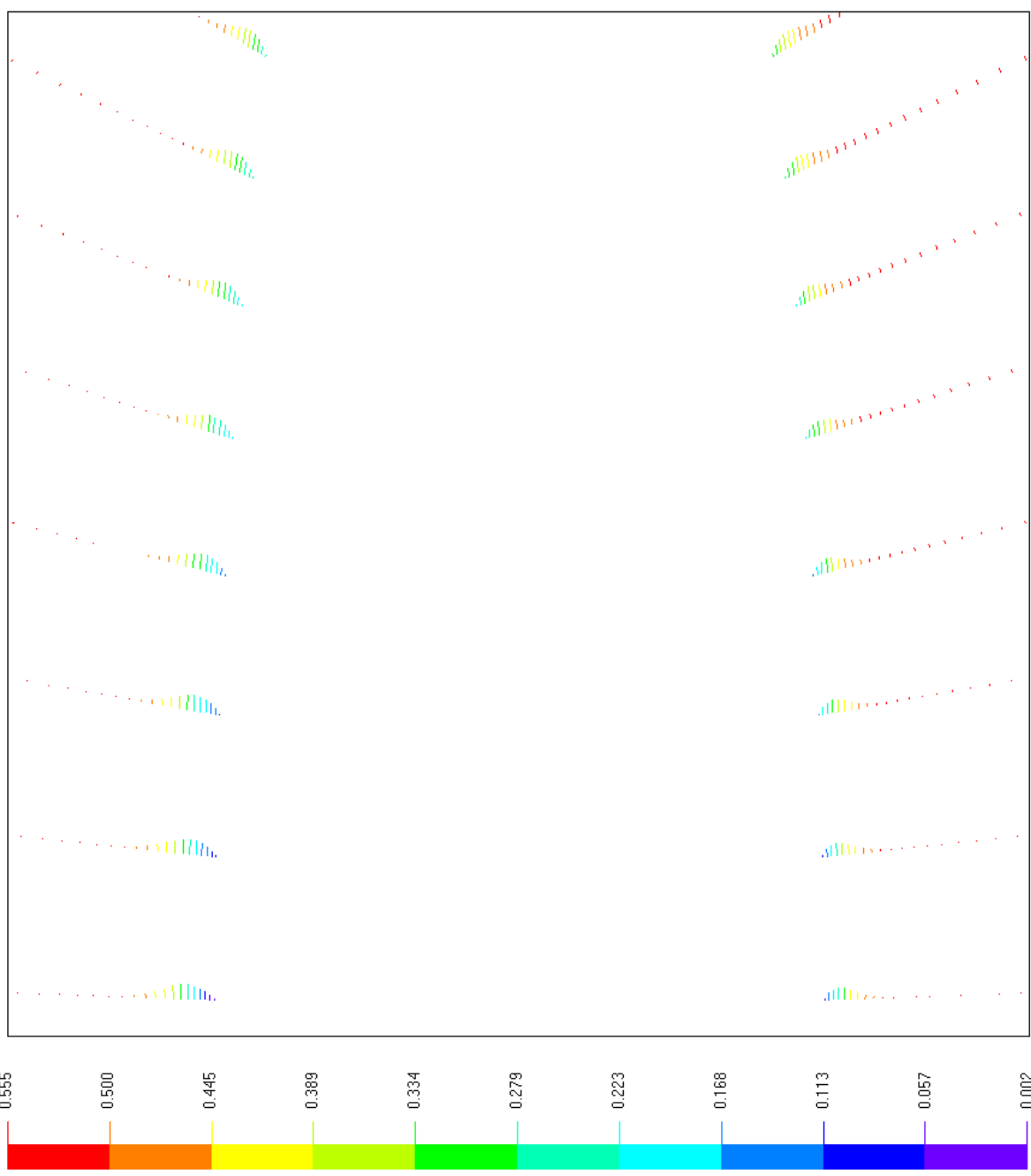
Mach #



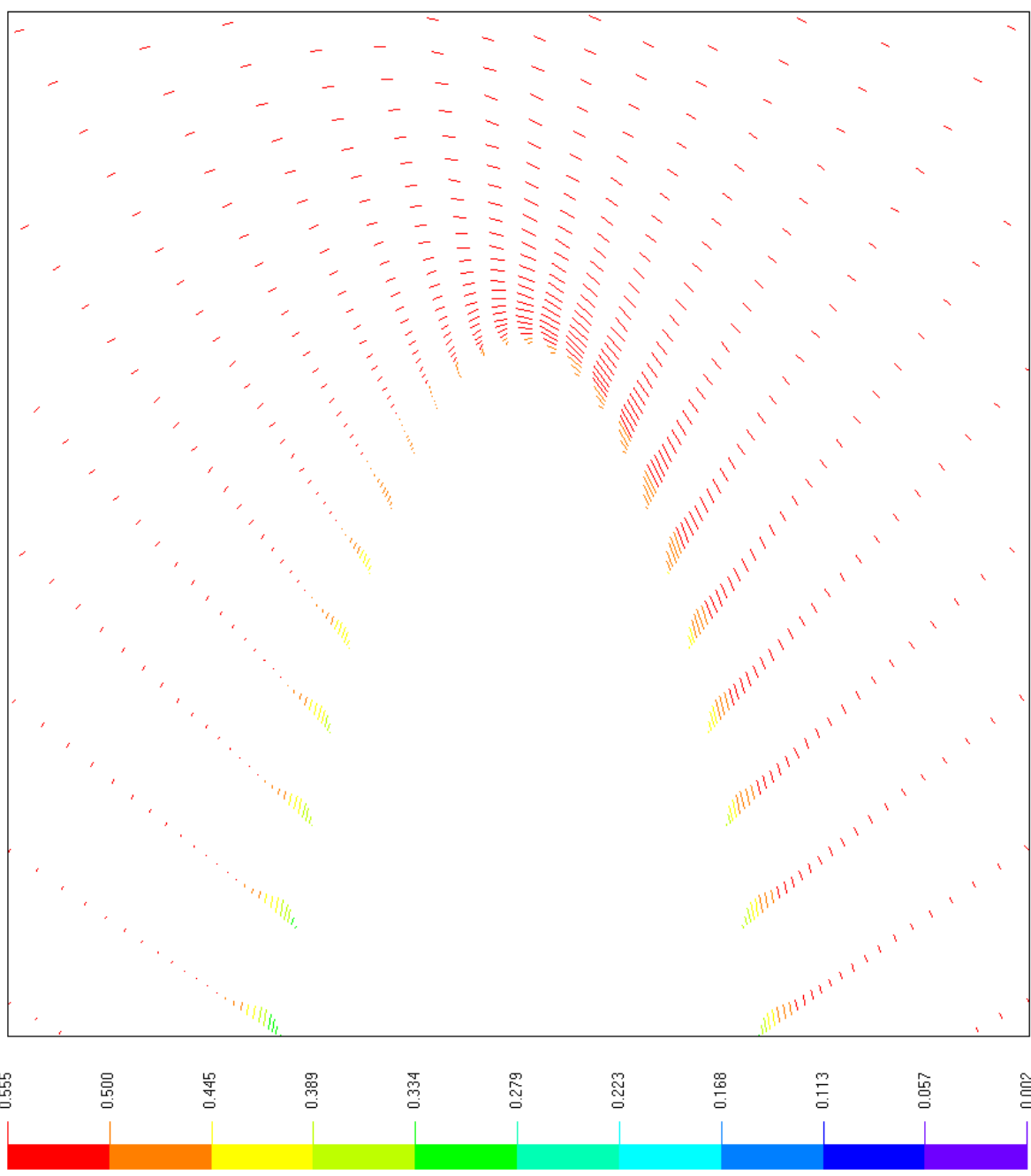
Front View: Mach Number

Test ID: ELL100.tst
 Mesh Resolution: 60 x 40 x 80
 Spin Ratio: SR = 1.00
 Reynolds Number: Re = 3.00E4
 Mach Number: M = 0.50
 Diameter (m): D = 0.010
 Angle of Attack (deg): $\alpha = 5$
 Static Pressure (hPa): P = 270
 Static Temperature (K): T = 296
 Gas Constant (J/kgK): R = 287
 Specific Heats Ratio: k = 1.40
 Run Time (s): t = 0.001000
 Time Step (ms): dt = 0.025
 Stop Time (s): T = 0.001000
 Drag Coefficient: Cd = 0.059
 Lift Coefficient: Cl = 0.111
 Left Coefficient: Ce = 0.004
 Lift-to-Drag Ratio: L/D = 1.893
 X-view: -0.15
 Y-view: 0.00
 Zoom: 25.00

Test ID: ELL100.tst
 Mesh Resolution: 60 x 40 x 80
 Spin Ratio: SR = 1.00
 Reynolds Number: Re = 3.00E4
 Mach Number: M = 0.50
 Diameter (m): D = 0.010
 Angle of Attack (deg): $\alpha = 5$
 Static Pressure (hPa): P = 270
 Static Temperature (K): T = 296
 Gas Constant (J/kgK): R = 287
 Specific Heats Ratio: k = 1.40
 Run Time (s): t = 0.001000
 Time Step (ms): dt = 0.025
 Stop Time (s): T = 0.001000
 Drag Coefficient: Cd = 0.059
 Lift Coefficient: Cl = 0.111
 Left Coefficient: Ce = 0.004
 Lift-to-Drag Ratio: L/D = 1.893
 X-view: 0.15
 Y-view: 0.00
 Zoom: 25.00



Test ID: ELL100.tst
 Mesh Resolution: 60 x 40 x 80
 Spin Ratio: SR = 1.00
 Reynolds Number: Re = 3.00E4
 Mach Number: M = 0.50
 Diameter (m): D = 0.010
 Angle of Attack (deg): $\alpha = 5$
 Static Pressure (hPa): P = 270
 Static Temperature (K): T = 296
 Gas Constant (J/kgK): R = 287
 Specific Heats Ratio: $k = 1.40$
 Run Time (s): $t = 0.001000$
 Time Step (ms): dt = 0.025
 Stop Time (s): T = 0.001000
 Drag Coefficient: Cd = 0.059
 Lift Coefficient: Cl = 0.111
 Left Coefficient: Ce = 0.004
 Lift-to-Drag Ratio: L/D = 1.893
 X-view: 0.45
 Y-view: 0.00
 Zoom: 25.00



Test ID: ELL100.tst

Mesh Resolution: 60 x 40 x 80

Spin Ratio: SR = 1.00

Reynolds Number: Re = 3.00E4

Mach Number: M = 0.50

Diameter (m): D = 0.010

Angle of Attack (deg): $\alpha = 5$

Static Pressure (hPa): P = 270

Static Temperature (K): T = 296

Gas Constant (J/kgK): R = 287

Specific Heats Ratio: k = 1.40

Run Time (s): t = 0.001000

Time Step (ms): dt = 0.025

Stop Time (s): T = 0.001000

Drag Coefficient: Cd = 0.059

Lift Coefficient: Cl = 0.111

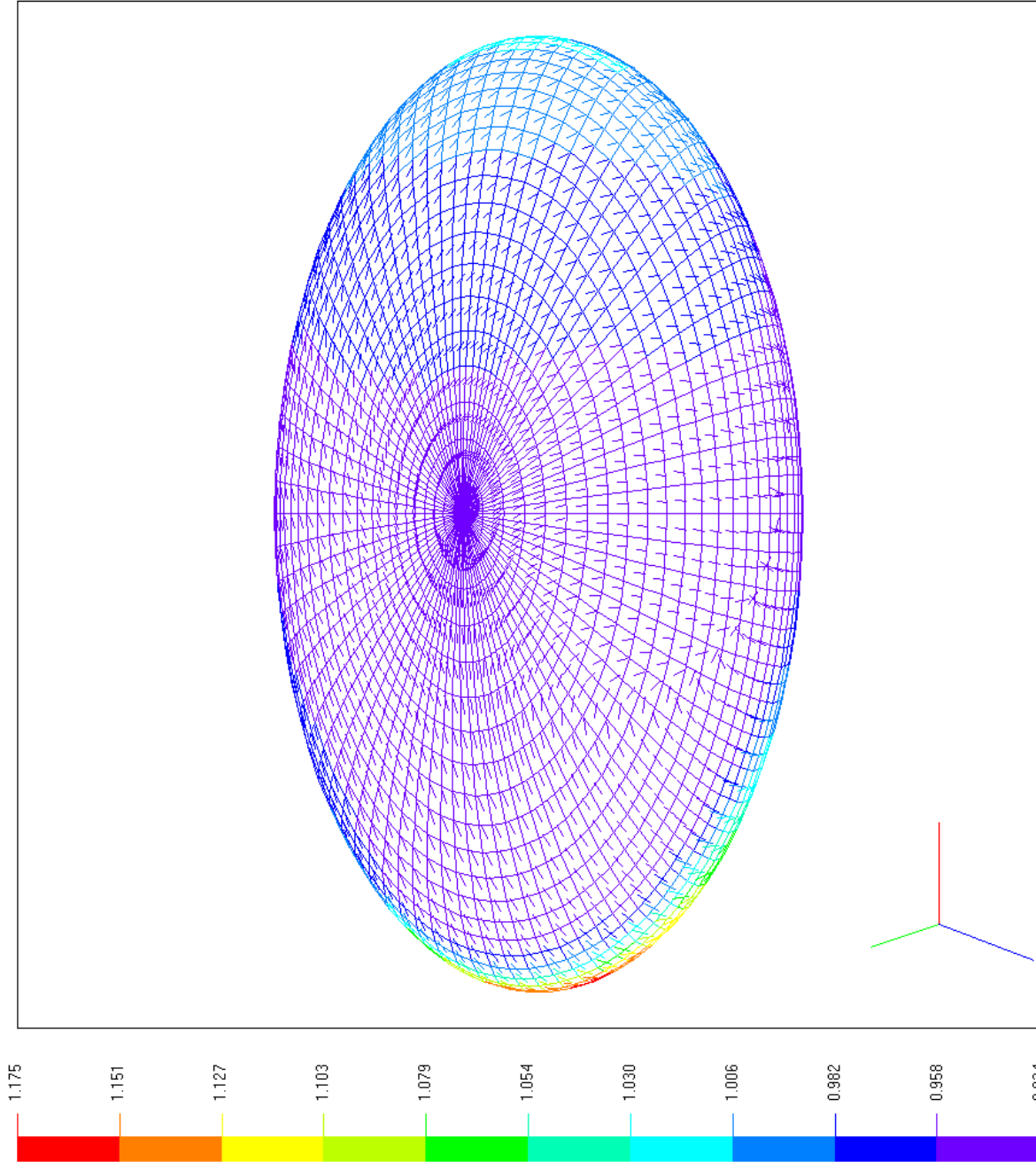
Left Coefficient: Ce = 0.004

Lift-to-Drag Ratio: L/D = 1.893

X-view: 0.00

Y-view: 0.00

Zoom: 1.00



Test ID: ELL100.tst

Mesh Resolution: 60 x 40 x 80

Spin Ratio: SR = 1.00

Reynolds Number: Re = 3.00E4

Mach Number: M = 0.50

Diameter (m): D = 0.010

Angle of Attack (deg): $\alpha = 5$

Static Pressure (hPa): P = 270

Static Temperature (K): T = 296

Gas Constant (J/kgK): R = 287

Specific Heats Ratio: k = 1.40

Run Time (s): t = 0.001000

Time Step (ms): dt = 0.025

Stop Time (s): T = 0.001000

Drag Coefficient: Cd = 0.059

Lift Coefficient: Cl = 0.111

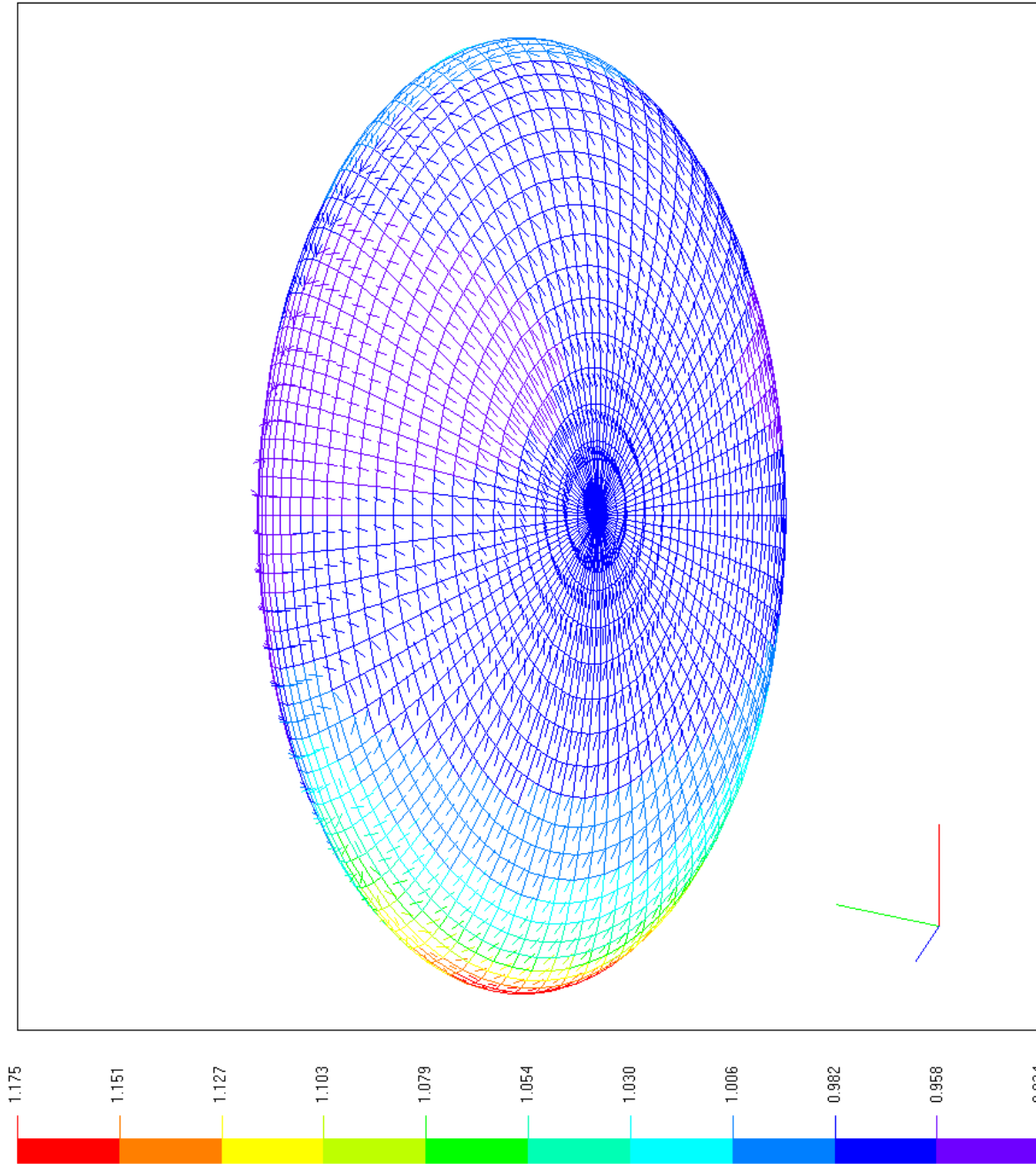
Left Coefficient: Ce = 0.004

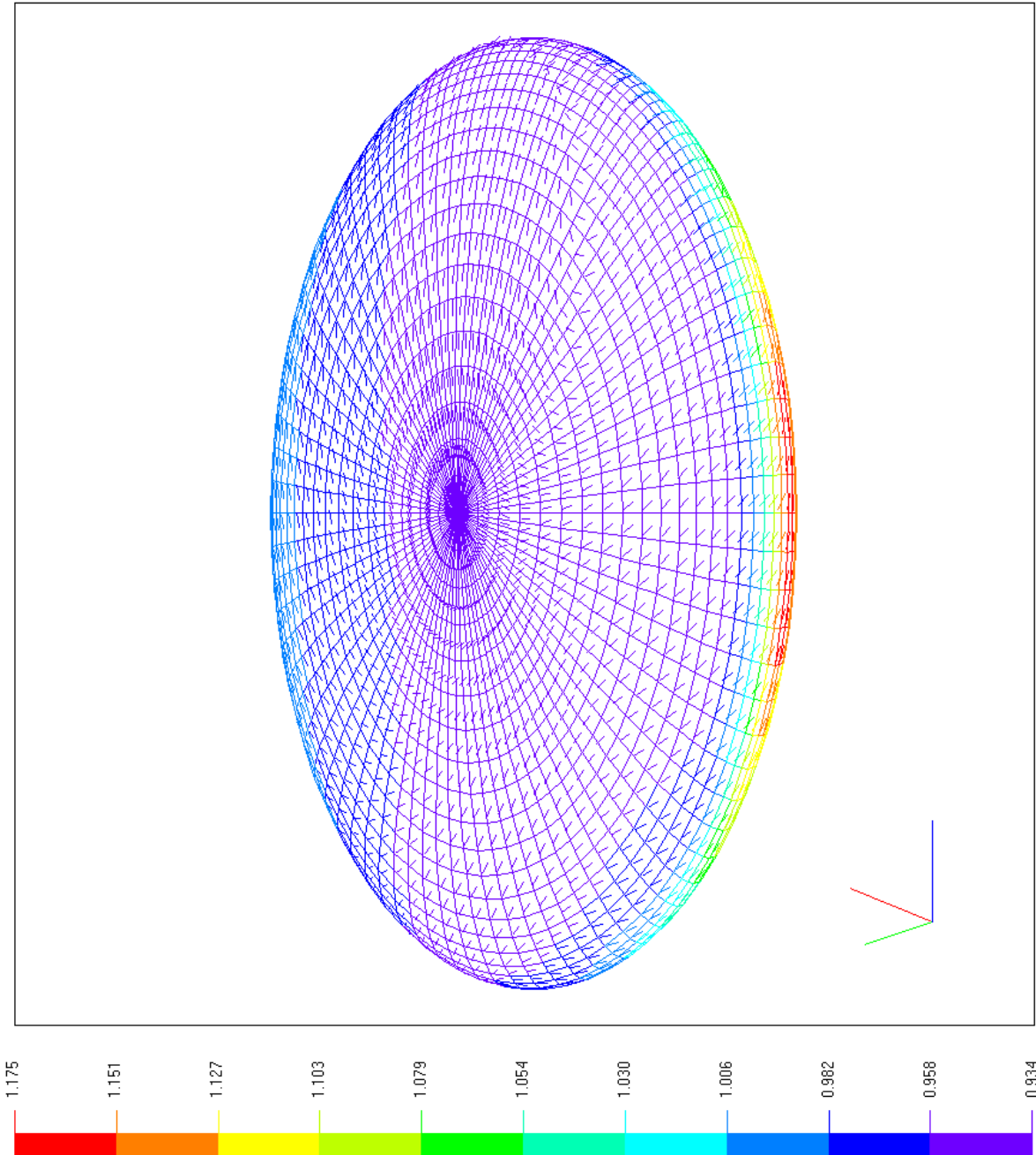
Lift-to-Drag Ratio: L/D = 1.893

X-view: 0.00

Y-view: 0.00

Zoom: 1.00





Test ID: ELL100.tst

Mesh Resolution: 60 x 40 x 80

Spin Ratio: SR = 1.00

Reynolds Number: Re = 3.00E4

Mach Number: M = 0.50

Diameter (m): D = 0.010

Angle of Attack (deg): $\alpha = 5$

Static Pressure (hPa): P = 270

Static Temperature (K): T = 296

Gas Constant (J/kgK): R = 287

Specific Heats Ratio: $k = 1.40$

Run Time (s): t = 0.001000

Time Step (ms): dt = 0.025

Stop Time (s): T = 0.001000

Drag Coefficient: Cd = 0.059

Lift Coefficient: Cl = 0.111

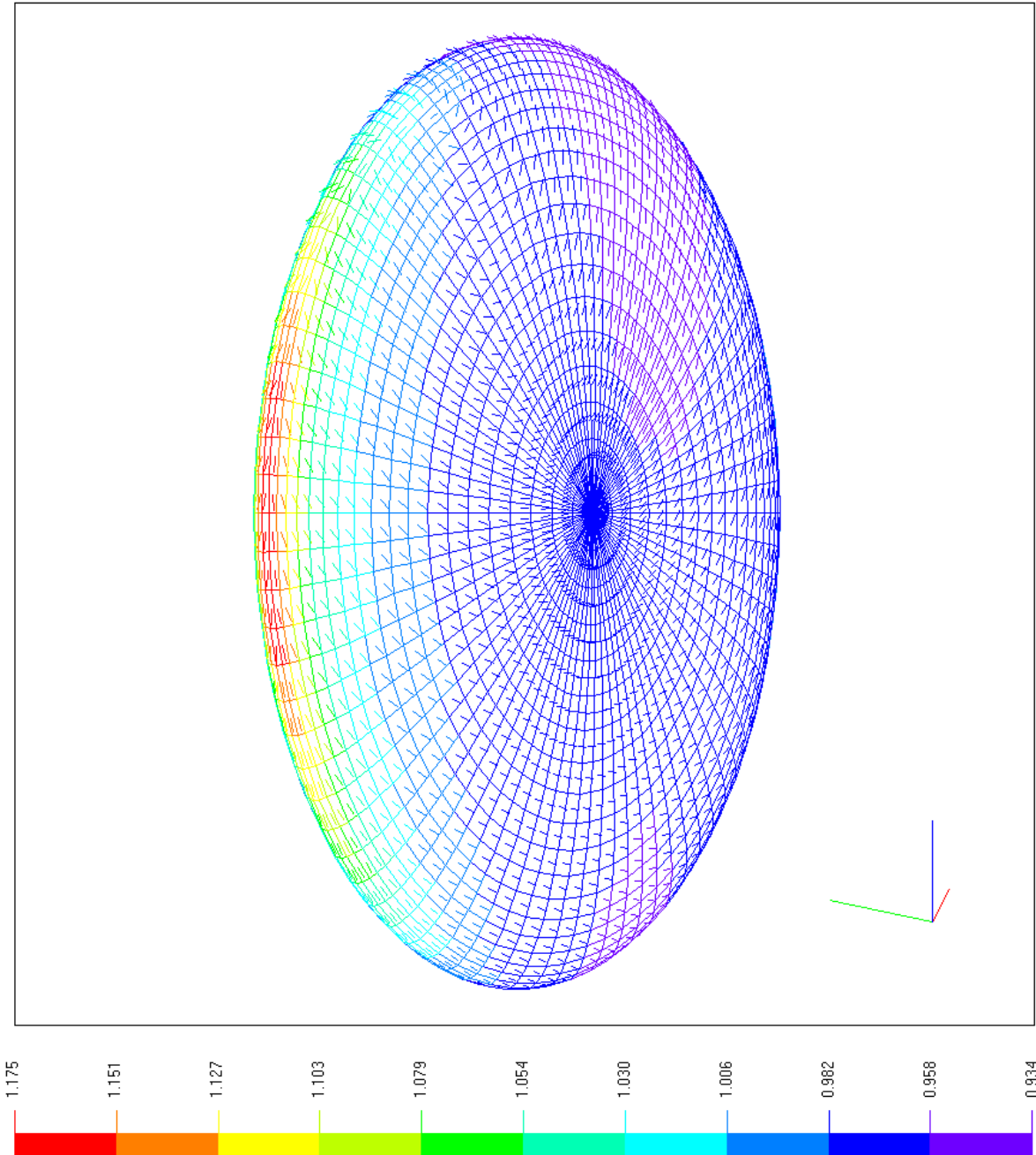
Left Coefficient: Ce = 0.004

Lift-to-Drag Ratio: L/D = 1.893

X-view: 0.00

Y-view: 0.00

Zoom: 1.00



Test ID: ELL100.tst

Mesh Resolution: 60 x 40 x 80

Spin Ratio: SR = 1.00

Reynolds Number: Re = 3.00E4

Mach Number: M = 0.50

Diameter (m): D = 0.010

Angle of Attack (deg): $\alpha = 5$

Static Pressure (hPa): P = 270

Static Temperature (K): T = 296

Gas Constant (J/kgK): R = 287

Specific Heats Ratio: k = 1.40

Run Time (s): t = 0.001000

Time Step (ms): dt = 0.025

Stop Time (s): T = 0.001000

Drag Coefficient: Cd = 0.059

Lift Coefficient: Cl = 0.111

Left Coefficient: Ce = 0.004

Lift-to-Drag Ratio: L/D = 1.893

X-view: 0.00

Y-view: 0.00

Zoom: 1.00

Test ID: ELL100.tst

Mesh Resolution: 60 x 40 x 80

Spin Ratio: SR = 1.00

Reynolds Number: Re = 3.00E4

Mach Number: M = 0.50

Diameter (m): D = 0.010

Angle of Attack (deg): $\alpha = 5$

Static Pressure (hPa): P = 270

Static Temperature (K): T = 296

Gas Constant (J/kgK): R = 287

Specific Heats Ratio: k = 1.40

Run Time (s): t = 0.001000

Time Step (ms): dt = 0.025

Stop Time (s): T = 0.001000

Drag Coefficient: Cd = 0.059

Lift Coefficient: Cl = 0.111

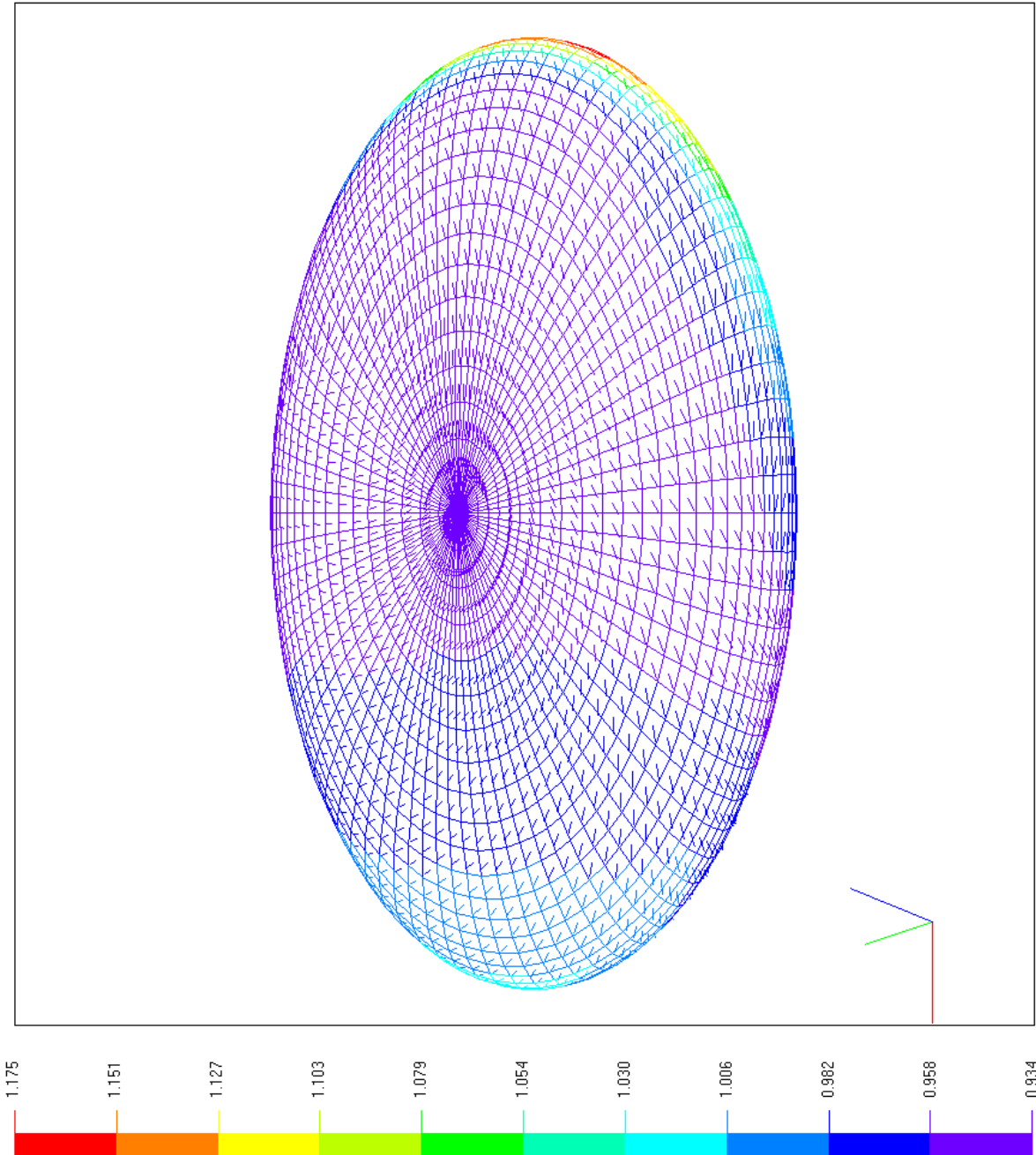
Left Coefficient: Ce = 0.004

Lift-to-Drag Ratio: L/D = 1.893

X-view: 0.00

Y-view: 0.00

Zoom: 1.00



Test ID: ELL100.tst

Mesh Resolution: 60 x 40 x 80

Spin Ratio: SR = 1.00

Reynolds Number: Re = 3.00E4

Mach Number: M = 0.50

Diameter (m): D = 0.010

Angle of Attack (deg): $\alpha = 5$

Static Pressure (hPa): P = 270

Static Temperature (K): T = 296

Gas Constant (J/kgK): R = 287

Specific Heats Ratio: k = 1.40

Run Time (s): t = 0.001000

Time Step (ms): dt = 0.025

Stop Time (s): T = 0.001000

Drag Coefficient: Cd = 0.059

Lift Coefficient: Cl = 0.111

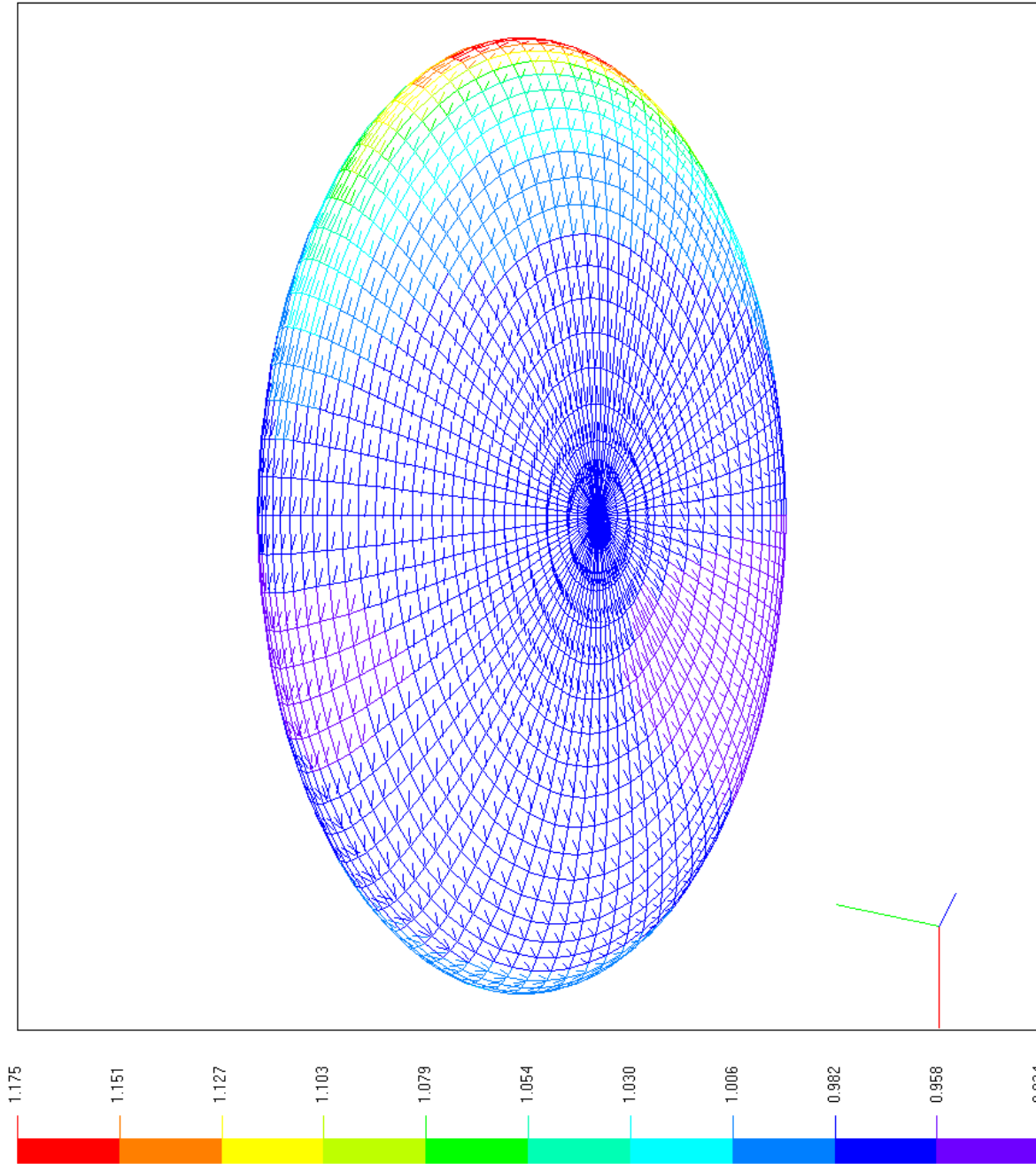
Left Coefficient: Ce = 0.004

Lift-to-Drag Ratio: L/D = 1.893

X-view: 0.00

Y-view: 0.00

Zoom: 1.00



Test ID: ELL100.tst

Mesh Resolution: 60 x 40 x 80

Spin Ratio: SR = 1.00

Reynolds Number: Re = 3.00E4

Mach Number: M = 0.50

Diameter (m): D = 0.010

Angle of Attack (deg): $\alpha = 5$

Static Pressure (hPa): P = 270

Static Temperature (K): T = 296

Gas Constant (J/kgK): R = 287

Specific Heats Ratio: k = 1.40

Run Time (s): t = 0.001000

Time Step (ms): dt = 0.025

Stop Time (s): T = 0.001000

Drag Coefficient: Cd = 0.059

Lift Coefficient: Cl = 0.111

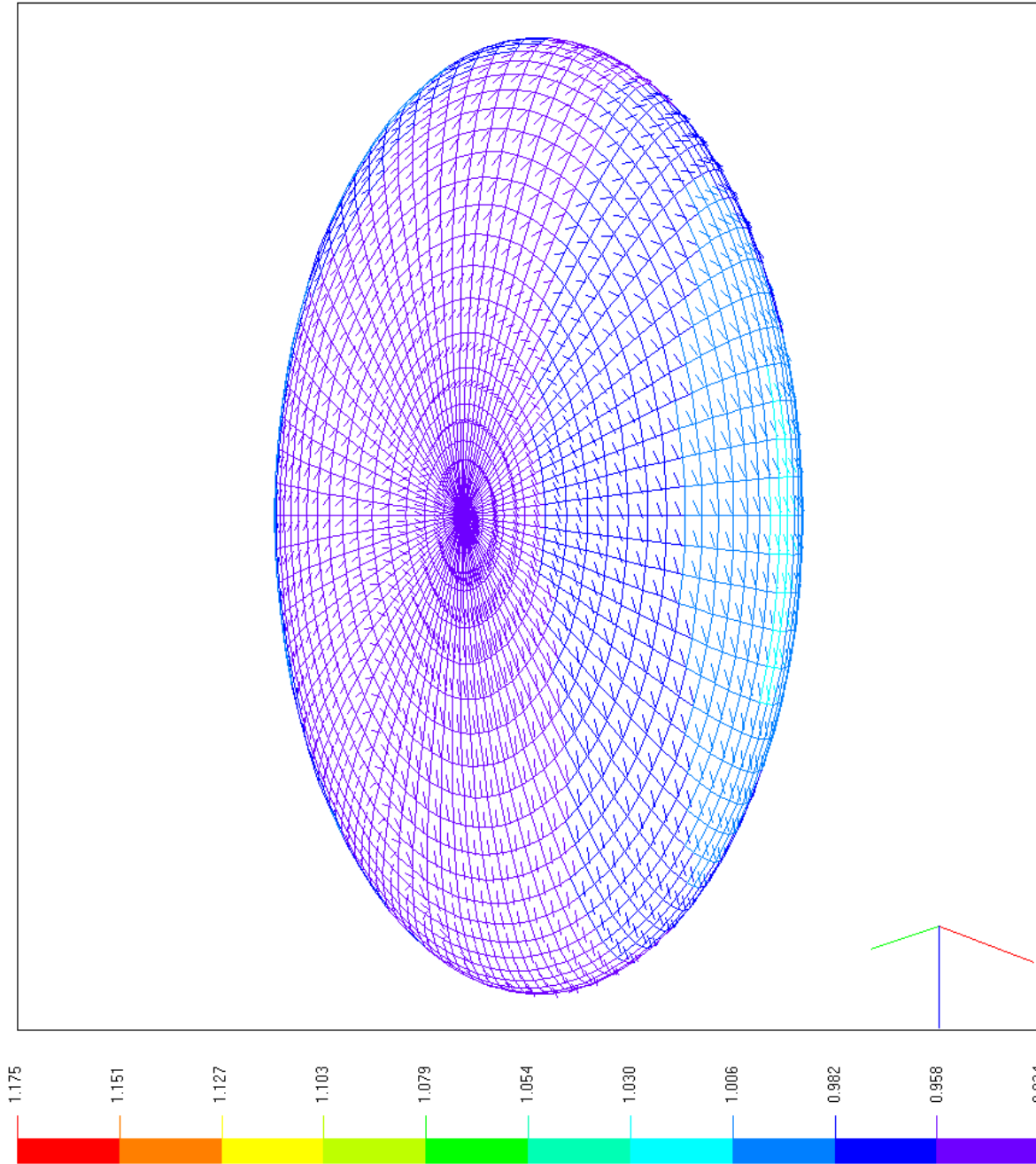
Left Coefficient: Ce = 0.004

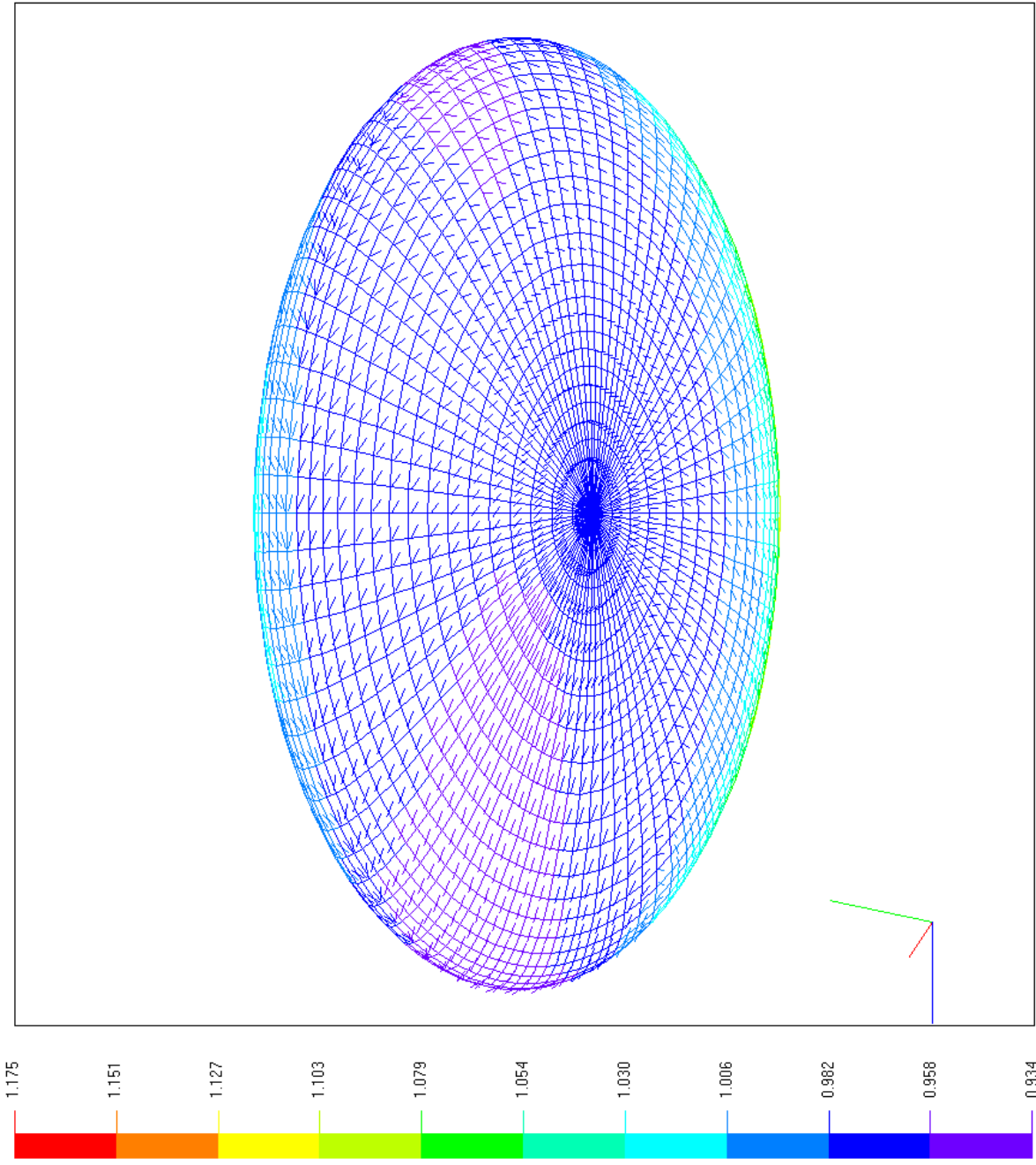
Lift-to-Drag Ratio: L/D = 1.893

X-view: 0.00

Y-view: 0.00

Zoom: 1.00





Test ID: ELL100.tst

Mesh Resolution: 60 x 40 x 80

Spin Ratio: SR = 1.00

Reynolds Number: Re = 3.00E4

Mach Number: M = 0.50

Diameter (m): D = 0.010

Angle of Attack (deg): $\alpha = 5$

Static Pressure (hPa): P = 270

Static Temperature (K): T = 296

Gas Constant (J/kgK): R = 287

Specific Heats Ratio: k = 1.40

Run Time (s): t = 0.001000

Time Step (ms): dt = 0.025

Stop Time (s): T = 0.001000

Drag Coefficient: Cd = 0.059

Lift Coefficient: Cl = 0.111

Left Coefficient: Ce = 0.004

Lift-to-Drag Ratio: L/D = 1.893

X-view: 0.00

Y-view: 0.00

Zoom: 1.00

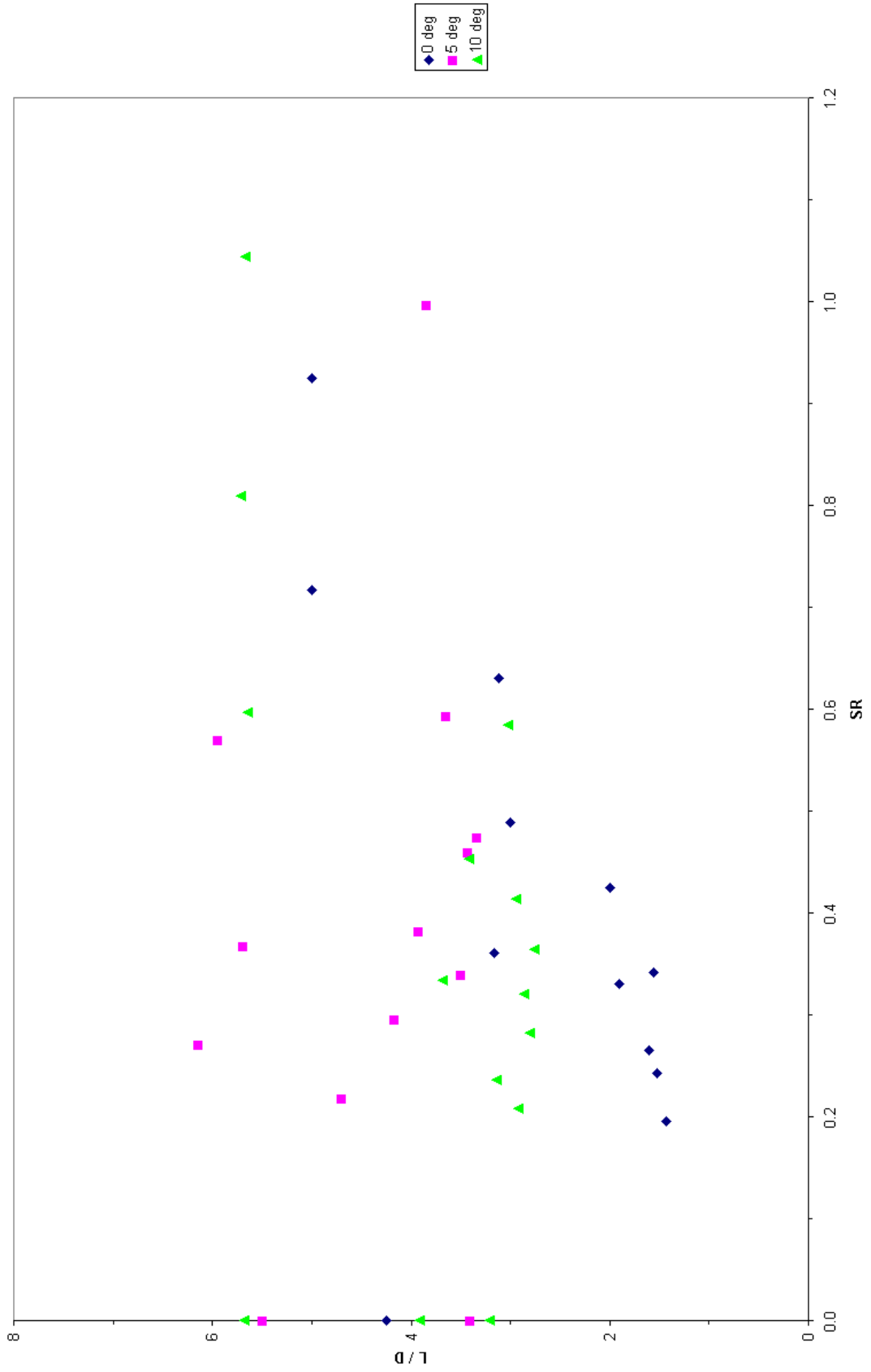
BLANK PAGE

APPENDIX C

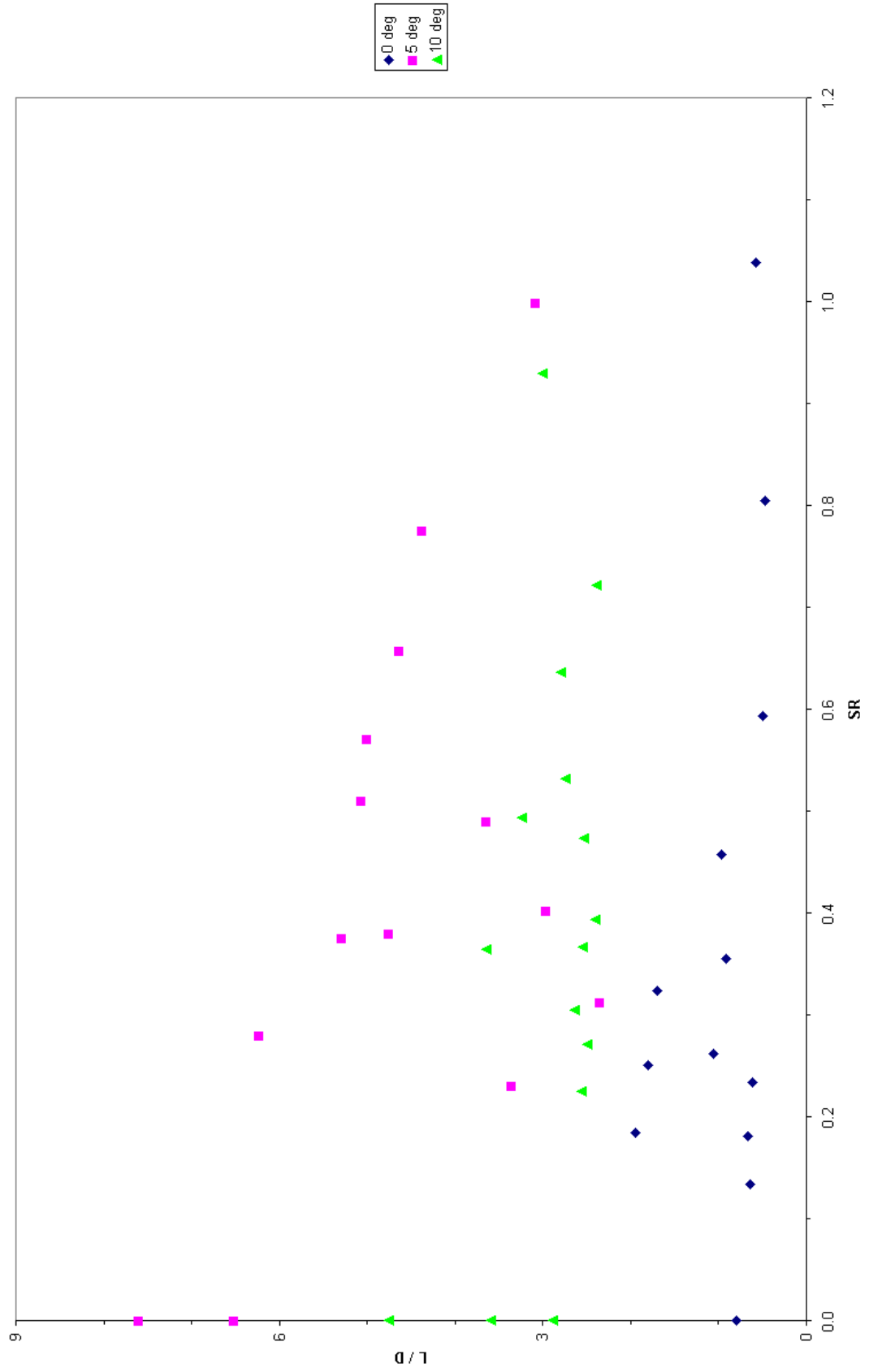
Wind Tunnel Test Results for Three Frisbee Molds
(Data from Brown University 1980 Student Report)

BLANK PAGE

Lift-to-Drag Ratio versus Spin Ratio (97g Mold)



Lift-to-Drag Ratio versus Spin Ratio (119g Mold)



Lift-to-Drag Ratio versus Spin Ratio (165g Mold)

